TECHNISCHE UNIVERSITÄT MÜNCHEN
Lehrstuhl T30d

Indirect Signatures of Unstable Dark Matter in Cosmic-Ray Antimatter and in the Gamma-Ray Sky

David Hoang Tran

Vollständiger Abdruck der von der Fakultät für Physik der Technischen Universität München zur Erlangung des akademischen Grades eines

Doktors der Naturwissenschaften (Dr. rer. nat.)

genehmigten Dissertation.

Vorsitzender:	Univ.-Prof. Dr. Lothar Oberauer
Prüfer der Dissertation:	1. Univ.-Prof. Dr. Alejandro Ibarra
	2. Univ.-Prof. Dr. Michael Ratz

Die Dissertation wurde am 05.07.2011 bei der Technischen Universität München eingereicht und durch die Fakultät für Physik am 18.07.2011 angenommen.

Indirect Signatures of Unstable Dark Matter in Cosmic-Ray Antimatter and in the Gamma-Ray Sky

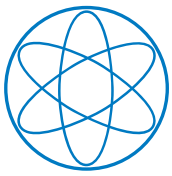

Doctoral Thesis in Physics

submitted by

David Tran

2011

Technische Universität München

Physik-Department

Contents

Zusammenfassung

Wir untersuchen die indirekten Signaturen dunkler Materie in der kosmischen Antimaterie, Gammastrahlung und in Neutrinos in einer Klasse von Modellen, in welchen die dunkler Materie des Universum instabil ist, aber mit kosmologischen Lebensdauern zerfällt. In Teil I stellen wir die zahlreichen Evidenzen für die Existenz der dunklen Materie dar und diskutieren ihre bekannten Eigenschaften. Wir bringen außerdem eine kurze Einführung in die kosmische Strahlung von geladenen Teilchen sowie in die kosmische Gammastrahlung, deren astrophysikalische Komponenten die „Hintergründe“ darstellen, gegen die wir mögliche Signaturen dunkler Materie zu identifizieren versuchen. Die restlichen Kapitel enthalten neue Ergebnisse und basieren auf in Fachzeitschriften veröffentlichten Artikeln, welche im Rahmen dieser Doktorarbeit angefertigt wurden wurden [1, 2, 3, 4, 5, 6, 7, 8, 9]. Es wird auch teilweise Bezug genommen auf einige Ergebnisse, die bereits in der Diplomarbeit des Autors veröffentlicht wurden [10, 11]. In Teil II leiten wir Einschränkungen an die Stabilität der dunklen Materie in verschiedenen Zerfallskanälen auf eine Weise her, die unabhängig vom zugrundeliegenden teilchenphysikalischen Modell der dunklen Materie ist. Wir interpretieren zunächst jüngst beobachtete Anomalien in der leptonischen kosmischen Strahlung als Signatur für den Zerfall dunkler Materie im galaktischen Halo und identifizieren passende Zerfallskanäle. Weiterhin untersuchen wir die Aussichten für eine Entdeckung von Antideuteronen in der kosmischen Strahlung, deren Produktion stark mit der von Antiprotonen korreliert ist. Danach beschäftigen wir uns mit Gammastrahlung und analysieren zunächst die dipolartige Anisotropie in der Zerfallsstrahlung dunkler Materie, welche durch unsere exzentrische Position im galaktischen Halo hervorgerufen wird. Danach untersuchen wir den radiativen Zerfall von „leptophiler“ dunkler Materie in monochromatische Photonen, welcher durch Quanteneffekte induziert wird. Weiterhin leiten wir Abschätzungen für die Einschränkungen her, welche zukünftige Neutrinobeobachtungen an Teleskopen von Kubikkilometer-Dimensionen liefern werden. Im Gegensatz zu diesen modellunabhängigen Studien untersuchen wir in Teil III die Signaturen in der kosmischen Strahlung zweier spezieller supersymmetrischer Modelle für die dunkle Materie, nämlich dem Gravitino in Szenarios mit gebrochener R-Parität, sowie dem Gaugino einer versteckten Abelschen Eichsymmetrie, welches durch kinetische Mischung mit der Hyperladungs-Eichgruppe des Standardmodells zerfällt.

Abstract

We discuss the indirect signatures in cosmic-ray antimatter and gamma rays which may arise in a class of models where the dark matter of the Universe is unstable but decays with cosmological lifetimes. Part I contains a review of the evidence for the existence of dark matter as well as its known properties. It also features a brief introduction to the Galactic propagation of cosmic rays as well as the cosmic gamma radation, the astrophysical components of which will constitute the "backgrounds" against which we try to identify possible dark matter signatures. The remaining chapters contain original work and are based on the author's peer-reviewed journal publications that were prepared in the context of the present doctoral dissertation [1, 2, 3, 4, 5, 6, 7, 8, 9]. Some results previously published in the context of the author's diploma thesis are also cited [10, 11]. In Part II we analyze constraints on dark matter stability in a manner that is independent of the underlying particle-physics model of the dark matter. We interpret recently observed anomalous results in leptonic cosmic rays in terms of the decay of dark matter in the Galactic halo and identify appropriate decay channels. We then analyze the prospects for the detection of antideuterons from dark matter decay, the production of which is closely correlated with the production of antiprotons. Next, we turn to gamma rays, analyzing first the dipole-like anisotropy in the gamma-ray signal from dark matter decay induced by our off-center position in the halo. We then analyze the radiative decays of "leptophilic" dark matter into monochromatic photons induced at the loop level. We further discuss projected constraints for upcoming neutrino observations at cubic-kilometer sized observatories. In contrast, in Part III we analyze two specific supersymmetric models of decaying dark matter with regards to their cosmic-ray signatures, namely the gravitino in models with R-parity violation and the gaugino of an Abelian hidden-sector gauge group which decays via kinetic mixing with the Standard Model hypercharge.

Introduction

The question of the particle nature of the dark matter, which makes up just over 80% of the matter of the Universe, is one of the most prominent questions in cosmology and particle physics today. Despite decades of experimental, observational and theoretical efforts, not much is known to date about the microscopic nature of the dark matter. In this thesis we examine the indirect signatures of a class of dark matter models where the dark matter is not perfectly stable, but instead decays with cosmological lifetimes. The instability of the dark matter then implies that its decay in the Galactic halo and at cosmological distances might leave visible traces in the cosmic radiation, in the flux of neutrinos as well as in cosmic radio waves, X-rays or gamma rays. Identifying and isolating possible dark matter signatures as anomalous excesses over astrophysical "backgrounds" and interpreting their implications is an approach known as indirect dark matter detection.

The field of indirect detection has experienced a surge of activity over the past few years fueled by a number of interesting and unexpected astrophysical observations that have been tentatively interpreted as dark matter signatures. In June 2006, the satellite-based cosmic-ray instrument PAMELA (Payload for Antimatter Matter Exploration and Light-nuclei Astrophysics) was launched. In late 2008 the collaboration reported a spectacular result regarding the abundance of positrons in the cosmic radiation relative to that of electrons, which is much larger than expected at energies above 10 GeV and actually increases with the energy up to at least 100 GeV. This behavior is in stark contrast with the standard picture of positron production by spallation of primary cosmic rays on the interstellar medium. At the same time, PAMELA observed a flux of antiprotons which is completely in agreement with astrophysical expectations.

In June 2008 the Fermi Gamma-ray Space Telescope (FGST, formerly named GLAST) was launched and has since performed full-sky measurements of unprecedented quality of the Galactic and extragalactic gamma-ray emission with its Large Area Telescope (LAT). It has also provided measurements of the combined flux of electrons and positrons over a large range of energies from a few GeV to about one TeV which complement the measurements of the positron fraction performed by PAMELA. Together, these data sets strongly indicate the presence of a significant primary component in the flux of positrons and electrons at high energies. These findings have attracted a lot of attention from both the astrophysical and the particle physics communities, with many authors attempting to find explanations for this puzzling discovery, both in terms of conventional astrophysics, such as the production of e^+e^- pairs by pulsars, and in terms of new fundamental physics, *i.e.*, the annihilation or decay of dark matter particles in the halo.

Independent of these recently observed anomalies, however, it is an interesting and important problem to constrain the lifetime of the dark matter in a model-independent fashion in order to determine which are the most stringent constraints on specific particle physics models and how the various constraints relate to each other. Namely, the different constraints are not independent and can, by means of their complementarity, help establish a more global, multi-messenger picture of indirect dark matter signatures that ensures consistency between different observables. The general understanding of the multifaceted aspects of indirect dark matter detection has significantly improved over the last few years as a side effect of the enormous theoretical activity triggered by the observation of the cosmic-ray anomalies.

The present thesis is organized as follows. In Chapter 1 we begin our discussion by reviewing the extensive evidence for the existence of dark matter and briefly discussing some of the leading candidates. We also introduce the idea of indirect dark matter detection, which is based on identifying anomalous contributions to the fluxes of gamma-rays, neutrinos and cosmic rays. In Chapter 2 we discuss the basic properties of the cosmic radiation, which comprises one of the principal channels for indirect dark matter detection. More precisely, the fluxes of cosmic-ray antimatter, *i.e.*, positrons and antiprotons, are sensitive to exotic contributions because these particles are only produced as secondary products by the astrophysical processes of cosmic-ray interactions and thus have low, calculable backgrounds. We explain how to calculate the fluxes of cosmic rays as they are measured locally, after primary particles are injected in the halo and propagate in a complicated manner, suffering the effects of diffusion, energy loss and annihilation. Next, in Chapter 3 we discuss the cosmic gamma radiation, which constitutes probably the most important channel to look for astrophysical traces of dark matter. We explain the production of gamma rays from inverse Compton scattering of energetic positrons and electrons on the interstellar radiation field.

After our preliminary discussion we examine in Part II various indirect detection channels and discuss possible constraints on the nature of the dark matter. We begin in Chapter 4 by a general examination of the anomalous results in leptonic cosmic rays observed by PAMELA, Fermi LAT, H.E.S.S., ATIC and PPB-BETS. We interpret the observed rise in the positron fraction in terms of dark matter decay and identify decay channels that can reproduce the observational data. We then turn in Chapter 5 to hadronic dark matter decay and analyze the production rate of cosmic-ray antideuterons. These particles have not been detected in the cosmic radiation so far, and only upper bounds on their flux exist. The formation of antideuterons by spallation of cosmic rays in interstellar gas is an exceedingly rare process. However, if the antiprotons and antineutrons that fuse into antideuterons originate in the fragmentation of a weak gauge boson or Higgs boson, then this process can be significantly enhanced over the astrophysical mechanism. We emphasize that even for antiproton fluxes that are compatible with existing measurements, an antideuteron signal from dark matter decay may be in the observable range. Next, we examine in Chapter 6 the peculiar angular dependence of a gamma-ray signal from dark matter decay in the Galactic halo. Due to our excentric location in the dark matter halo, the prompt radiation from dark matter decay exhibits a dipole-like anisotropy. We estimate the size of this anisotropy in the overall gamma-ray flux in different scenarios and find that it can be sizable. The observation of a signal with the correct dipole-like anisotropy would lend support to the idea of dark matter decaying in the halo, or otherwise yield constraints on this scenario. The non-observation of an excess in antiprotons has led many authors to consider "leptophilic" models of dark

matter, which are exlusively or predominantly coupled to charged leptons. Due to this property, such models evade constraints on antiproton overproduction, motivating efforts to find different ways to test them. In Chapter 7 we examine a next-to-leading order effect of such models, namely the decay into monochromatic photons. To this end, we consider a toy model of leptophilically decaying dark matter and study the ratio of one-loop decays into photons to the leading-order decays into leptons and demonstrate that the radiative decays can have some relevance to indirect dark matter detection despite being loop suppressed. We discuss how to search for these lines in observations of the halo as well as of extragalactic sources. In Chapter 8 we then examine a set of different constraints stemming from the analysis of anomalous neutrino signatures induced by dark matter decay. These neutrino signatures almost inevitably accompany other indirect signatures and can provide an important cross check. Due to the presence of large atmospheric neutrino fluxes, dark matter contributions to the neutrino flux are difficult to disentangle from the background. Furthermore, the low interaction cross-sections of neutrinos require very large detectors to be sensitive to the very small fluxes expected from dark matter decay. Current constraints from SuperKamiokande are not competitive with those in gamma rays and cosmic-ray antimatter. However, the upcoming generation of neutrino telescopes of km^3 dimensions should reach the necessary sensitivity to confirm or exclude a sizable contribution from dark matter to the cosmic-ray fluxes within a reasonable timeframe. We estimate projected constraints attainable with this new generation of neutrino telescopes, in particular with the recently completed IceCube detector.

Finally, in Part III we discuss two specific supersymmetric models of decaying dark matter. In Chapter 9 we examine the scenario of gravitino dark matter in the presence of R-parity violation, which is motivated by cosmological considerations. Finally, in Chapter 10 we analyze a scenario where a subdominant component of the dark matter is composed of the gauginos of an additional Abelian hidden-sector gauge group which decays via kinetic mixing via the Standard Model hypercharge gauge group. We try to interpret the observed leptonic cosmic-ray anomalies in these models and discuss constraints. The gravitino does not possess the required leptophilic coupling to matter to be a viable explanation of both the rise in the positron fraction and the hard electron spectrum at high energies while remaining in agreement with antiproton constraints. However, we show that existing constraints on the antiproton flux leave some room for distinct gamma-ray signatures of this scenario, which may include a monochromatic line at the end of the spectrum, making the scenario of gravitino dark matter testable by gamma-ray observations. The scenario where a portion of the dark matter is composed of hidden gauginos, on the other hand, rather naturally yields leptophilic and flavor-blind couplings which can reproduce the cosmic-ray anomalies in a scenario where the hidden gaugino decays into the lightest neutralino or vice versa. In particular, for a hidden gaugino with a mass around 600 – 1200 GeV and a lightest neutralino in the coannihilation region of minimal supergravity (mSUGRA), it is possible to reproduce the positron fraction in a cosmologically consistent model while remaining in agreement with antiproton overproduction constraints. We also discuss how this scenario can be tested by gamma-ray observations.

Part I

Preliminaries

Chapter 1

The Dark Universe

One of the most surprising findings to emerge from cosmological and astronomical studies over the last decades is that most of the energy density of the Universe is of an unknown type – about 70% of the total energy budget is in the form of so-called dark energy, while 26% is comprised of dark matter, which has no significant interactions with light, neither through emission nor absorption. The ordinary baryonic matter that we and the world of our immediate experience are made of makes up a mere 4% of the total energy content of the Universe. It is thus a rather surprising discovery that the matter content of the Universe is dominated by an unknown form of non-luminous matter which outweighs ordinary baryonic matter by about a factor of five.

While the nature of the dark energy, which drives the accelerated expansion of the Universe, remains positively mysterious, the dark matter is most likely comprised of some hitherto undiscovered type of elementary particle. While the discovery that most of the matter in the Universe is dark was certainly surprising at first, the existence of dark matter is perfectly natural since there is no good reason to expect that all matter particles in Nature should interact electromagnetically (and we have long known about the existence of neutrinos which have no electromagnetic interactions and make up a small fraction of the dark matter). In fact, many extensions of the Standard Model of particle physics, intended to address some of the deficiencies of the Standard Model, also predict the existence of new particles that in principle have the appropriate properties to constitute the dark matter. Despite decades of experimental, observational and theoretical efforts, however, not much is known about the microscopic nature of the dark matter to date. The abundance of dark matter has been accurately determined from cosmological observations, but its identity remains unknown, and it remains at present unclear whether dark matter has any non-gravitational interactions.

In this chapter we review the extensive evidence for the existence of dark matter and then outline some of its established properties. We introduce some leading dark matter candidates and discuss the concept of unstable dark matter, which can give rise to an alternative to the standard picture of indirect detection by pair-annihilation of WIMPs. For some good introductory and review articles on the topic of dark matter, see [12, 13, 14, 15, 16].

1.1 Evidence for the Existence of Dark Matter

A discrepancy between the amounts of visible matter and gravitationally interacting matter both in the Milky Way and in galaxy clusters was first noticed in the early 1930s. Oort studied the Doppler shifts of stars near the Galactic plane in 1932, finding stellar velocities that exceed the escape velocity of the Milky Way, unless there exists some significant amount of unseen mass in the Galaxy that is sufficient to bind these stars to their orbits [17]. Almost at the same time, Zwicky inferred in 1933 from Doppler-shift studies of the velocity dispersion of galaxies in the Coma cluster that the total mass of the cluster must vastly exceed the luminous mass. He did this by using well-established mass-to-light (M/L) ratios to estimate the luminous cluster mass and by applying the virial theorem to estimate the gravitationally interacting mass from the measured velocity dispersion [18].

These findings did not attract much attention until in the 1970s, Rubin and collaborators, as well as Bosma, systematically studied the rotation curves of M31 and other edge-on spiral galaxies based on the redshift/blueshift of spectral lines, finding a significant deviation from the behavior expected from Newtonian gravity [19, 20, 21]. Namely, beyond a certain luminosity radius that contains most of a galaxy's mass, one would expect the rotation curves to fall off with the radial distance like $\propto 1/\sqrt{r}$. Instead, the rotation curves are observed to flatten, *i.e.*, the rotational velocities stay nearly constant or fall off much more slowly than expected from the stability of the galaxies. From this, one can infer that the majority of the total mass of these spiral galaxies cannot be concentrated in the central bulge, unlike the bulk of the luminous mass, since otherwise the outer stars would exceed escape velocity. If the rotation curves become essentially independent of the radius beyond the luminosity distance, this implies that a spherically symmetric total mass distribution would have to go with the radial distance like $\rho(r) \propto r^{-2}$ beyond this radius. This means that the distribution of luminous matter in the form of stars and interstellar gas is dramatically different from the distribution of the entirety of the gravitationally interacting matter. Flat rotation curves have since been observed in many other spiral galaxies, including our own [22, 23]. Further kinematical evidence on galactic scales has also been found from the velocity dispersion of dwarf galaxies in the Local Group [24].

Another technique to probe mass distributions on cluster scales became available around the same time as the studies of galactic rotation curves, namely the use of gravitational lensing of light as predicted by general relativity. Strong lensing surveys search for the (partial) arks and multiple images caused by the bending of light from distant objects caused by the presence of large amount of matter along the line of sight. Galaxy clusters can serve as sources for strong lensing and have been found in this way to contain much more matter that the luminous matter [25]. Strong lensing effects are rare, however. Evidence for dark matter also exists from weak lensing [26], which makes use in a statistical manner of the effect of systematic alignment and distortion of light sources around a lensing foreground mass. Weak lensing can be used in this way to probe the mass distribution along the line of sight and thus map the spatial distribution of dark matter in three dimensions [27].

Evidence for dark matter further comes from hot intracluster gas in galaxy clusters, in which the majority of the baryonic cluster mass resides. The ratio of the fraction of gas to the total mass allows a determination of the dark matter content of the clusters (see,

e.g, [28]). The gas density of the cluster can be determined from its X-ray emission or from the Sunyaev–Zel'dovich effect [29], while the total cluster mass can be inferred from the peculiar motions of the galaxies within the cluster, from assuming that the intracluster gas is in hydrostatic equilibrium or from weak gravitational lensing. Furthermore, if one assumes that the composition of rich clusters on scales of several Mpc is a representative sample of the overall matter composition on cosmological scales, one can extrapolate the gas-to-total mass fraction to yield an estimate of the overall baryon-to-mass ratio in the Universe. Such determinations agree [30] with other determinations from cosmological observations of the cosmic microwave background (CMB), primordial nucleosynthesis and large-scale structure, as discussed below.

The above kinematical evidence points to the existence of some form of matter on galactic and cluster scales that is "dark" in the sense that it does not significantly emit, absorb or reflect light. However, observations of the gravitational effects of this unseen matter on the kinematics of stars and galaxy clusters and on the propagation of light do not necessarily imply that this dark matter necessarily be composed of some kind of new elementary particle. Indeed, maybe the most straightforward idea to account for the above observations is to assume that the dark matter is composed of compact baryonic objects with very low mass-to-light ratios, such as brown dwarfs, neutron stars, unassociated exoplanets or primordial black holes. Collectively, such astrophysical objects are known by the name of "massive compact halo objects" (MACHOs). These objects would distort light emission of distant objects through a change in the apparent brightness of light sources [31] and have thus been searched for in microlensing studies. The collaborations MACHO [32] and EROS-2 [33] have been able to significantly constrain the MACHO hypothesis by observing the luminosities of stars in the Large and Small Magellanic Clouds. They observed very few microlensing candidates, implying that only a fraction of the Galactic dark matter (less than 8% according to EROS and less than 40% according to MACHO) can be contained in compact baryonic objects, and that the dark matter cannot be strongly concentrated. Some fraction of the dark matter may be contained within diffuse baryonic interstellar and intercluster gas, however.

Modern evidence for dark matter comes primarily from cosmology in the form of observations of the large-scale structure of the Universe, distant supernovae and the temperature anisotropies of the CMB, as well as from the synthesis of primordial elements. These cosmological observations yield the crucial piece of information that the dark matter cannot be composed of baryons and, as a corollary, of Standard Model particles. An important source of information in this respect is Big Bang nucleosynthesis (BBN), the process by which the light elements were formed in the early Universe [34, 35]. The synthesis of primordial elements is described in terms of a network of coupled Boltzmann equations for the nuclear reaction network, where the reaction rates are sensitive to the overall baryon density. BBN thus gives a prediction for the light element abundances as a function of the baryon-to-photon ratio η, and can thus give a value for the baryon content of the Universe at that epoch by comparing the predictions with the observed light element abundances. This yields a determination of Ω_{B} that is completely independent from the one inferred from CMB observations (described below), using different physics and processes taking place at very different epochs. From a combined fit to the abundances of the light elements ^{4}He, D, ^{3}He and ^{7}Li one finds [35]

$$0.019 \leq \Omega_{\mathrm{B}} h^2 \leq 0.024 \quad (95\%\ \mathrm{C.L.})\,, \tag{1.1}$$

which agrees well with the determination of $\Omega_{\rm B}$ from the WMAP observations of the CMB, see Eq. (1.3) below. As we will see, however, from other cosmological observations one finds $\Omega_{\rm B} < \Omega_{\rm M}$, implying that baryonic matter can only make up a fraction of the total matter.

Evidence for dark matter is also available from large scale structure [36], both from the observational and the computational side. N-body simulations of structure formation indicate a need for dark matter. Namely, without dark matter the simulations fail to reproduce the observed large-scale structure of filaments and voids as observed by the Sloan Digital Sky Survey (SDSS) [37]. More specifically, one also finds that the dark matter should be non-relativistic, or "cold," during structure formation [38, 39]. Dark matter which is relativistic, or "hot," leads to a washout effect that delays the formation of structure. The reason is that the collisionless dark matter dampens primordial density fluctuations below the dark matter free-streaming length as it flows from overdense to underdense regions. The large damping scales from the free streaming of relativistic dark matter from high-density regions then leads to a top-down type of structure formation where the largest structures form first, with smaller structures subsequently fragmenting from larger ones [40], as opposed to the observed bottom-up hierarchical type of structure formation [41]. For this reason, significant fractions of hot dark matter are now disfavored. Stringent constraints on hot dark matter can be imposed especially when also taking data from the Lyman-α forest into account [42, 43]. Cold dark matter, on the other hand, allows for clumping on small scales, and N-body simulations containing cold dark matter can successfully reproduce the observed large-scale structure [44, 45]. Furthermore, surveys of the three-dimensional distribution of stars, galaxies are quasars can, by making statistical inferences from the spatial distribution of these objects, yield an observational determination of the matter power spectrum whose peak is sensitive $\Omega_{\rm M}$, while its shape is affected by $\Omega_{\rm B}$ through baryon acoustic oscillations. The SDSS collaboration finds from their data $\Omega_{\rm M} = 0.286 \pm 0.018$ [46], which is again compatible with the value inferred from BBN and CMB observations.

The redshift evolution of the Hubble rate is influenced by the total amount of matter and radiation in the Universe and can be probed by observations of supernovae. More specifically, type Ia supernovae are commonly used as standard candles in observational cosmology due to their highly regular peak luminosities, which can be determined from measurements of the light curves. The peak luminosities of type Ia supernovae can therefore be used to establish luminosity distances. Combined with redshift measurements this enables the determination of luminosity distance–redshift relations which are sensitive to the evolution of the Hubble rate and hence to the energy composition of the Universe [47, 48, 49, 50]. Constraints on the Ω_Λ–$\Omega_{\rm M}$ parameter space from type Ia supernova observations are plotted in Fig. 1.1. They converge with other kinds of measurements including baryon acoustic oscillations (BAO) and CMB anisotropies, indicating that the Universe is flat and dominated by some form of negative-pressure dark vacuum energy which accelerates the expansion of the Universe. This dark energy can be well described by a tiny, but non-vanishing cosmological constant with an equation of state $p = -\rho$.

The most precise determination of the overall dark matter abundance comes from CMB observations. The CMB is composed of photons that were emitted at the time of recombination at redshift $z \sim 1100$ when electrons combined with hydrogen and helium nuclei, with the consequence of the Universe becoming transparent to photons. These photons from the last

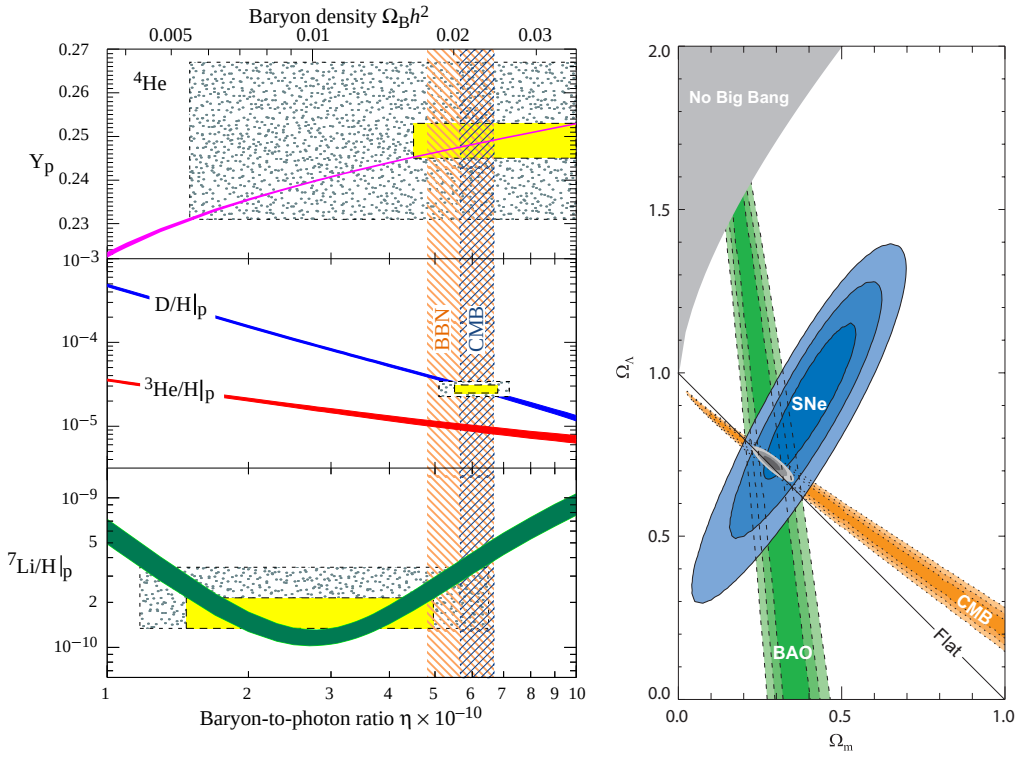

Figure 1.1: *Left:* Predictions for light element abundances from BBN as a function of the baryon-to-photon ratio η (from [35]). *Right:* Different constraints on the Ω_Λ–Ω_M parameter space in concordance cosmology using CMB observations, supernova data and large-scale structure (from [50]). The different techniques yield consistent values for the cosmological parameters.

scattering surface carry information about the acoustic oscillations of the baryon–photon fluid at the time of their decoupling. Observations by the Cosmic Background Explorer (COBE) revealed that the CMB is a near-perfect black body at a temperature of 2.73 K, although the radiation exhibits minute temperature fluctuations [51]. On large angular scales these fluctuations are due to the Sachs–Wolfe effect, while the small-scale anisotropies are sensitive to the dynamics of the acoustic oscillations. In this way the temperature fluctuations probe the baryon density at the time of recombination.

According to concordance cosmology, these temperature fluctuations are due to primordial quantum fluctuations blown up to cosmological scales by inflation. The primordial temperature fluctuations observed by COBE are tiny, however – the CMB is uniform to one part in 10^5, and therefore the primordial fluctuations are too small to serve as the seeds of structure formation within the available timeframe [51]. The reason is that the electrostatic repulsion of baryonic matter, which only becomes electrically neutral at the time of recombination, prevents efficient clumping into gravitational wells and thus delays structure formation to the point that there would not have been enough time between recombination and the present day to evolve the observed structure. Therefore, some form of electrically neutral dark matter is required that can begin undergoing gravitational collapse well before recombination.

The primordial temperature fluctuations in the CMB have since been mapped with high precision by the Wilkinson Microwave Anisotropy Probe (WMAP). The temperature fluctuations can be decomposed into an angular power spectrum, where the relative heights of the acoustic peaks are sensitive to the baryon density $\Omega_{\rm B}$ and the matter density $\Omega_{\rm M}$. The position of the first acoustic peak provides a measure of the overall energy density of the Universe, *i.e.*, the sum $\Omega_0 = \Omega_\Lambda + \Omega_{\rm M}$ (radiation contributes a negligible amount to the total energy density). From fits of these cosmological parameters to the observed temperature fluctuations, the WMAP observations prefer a value of $\Omega_\Lambda + \Omega_{\rm M} \simeq 1$, corresponding to a flat universe. When combined with information from supernovae, galaxy clusters and structure formation, the data strongly favor $\Omega_\Lambda + \Omega_{\rm M} = 1$ (see Fig. 1.1).

The dark energy density makes up the major part of the total energy budget. In the ΛCDM model the WMAP collaboration finds from their seven-year data alone [52]

$$\Omega_\Lambda = 0.727^{+0.030}_{-0.029}\,, \tag{1.2}$$

where the errors indicate 68% C.L. For the baryon density, on the other hand, the WMAP collaboration finds

$$\Omega_{\rm B}h^2 = 0.02249^{+0.0056}_{-0.0057}\,, \tag{1.3}$$

where $h = 0.704 \pm 0.025$ [53] is the present-day reduced Hubble rate in units of 100 km s^{-1} Mpc^{-1}. It is clear that the amount of baryonic matter alone is insufficient to close the Universe. For the dark matter density one finally obtains

$$\Omega_{\rm DM}h^2 = 0.1120 \pm 0.0056\,, \tag{1.4}$$

with $\Omega_{\rm DM}/\Omega_{\rm B} \simeq 5$, or more than 80% of the matter in the Universe being non-baryonic dark matter. The matter density can be derived from the above quantitites with the result

$$\Omega_{\rm M}h^2 = 0.1345^{+0.0056}_{-0.0055}\,. \tag{1.5}$$

Clearly, the values of $\Omega_{\rm B}$ and $\Omega_{\rm M}$ differ significantly. The WMAP data can be combined with other cosmological data from large-scale structure and supernova observations to improve the accuracy of the determinations of the cosmological parameters, but this introduces additional systematics. We will use the above values for the ΛCDM cosmological parameters (or the numerically similar values from the five-year WMAP data) in the following chapters.

Recently, some spectacular observations of cluster mergers have delivered direct proof of the existence of dark matter on cluster scales. The so-called Bullet cluster provides direct evidence of the existence of dark matter on the scale of large clusters [54]. The name refers a subcluster that collided with the main cluster 1E 0657-56 about 150 million years ago. The cluster merger led to the compression and shock-heating of the intracluster gas, which constitutes the bulk of the baryonic mass of the cluster, while the individual galaxies within the clusters simply passed through each other. The hot gas emitted large amounts of X-rays which were detected by the Chandra X-ray Observatory and used to map the distribution of the baryonic cluster mass. The gravitational mass distribution of the cluster, on the other hand, was determined by weak lensing as observed by the Hubble Space Telescope. It was found that the total center of mass followed the galactic trajectories and was significantly

displaced by the merger from the center of the baryonic mass, which is just what one would expect if the cluster mass is dominated by collisionless dark matter. Another very similar cluster merger involving a cluster named MACS J0025.4-1222 was discovered in 2008 [55].

In spite of all this impressive evidence, it should be noted that it has been attempted to avoid the introduction of dark matter by modifying gravity at the Newtonian level. Such efforts are known by the name of "modified Newtonian dynamics" (MOND) [56]. Theories of modified gravity can reproduce the rotation curves of spiral galaxies well and automatically deliver the Tully-Fisher relation [57] (which notably fails on cluster scales, however). Nevertheless, theories with modified dynamics have many problems, such as MOND not working for dwarf spheroidal galaxies and for galaxy clusters [58]. Furthermore, MOND cannot account for observations like the Bullet cluster without introducing dark matter on top of the modified dynamics [58]. Problematically, it is difficult to embed MOND into relativistic theories and therefore to discuss the cosmology of such theories. However, sucessful efforts, such as Tensor-Vector-Scalar (TeVeS) gravity [59], have been made to construct relativistic theories that lead to non-Newtonian dynamics. However, the cosmological implications of TeVeS gravity have been studied and found to fail to reproduce the CMB power spectrum as well as the matter power spectrum [60].

To summarize, one has overwhelming evidence from a substantial number of independent observations based on entirely different underlying physics which require the existence of substantial amounts of dark matter over a vast hierarchy of scales ranging from individual dwarf and satellite galaxies to the largest structures in the Universe, the superclusters and filaments. Since this dark matter must be non-baryonic, this strongly hints at the existence of a new type of elementary particle.

The only particles within the Standard Model that could potentially constitute the dark matter would be massive neutrinos, but it is known that due to their tiny masses, they only contribute a fraction of the observed dark matter abundance. In fact, for the current limits on light neutrino masses the upper bound on the contribution of neutrinos to the energy density is [61]

$$\Omega_\nu h^2 \leq 0.0067 \quad (95\% \text{ C.L.})\,. \tag{1.6}$$

Furthermore, neutrinos are relativistic and hence constitute hot dark matter, which is strongly constrained as mentioned above. Therefore, the observation of large quantities of non-baryonic dark matter in the Universe and the absence of any known suitable particle candidate is a very strong empirical case for the existence of physics beyond the Standard Model.

Despite the successes of the CDM paradigm, it should be noted that there remain some open problems. Namely, N-body simulations typically predict more substructures in CDM halos than actually observed in the form of satellite galaxies [62, 63]. Furthermore, such simulations generally find "cuspy" profiles which are divergent at the center of the halos, contrary to the cored profiles inferred from observations of gas-rich dwarf spiral and low surface brightness galaxies [64, 65]. Whether these discrepancies are due to observational problems, technical limitations of the simulations, *e.g.* the neglect of baryon–dark matter interactions, or due to genuine deficiencies in the understanding of the underlying physics is presently unclear.

1.2 Approaches to Dark Matter Identification

Aside from the large amounts of gravitational evidence for the existence of dark matter we also have a distinct lack of evidence for any non-gravitational interactions, which allows us to infer some fundamental properties of the dark matter. We have already mentioned the requirement that dark matter should not be hot. Furthermore, negative searches for exotic isotopes imply that the dark matter has to be electrically neutral. Although specific bounds have a degree of model dependence, electrically charged dark matter is practically ruled out [66]. Likewise, dark matter with $SU(3)_C$ charge is essentially ruled out over a wide range of masses. See [66] for a discussion on constraints on electrially charged (and milli-charged), as well as strongly interacting dark matter. There also exist indirect constraints on the nature of the dark matter from the requirement that it should not disturb the successful predictions of primordial nucleosynthesis [67] or affect stellar evolution (see [66] for a detailed discussion and references).

We can summarize that at the very least, any viable dark matter candidate should have the properties of being massive, electrically neutral, colorless, non-baryonic, cold (or possibly warm), and stable on cosmological timescales. All of the above properties have been inferred from the gravitational interactions (and absence of evidence for non-gravitational interactions) of the dark matter. Due to the universality of gravity, a determination of the particle nature of the dark matter from its gravitational interactions alone is impossible. Since from a particle physics point of view it is highly desirable to determine the particle identity of the dark matter, there is a strong motivation to find non-gravitational dark matter signatures.

There are three main approaches to finding non-gravitational dark matter signatures:

- Collider searches aim to produce dark matter particles directly via particle collisions at high energies. Assuming that this is possible, they would escape without interacting with the detectors due to their weak interactions with ordinary matter. Thus, the dark matter would show up in experiments as missing energy and momentum in a manner similar to neutrinos. By determining the mass and couplings of the invisible particles to other particles, one could then calculate the corresponding relic abundance [68] and compare it with the observational value to determine whether the invisible particles could constitute the dark matter of the Universe.

- Direct detection of dark matter is based on the idea that WIMPs which are gravitationally bound to our galaxy may interact with a detector by scattering with target nuclei [69] or electrons, depositing energy in the form of phonons, scintillation light or ionization. For typical WIMP masses between 10 GeV and 10 TeV, the nuclear recoil energies deposited by elastic scattering are expected to be of order 1 to 100 keV [61]. To be sensitive to such low energies, detectors must be shielded from cosmic radiation and natural radioactivity are are therefore located in underground laboratories. Another possibility of detecting a WIMP signal is the idea of trying to detect a seasonal variation in the overall signal due to the Earth's movement relative to the WIMP halo [14].

- Indirect detection is based on the idea of detecting the annihilation or decay products of dark matter in the cosmic radiation or in photons or neutrinos. It originated in the realization that the very same self-annihilation processes that can lead to the correct relic abundance of WIMPs may still occur today at a rate large enough to detect the

annihilation products as anomalous contributions to the fluxes of cosmic particles reaching us from space. Suitable channels to look for dark matter signatures are those that have low, ideally well-understood backgrounds. This includes primarily cosmic-ray antimatter, photons in the X-ray to gamma-ray energy range, as well as neutrinos. In the present thesis we focus on this approach. For pioneering work on indirect dark matter detection see, *e.g.*, [70, 71] on gamma rays from dark matter annihilation and [72] on antiprotons and positrons, as well as [73] on neutrinos from dark matter annihilation in the Sun.

1.3 Particle Candidates for Dark Matter

In principle, the easiest way to fulfill the above requirements is to postulate a particle that has only gravitational interactions. However, this possibility is unappealing from the phenomenological perspective since it lacks predictiveness, testability and is not connected to any kind of new physics. However, there is no lack of dark matter candidates motivated by shortcomings of the Standard Model of particle physics. Namely, even though the Standard Model describes the interactions of elementary particles with an accuracy beyond any reasonable expection, it contains some theoretical flaws, such as the hierarchy problem and the strong *CP* problem. Many proposed extensions of the Standard Model that seek to address such problems also predict the existence of new particles that may play the role of the dark matter.

Strictly speaking, any microscopic theory of dark matter is only viable if there exists some mechanism to produce the dark matter particles with the observed relic abundance, Eq. (1.4). This requirement is one of the reasons that the most popular type of dark matter candidate is a class of models called weakly interacting massive particles (WIMPs). Interestingly enough, it has been observed that stable particles with weak interactions and weak-scale mass can rather naturally reproduce the observed relic abundance if they were produced thermally in the early Universe. More precisely, in the hot early Universe WIMPs are in thermal equilibrium. When the temperature of the Universe drops below the WIMP mass, the WIMP particles then decouple chemically, and their abundance becomes Boltzmann-suppressed. The expansion of the Universe, however, eventually causes the dark matter self-annihilation processes to become too inefficient to substantially alter the comoving number density of WIMPs, which then becomes "frozen" into the thermal relic abundance.

Numerically, the number density $n(t)$ of WIMPs is governed by a Boltzmann equation [12, 14],

$$\frac{dn}{dt} + 3Hn = \langle \sigma v \rangle \left(n^2 - n_{\mathrm{eq}}^2 \right), \tag{1.7}$$

where H is the Hubble rate, $\langle \sigma v \rangle$ is the thermally averaged effective annihilation cross-section and the equilibrium number density n_{eq} is a function of the temperature. By solving this equation numerically, one can determine the present relic abundance as a function of the particle self-annihilation cross-section $\langle \sigma v \rangle$. In the case that the annihilation cross-section is determined by the WIMP mass only, one finds for a weak-scale mass $\sim 100\,\mathrm{GeV}$, one finds for the s-wave annihilation cross-section that yields the correct order of magnitude for the relic abundance

$$\langle \sigma_A v \rangle \simeq \frac{g^4}{16\pi^2 m_{\mathrm{WIMP}}^2} \approx 3 \times 10^{-26}\,\mathrm{cm}^3\,\mathrm{s}^{-1}\,, \tag{1.8}$$

which is of the order of a typical weak-interaction cross-section. This fact is often referred to as the "WIMP miracle." This astounding coincidence has convinced many authors that the dark matter probably is a stable, weakly interacting particle.

Probably the most straightforward realization of a WIMP would be a stable heavy neutrino. However, the relic abundance of a pure $SU(2)_L$ doublet neutrino would be too low if the neutrino is heavier than $M_Z/2$, as required by LEP bounds [61]. In extensions such the Standard Model with low-energy supersymmetry, such as the minimal supersymmetric Standard Model (MSSM) (see [74] for an introduction), one naturally finds weakly interacting, electrically neutral candidates for the dark matter, namely the lightest neutralino and the lightest sneutrino (which is now ruled out as a dark matter candidate [75]). Neutralinos are mixtures of Binos, Winos and neutral Higgsinos, where the lightest neutralino can be a viable dark matter candidate if it is also the lightest supersymmetric particle (LSP). However, it should be noted that a priori there is no reason why a massive, weakly interacting particle should be stable, and indeed the neutralino decays far too quickly, unless it is stabilized by introducing a discrete symmetry. In supersymmetric models, R-parity is typically the symmetry of choice to ensure the stability of both the LSP and of the proton, which would otherwise decay too fast. We will examine a scenario with two-component dark matter in Chapter 10, where one of the components is made of neutralinos.

However, it should be noted that it is by no means clear that thermal freezeout is the correct mechanism to produce the relic dark matter abundance. For baryons, the relic abundance is clearly not thermal [76] but the result of some baryogenesis process [77]. An analogous process might be responsible for the observed dark matter abundance. Indeed, the fact that the abundances of dark matter and baryonic matter are the same to within an order of magnitude may suggest that the two share a common origin (see, *e.g.*, [78, 79] for proposals to relate the baryon density to the dark matter density). Therefore, while the WIMP miracle is certainly impressive, regarding only WIMPs as potential dark matter candidates appears overly restrictive. There are other types of well-motivated dark matter candidates, including some that are even less than weakly interacting, the so-called superWIMPs [80]. The canonical example of this class of dark matter candidates is the gravitino, the spin-3/2 superpartner of the graviton. The gravitino, which arises when supersymmetry is promoted to a local symmetry, is an excellent dark matter candidate since it is non-baryonic, neutral and cold over most of its possible mass range [81, 82] and can be produced thermally after reheating with the correct relic abundance if the Universe was very hot [83]. The gravitino constitutes a supersymmetric dark matter candidate which is viable even without R-parity conservation. We examine the cosmic-ray signatures in the scenario of gravitino dark matter with broken R-parity in Chapter 9.

Alternatively, the abundance of superWIMPs could be produced from the decays of heavier particles. For instance, superWIMPs can inherit the correct relic abundance from a thermally produced abundance of WIMPs. If every WIMP decays into a super-WIMP, one simply gets [80, 84]

$$\Omega_{\rm superWIMP} = \frac{m_{\rm superWIMP}}{m_{\rm WIMP}} \Omega_{\rm WIMP} \,, \tag{1.9}$$

where the abundance of superWIMPs is simply rescaled from the WIMP abundance by the ratio of the particle masses. In the class of superWIMP scenarios, the dark matter particle

itself is typically inaccessible to collider searches due to its very weak couplings. However, indirect inferences can be made from the existence of long-lived particles that eventually decay into the superWIMP, such as in the case of a gravitino LSP with a charged stau NLSP [85]. Such long-lived particles can be dangerous if they are present in the Universe during or after nucleosynthesis [67], so appropriate care has to be taken to not upset the successful BBN predictions.

Other well-motivated dark matter candidates include the axion, which was proposed to solve the strong *CP* problem of QCD [86, 87, 88], but which may also play the role of dark matter [89, 90]. Furthermore, in supersymmetric scenarios the superpartner of the axion, the axino, is easily the lightest supersymmetric particle and may also be a viable dark matter candidate [91, 92]. Another frequently discussed example is the lightest Kaluza-Klein particle in theories with compactified universal extra dimensions [93].

1.4 Unstable Dark Matter

In most studies, it is assumed that the dark matter is perfectly stable. A likely reason for the popularity of this assumption is that in the most popular class of dark matter candidates, the weakly interacting massive particles (WIMPs, in particular the lightest neutralino in supersymmetry), it is difficult to plausibly achieve a sufficiently long lifetime unless dark matter decay into Standard Model particles in completely forbidden by a symmetry. However, we emphasize that perfect dark matter stability is an assumption that might not be justified.

As with baryonic matter itself, there are good reasons to consider the case of unstable dark matter. From the theoretical point of view, we expect at least gravity to violate any global symmetry. It can also happen that the parity symmetry stabilizing the dark matter is only approximate from the start or spontaneously broken, as it occurs in some models of R-parity breaking [94, 95, 96, 97, 98]. Alternatively, the coupling involved in the decay may be very strongly suppressed as, for example, in the case of a tiny kinetic mixing between visible sector and hidden sector [99, 100]. In those cases it is natural to expect a very long lifetime for the dark matter particle.

From the observed Hubble rate one can calculate that the age of the Universe is about $\tau_0 \simeq 4.3 \times 10^{17}\,\mathrm{s}$ [52]. Therefore, from the requirement that any relic population of dark matter particles must have survived from its production in the early Universe to the present day, we can infer the absolute minimum dark matter lifetime

$$\tau_{\mathrm{DM}} \gtrsim 4 \times 10^{17}\,\mathrm{s}\,, \tag{1.10}$$

which is a far cry from the (mode-dependent) lower bounds on the proton lifetime, $\tau_p \gtrsim 10^{40}\,\mathrm{s}$ [61]. If the dark matter is unstable but exclusively decays into the hidden sector, the constraints are not much stronger and can only be inferred from the impact of dark matter decay on the expansion history of the Universe [101, 102]. However, if the dark matter decays into Standard Model particles, in particular photons, neutrinos, positrons, antiprotons and antideuterons, much more stringent constraints on the dark matter lifetime apply. We will examine some of these constraints in details in the following chapters.

Interestingly, the typical order of magnitude for constraints on the dark matter lifetime is on the order $\tau_{\rm DM} \gtrsim 10^{26}\,{\rm s}$, which exceeds the age of the Universe by a factor of 10^9. Dark matter particles with such long lifetimes can be considered perfectly stable from the cosmological point of view, with the dark matter instability having no impact on the expansion history of the Universe or on structure formation, for instance. Nevertheless, due to the enormous amounts of dark matter particles in the Universe, the transparency of the interstellar and intergalactic medium to the messenger particles and the relatively low backgrounds in the appropriate channels, dark matter lifetimes of this order can be constrained by present astrophysical observations of gamma rays [11, 94, 103, 104], neutrinos [2, 9, 105, 106, 107], positrons [4, 8, 10, 104] and antiprotons [4, 10, 104].

In some well-motivated models the dark matter is unstable and decays with lifetimes that exceed the age of the Universe by many orders of magnitude. An interesting example of decaying dark matter is sterile neutrino dark matter (see, *e.g.*, [108]), where one introduces right-handed neutrinos that have to be singlets under the Standard Model gauge group. The mass eigenstates of the neutrino mass matrix are then mixtures of left-handed and right-handed neutrinos, where the dominantly left-handed eigenstates are referred to as active neutrinos, while the dominantly right-handed neutrinos are called sterile. The lightest sterile neutrino typically has a mass of order 10 keV and constitutes a possible (warm) dark matter candidate. The longevity of the sterile neutrino is guaranteed by the smallness of its Yukawa couplings. It can decay with a cosmological lifetime into a photon and an active neutrino, $\nu_{\rm s} \to \gamma\nu$, where X-ray observations yield stringent constraints on this scenario [108]. Another example of decaying dark matter is the gravitino, the superpartner of the graviton in locally supersymmetric theories. If R-parity is slightly broken, the gravitino may still be a viable dark matter candidate [109]. The longevity of the gravitino in this case is due a double suppression of its decay rate by its extremely feeble, Planck-scale suppressed interactions as well as the smallness of the R-parity violation.

Particles that are stable at the renormalizable level by virtue of a symmetry that forbids all decay-inducing dimension-four operators can also be made unstable by decays via higher-dimensional operators. Interestingly, it has been observed (see, *e.g.*, [110, 111]) that the lifetime of a TeV-scale particle decaying via a dimension-six operator happens to be of the order of magnitude indicated above, $\tau_{\rm DM} \sim 10^{26}\,{\rm s}$, if the particle has a mass $m_{\rm DM}$ of order TeV and if the energy scale M_* of the non-renormalizable operator is close to the scale of Grand Unification, $M_{\rm GUT} \simeq 2 \times 10^{16}\,{\rm GeV}$ [74]. A simple dimensional analysis gives the estimate for the two-body decay lifetime

$$\tau_{\rm DM} \sim 8\pi \frac{M_*^4}{m_{\rm DM}^5} \simeq 2 \times 10^{26}\,{\rm s} \left(\frac{1\ {\rm TeV}}{m_{\rm DM}}\right)^5 \left(\frac{M_*}{10^{16}\,{\rm GeV}}\right)^4 . \tag{1.11}$$

This suggests the exciting possibility that the physics of Grand Unification may be testable by present cosmic-ray observations if the dark matter is destabilized by such higher-dimensional interactions. However, since the mass scales enter in the fourth and fifth power, respectively, the numerical coincidence is rather sensitive to multiplicative factors and thus not very robust. Furthermore, the lifetime is sensitive to the number of particles in the final state. Therefore, while this coincidence is certainly suggestive, it remains unclear whether the connection is meaningful. It was also pointed out in [111] that particle decays by dimension-five operators

lead to lifetimes $\mathcal{O}(100\,\mathrm{s})$, with possible impact on BBN.

We will discuss another example of a decaying dark matter candidate in Chapter 10, where the dark matter is composed of a mixture of neutralinos and the gauginos of an Abelian hidden-sector gauge group. Depending on the mass spectrum, the heavier of the two particles can decay via kinetic mixing of the hidden-sector gauge group with the Standard Model hypercharge gauge group. If this mixing is small enough, the lifetime of the dark matter can be sufficiently long, while its decays leave detectable signatures.

1.5 The Distribution of Dark Matter

The spatial distribution of dark matter is not very well determined. As far as the halo of our own galaxy is concerned, observations from kinematic surveys of the SDSS indicate that the total dark matter mass contained within a sphere of 60 kpc around the center of the Milky Way halo is $M_{60} = 4.7 \times 10^{11} M_\odot$ [23]. The exact distribution of the dark matter cannot be inferred in this way, however. Nevertheless, for the computation of cosmic-ray and gamma-ray fluxes one needs an explicit expression for the dark matter density in the Galactic halo. The spatial distribution of the dark matter is therefore usually inferred from computational N-body simulations [112, 113] of hierachical clustering of cold dark matter based on gravitational interactions and sometimes including baryon–dark matter interactions. The results of those simulations are generally fitted as spherically symmetric parametrizations of the energy density, although spherical symmetry is only an approximation to the triaxial halos found in the simulations. Interestingly, those simulations that do include baryons tend to find profiles that are steeper at the core than those that only include dark matter (see, *e.g.*, [114, 115]).

Halo model	α	β	γ	r_s [kpc]
Cored isothermal [116]	2	2	0	3.5
Navarro, Frenk & White [117, 118]	1	3	1	20
Moore *et al.* [119]	1.5	3	1.5	28
Burkert [120]	2	3	1	11.7

Table 1.1: Parameters used in Eq. (1.13), characterizing some commonly used halo models. Add:

For the calculation of the cosmic-ray and gamma-ray signatures of decaying dark matter, we will need to make some assumptions on the distribution of the dark matter in the Milky Way halo, although our results for the fluxes generally turn out to be rather insensitive to the particular choice of halo model. Some of the most commonly used dark matter density profiles can be written parametrically as

$$\rho_\mathrm{DM}(r) = \rho_\odot \left(\frac{R_\odot}{r}\right)^\gamma \left(\frac{1+(R_\odot/r_\mathrm{s})^\alpha}{1+(r/r_\mathrm{s})^\alpha}\right)^{(\beta-\gamma)/\alpha} , \tag{1.12}$$

with $R_\odot = 8.5$ kpc being the distance between the Sun and the Galactic center [121]. Alternatively, Eq. (1.12) can be written without reference to the solar radial distance as

$$\rho_\mathrm{DM}(r) = \frac{\rho_0}{(r/r_\mathrm{s})^\gamma [1+(r/r_\mathrm{s})^\alpha]^{(\beta-\gamma)/\alpha}} . \tag{1.13}$$

The values of the parameters in this parametrization are given in Table 1.1 for some of the most commonly used halo profiles. The coefficient ρ_0 is normalized in each case to the local dark matter density $\rho_\odot$ such that $\rho_{\rm DM}(R_\odot) = \rho_\odot$. The local dark matter density is significantly larger than the average density in the Universe due to structure formation. Most studies report values between 0.3 and $0.4\,{\rm GeV}/\,{\rm cm}^3$, which is a factor of 10^5 larger than the overall dark matter density. The most recent studies tend to find values around the upper end of this range (see, *e.g.*, [122]). The value most commonly used in the literature is $\rho_\odot = 0.3\,{\rm GeV\,cm}^{-3}$, however.

Another very commonly used profile is the Einasto profile [123, 124], which appears to be favored by more recent simulations [125],

$$\rho^{\rm Ein}_{\rm DM}(r) = \rho_0 \exp\left[-\frac{2}{\alpha}\left(\left(\frac{r}{r_{\rm s}}\right)^\alpha - 1\right)\right] . \tag{1.14}$$

The Einasto profile does not converge toward a power law toward the Galactic center, and is even steeper than the NFW profile. Simulations find a value of $\alpha = 0.17$ for the shape parameter and $r_{\rm s} = 20\,{\rm kpc}$ for the scale radius.

The different dark matter profiles look very similar at radial distances as far out as the position of the Sun. They differ mostly near the center of the Galaxy, and the "cuspiness" of dark matter profiles is an open question. Nevertheless, as long as the particles generated by dark matter decay or annihilation come mostly from the near the solar neighborhood or from relatively high latitudes in the case of gamma rays, the choice of halo profile has relatively little impact on the results.

It is worth noting in this context that the indirect signatures of decaying dark matter are simply proportional to the dark matter density $\rho_{\rm DM}(r)$, as opposed to the case of self-annihilating dark matter where the fluxes depend on the square of the density, $\rho^2_{\rm DM}(r)$. This implies that dark matter substructures can lead to strongly amplified signals in the case of dark matter annihilation, but it also means that indirect signatures from decaying dark matter are more homogeneous across the sky and do not experience the strong amplification of signals in regions of high dark matter density. Such overdense regions are found in deep gravitational wells such as the center of the Galaxy or the Sun and Earth, where dark matter particles can get trapped when they get scattered to below the escape velocity. The detection strategies therefore differ between the two cases, where for example the search for neutrinos from WIMPs captured in the Sun is not promising in the case of dark matter decay. Because of the absence of this amplification of signals, decaying dark matter is less constrained than annihilating dark matter by gamma and radio observation of the Galactic center [104]. We will discuss the origin of such indirect dark matter signals in more detail in the next two chapters.

Chapter 2

Cosmic Rays

The Earth's atmosphere is constantly exposed to a flux of energetic particles from outer space. The existence of this cosmic radiation was first suspected at the beginning of the 20th century and eventually discovered observationally by Hess in a series of balloon flights in 1912. Millikan later established the extraterrestrial origin of these particles and introduced the (somewhat misleading) name "cosmic rays." Historically, the cosmic radiation has been central to some important discoveries, as the positron (and thus antimatter) as well as the muon were first discovered in cosmic rays in 1932 and 1936, respectively. In this chapter we review some of the general features of cosmic rays and discuss a semi-analytical two-zone diffusion model to describe the complicated process of the propagation of stable charged particles in the Galaxy. We also briefly discuss the effect of solar modulation on charged-particle spectra.

2.1 General Properties

The observed spectrum of cosmic rays extends over some 12 orders of magnitude, with the highest-energy cosmic rays reaching energies in excess of $10^{19}\,\mathrm{eV}$. The low-energy cutoff is found at a few hundred MeV, due to solar modulation preventing particles with even lower energies from reaching us (see Section 2.3). Cosmic rays follow a featureless power law with an index ~ 2.75 up to energies of $\sim 3 \times 10^{15}\,\mathrm{eV}$, where the spectrum steepens at the so-called "knee." The spectrum further steepens at the "second knee" before flattening again at the "ankle" and finally terminating at about $5 \times 10^{19}\,\mathrm{eV}$ [126], most likely due to the GZK effect [127, 128] of photo-pion production by ultra-high energy cosmic rays on the CMB. At least for energies below the knee, cosmic rays are believed to be of Galactic origin, whereas at energies above $\sim 10^{18}\,\mathrm{eV}$ their Larmor radius becomes larger than the radius of the Galaxy, indicating an extragalactic origin. The composition of cosmic rays is a function of their energy, but as a rule of thumb at energies 10 – 100 GeV about 90% of cosmic rays are protons, 9% are helium nuclei, and almost 1% are electrons. Heavier nuclei and antimatter make up less than 1% of the cosmic radiation. Antimatter is a particularly rare component of cosmic rays, which makes it a preferred target for indirect dark matter searches. (The ratio of antiprotons to protons is at the level $\sim 2 \times 10^{-4}$ at an energy of 10 GeV [129].) Furthermore, cosmic rays, at least up to energies of about $10^{19}\,\mathrm{eV}$, are highly isotropic and therefore provide practically no directional information on their origin.

The origin and acceleration mechanism of cosmic rays remains speculative, although it is very plausible that they originate in the shocked shells of supernova remnants, where they are accelerated by diffusive shock acceleration [130] via first-order Fermi acceleration by stochastic scattering on magnetic turbulence (Fermi's original proposal [131] leads to second-order acceleration).

After their creation in the sources, cosmic rays propagate through the interstellar medium, where they interact with the Galactic magnetic field, the interstellar radiation field and the interstellar gas. It is generally assumed that the initial acceleration and subsequent propagation of cosmic rays can be treated separately, which is supported by measurements of secondary/primary ratios that would be sensitive to acceleration in the interstellar medium. Over the last decades, consensus has emerged that diffusion is the correct effective description of the microscopic interactions of the charged cosmic-ray particles with the tangled Galactic magnetic fields. The diffusion picture explains the isotropy of the cosmic radiation as well as the long storage times of ~ 150 Myr [61] inferred from measurements of radioactive isotopes, which can serve in this manner as "clocks."

The chemical abundances of elements in cosmic rays generally agree with Solar System abundances, with a few important exceptions. Some elements, such as Boron, are rare in the Solar System, but abundant in cosmic rays. These deviations are interpreted as being due to secondary production of these elements by the spallation of primary cosmic rays on the interstellar medium. This picture yields a prediction for the grammage traversed by primary cosmic rays in order to produce the observed abundance of secondaries. The energy-dependence of secondary-to-primary flux ratios constitutes an essential test of the validity of propagation models. The benchmark flux ratio in this respect is usually the Boron-to-Carbon (B/C) ratio since Boron is a purely secondary component of the cosmic radiation, and the B/C ratio is rather accurately determined up to energies of about 100 GeV, although measurements exist for energies up to 1 TeV [132]. Similarly, antiprotons are believed to be entirely produced by secondary production.

2.2 The Transport Equation

In this section we discuss the general transport equation, which we use to describe the effects of the propagation of primary particles injected by a process such as dark matter annihilation or decay from some point in the Milky Way halo to our local position. After their production in the Galactic halo, cosmic rays produced by dark matter propagate through the Milky Way's magnetic halo, suffering the effects of diffusion, energy losses and gains, convection, reacceleration and elastic and inelastic scatterings. To describe this complicated problem, we will treat the propagation of cosmic rays in the Galaxy in a stationary two-zone diffusion model with free cylindrical boundary conditions (for reviews see, *e.g.*, [133, 134]).

In the diffusion framework with inclusion of convection, the cosmic-ray propagation equation for any particle species can be written in terms of the number density $f(p)$ as a function

of momentum, [133, 134]

$$\frac{\partial}{\partial t} f(p,\vec{r},t) = Q(p,\vec{r},t) + \vec{\nabla}\cdot(K\,\vec{\nabla} f - \vec{V}_{\rm c} f) + \frac{\partial}{\partial p} p^2 D_{pp} \frac{\partial}{\partial p}\frac{1}{p^2} f \\ - \frac{\partial}{\partial p}\left[\frac{dp}{dt} f - \frac{p}{3}(\vec{\nabla}\cdot\vec{V}_{\rm c}) f\right] - \frac{1}{\tau_{\rm f}} f - \frac{1}{\tau_{\rm r}} f\,. \tag{2.1}$$

The first term on the right-hand side is the source term describing the injection of primary particles. In the case of indirect detection, this term is determined by the self-annihilation or decay of dark matter particles. The second term describes the diffusion of cosmic rays due to resonant pitch-angle scattering on magnetic inhomogeneities, which induces a random walk-like particle motion through the interstellar medium. Although on small scales diffusion is strongly anisotropic since the random turbulent component is much smaller than the average magnetic field, $\delta B \ll B$, on scales of order 100 pc the random variations in the magnetic field become comparable to the average field, resulting in an effectively isotropic particle density [134]. The third term describes convection by a Galactic wind of cosmic-ray particles emitted perpendicular to the Galactic disk. There is some evidence of the effects of a convective wind driven by supernova remnants in other galaxies, so the possibility exists that convection may also play a role in the propagation of cosmic rays in our Galaxy. The fourth describes diffusive reacceleration as diffusion in momentum space, which is caused by stochastic acceleration of cosmic rays by scattering on random magneto-hydrodynamic waves. The fifth term describes continuous energy losses, which result from ionization and Coulomb interactions for all cosmic rays, as well as by bremsstrahlung, synchrotron radiation and inverse Compton scattering for electrons and positrons. The sixth term describes adiabatic energy gains or losses, respectively, which can result from Galactic winds that are non-uniform, for example for convective velocities that are increasing with the distance from the disk. Finally, the last two terms describe losses from fragmentation and radioactive decay, respectively, whose time scales are given by $\tau_{\rm f}$ and $\tau_{\rm r}$.

We particularize this framework by regarding only stable primary particle species and neglecting adiabatic energy losses and reacceleration, which only play a role at lower energies. The number density of particles $f(T,\vec{r},t)$ as a function of kinetic energy[1] T is described by the following diffusion–loss transport equation, which is valid for both electrons/positrons and antiprotons/antideuterons:

$$\frac{\partial}{\partial t} f(T,\vec{r},t) = \vec{\nabla}\cdot[K(T,\vec{r})\vec{\nabla} f] + \frac{\partial}{\partial T}[b(T,\vec{r}) f] - \vec{\nabla}\cdot[\vec{V}_{\rm c}(\vec{r}) f] - 2h\delta(z)\Gamma_{\rm ann} f + Q(T,\vec{r})\,. \tag{2.2}$$

By use of the delta function, we confine annihilating scatterings to the disk at $z = 0$. In the following we shall assume that the stationary limit holds, $\partial f/\partial t = 0$, which is valid when the typical timescale of cosmic-ray propagation [135] is small compared to the timescale on which Galactic propagation conditions change. The boundary conditions are usually chosen such that the number density of particles vanishes on the boundary of the diffusion zone, where particles can escape freely into intergalactic space.

For the radius of the diffusive halo, one usually assumes a value of $R = 20\,\mathrm{kpc}$, where the local fluxes are not substantially affected by the choice of the exact value for R. The

[1] In the case of nuclei, T conventionally refers to the kinetic energy per nucleon.

half-height L of the diffusive halo is usually assumed to lie in the range $L = 1 - 15\,\mathrm{kpc}$. This parameter can have a crucial impact on the magnitude of the locally measured fluxes, in particular when the sources of cosmic rays lie outside the Galactic disk as is the case for dark matter decay or annihilation.

The diffusion coefficient $K(T, \vec{r})$ is assumed to be spatially constant throughout the diffusion zone and is parametrized by [134]

$$K(T) = K_0 \beta(T) \mathcal{R}^\delta \,, \tag{2.3}$$

where $\beta = v/c$ is the velocity of the particle in units of c and $\mathcal{R}$ is the rigidity of the particle, defined as the momentum in units of GeV per unit charge, $\mathcal{R} \equiv p[\mathrm{GeV}]/|Z|$. The values of K_0 and the spectral index δ are related to the magneto-hydrodynamical properties of the interstellar medium, and are determined by fits to secondard-to-primary flux ratios (see Fig. 2.1 for constraints on the parameter space of K_0, L and δ from fits to the B/C ratio).

Under the assumptions we have stated, the propagation can be described in terms of a small number of parameters that have to be determined from experiment, namely K_0, δ and L, as well as V_c in the case of nuclei. A determination of the height of the diffusive halo from fits to secondary/primary ratios is difficult, however, because for stable nuclei the ratios are only sensitive to the ratio K_0/L. Therefore, there is a degeneracy between the normalization of the diffusion coefficient and the halo height which can lead to identical secondary/primary ratios, but vastly different results for the fluxes of primary cosmic rays from dark matter. Indeed, the fluxes of primary antiprotons can vary by as much as two orders of magnitude depending on the choice of transport parameters [10]. The reason for this large uncertainty in the antiproton flux from dark matter as opposed to the astrophysical background is that the injection of antiprotons from dark matter takes place all over the halo, while antiprotons from spallation are produced only in the disk. Therefore, variations of L have little impact on the astrophysical contribution, while they drastically modify the amount of dark matter contained within the magnetic halo and thus the injection of primary antiprotons.

The half-height L can be constrained by flux ratios that include radioactive isotopes, *i.e.*, when one has unstable secondaries. This can help break the degeneracy between K_0 and L because the flux of unstable nuclei depends on the time since creation, not the traversed grammage. The ratio between stable and unstable isotopes depends on the storage (confinement) time of cosmic rays, which is related to a combination of the height of the diffusive halo L and the diffusion coefficient K_0. The most precise determination is in the ratio $^{10}\mathrm{Be}/^{9}\mathrm{Be}$, where the unstable isotope ^{10}Be has a half-life of 1.4×10^6 yr, which is smaller than the typical cosmic-ray storage time. Such measurements, combined with fits to the B/C ratio, seem to indicate that a halo half-height of $L \simeq 4\,\mathrm{kpc}$ is preferred (see, *e.g.*, [136, 137]), although the data at present do not allow for a truly independent determination of K_0 and L.

The source term $Q(T, \vec{r})$ describes the production rate of particles from dark matter decay or annihilation per unit energy and unit volume at a position $\vec{r}$ with respect to the center of the Milky Way. For any particle species i, in the case of dark matter decay the source term has the form

$$Q_i(T, \vec{r}) = \frac{1}{\tau_\mathrm{DM} m_\mathrm{DM}} \rho_\mathrm{DM}(\vec{r}) \frac{dN_i}{dT} \,, \tag{2.4}$$

where dN_i/dT is the energy spectrum of particles produced per decay. The spatial distribution of the source term is given by the dark matter energy density $\rho_{\rm DM}(r)$, for which we assume one of the spherically symmetric halo profiles discussed in Chapter 1.

Generally, to solve the transport equation one has the choice between a fully numerical treatment as implemented, *e.g.*, in the `GALPROP` code [138] or by applying certain simplifications and attempting to solve the transport equation analytically by making use of appropriate symmetries. Namely, under certain simplifying assumptions (mostly neglecting spatial dependencies of diffusion, convection and energy losses), the transport equation can be solved semi-analytically by exploiting the cylindrical symmetry of the problem. The solution can then be expressed as a series in Bessel functions and trigonometric functions which fulfill the appropriate boundary conditions. The fully numerical treatment has the advantage of not requiring simplifying assumptions. On the other hand, the analytical treatment allows more understanding of the impact of varying model parameters and lends itself more to scans of the parameter space.

Formally, the solution of the transport equation at our position in the Galaxy ($r = R_\odot$, $z = 0$) can be written as an integral over a Green's function that encodes the effects of propagation and the energy spectrum at injection,

$$f_i(T) = \frac{1}{m_{\rm DM}\tau_{\rm DM}} \int_0^{T_{\rm max}} dT'\, G_i(T, T') \frac{dN}{dT'} \,. \tag{2.5}$$

The Green's function $G_i(T, T')$ encodes all the information about astrophysics (such as the details of the halo profile and the propagation of cosmic rays in the Galaxy), while the remaining part depends on the particle-physics model of the dark matter that is adopted. From the number density, the interstellar flux at the heliospheric boundary is then determined as

$$\Phi_i^{\rm IS}(T) = \frac{v(T)}{4\pi} f_i(T) \,, \tag{2.6}$$

where v is the velocity of the particle. The flux has units of particles per unit area, solid angle, unit time and unit energy. We will give explicit expressions for the Green's function, both analytical and numerical, in the following sections for the limiting cases of electrons/positrons and antiprotons/antideuterons.

2.2.1 Propagation of Electrons and Positrons

Positrons and electrons at the energies we are interested in move essentially at the speed of light, $v \approx c$, and for the energy range of interest (above ~ 10 GeV) we can neglect diffusive reacceleration, annihilation in the disk and convection (see, *e.g.*, [139, 140]). The diffusion equation then takes on the simplified form [141, 142]

$$0 = \vec{\nabla} \cdot [K(T, \vec{r}) \vec{\nabla} f] + \frac{\partial}{\partial T}[b(T, \vec{r}) f] + Q(T, \vec{r}) \,. \tag{2.7}$$

Under the above approximations, the propagation of electrons and positrons can be described in terms of just three free parameters that have to be determined from observation, namely δ, K_0 and L. We list in Table 2.1 three sets of parameters that provide good fits to the B/C ratio and yield minimal, median and maximal fluxes of electrons and positrons [142].

Model	δ	K_0 [kpc^2/Myr]	L [kpc]
M2	0.55	0.00595	1
MED	0.70	0.0112	4
M1	0.46	0.0765	15

Table 2.1: Parameters of the propagation model for positrons yielding a minimal, median, and maximal flux, as given in [142].

The energy loss term is determined, among other factors, primarily by inverse Compton scattering, synchrotron losses and ionization (see Section 3.3 for more details on the contribution of inverse Compton to the energy loss rate). In the case of electrons and positrons, we assume for simplicty that the energy loss rate is spatially constant and can be parametrized as [141, 142]

$$b(T,\vec{r}) = b(T) = \frac{T^2}{T_0 \tau_{\rm E}}\,, \tag{2.8}$$

where we have defined $T_0 = 1\,\text{GeV}$ and $\tau_{\rm E} = 10^{16}\,\text{s}$, which represents the typical energy loss time scale at our position in the Galaxy. We have assumed that the energy loss is position independent and goes quadratically with the energy. At high energies the energy loss term is mostly determined by inverse Compton scattering on the interstellar radiation field and synchrotron radiation from interactions with the Galactic magnetic field, while ionization is only relevant at low energies. See Section 3.3 for a more thorough discussion of the physical origin of the energy loss term and a comparison between the approximate value used here and a more realistic expression (which precludes an analytical solution of the transport equation, however).

Under the above approximations, the Green's function of Eq. (2.5) for the case of electrons and positrons can be written as [141, 142]

$$G_{e^+}(T,T') = \sum_{n,m=1}^{\infty} B_{nm}(T,T') J_0\left(\zeta_n \frac{R_\odot}{R}\right) \sin\left(\frac{m\pi}{2}\right)\,, \tag{2.9}$$

where J_0 is the zeroth-order Bessel function of the first kind, whose successive zeros are denoted by ζ_n. The coefficients of the expansion are defined as

$$B_{nm}(T,T') = \frac{\tau_{\rm E} T_0}{T^2} C_{nm} \exp\left\{\left(\frac{\zeta_n^2}{R^2} + \frac{m^2\pi^2}{4L^2}\right)\frac{K_0 \tau_{\rm E}}{\delta - 1}\left[\left(\frac{T}{T_0}\right)^{\delta-1} - \left(\frac{T'}{T_0}\right)^{\delta-1}\right]\right\}\,, \tag{2.10}$$

with

$$C_{nm} = \frac{2}{J_1^2(\zeta_n) R^2 L}\int_0^R dr'\, r' \int_{-L}^{L} dz' \rho_{\rm DM}(\vec{r}\,') J_0\left(\zeta_n \frac{r'}{R}\right) \sin\left[\frac{m\pi}{2L}\left(L - z'\right)\right]\,, \tag{2.11}$$

where J_1 is the first-order Bessel function of the first kind.

The solution implies that the typical diffusion length for electrons and positrons is given by the expression [143]

$$\lambda_{\rm D}(T,T') = \left\{\frac{4K_0\tau_{\rm E}}{1-\delta}\left(\left(\frac{T}{T_0}\right)^{\delta-1} - \left(\frac{T'}{T_0}\right)^{\delta-1}\right)\right\}^{1/2} \tag{2.12}$$

as a function of the initial and final particle energy.

Model	a	b
M2	-0.9716	-10.012
MED	-1.0203	-1.4493
M1	-0.9809	-1.1456

Table 2.2: Coefficients of the interpolating function Eq. (2.13) for the positron Green's function, assuming an NFW halo profile, and for the different diffusion models in Table 2.1.

For practical applications, it is often convenient to have a numerical approximation to the above Green's function that is easier to implement computationally. We find that the Green's function for positrons can be numerically well approximated by the following simple expression [10],

$$G_{e^+}(T, T') \simeq \frac{10^{16}}{T^2} e^{a+b(T^{\delta-1}-T'^{\delta-1})} \theta(T'-T)\,\mathrm{cm}^{-3}\,\mathrm{s}\,, \tag{2.13}$$

where θ is the Heaviside step function and T and T' are expressed in units of GeV. We list values of the coefficients a and b in Table 2.2 for the NFW profile and the different propagation models listed in Table 2.1. This approximation works better than $15\% - 20\%$ over the whole range of energies. We find numerically that the Green's function is not very sensitive to the choice of halo profile. Therefore, the corresponding coefficients can be well approximated by Table 2.2. In the following chapters, however, we always use the analytical expressions above to calculate the cosmic-ray fluxes of electrons and positrons.

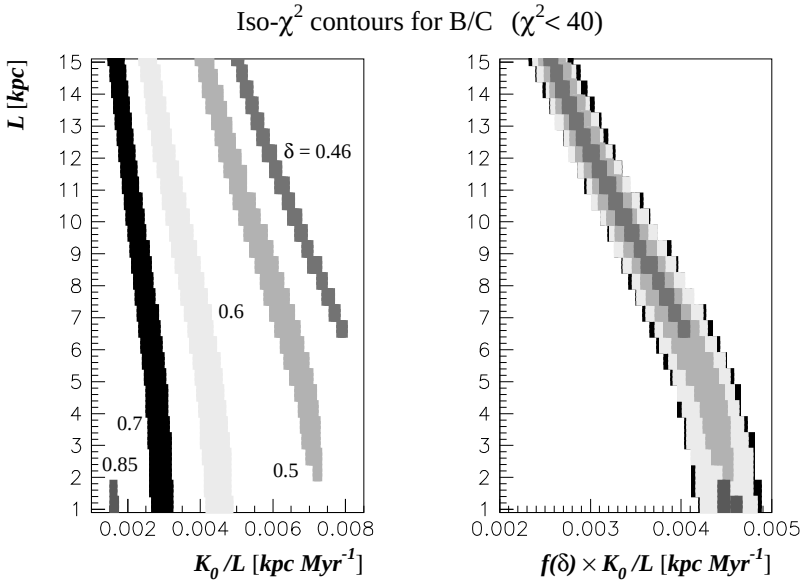

Figure 2.1: Isocontours of the χ^2 values in the (degenerate) determination of the transport parameters K_0 and L from the B/C ratio for different values of δ (from [137]).

2.2.2 Propagation of Light Nuclei

In this subsection we consider the propagation of light (anti)matter nuclei, in particular antiprotons and antideuterons. Contrary to the case of electrons and positrons, for light nuclei one can essentially neglect energy losses in the energy range of interest. Namely, due to their higher mass, antiprotons and antideuterons lose very little energy via synchrotron radiation and scatterings with photons. The transport equation for light nuclei is therefore dominated by the effects of diffusion [144] and assumes the form [144, 141],

$$0 = \vec{\nabla} \cdot [K(T,\vec{r})\vec{\nabla} f] - \vec{\nabla} \cdot [\vec{V}_{\rm c}(\vec{r}) f] - 2h\delta(z)\Gamma_{\rm ann} f + Q(T,\vec{r})\,. \tag{2.14}$$

For nuclei, however, convection may be of some importance. Following [137, 145] we assume that the convective Galactic wind has constant magnitude and axial direction,

$$\vec{V}_{\rm c}(\vec{r}) = V_{\rm c}\,{\rm sign}(z)\vec{e}_z\,, \tag{2.15}$$

where $\vec{e}_z$ is a unit vector pointing away from the Galactic disk.

Model	δ	K_0 [kpc^2/Myr]	L [kpc]	$V_{\rm c}$ [km/s]
MIN	0.85	0.0016	1	13.5
MED	0.70	0.0112	4	12
MAX	0.46	0.0765	15	5

Table 2.3: Parameters of the propagation model for antiprotons/antideuterons yielding a minimal, median, and maximal flux, as given in [145].

Regarding the annihilating scatterings of antiprotons and antideuterons, we treat the gaseous disk of the Milky Way as "infinitely thin" for calculational purposes, while we assume a value for the disk half-height of $h = 100$ pc. The annihilation rate can be calculated from the interstellar gas densities and the nuclear cross sections. Since most of the interstellar gas is in the form of hydrogen and helium, we can write for the antiproton annihilation rate in the disk

$$\Gamma_{\rm ann} = (n_{\rm H} + 4^{2/3} n_{\rm He})\sigma^{\rm ann}_{\bar{p}p} v_{\bar{p}}\,. \tag{2.16}$$

In this expression we have assumed that the annhilation cross-section between an antiproton and a helium nucleus is related to the annihilation cross-section between an antiproton and a proton by the simple geometrical factor $4^{2/3}$. For the interstellar gas densities in the Galactic disk we assume the values $n_{\rm H} \sim 1\,{\rm cm}^{-3}$ for the number density of Hydrogen in the Milky Way and $n_{\rm He} \sim 0.07\, n_{\rm H}$ for the number density of Helium. For the annihilation cross-section between protons and antiprotons we adopt the parametrization given in [146, 147],

$$\sigma^{\rm ann}_{\bar{p}p}(T) = \begin{cases} 661\,(1 + 0.0115\,T^{-0.774} - 0.948\,T^{0.0151})\ {\rm mb}, & T < 15.5\,{\rm GeV}\,, \\ 36\,T^{-0.5}\ {\rm mb}, & T \geq 15.5\,{\rm GeV}\,. \end{cases} \tag{2.17}$$

Energy losses from non-annihilating scatterings result in so-called tertiary cosmic rays, which we neglect since they are only relevant at lower energies.

Finally, under the above assumptions the solution for the Green's function of Eq. (2.5) for antiprotons and antideuterons can be written as [141]

$$G_{\bar{p}} = \sum_{i=1}^{\infty} \exp\left(-\frac{V_c L}{2K(T)}\right) \frac{y_i(T)}{A_i(T)\sinh(S_i(T)L/2)} J_0\left(\zeta_i \frac{R_\odot}{R}\right) \delta(T - T') \,, \tag{2.18}$$

where we have defined

$$\begin{aligned} y_i(T) = \frac{4}{J_1^2(\zeta_i) R^2} \int_0^R dr'\, r' J_0\left(\zeta_i \frac{r'}{R}\right) \times \\ \times \int_0^L dz' \exp\left(\frac{V_c(L-z')}{2K(T)}\right) \sinh\left(\frac{S_i(L-z')}{2}\right) \rho_{\rm DM}(r') \end{aligned} \tag{2.19}$$

and

$$A_i(T) = 2h\Gamma_{\rm ann}(T) + V_c + K(T) S_i(T) \coth\left(\frac{S_i(T)L}{2}\right) \,, \tag{2.20}$$

$$S_i(T) = \sqrt{\frac{V_c^2}{K(T)^2} + \frac{4\zeta_i^2}{R^2}} \,. \tag{2.21}$$

We list values for the parameters yielding minimal, median and maximal antiproton and antideuteron fluxes [145] in Table 2.4.

In the case of antiprotons, too, we can numerically approximate the Green's function by a simple expression [10],

$$G_{\bar{p}}(T, T') \simeq 10^{14}\, e^{x + y \ln T + z \ln^2 T} \delta(T' - T)\, {\rm cm}^{-3}\, {\rm s} \,. \tag{2.22}$$

The coefficients x, y and z for the NFW profile are listed in Table 2.4. In this case the approximation is accurate to a level of $5 - 10\%$. Again, the dependence on the particular choice of halo profile is rather weak. We have also performed a fit to the Green's function for the case of antideuterons. The values of the numerical coefficients can be found in Chapter 5. However, or our calculations of antiproton and antideuteron fluxes in the following chapters, we will always use the full analytical expressions,.

Model	a	b
M2	-0.9716	-10.012
MED	-1.0203	-1.4493
M1	-0.9809	-1.1456

Table 2.4: Coefficients of the interpolating function Eq. (2.13) for the antiproton Green's function, assuming an NFW halo profile, and for the different diffusion models in Table 2.3.

2.3 Solar Modulation

Calculating the fluxes of charged particles at the top of the Earth's atmosphere is complicated by the influence of the Sun on charged particles in the heliosphere. This effect, which is

dependent on the point in time in the eleven-year solar cycle, is known as solar modulation. The solar wind, a stream of plasma consisting mainly of electrons and protons ejected from the Sun's upper atmosphere, sweeps low-energy particles away from the heliosphere, thereby flattening the spectrum and redistributing particles toward lower energies. To take solar modulation into account, we use a simple effective description in terms of the spherically symmetric and charge-independent force field model [148, 149], which treats solar modulation as an effective electric potential in which particles lose energy as they traverse the potential. The flux $\Phi_{\rm TOA}$ at the top of the atmosphere of a particle species i carrying electric charge Z (in units of the elementary charge) is related to the interstellar flux $\Phi_{\rm IS}$ by [150]

$$\Phi_i^{\rm TOA}(T_{\rm TOA}) = \frac{p_{\rm TOA}^2}{p_{\rm IS}^2}\Phi_i^{\rm IS}(T_{\rm IS}) = \left(\frac{2m_i T_{\rm TOA} + T_{\rm TOA}^2}{2m_i T_{\rm IS} + T_{\rm IS}^2}\right)\Phi_i^{\rm IS}(T_{\rm IS})\,, \tag{2.23}$$

where $T_{\rm IS} = T_{\rm TOA} + |Ze|\phi_{\rm F}$, with $T_{\rm IS}$ and $T_{\rm TOA}$ being the antiproton kinetic energies at the heliospheric boundary and at the top of the Earth's atmosphere, respectively, and $\phi_{\rm F}$ being the solar modulation parameter (or Fisk potential), which varies between 500 MV and 1.3 GV [141] over the eleven-year solar cycle. Since most observations during the late 1990s and the late 2000s were undertaken near solar minimum activity, we will choose $\phi_{\rm F} = 500 - 550$ MV for our numerical analyses in order to compare our predicted flux with the collected data. For this choice of modulation potential, solar modulation becomes negligible for cosmic-ray energies above $\sim 10\,\text{GeV}$.

Chapter 3

The Gamma-Ray Sky

Since in this work we mostly consider dark matter masses of order 100 GeV – 10 TeV, the corresponding photon emission from dark matter decay is in the gamma-ray energy range. Gamma rays constitute an ideal probe to search for indirect signatures of dark matter annihilation or decay since they are sensitive to sources over a wide range of distances. They also have the advantageous properties of essentially propagating freely and not being deflected or absorbed on Galactic scales, thus preserving spectral as well as directional information about their origin. In this chapter we briefly discuss the different components of the diffuse gamma-ray sky and explain how to calculate the dark matter contribution to the gamma-ray flux from Galactic and extragalactic dark matter, as well as from inverse Compton scattering.

In the 1990s, a full-sky observation of the gamma-ray flux was performed by the Energetic Gamma Ray Experiment Telescope (EGRET). It discovered a number of resolved sources [151], such as blazars, as well as an unresolved diffuse component [152, 153], which can be attributed almost entirely to Galactic emission. For the purposes of indirect dark matter detection, we are interested in the diffuse part of the Galactic gamma-ray emission, which is composed of contributions from π^0 production by cosmic rays scattering on interstellar gas, as well as a bremsstrahlung ("free–free emission") component, both of which are dependent on the HI, H_2 and HII gas distributions in the Galaxy. There is also a contribution from inverse Compton scattering of electrons on the interstellar radiation field. The propagation of cosmic rays and the diffuse gamma-ray emission are therefore tightly correlated and can provide complementary information. While the microscopic physics of the processes underlying the Galactic gamma-ray emission are well understood, the actual intensity of their contributions depends on various astrophysical uncertainties, including the interstellar radiation field, the interstellar magnetic field and the Galactic gas distributions. Nevertheless, current models of the Galactic emission can reproduce observations with satisfactory accuracy. Our reference model of the diffuse Galactic emission will be the conventional model by Strong and Moskalenko obtained using the `GALPROP` code [138].

The diffuse gamma-ray flux also contains a faint isotropic component of truly extragalactic origin, which was first observed by SAS-2 at energies in the $40 - 200\,\mathrm{MeV}$ range [154], later by EGRET in the $30\,\mathrm{MeV} - 100\,\mathrm{GeV}$ range [155], and most recently by the Large Area Telescope (LAT) aboard the Fermi Gamma-Ray Space Telescope [156]. This isotropic extragalactic component, the extragalactic gamma-ray background (EGBG), is assumed to be

composed of a number of distinct components originating from both truly diffuse processes as well as unresolved sources including active galactic nuclei, BL Lac objects, star-forming galaxies, starburst galaxies, structure formation shocks in galaxy clusters and flat-spectrum radio quasars [157]. The combined emission of these sources is believed to follow a simple power law. The extragalactic background is of special interest for dark matter searches because photons from dark matter decay or annihilation, both from the Galactic halo and from extragalactic distances, may initially show up in analyses as a misidentified part of this emission due to the fact that it is not part of the models of the Galactic foreground emission. A dark matter contribution might conceivably manifest itself in the form of a deviation from the expected power-law behavior of the diffuse extragalactic background. The decay of dark matter in the Galactic halo would also introduce a degree of anisotropy in this signal, which might enable an identification of this component as being due to dark matter. We will discuss the possible identification of a dark matter contribution to the diffuse gamma-ray flux via this anisotropy in detail in Chapter 6.

Aside from the observation of diffuse fluxes, information can also be gained from observations of sources with low gamma-ray emissions such as dwarf galaxies and galaxy clusters. Indeed, strong constraints on decaying dark matter have been derived recently from gamma-ray observations of galaxy clusters and nearby galaxies [158]. Furthermore, if gamma rays are emitted by a fundamental particle-physics process, there may exist a unique signature in the form of monochromatic lines, for which there exists no astrophysical background. Thus, the observation of a gamma-ray line would constitute a so-called smoking-gun signature of dark matter annihilation or decay, with potentially far-reaching implications. Such a line could show up in observations of the Galactic halo as well as observations of extragalactic targets like galaxies or clusters. We will discuss searches for gamma-ray lines in some detail in Chapter 7.

3.1 Extragalactic Gamma Rays

Photons emitted at cosmological distances are redshifted by the expansion of the Universe. Therefore decay of dark matter particles at cosmological distances therefore produces a gamma-ray flux that is determined by an integral over the redshift z [103],

$$\frac{dJ_{\rm eg}}{dE_\gamma} = \frac{\Omega_{\rm DM}\rho_{\rm c}}{4\pi m_{\rm DM}\tau_{\rm DM}} \int_0^\infty dz \, \frac{1}{H(z)} \frac{dN_\gamma}{dE_\gamma} \left[(1+z)E_\gamma\right] e^{-\tau(E_\gamma,z)} \,, \tag{3.1}$$

where dN_γ/dE_γ is the energy spectrum of photons, $\rho_{\rm c} = 3H_0^2/(8\pi G_{\rm N}) \simeq 5.5 \times 10^{-6}\,{\rm GeV\,cm^{-3}}$ is the critical density of the Universe and

$$H(z) = H_0 \sqrt{\Omega_\Lambda + \Omega_{\rm M}(1+z)^3} \tag{3.2}$$

is the Hubble expansion rate as a function of redshift for a matter and dark energy-dominated Universe, as the observed extragalactic photons mostly come from very low redshifts. We assume throughout this work a flat-universe ΛCDM cosmology with $\Omega_\Lambda = 0.73$, $\Omega_{\rm M} = 0.27$, $\Omega_{\rm DM} = 0.23$ and $h \equiv H_0/(100\,{\rm km\,s^{-1}\,Mpc^{-1}}) = 0.70$ (*cf.* Chapter 1).

Highly energetic gamma-rays can be absorbed by e^+e^- pair production on the interstellar (intergalactic) medium. This attenuation of high-energy photons in the intergalactic medium

is taken into account by the function τ describing the optical depth, or absorption at redshift z. We plot the isocontours of the optical depth in Fig. 3.1. It is apparent from the plot that gamma rays fluxes with high energies around 1 TeV are strongly attenuated and come mainly from redshifts $z \lesssim 0.05$. On the other hand, the flux of gamma rays originating in the decay of dark matter in the Galactic halo is barely attenuated by pair production on the ISRF at energies below 10 TeV [159], so we will ignore this effect for gamma rays produced in the Milky Way halo.

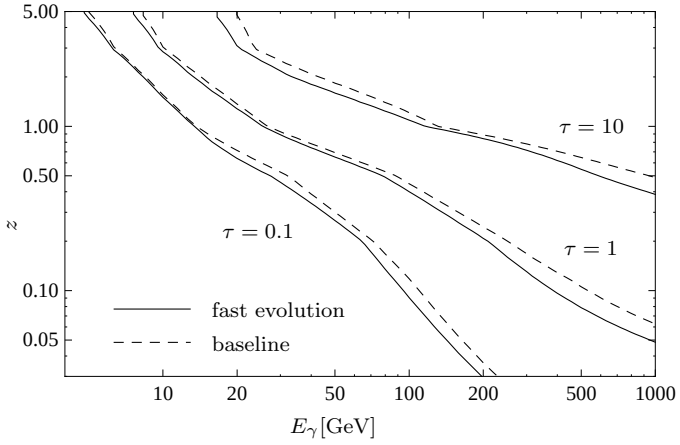

Figure 3.1: Isocontours of the optical depth $\tau(E_\gamma, z)$ of gamma-ray photons emitted at redshift z and observed at Earth with energy E_γ. We show results for two different models of the intergalactic background light [160, 161]. Throughout this work we will adopt the "fast evolution" model.

3.2 Galactic Gamma Rays

The flux of gamma rays from dark matter, in turn has several components. First, there is the so-called prompt radiation which includes photons generated directly in the decay or annihilation of dark matter particles. This includes photons produced directly in the decay of dark matter or in the decay or fragmentation of daughter particles, as well as bremsstrahlung from the decay or annihilation process itself.

The flux of prompt gamma rays from dark matter decay in the Milky Way halo is given by [103]

$$\frac{dJ_{\rm halo}}{dE_\gamma}(l,b) = \frac{1}{4\pi m_{\rm DM}\tau_{\rm DM}}\frac{dN_\gamma}{dE_\gamma}\int_0^\infty ds\,\rho_{\rm DM}[r(s,l,b)]\,. \tag{3.3}$$

The integration extends over the line of sight and is parametrized by the distance s from our position. Furthermore, l and b denote Galactic latitude and longitude, respectively. The celestial Galactic coordinate system (s, l, b) is defined such that s is the distance from the Sun, b is the angle between the line of sight and the Galactic plane, while l is the angle between the line of sight and the direction of the Galactic center. The radial parameter r of the halo

density profile is related to the distance parameter s and Galactic latitude and longitude by

$$r(s,l,b) = \sqrt{s^2 + R_\odot^2 - 2\,sR_\odot \cos b \cos l}\,, \tag{3.4}$$

where $R_\odot$ is the distance of the Sun from the Galactic center. The halo signal of gamma rays from dark matter decay has an angular dependence and does not appear isotropic from our location since we are located about 8.5 kpc away from the center of the halo. We will study this effect in details in Chapter 6. We generally assume that the dark matter halo is smooth, *i.e.*, we ignore the possible effects of substructure on the gamma-ray emission. This is particularly justified in the case of dark matter decay as opposed to dark matter annihilation, since for decaying dark matter the gamma-ray emission only depends linearly on the dark matter density.

Apart from the prompt radiation stemming directly from the decay process of the dark matter itself or its daughter particles, there is also a secondary contribution produced by inverse Compton scattering if the dark matter decays or annihilates into electrons and positrons (either directly or through the decay/fragmentation of intermediate particles). We will discuss this contribution in detail in the next section.

3.3 Inverse Compton Scattering

As mentioned above, the process of inverse Compton scattering is one of the main mechanisms of energy loss for electrons and positrons propagating in the interstellar or intergalactic medium. The process consists in the upscattering to gamma-ray energies of initially low-energy photons in the interstellar radiation field (ISRF) by electrons and positrons. As such, inverse Compton scattering can show up in gamma-ray observations as an indirect signature of the presence of a population of highly energetic charged leptons propagating in the halo, as well as in intergalactic space. Thus, this effect provides some complementarity between leptonic cosmic rays and gamma-ray production. For an introduction to the topic, see [162]. In this section we follow our brief review of inverse Compton scattering in [3].

The production rate of gamma rays with energy E_γ per unit volume and unit time at the position $\vec{r}$ in the Galaxy due to inverse Compton scattering of electrons or positrons on the interstellar radiation field is given by

$$\frac{dR_\gamma^{\rm IC}}{dE_\gamma}(\vec{r}) = \int_0^\infty d\varepsilon \int_{m_e}^\infty dE_e \frac{d\sigma^{\rm IC}}{dE_\gamma}(E_e,\varepsilon) f_{e^\pm}(E_e,\vec{r}) f_{\rm ISRF}(\varepsilon,\vec{r})\,, \tag{3.5}$$

where $f_{e^\pm}(E_e,\vec{r})$ and $f_{\rm ISRF}(\varepsilon,\vec{r})$ denote the number densities per unit energy of electrons or positrons and ISRF photons, respectively. Furthermore, $d\sigma^{\rm IC}/dE_\gamma$ denotes the differential cross-section of inverse Compton scattering of an electron with energy E_e, where an ISRF photon with energy ε is upscattered to an energy between E_γ and $E_\gamma + dE_\gamma$. There are three main components of the interstellar radiation field: the cosmic microwave background, diffuse starlight and rescattererd thermal dust radiation. For the ISRF we adopt the model presented in [163], which is implemented in the `GALPROP` code. From there, we take the tabulated energy density of the different radiation field components on a three-dimensional lattice. We show a plot of the different ISRF components in this model in Fig. 3.2.

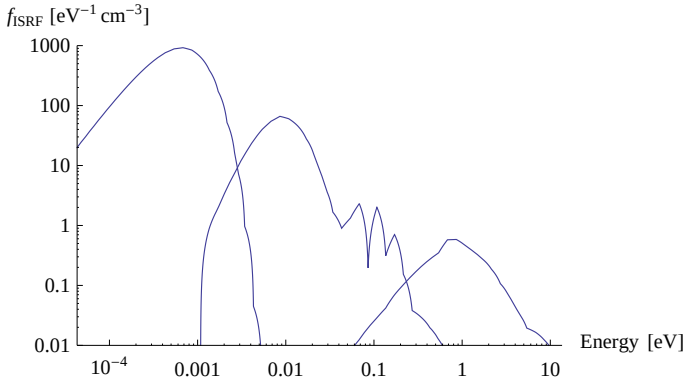

Figure 3.2: Spatially averaged number densities per unit energy of the interstellar radiation field in the microwave, infrared and optical bands. *From left to right:* cosmic microwave background, thermal dust radiation, and diffuse starlight. We use the ISRF model presented in [163], which is included in the `GALPROP` code.

The inverse Compton scattering cross-section between electrons and photons can be derived from the Klein-Nishina formula and is given by

$$\frac{d\sigma^{\rm IC}}{dE_\gamma}(E_e,\vec{r}) = \frac{3}{4}\frac{\sigma_{\rm T}}{\gamma_e^2\varepsilon}\left[2q\ln q + 1 + q - 2q^2 + \frac{1}{2}\frac{(q\,\Gamma)^2}{1+q\,\Gamma}(1-q)\right], \tag{3.6}$$

where again ε, E_γ and E_e denote the energy of the initial-state ISRF photon, the upscattered final-state gamma-ray photon and the energy of the scattering electron, respectively. $\sigma_{\rm T} = 8\pi r_e^2/3 \approx 0.67\,\mathrm{b}$ is the Compton scattering cross-section in the Thomson limit, with r_e being the classical electron radius. In the above expression, γ_e is the relativistic Lorentz factor of the electron, $\gamma_e \equiv E_e/m_e$. Furthermore, we have introduced the abbreviations $\Gamma \equiv 4\gamma_e\varepsilon/m_e$ and $q \equiv E_\gamma/\Gamma(E_e - E_\gamma)$. Eq. (3.6) holds in the limit where ε, $m_e \ll E_e$. Kinematics and the neglect of downscattering require that $\varepsilon \leq E_\gamma \leq (1/E_e + 1/(4\gamma_e^2\varepsilon))^{-1} \equiv E_\gamma^{\rm max}$. For the calculations we will assume that the photon and electron fields are isotropic; taking into account the anisotropy of the photons, which are mainly produced in the Galactic disk, would give $\mathcal{O}(10\% - 20\%)$ corrections to the gamma-ray fluxes from inverse Compton [164].

The gamma-ray flux from inverse Compton scattering in the halo that is received at Earth reads

$$\frac{dJ^{\rm IC}}{dE_\gamma} = 2\cdot\frac{1}{4\pi}\int_0^\infty ds\,\frac{dR_\gamma^{\rm IC}}{dE_\gamma}[r(s,l,b)]\,, \tag{3.7}$$

where the factor 2 takes into account the fact that electrons and positrons from dark matter decay contribute equally to the total inverse Compton emission.

The number density of electrons and positrons from dark matter decays in principle follows from solving the appropriate transport equation for electrons and positrons, Eq. (2.7), which incorporates the effects of diffusion, reacceleration and convection in the Galactic magnetic field, and energy losses due to synchrotron emission and inverse Compton scattering on the ISRF. However, at energies above a few tens of GeV, the transport equation is dominated by the effects of energy loss, and the number density of electrons and positrons can be

approximated by

$$f_{e^\pm}(E_e, \vec{r}) = \frac{1}{b(E_e, \vec{r})} \frac{\rho_{\rm halo}(\vec{r})}{m_{\rm DM} \tau_{\rm DM}} \int_{E_e}^{\infty} d\tilde{E}_e \frac{dN_{e^\pm}}{d\tilde{E}_e} \,. \tag{3.8}$$

Substituting this expression back into Eq. (3.5) allows us to calculate the rate of inverse Compton scattering. Here, the energy loss rate $b(E_e, \vec{r})$ is essentially given by a part that is due to inverse Compton scattering on the ISRF and a part that is due to synchrotron energy losses from interactions of electrons with the Galactic magnetic field. We therefore write $b = b_{\rm IC} + b_{\rm syn}$, where the inverse Compton part of the energy loss term reads

$$b_{\rm IC}(E_e, \vec{r}) = \int_0^{\infty} d\varepsilon \int_{\varepsilon}^{E_\gamma^{\rm max}} dE_\gamma \; (E_\gamma - \varepsilon) \frac{d\sigma^{\rm IC}}{dE_\gamma}(E_e, \varepsilon) f_{\rm ISRF}(\varepsilon, \vec{r}) \,. \tag{3.9}$$

For an electron energy $E_e = 1\,\text{GeV}$, the inverse Compton energy loss rate $b_{\rm IC}$ ranges between $4.1 \times 10^{-17}\,\text{GeV}\,\text{s}^{-1}$ and $1.9 \times 10^{-15}\,\text{GeV}\,\text{s}^{-1}$, depending on the position $\vec{r}$. At higher energies $b_{\rm IC}$ approximately scales like $\sim E_e^2$. This is in general agreement with the simplified form of the position-independent energy loss rate $b(T)$ which we assume in the transport equation for electrons and positrons (*cf.* Eq. (2.8)). On the other hand, the synchrotron energy loss part is given by

$$b_{\rm syn}(E_e, \vec{r}) = \frac{4}{3} \sigma_{\rm T} \, \gamma_e^2 \frac{B^2}{2} \,, \tag{3.10}$$

where $B^2/2$ is the energy density of the Galactic magnetic field and $\gamma_e \equiv E_e/m_e$. In the following we assume the standard parametrization of the magnetic field [152], where for definiteness we adopt the values [165]

$$B(r, z) = 6\,\mu\text{G} \exp\left(-\frac{|z|}{5\ \text{kpc}} - \frac{r}{20\ \text{kpc}} \right) \,. \tag{3.11}$$

For this choice of parameters, the energy loss due to synchrotron radiation from interactions of electrons with the Galactic magnetic field turns out to be subdominant compared to the one from inverse Compton scattering on the ISRF everywhere except close to the Galactic center, and for high electron/positron energies. Nevertheless, we include this contribution for completeness. At the position of the Sun, we find a synchrotron energy loss rate of

$$b_{\rm syn}(E_e) \simeq 4.0 \times 10^{-17} \left(\frac{E_e}{\text{GeV}} \right)^2 \text{GeV}\,\text{s}^{-1} \,. \tag{3.12}$$

Using the above prescription, we can calculate the inverse Compton emission that is generated by electrons and positrons from dark matter decay in the halo. We also take into account inverse Compton scattering at cosmological distances by scattering on the CMB, whose number density as a function of redshift z is given by

$$f_{\rm CMB}(z, \varepsilon) = \frac{1}{\pi^2} \frac{\varepsilon^2}{\exp\left[\varepsilon/(k_{\rm B} T_{\rm CMB}(z+1))\right] - 1} \,. \tag{3.13}$$

with the Boltzmann constant $k_{\rm B}$ and $T_{\rm CMB} = 2.725$ K [52], while energy losses are calculated in the Thomson limit.

Part II

Model-Independent Considerations

Chapter 4

Charged Leptons from Decaying Dark Matter

A series of experiments measuring high-energy cosmic rays have recently reported strong indications for the existence of an excess of high-energy electrons and positrons compared to the background expected from spallation of cosmic rays. An indication of the possible existence of an anomalous component in the positron fraction was already present in the data from cosmic-ray observatories HEAT, AMS-01, as well as from even earlier measurements. However, while a possible excess in the positron fraction and potential explanations were already discussed more than 20 years ago [166, 167], conclusive evidence of the presence of a significant primary component has only emergerged recently.

In late 2008, the PAMELA collaboration announced the spectacular observation of a steep rise in the positron fraction extending up to at least 100 GeV. This behavior is in stark contrast with the expectation from the standard picture of cosmic-ray production and propagation [168]. Furthermore, cosmic-ray observatories Fermi LAT, as well as H.E.S.S., PPB-BETS and ATIC have measured the combined electron + positron flux and found it to be harder than expected at energies up to 1 TeV, also possibly hinting at the existence of a source of primary positrons and electrons. In this chapter, which is based on the publications [4, 8], we examine the anomalous results in leptonic cosmic-rays reported by the PAMELA and Fermi LAT collaborations under the hypothesis that they are caused by the injection of primary electrons and positrons into the Galactic halo from the decay of unstable dark matter particles.

If interpreted in terms of the decay of dark matter particles, the PAMELA measurements of the positron fraction and the Fermi LAT measurements of the total electron-plus-positron flux restrict the possible decaying dark matter scenarios to a few cases. Analyzing different decay channels in a model-independent manner, and adopting a conventional diffusive reacceleration model for the background fluxes of electrons and positrons, we identify some promising scenarios of dark matter decay and calculate the predictions for the diffuse extragalactic gamma-ray flux, including the contributions from inverse Compton scattering with the interstellar radiation field.

4.1 Introduction

Different experiments measuring high-energy cosmic rays have recently reported a wealth of new results pointing toward the existence of an exotic source of high-energy electrons and positrons. The PAMELA collaboration has reported evidence for a sharp rise in the positron fraction at energies of $7-100\,\mathrm{GeV}$ [169], possibly extending to even higher energies, compared to the expectations from spallation of primary cosmic rays on the interstellar medium [168] (see Fig. 4.1). This result confirmed previous hints about the existence of a positron excess from HEAT [170], CAPRICE [171] and AMS-01 [172]. Almost at the same time, the balloon-borne experiments ATIC [173] and PPB-BETS [174] independently reported the discovery of a shoulder-like feature in the total electron + positron flux at energies of $600 - 700$ GeV, while the H.E.S.S. collaboration [175] reported a substantial steepening in the high-energy electron-plus-positron spectrum above 600 GeV compared to lower energies.

These results have raised a great deal of interest in the astrophysics and particle physics communities, leading to many proposals trying to explain this excess. One of the most popular astrophysical explanations of the positron excess is in terms of the electron–positron pairs produced by the interactions of high-energy photons in the strong magnetic field of pulsars [176, 177, 178]. However, this interpretation requires a rather large fraction of the spin-down power being injected in the form of electron–positron pairs or a rather large rate of gamma-ray pulsar formation. A number of alternative astrophysical explanations exist, which we briefly review in Section 4.3.

An arguably more exciting explanation of the cosmic-ray positron excess is the possibility that the positrons are produced in the annihilation or the decay of dark matter particles, where the idea that there may be a contribution from dark matter to the cosmic-ray positron flux goes back to the late 1980s (see, *e.g.*, [179, 180, 181]). Should this interpretation be confirmed by complementary studies in the future, then the positron excess would constitute the first non-gravitational evidence for the existence of dark matter in our Galaxy. The interpretation of the PAMELA excess in terms of dark matter is subject to constraints from the flux measurements of other cosmic-ray species. A very important constraint arises from the measurements of the antiproton flux by PAMELA [129], BESS95 [182], BESS95/97 [183], CAPRICE94 [184], CAPRICE98 [185] and IMAX [186], which are consistent with the expectations from conventional propagation models, thus excluding the possibility of a large antiproton flux from dark matter annhilation or decay [187, 188].

The steep rise in the positron fraction observed by PAMELA can be explained by dark matter annihilation in the center of the Milky Way, provided that the dark matter particle has a mass larger than $\sim 150\,\mathrm{GeV}$ and annihilates preferentially into charged leptons [189]. This interpretation of the positron excess, however, typically requires the *ad hoc* introduction of large "boost factors" that enhance the annihilation cross section for a thermal relic, Eq. (1.8), by two to three order of magnitude [190]. Furthermore, it has been argued that if dark matter annihilations are the origin of the PAMELA anomaly, then the predicted inverse Compton emission from the center of the Galaxy is in conflict with the H.E.S.S. observations for typical cuspy halo profiles [191, 192, 193], as well as radio emissions from the Galactic center [165, 191, 194, 195, 196, 197]. On the other hand, if the positron excess is due to the decay of dark matter, the dark matter particles must have a mass larger than $\sim 300\,\mathrm{GeV}$, a

lifetime around 10^{26} s, and must decay with a large branching fraction into hard leptons of the first or second generation [8]. In this case, no boost factors are required and the gamma and radio emissions are consistent with present measurements [104]. Some recent work on the indirect detection of decaying dark matter can be found in [99, 103, 111, 198, 199, 200, 201, 202, 203, 204, 205, 206, 207, 208, 209, 210, 211, 212, 213, 214, 215].

More recently, the Fermi LAT collaboration has published measurements of the electron + positron flux from 20 GeV to 1 TeV of unprecedented accuracy [216], revealing an energy spectrum that roughly follows a power law $\propto E^{-3.0}$ without any prominant spectral features. Simultaneously, the H.E.S.S. collaboration reported a measurement of the cosmic-ray electron + positron spectrum at energies larger than 340 GeV, confirming the Fermi LAT result of a power-law spectrum with a spectral index of 3.0 ± 0.1 (stat.) ± 0.3 (syst.), which furthermore softens to a spectral index ~ 4 at energies above 1 TeV [217]. The measured electron energy spectrum is harder than expected from conventional diffusive models, although it can be accommodated by an appropriate change of the injection spectrum of primary electrons. However, when taken together with the steep rise in the positron fraction as seen by PAMELA up to energies of 100 GeV, the Fermi LAT data suggest the existence of additional sources of high-energy positrons and electrons with energies up to a few TeV. Furthermore, it should be borne in mind that the determination of the correct Galactic cosmic-ray scenario is still an open problem, and while an electron injection spectrum harder than the conventional one could reproduce the Fermi data, it fails to account for the AMS-01 and HEAT data below 20 GeV and the H.E.S.S. data above 1 TeV [218].

In this chapter we analyze the constraints that the results of the PAMELA and Fermi LAT collaborations impose on the scenario of decaying dark matter, assuming a conventional `GALPROP` model as our Galactic cosmic-ray scenario. To this end, we pursue a model-independent approach, calculating the results for the positron fraction and the total electron + positron flux for various decay channels of both a fermionic and a scalar dark matter particle. We identify the most promising decay channels in the of the PAMELA and Fermi data, and we calculate for those scenarios the predictions for the antiproton flux and the diffuse extragalactic gamma-ray flux. Some related work has recently appeared [5, 219, 97, 98, 220].

This chapter is organized as follows. In Section 4.2 we review the observational situation regarding the positron fraction and the total electron + positron flux. Next, in Section 4.3 we examine some of the astrophysical explanations that have been proposed for the leptonic cosmic-ray anomalies. In Section 4.4 we present our model-independent analysis of the cosmic-ray anomalies in terms of decaying dark matter before presenting our conclusions in Section 4.5.

4.2 The Positron Excess

Instead of reporting the absolute positron flux, measurements of cosmic positrons are often reported in the form of the positron fraction, which is defined as the ratio between the flux of positrons and the combined flux of positrons and electrons,

$$R_{e^+}(E) = \frac{\Phi_{e^+}(E)}{\Phi_{e^+}(E) + \Phi_{e^-}(E)} \,. \tag{4.1}$$

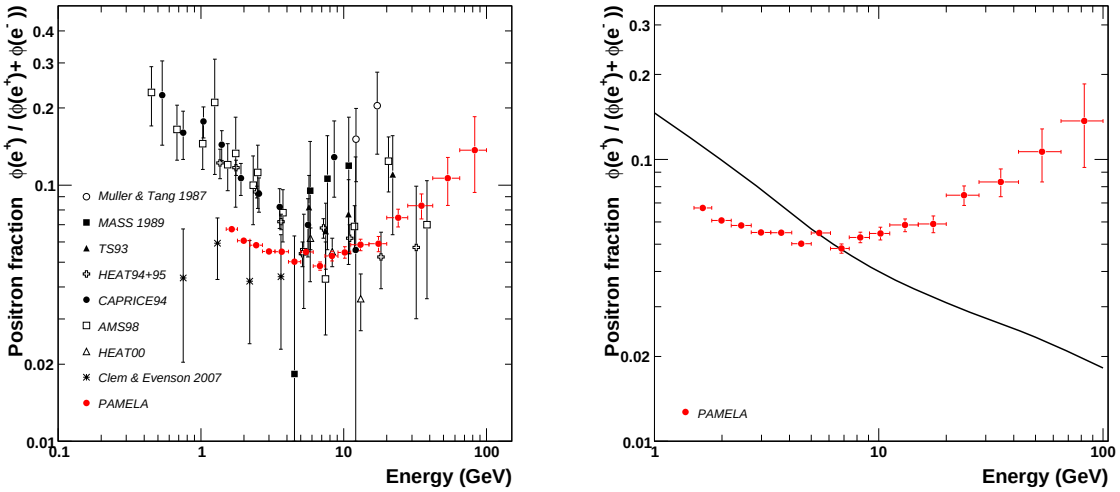

Figure 4.1: *Left:* The positron fraction as measured in various observations: Müller & Tang [221], TS93 [222], HEAT (1994+1995) [170], HEAT (2000) [223], AMS-01 [172] and PAMELA [169]. *Right:* The positron fraction observed by PAMELA compared to the conventional model by Moskalenko and Strong [168]. The discrepancy below 10 GeV is believed to be due to solar modulation [224]. Figures from [169].

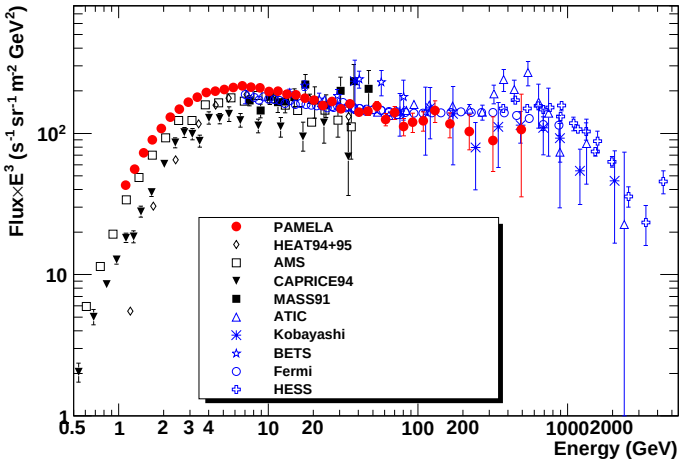

Figure 4.2: The cosmic-ray flux of electrons + positrons as measured by PAMELA [225], HEAT [226], AMS-01 [227], CAPRICE94 [171], MASS91 [228], ATIC [173], Kobayashi *et al.* [229], BETS [230], Fermi LAT [231], and H.E.S.S. [175]. Figure from [225]. ATIC and PPB-BETS [174] report the observation of a sharp shoulder-like spectral feature in the flux, but this claim is contradicted by Fermi LAT and H.E.S.S. measurements.

The advantage of using the positron fraction is that certain systematic uncertainties such as detector acceptance and trigger efficiency cancel. Some instruments can only measure the

combined flux of electrons and positrons (often simply referred to as the "electron flux"), since they lack the ability to distinguish the two based on their charge due to the lack of a magnetic field. In Fig. 4.1 we show determinations of the positron fraction obtained using various balloon and satellite-based instruments over the past decades. In Fig. 4.2, on the other hand, we show measurements of the combined electron + positron flux.

The high-energy behavior of the positron fraction is completely opposite to astrophysical expectations when the positrons are of secondary origin, which was generally believed to be the case before significant evidence of the rise in the positron fraction emerged. While there is a discrepancy between the measurement and the astrophysical model at energies below 10 GeV, as evident from Fig. 4.1, this difference is believed to be caused by solar modulation [224] and not to be an indication of any kind of new physics. Specifically, the positron fraction was expected to be lower than in previous measurements because of the reversal of the solar magnetic field polarity in 2001 [61].

What is puzzling about the behavior of the positron fraction is not only the large quantitative discrepancy with respect to the standard theoretical expectation, but especially the observed *increase* toward higher energies, which is completely opposite to the behavior that is qualitatively expected if the positrons are of secondary origin. Namely, within the leaky-box framework [232] it is relatively straightforward to demonstrate that a ratio of secondaries to primaries, as tentatively the case for the positron fraction, should decrease monotonically with the energy approximately like $R_{e^+}(E) \propto E^{-\delta}$ at energies above a few GeV if the primary spectral indices of electrons and positrons at injection are similar [233]. The only way to produce a rise in the positron fraction would be to postulate greatly different source spectral indices for electrons and protons, which seems highly implausible from astrophysical considerations. The standard picture of diffusive shock acceleration of cosmic rays predicts that the source spectral indices of electrons and protons should be similar [130, 234].

In a more involved model of cosmic-ray propagation this is somewhat more complicated to demonstrate, but it appears to be a rather robust prediction that the secondary flux should be softer than the primary flux [139], and that the positron fraction should therefore decrease with energy [233, 235]. Therefore, the fact that the positron fraction increases with the energy is completely at odds with the assumption that the high-energy positrons are produced as secondaries, and thus a strong indication of the presence of a primary component in the positron flux. What is more, Eq. (2.12), which describes the typical diffusion length $\lambda_{\rm D}(T, T')$ of electrons and positrons, implies that at the energies of interest the propagation length is on the order of kpc and decreasing with the positron energy, implying that the source of the primary high-energy positrons must be a local and located within a few kpc around the Solar neighborhood, where the highest-energy positrons come from the shortest distances.

It should be noted that unlike the positron fraction, the hardness of the observed e^+e^- spectrum does not necessarily imply the existence of an additional source of positrons and electrons. With a sufficiently hard primary injection spectrum, the observed flux $\propto E^{-3.0}$ can be reproduced [218] at the cost of a worse agreement with the low-energy data. The Fermi LAT electron data exhibit a slight break in the spectrum, however, which might be interpreted as the onset of a dominant primary component of electrons and positrons above ~ 100 GeV, which is compatible with a smooth continuation of the PAMELA excess of positrons to even

higher energies, as we show in the following.

4.3 Astrophysical Interpretations of the Positron Excess

A number of astrophysical explanations of the cosmic-ray excesses have been put forward that do not require any kind of new fundamental physics. The most common astrophysical explanation of the electron/positron excesses is the electron-positron pair production by the interactions of high-energy photons in the strong magnetic field of nearby mature pulsars such as Geminga or Monogem [177, 178, 236, 237, 238]. Pulsars, which are rapidly spinning, highly magnetized neutron stars, may serve in this manner as a significant source of high-energy positrons and electrons. They have already been discussed as a source of primary electrons and positrons since the late 1980s [176, 239, 240, 241]. Pulsars are a popular explanation of the positron excess since they undisputedly produce positrons and electrons at some level, while they do not produce antiprotons, making them naturally compatible with the absence of an excess in the antiproton flux.

Pulsars convert some of their rotational energy into a magnetized wind by so-called spin-down. In the pulsar magnetosphere electrons can be accelerated to very high energies and radiate hard gamma rays from bremsstrahlung on the pulsar's intense magnetic fields. This can induce electromagnetic cascades involving photons above the e^+e^- pair production threshold. These e^+e^- pairs produced on the pulsar's magnetic fields can then escape from the magnetosphere, provided that the pulsar is sufficiently mature. Pulsars younger than $\sim 10^5$ yr likely confine electrons and positrons within their pulsar wind nebulae [177], delaying their escape into the interstellar medium.

However, if a single pulsar is responsible for the observed high-energy fluxes, this requires a very large portion of the total spin-down power being injected in the form of electron-positron pairs, namely about 40%, and a large cutoff of the electron/positron energy spectrum at about 1 TeV [218]. For this reason, a single pulsar as the source of the PAMELA and Fermi LAT data appears disfavored [236]. Alternatively, the electron/positron excesses could be explained by the combined emission of both nearby and distant pulsars [177, 218], this solution requiring a converted percentage of the spin-down power in the range of $10\% - 30\%$ and, again, a large cutoff in the energy spectrum around $800 - 1400$ GeV [218]. Pulsars may therefore consitute an important component of primary positrons. However, it should be noted that the pulsar spectrum depends on unknown environmental parameters, preventing a genuine prediction of their contribution to the electron–positron fluxes. If the pulsar emission is dominated by one or a few nearby sources, this may induce a detectable anisotropy in the respective fluxes, which might allow a distinction of this explanation from dark matter explanations [177, 236].

An alternative proposal to explain the cosmic-ray excesses is that they were caused by a nearby gamma-ray burst (or a gamma-ray burst-like event) that occured $\sim 10^5$ years ago [242], which could produce a primary spectrum harder than the secondary spectrum from cosmic rays accelerated by supernova remnants. Depending on the injection spectral index, the electron–positron flux from a gamma-ray burst may reproduce the Fermi LAT spectrum or even the spectral feature observed by ATIC and PPB-BETS. This interpretation also implies that there should exist a clear anisotropy in the fluxes of electrons and positrons that should

be detectable by Fermi LAT or AMS-02.

The positron excess may also be a consequence of an inhomogeneous distribution of supernova remnants in the Galactic disk [243]. Another explanation is the acceleration of additional secondary positrons produced by hadronic interactions within the sources of cosmic rays [235, 244], which would predict a rise in the antiproton-to-proton ratio and other secondary-to-primary ratios at higher energies [245]. Moreover, it has been proposed that one or several recent supernova explosions close to Earth may have produced hard positrons and electrons within the dense gas clouds surrounding old supernova remnants [246]. Finally, nested leaky-box models can also reproduce the rise in the positron fraction [247, 248].

Whatever the correct explanation of the observed cosmic-ray anomalies may be, the existence of various potential astrophysical sources makes it clear that one has to take appropriate caution in interpreting the anomalous results in terms of dark matter.

4.4 Positrons and Electrons from Decaying Dark Matter

We present in this section the calculations for the positron fraction and the total electron + positron flux when including a contribution from dark matter decay in order to account for the anomalies observed by PAMELA and Fermi LAT. To keep the analysis as model-independent as possible, we analyze several different scenarios of dark matter decay, computing the predictions for the positron fraction and the electron + positron flux for bosonic and fermionic dark matter particles that decay into various channels with a branching ratio of 100%. For a concrete dark matter model with realistic branching ratios, our results can then easily be rescaled. We determined for each of these decay channels the energy spectrum of electrons and positrons using the event generator `PYTHIA 6.4` [249].[1] Thus, from the particle physics point of view, the only free parameters are the dark matter mass and lifetime. From the astrophysics point of view there are a number of uncertainties, such as the choice of propagation parameters as discussed in Chapter 2 and the choice of the background fluxes of electrons and positrons.

For the propagation of the antiparticle spectra, we implement the stationary two-zone model outlined in Chapter 2, using the full semi-analytical solutions given there. For definiteness, we assume for the dark matter halo profile the Navarro-Frenk-White profile as defined in Eq. (1.13) with a dark matter density $\rho_0 = 0.26\,\mathrm{GeV\,cm^{-3}}$ and the values of the parameters given in Table 1.1, although our results are almost independent of the choice of halo profile.[2] For the propagation parameters of the model we adopt the MED propagation model defined in [137, 145] (see Table 2.1), which provides the best fit to the Boron-to-Carbon (B/C) ratio. The results for the charged leptons turn out to be not very sensitive to the particular choice of propagation parameters. This is due to the fact that at energies above a few tens of GeV energy losses dominate over the effects of diffusion, rendering the exact propagation model

[1] See [250] for a discussion of the differences between `PYTHIA` and the `HERWIG` Monte Carlo for the generation of particle spectra in the context of indirect dark matter detection.

[2] Due to the effective energy loss of electrons, the high-energy component of the spectrum mostly originates from sources within the Galactic neighborhood of a few kpc for the Solar System, where the different halo profiles are very similar. We have checked that choosing different halo profiles has a neglibible effect on our results (see also [8]).

parameters less relevant. We illustrate the dependence of the results on the adopted model parameters for a particular example below. The fluxes of antiprotons, however, are drastically affected by the choice of transport parameters, as discussed in Chapter 2. Therefore, we will show results for antiprotons corresponding to all three sets of transport parameters listed in Table 2.3 to illustrate the range over which the results can vary.

On the other hand, to compare the predictions with observations, it is necessary to make assumptions on the astrophysical backgrounds of secondary positrons and electrons. As explained above, these background fluxes are produced by the scattering of primary cosmic rays with the interstellar gas. For the interstellar background fluxes of electrons and positrons, we will adopt in this chapter the spectra corresponding to the "model 0" proposed by the Fermi LAT collaboration [218], which agree well with low-energy measurements, but are softer than the electron + positron spectrum observed by Fermi LAT at high energies. We perform a fit to the electron and positron spectra given by the collaboration, obtaining the following parametrization of the "model 0" background:

$$\Phi_{e^-}^{\rm bkg}(E) = \left(\frac{82.0\,\varepsilon^{-0.28}}{1 + 0.224\,\varepsilon^{2.93}} \right) \,{\rm GeV}^{-1}\,{\rm m}^{-2}\,{\rm s}^{-1}\,{\rm sr}^{-1}\,, \tag{4.2}$$

$$\Phi_{e^+}^{\rm bkg}(E) = \left(\frac{38.4\,\varepsilon^{-4.78}}{1 + 0.0002\,\varepsilon^{5.63}} + 24.0\,\varepsilon^{-3.41} \right) \,{\rm GeV}^{-1}\,{\rm m}^{-2}\,{\rm s}^{-1}\,{\rm sr}^{-1}\,, \tag{4.3}$$

where $\varepsilon = E/(1\,{\rm GeV})$. In the energy regime between 2 GeV and 1 TeV these parametrizations agree with the model given by the Fermi collaboration to an accuracy better than 5%. Note that these are parametrizations of the interstellar fluxes, so that solar modulation has to be taken into account to relate the fluxes at the heliospheric boundary to the top-of-atmosphere fluxes (see Section 2.3). We adopt in this analysis a value of $\phi_{\rm F} = 550$ MV for the modulation potential.

We will allow for a shift in the normalization of the background flux of electrons, which is dominated by primaries, due to our ignorance of the amount of electrons injected in the interstellar medium. In other words, we explicitly decompose the positron fraction, Eq. (4.1), as follows,

$$R_{e^+}(E) = \frac{\Phi_{e^+}^{\rm prim}(E) + \Phi_{e^+}^{\rm sec}(E)}{\Phi_{e^+}^{\rm prim}(E) + \Phi_{e^+}^{\rm sec}(E) + k\,\Phi_{e^-}^{\rm prim}(E) + \Phi_{e^-}^{\rm sec}(E)}\,. \tag{4.4}$$

We will generally assume throughout this thesis that the decay of dark matter produces matter and antimatter in equal quantities, or that *CP* is (at least approximately) conserved. Under the assumption of charge symmetry, the positron fraction can in principle increase up to a value of 1/2 at energies above 100 GeV if it becomes completely dominated by the dark matter contribution.

We will also calculate the gamma-ray fluxes from dark matter, both from prompt radiation and from inverse Compton scattering of the energetic electrons and positrons injected into the interstellar medium by dark matter decay. To calculate the contributions from prompt radiation and inverse Compton radiatio, we follow the procedure outlined in Chapter 3. We compare our results to the two extractions of the extragalactic gamma-ray background performed by Sreekumar *et al.* [155] and the later reanalysis by Strong, Moskalenko and Reimer [251].

In our analysis of we will sample several dark matter masses and treat the dark matter lifetime and the normalization of the background flux of electrons as free parameters which will be determined so as to provide a qualitatively good fit to the PAMELA and Fermi measurements. Note that below energies of 10 GeV, the data is best fitted for normalizations $k \simeq 1$. In all of the plots in the remainder of this chapter, normalization factors $0.8 \geq k \geq 1$ are used. In view of the astrophysical uncertainties including the determination of the background fluxes, the local dark matter density and the transport properties of the interstellar medium, we do not quantify the quality of the fits in terms of χ^2 values unlike some other authors [104]. Let us now discuss the cases of fermionic and scalar dark matter separately.

4.4.1 Fermionic Dark Matter

In the case where the dark matter particle is a fermion $\psi_{\rm DM}$, we consider the following decay channels:[3]

$$\begin{aligned} \psi_{\rm DM} &\to Z^0 \nu \,, \\ \psi_{\rm DM} &\to W^{\pm} \ell^{\mp} \,, \\ \psi_{\rm DM} &\to \ell^+ \ell^- \nu \,, \end{aligned} \tag{4.5}$$

where ν stands for any massless (or very light) neutral fermion, in particular a neutrino. The three-body decay into charged leptons and a neutrino is assumed to be mediated by the exchange of a virtual scalar particle, motivated by the interesting scenario of a hidden gaugino as the dark matter particle [7, 100, 211]. See Chapter 10 for a detailed analysis of this scenario.

The predicted positron fraction in the case where the dark matter particle decays via $\psi_{\rm DM} \to Z^0 \nu$ is shown in the left panel of Fig. 4.3, compared to the PAMELA, HEAT, CAPRICE and AMS-01 data, for the sample dark matter masses $m_{\rm DM} = 5\,{\rm TeV}$ and $m_{\rm DM} = 100\,{\rm TeV}$. In the right panel we show the corresponding total electron + positron flux compared to the results from Fermi LAT, H.E.S.S., PPB-BETS, BETS, ATIC, HEAT, CAPRICE, and AMS-01. The dark matter lifetimes and the normalization factors k of the primary electron flux have been chosen in each case to provide a reasonable fit to the PAMELA and Fermi data points. In this decay channel, the dominant source of electrons and positrons is the fragmentation of the Z^0 boson (with a rather small branching ratio of Z^0 decays into a pair of charged leptons), which produces a spectrum of relatively soft particles. As a result, even though this decay mode can produce a visible excess in the positron fraction, the energy spectrum is in general too flat to explain the steep rise observed by PAMELA. An exception occurs when the dark matter mass is very large, $m_{\rm DM} \gtrsim 50\,{\rm TeV}$. In this case, the electrons and positrons from dark matter decay are boosted to high enough energies to produce a sufficiently steep rise in the positron fraction. However, these large dark matter masses seem to be in conflict with the H.E.S.S. observations, which require a steepening in the total electron + positron spectrum above $\sim 1\,{\rm TeV}$. Furthermore, decay channels involving weak gauge bosons are subject to stringent constraints from antiproton overproduction.

In Fig. 4.4 we show the predictions for the cosmic-ray electron and positron fluxes when a fermionic dark matter particle decays as $\psi_{\rm DM} \to W^{\pm} \ell^{\mp}$ for different dark matter masses and

[3] We do not include quarks or Higgs bosons in the list since they yield similar signatures to gauge boson fragmentation. Furthermore, we only consider decay channels with two or three final-state particles.

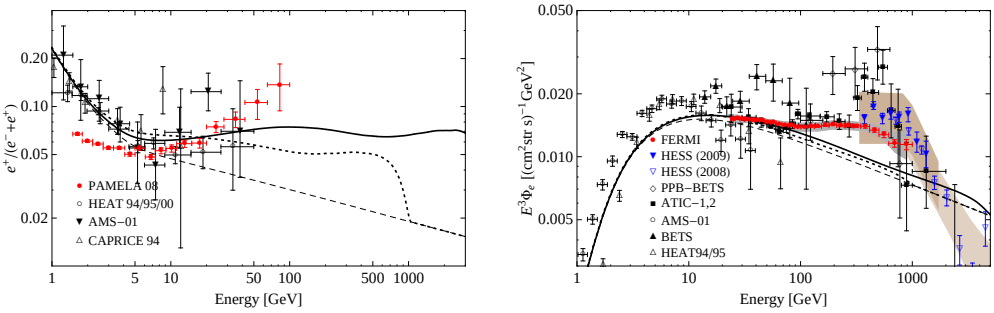

Figure 4.3: Positron fraction (left panel) and total electron + positron flux (right panel) for the decay channel $\psi_{\rm DM} \to Z^0\nu$ with $m_{\rm DM} = 100\,{\rm TeV}$ (solid) and 5 TeV (dotted). The dashed line shows the background fluxes as discussed in the text. Solar modulation is taken into account using the force field approximation with $\phi_{\rm F} = 550$ MV. The shaded areas in the right-hand plot indicate the systematic errors of the H.E.S.S. measurement.

lepton flavors. This case is particularly interesting because of the presence of hard charged leptons in the two-body decay of the dark matter, which can give rise to highly energetic electrons and positrons. The electrons and positrons created in the fragmentation of the $W^\pm$ gauge bosons produce a rather flat contribution to the positron fraction, similar to the case of Z^0 fragmentation. However, the hard electrons and positrons resulting from the decay of the $\mu^\pm$ or $\tau^\pm$ leptons or directly from the dark matter two-body decay into $e^\pm$ produce a significant rise in the total energy spectrum and in the positron fraction. The flavor of the charged leptons is of importance here. Namely, the decay mode $\psi_{\rm DM} \to W^\pm e^\mp$, which can produce a steep rise in the positron fraction and is thus compatible with the PAMELA observations, also produces a prominent spectral feature in the electron + positron flux, namely a step-like rise and falloff. This feature is not observed by Fermi, however. Thus, the possibility that the dark matter particles decay preferentially in this decay mode, which is well compatible with the PAMELA observations, is clearly disfavored by the Fermi results on the total electron + positron flux. The decay $\psi_{\rm DM} \to W^\pm\tau^\mp$ does not produce any problematic spectral features, but results in spectra that are softer than observed.

The decay mode $\psi_{\rm DM} \to W^\pm\mu^\mp$, however, can nicely accommodate the PAMELA and Fermi observations when the dark matter mass is $m_{\rm DM} \simeq 3\,{\rm TeV}$ and the lifetime is $\tau_{\rm DM} \simeq 2.1 \times 10^{26}\,{\rm s}$. In this decay mode, the fragmentation of the $W^\pm$ gauge bosons also produces fluxes of primary antiprotons and gamma rays, which are severely constrained by present experiments. Once the dark matter mass and lifetime are fixed by the fit to the electron/positron data, one can calculate the predicted fluxes of diffuse gamma rays and antiprotons. The predictions for the gamma-ray and antiproton fluxes for this particular decay mode are shown in Figs. 4.5 and 4.6, respectively; the former figure shows the gamma-ray fluxes from final-state radiation and $W^\pm$ fragmentation (green), and from Galactic (blue) and extragalactic (red) inverse Compton scattering of electrons and positrons originating from dark matter decay. We also show the total flux compared to the extraction of the extragalactic diffuse gamma-ray flux by Sreekumar *et al.* [155] and by Strong, Moskalenko and Reimer [251], averaging our anisotropic signal over the whole sky, excluding the region of the Galactic plane with latitudes

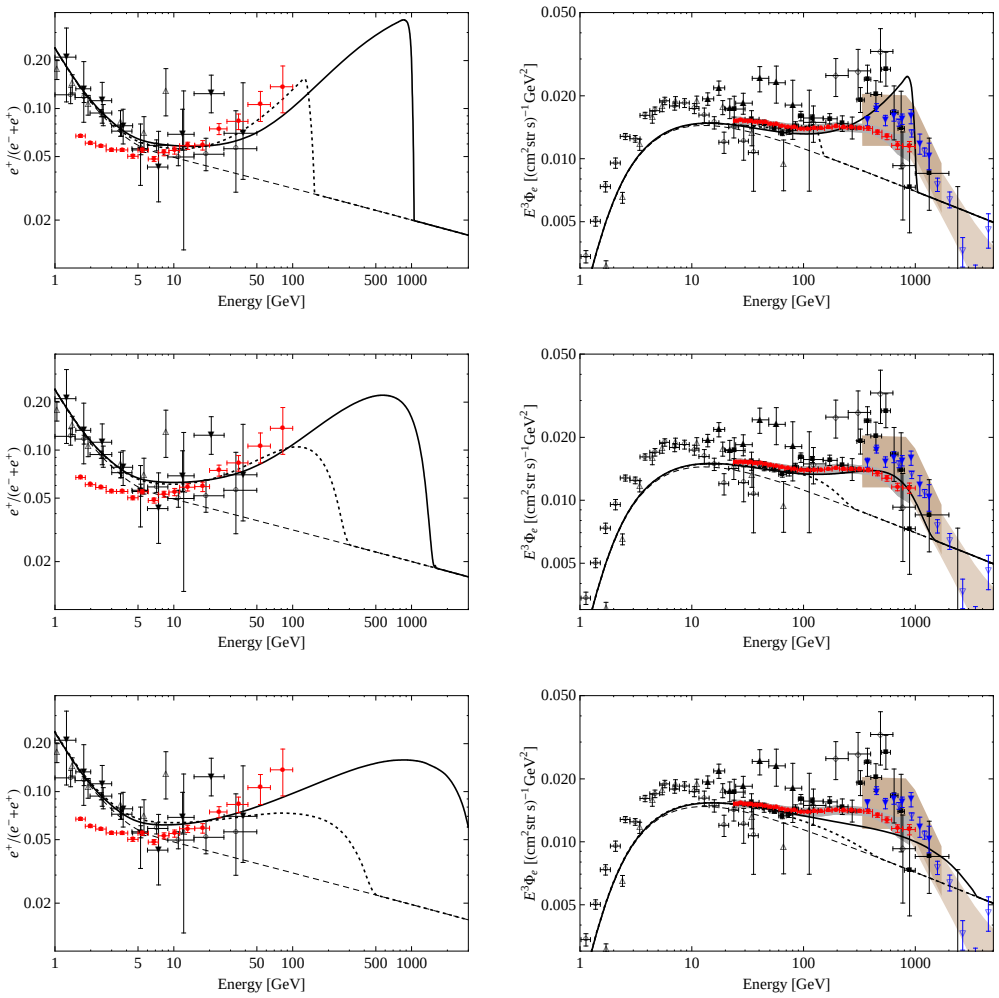

Figure 4.4: Same as Fig. 4.3, but for the decay channels $\psi_{\rm DM} \to W^\pm \ell^\mp$. Upper panels: $\psi_{\rm DM} \to W^\pm e^\mp$ with $m_{\rm DM} = 2000\,{\rm GeV}$ (solid) and $300\,{\rm GeV}$ (dotted). Middle panels: $\psi_{\rm DM} \to W^\pm \mu^\mp$ with $m_{\rm DM} = 3000\,{\rm GeV}$ (solid) and $600\,{\rm GeV}$ (dotted). Lower panels: $\psi_{\rm DM} \to W^\pm \tau^\mp$ with $m_{\rm DM} = 8000\,{\rm GeV}$ (solid) and $1000\,{\rm GeV}$ (dotted).

$|b| < 10^\circ$ and assuming a power law for the the genuinely extragalactic component. On the other hand, the latter figure shows the prediction for the antiproton flux and the antiproton-to-proton ratio with an uncertainty band corresponding to the MIN, MED and MAX models, whose parameters are listed in Table 2.3. While the absolute flux is compatible with existing measurements, it is apparent from the figure that the antiproton-to-proton ratio is in some tension with the results at the highest energies explored by PAMELA. The fragmentation also produces a sizable contribution to the total gamma-ray flux at high energies, which could be visible by the Fermi LAT as a bump over the background, which is assumed to follow a power law, especially if it has a large index as in the extraction of the extragalactic flux from the EGRET data by Strong, Moskalenko and Reimer. Lastly, the decay mode $\psi_{\rm DM} \to W^\pm \tau^\mp$ predicts, for a wide range of dark matter masses, a positron fraction and an electron + positron

flux that are too flat to explain the anomalies observed by PAMELA and Fermi.

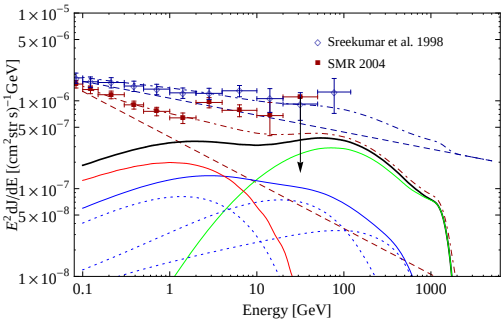

Figure 4.5: Extragalactic diffuse gamma-ray flux for $\psi_{\rm DM} \to W^{\pm}\mu^{\mp}$ with $m_{\rm DM} = 3000\,\text{GeV}$ and $\tau_{\rm DM} = 2.1 \times 10^{26}\,\text{s}$. The gamma-ray flux is averaged over the whole sky, excluding the Galactic plane, $|b| < 10°$. We included gamma rays produced directly in the final-state radiation of the muons and the fragmentation of the $W^{\pm}$ (green line), gamma rays from inverse Compton scattering of electrons and positrons from dark matter decay on the interstellar radiation field (solid blue line; the dotted blue lines show, from left to right, the fluxes that come from scattering on the CMB, on the thermal radiation from dust, and on starlight) as well as gamma rays from inverse Compton scattering outside of our Galaxy (red). The solid black line shows the overall flux. The dark red and dark blue lines show the total flux (dash-dotted) after adding an isotropic extragalactic background (dashed) with a power-law spectrum. Normalization and index are chosen to fit one of the two data sets shown [155, 251].

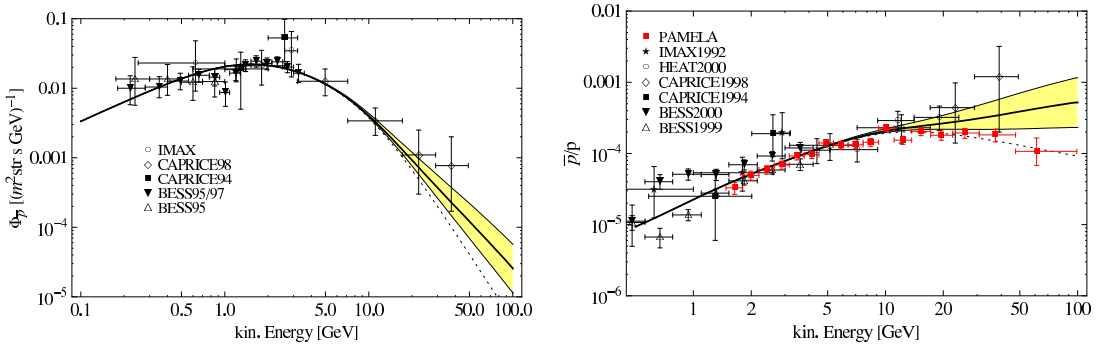

Figure 4.6: Antiproton flux *(left panel)* and the corresponding antiproton-to-proton ratio *(right panel)* for $\psi_{\rm DM} \to W^{\pm}\mu^{\mp}$ with $m_{\rm DM} = 3000\,\text{GeV}$ and $\tau_{\rm DM} = 2.1 \times 10^{26}\,\text{s}$. For the antiproton flux we adopt the background from [252], while the antiproton-to-proton ratio is plotted using the background from [253]. The yellow band indicates the uncertainties from the propagation model. The solid black line corresponds to the MED model of Table 2.3.

In some typical decaying dark matter scenarios, the dark matter particles decay into a mixture of different charged lepton flavors and not exclusively in one the channels discussed

above. For instance, in the scenario with hidden gauginos as discussed in Chapter 10 the decays proceed equally into all three flavors. As an illustration of the predictions of this class of scenarios, we show in Fig. 4.7 the positron fraction and the total electron + positron flux for a dark matter particle that decays democratically into the three flavors, for $m_{\rm DM} = 2000\,\text{GeV}$ (solid) and 300 GeV (dotted). Although these scenarios could explain the PAMELA excess, the predicted spectral shape of the total flux is not consistent with the Fermi data: either the energy spectrum falls off at too low energies or it presents a sharp peak at high energies due to the large branching ratio into hard electrons and positrons. Scenarios with a smaller branching ratio into electron flavor and larger branching ratio into muon flavor could, however, explain both anomalies simultaneously.

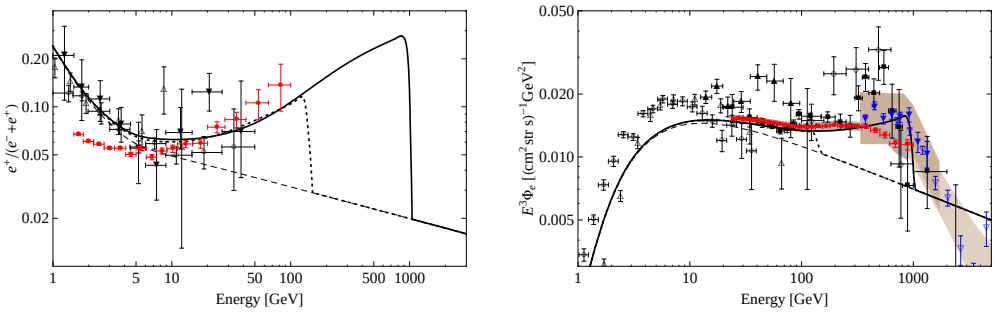

Figure 4.7: Same as Fig. 4.3, but for the flavor-democratic decay $\psi_{\rm DM} \to W^\pm \ell^\mp$ with equal branching ratios into the three charged lepton flavors, for $m_{\rm DM} = 2000\,\text{GeV}$ (solid) and 300 GeV (dotted).

The dark matter particles could also decay into three fermions, namely into a lepton–antilepton pair and a neutrino, $\psi_{\rm DM} \to \ell^+\ell^-\nu$. In this case many possibilities could arise depending on the specific particle-physics scenario. We will just concentrate here on the case where the lepton and antilepton carry the same flavor and the decay is mediated by a heavy scalar.[4] The results for the positron fraction and the electron + positron flux are shown in Fig. 4.8. The spectrum produced in the decay into electron–positron pairs, $\psi_{\rm DM} \to e^+e^-\nu$, is flatter in this case than in the two-body decay $\psi_{\rm DM} \to W^\pm e^\mp$, although it still produces a rather prominent bump in the electron spectrum at high energies, which is not observed by Fermi. More promising is the decay channel $\psi_{\rm DM} \to \mu^+\mu^-\nu$, which can reproduce quite nicely the Fermi electron + positron data and the rise in the positron fraction when the dark matter mass is $m_{\rm DM} \simeq 3500\,\text{GeV}$ and the lifetime is $\tau_{\rm DM} \simeq 1.1 \times 10^{26}\,\text{s}$. Lastly, decays into tau flavor can also qualitatively reproduce the steep rise in the positron fraction for dark matter masses above $\sim 2.5\,\text{TeV}$, although as one can see from Fig. 4.8, lower right panel, the resulting electron + positron spectrum has an energy dependence much steeper than $\sim E^{-3.0}$ at high energies, in tension with the Fermi measurements. In this case an additional source of high-energy positrons coming, for example, from pulsars, must be invoked in order to reproduce the electron spectrum observed by Fermi LAT.

[4] Our results are not very sensitive to the mass splitting between dark matter particle and virtual scalar.

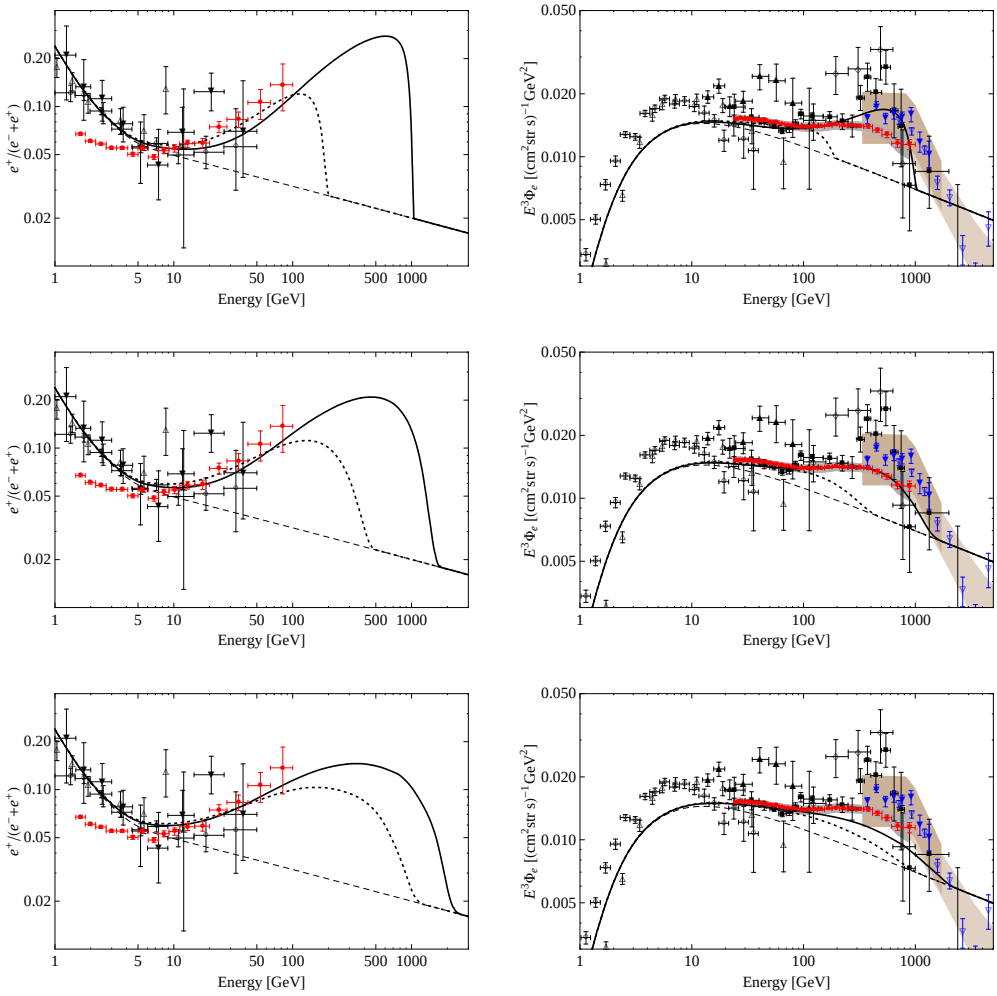

Figure 4.8: Same as Fig. 4.3, but for the decay channels $\psi_{\rm DM} \to \ell^\pm \ell^\mp \nu$. *Upper panels:* $\psi_{\rm DM} \to e^+ e^- \nu$ with $m_{\rm DM} = 2000\,{\rm GeV}$ (solid) and $400\,{\rm GeV}$ (dotted). *Middle panels:* $\psi_{\rm DM} \to \mu^+ \mu^- \nu$ with $m_{\rm DM} = 3500\,{\rm GeV}$ (solid) and $1000\,{\rm GeV}$ (dotted). *Lower panels:* $\psi_{\rm DM} \to \tau^+ \tau^- \nu$ with $m_{\rm DM} = 5000\,{\rm GeV}$ (solid) and $2500\,{\rm GeV}$ (dotted).

As for the two-body decays $\psi_{\rm DM} \to W^\pm \ell^\mp$, the dark matter particle could also decay into charged fermions with different flavor. We illustrate such a situation showing in Fig. 4.9 the predictions for the positron fraction and the total electron + positron flux when the dark matter particles decay democratically into all three flavors, for dark matter masses $m_{\rm DM} = 600\,{\rm GeV}$ (dotted) and $2500\,{\rm GeV}$ (solid). In particular, this is the case in scenarios where neutralino dark matter decays into light hidden gauginos via kinetic mixing, or vice versa [7, 100, 211]. See Chapter 10 for a detailed analysis. It is interesting that these scenarios can simultaneously explain the PAMELA and Fermi anomalies when the dark matter mass is $m_{\rm DM} \simeq 2500\,{\rm GeV}$. For the two cases of three-body decay into muon flavor, $\psi_{\rm DM} \to \mu^+ \mu^- \nu$ and the flavor-democratic decay $\psi_{\rm DM} \to \ell^+ \ell^- \nu$ we show the predictions for the extragalactic diffuse gamma-ray fluxes in Fig. 4.10. In both cases they are consistent with the present data

and show a deviation from the putative power-law behavior of the astrophysical background, which could be observed by the Fermi LAT, depending on the precise spectrum of the genuinely extragalactic contribution to the flux.

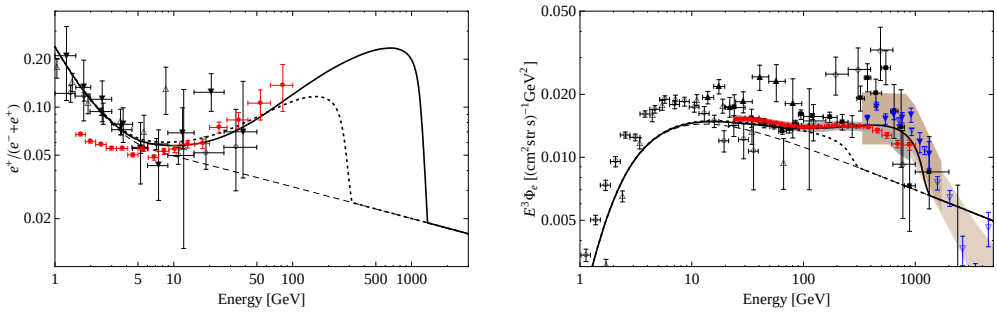

Figure 4.9: Same as Fig. 4.3, but for the flavor-democratic decay $\psi_{\rm DM} \to \ell^\pm \ell^\mp \nu$ with equal branching ratios into the three charged lepton flavors, for $m_{\rm DM} = 2500\,\text{GeV}$ (solid) and 600 GeV (dotted).

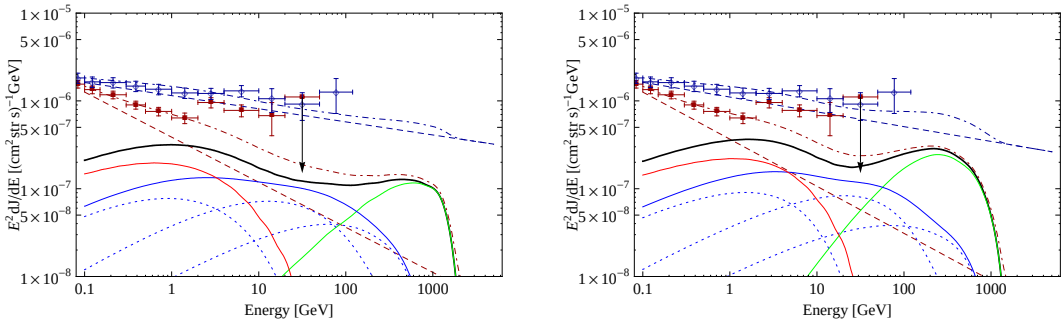

Figure 4.10: Same as Fig. 4.5, but for $\psi_{\rm DM} \to \mu^+\mu^-\nu$ (*left panel*, with $m_{\rm DM} = 3500\,\text{GeV}$), and for the democratic decay $\psi_{\rm DM} \to \ell^+\ell^-\nu$ (*right panel*, with $m_{\rm DM} = 2500\,\text{GeV}$).

The impact of choosing other sets of propagation parameters is illustrated in Fig. 4.11 for the sample decay mode $\psi_{\rm DM} \to \mu^+\mu^-\nu$. The MED and MAX propagation model yield virtually identical fluxes, while the MIN model, which possesses a thin diffusive halo with $L = 1\,\text{kpc}$, predicts a somewhat harder flux and a slightly steeper positron fraction. The reason for the similarity between the results for the MED and MAX models is that the height of the diffusion zone becomes irrelevant above a few kpc for high-energy electrons from local sources since the typical propagation length becomes smaller than the height of the diffusive halo. We have also examined the effects of choosing different dark matter halo profiles, with the differences being entirely negligible.

We summarize our results for the promising fermionic dark matter channels, together with the corresponding dark matter masses and lifetimes that yield the best fit, in Table 4.1.

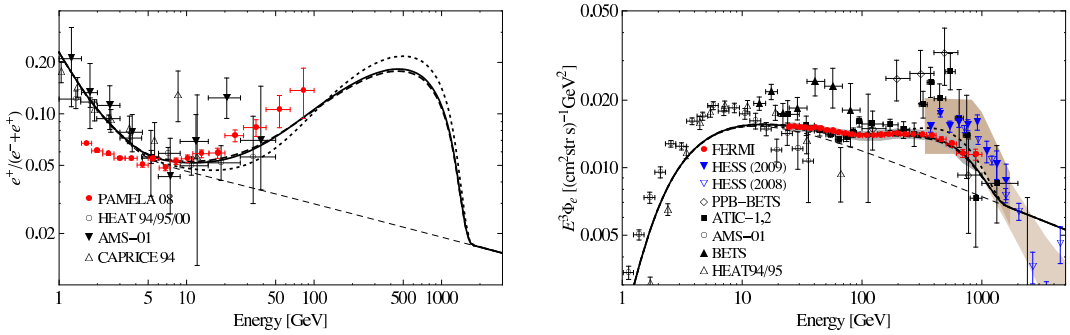

Figure 4.11: Illustration of the dependence on the choice of transport parameters. Same as Fig. 4.8, middle panels, but only for a dark matter mass $m_{\rm DM} = 3500\,\text{GeV}$. The solid, dashed and dotted lines correspond to the MED, MAX, and MIN model parameters, respectively. The results for the MED and MAX model are very similar because the height of the diffusion zone becomes irrelevant above a few kpc for high-energy electrons from local sources.

4.4.2 Scalar Dark Matter

For scalar dark matter particles, we examine the following decay channels:[5]

$$\begin{aligned} \phi_{\rm DM} &\to Z^0 Z^0\,, \\ \phi_{\rm DM} &\to W^+ W^-\,, \\ \phi_{\rm DM} &\to \ell^+ \ell^-\,. \end{aligned} \tag{4.6}$$

We show in Figs. 4.12, 4.13 the positron fraction and the total electron + positron flux for a scalar dark matter particle that decays exclusively into weak gauge bosons, $\phi_{\rm DM} \to Z^0 Z^0$ and $\phi_{\rm DM} \to W^+ W^-$, for dark matter masses $m_{\rm DM} = 2\,\text{TeV}$ and $10\,\text{TeV}$. As generically expected from decays into weak gauge bosons after the discussion in the previous subsection, the electrons and positrons produced are relatively soft, resulting in a positron fraction which is too flat to explain the steep rise in the positron fraction (for an exception with very large dark matter masses see Fig. 4.3.) Additionally, such decays produce a rather large flux of antiprotons, further disfavoring them as an explanation of the data.

Decays into harder electrons and positrons can arise in scenarios where the scalar dark matter particle decays into a lepton–antilepton pair. We show in Fig. 4.14 the predictions for the positron fraction and the total electron-plus-positron flux when the scalar dark matter particle decays into fermions of the same generation, for dark matter masses between $m_{\rm DM} = 300\,\text{GeV}$ and $5\,\text{TeV}$. The decay $\phi_{\rm DM} \to e^+ e^-$ can explain the rise in the positron fraction as observed by PAMELA. However, it is apparent from Fig. 4.14 that the dark matter decay into this channel is not compatible with the high-energy e^+e^- data from Fermi. The situation is similar when one considers democratic decay into all three flavors, which still produces a distinct spectral feature as illustrated in Fig. 4.15. Decays into softer electrons and positrons, as in the case where the dark matter particles decay exclusively via $\phi_{\rm DM} \to \mu^+ \mu^-$, are more promising. In particular, a scalar dark matter particle with a mass

[5] Again, we do not include quarks or Higgs bosons in the list. Three-body decay modes like $\phi_{\rm DM} \to \ell^+ \ell^- \gamma$ are expected to yield results similar to the case of fermionic dark matter.

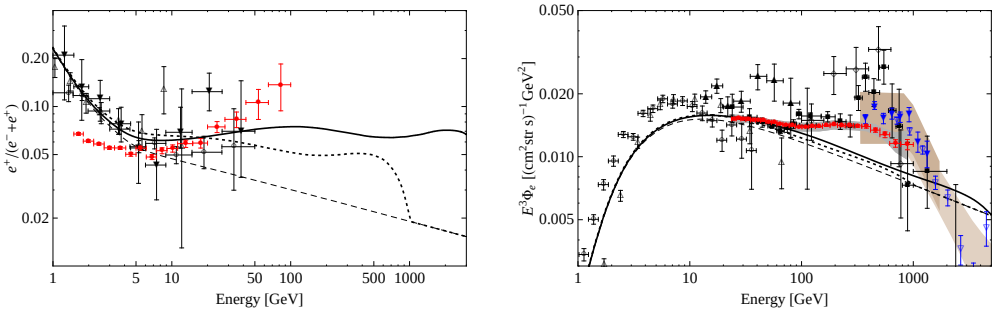

Figure 4.12: Same as Fig. 4.3, but for the decay channel $\phi_{\rm DM} \to Z^0 Z^0$ with $m_{\rm DM} = 10\,{\rm TeV}$ (solid) and 2 TeV (dotted).

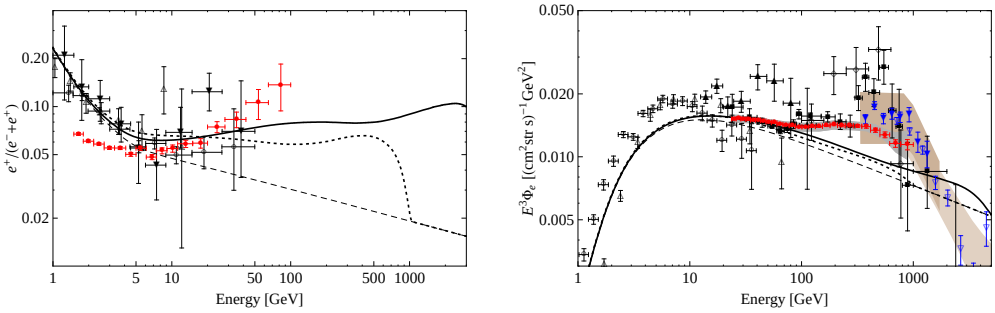

Figure 4.13: Same as Fig. 4.3, but for the decay channel $\phi_{\rm DM} \to W^+ W^-$ with $m_{\rm DM} = 10\,{\rm TeV}$ (solid) and 2 TeV (dotted).

$m_{\rm DM} \simeq 2500\,{\rm GeV}$ and a lifetime $\tau_{\rm DM} \simeq 1.8 \times 10^{26}\,{\rm s}$, which decays exclusively into $\mu^+\mu^-$ pairs, can reproduce both the steep rise in the spectrum observed by PAMELA and the total electron + positron spectrum measured by Fermi. The same holds true for decays into tau flavor, with $m_{\rm DM} \simeq 5000\,{\rm GeV}$ and $\tau_{\rm DM} \simeq 0.9 \times 10^{26}\,{\rm s}$. For these two decay channels, we also show the predictions for the gamma-ray fluxes in Fig. 4.16, which are again compatible with the present data and exhibit a spectral shape which could be visibly different from a power law, depending on the index of the genuinely extragalactic component.

A summary of our results can be found in Table 4.1, where we list the decay modes that yield the best agreement with the data together with the corresponding masses and lifetimes.

4.5 Conclusions

In some well-motivated dark matter scenarios, the dark matter particles are unstable and decay with a lifetime much longer than the age of the Universe. In this chapter we have investigated whether the anomalies in the positron fraction and the total electron + positron flux reported by the PAMELA and Fermi LAT collaborations, respectively, could be inter-

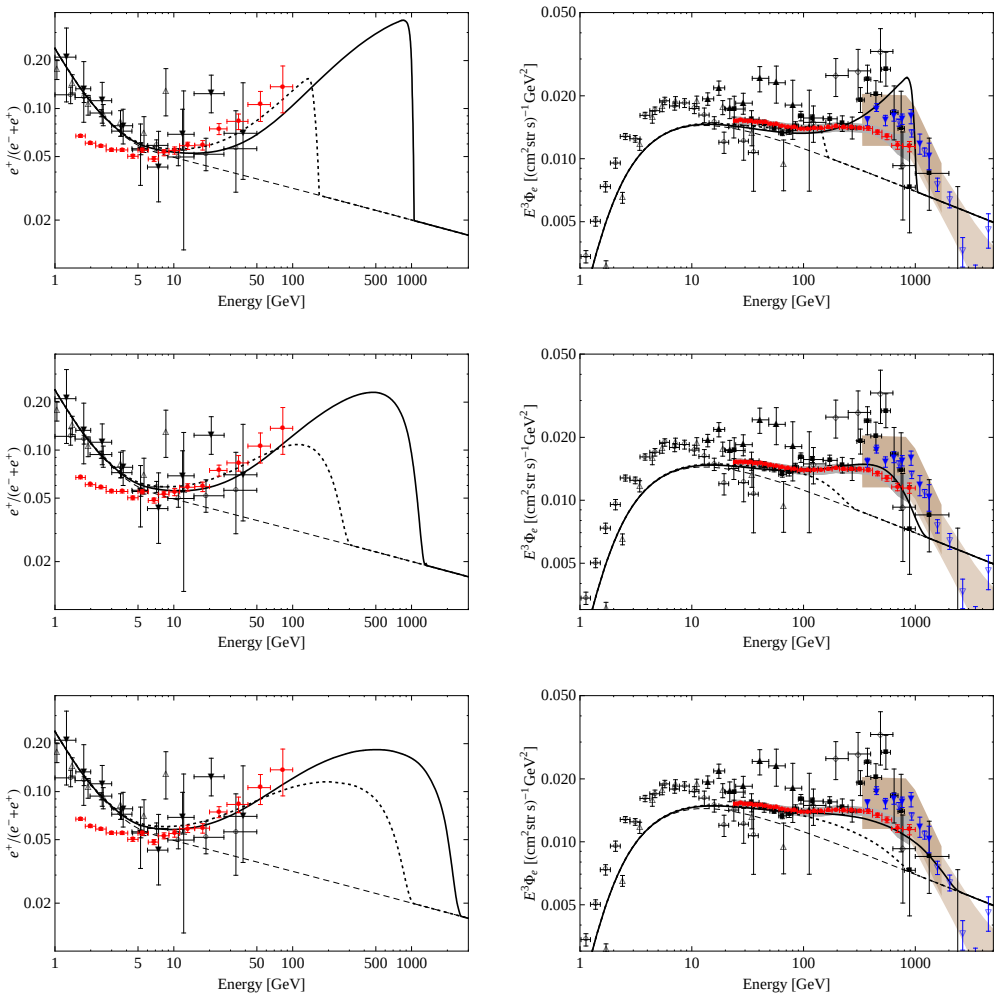

Figure 4.14: Same as Fig. 4.3, but for the decay channels $\phi_{\rm DM} \to \ell^+\ell^-$. *Upper panels:* $\phi_{\rm DM} \to e^+e^-$ with $m_{\rm DM} = 2000\,{\rm GeV}$ (solid) and $300\,{\rm GeV}$ (dotted). *Middle panels:* $\phi_{\rm DM} \to \mu^+\mu^-$ with $m_{\rm DM} = 2500\,{\rm GeV}$ (solid) and $600\,{\rm GeV}$ (dotted). *Lower panels:* $\phi_{\rm DM} \to \tau^+\tau^-$ with $m_{\rm DM} = 5000\,{\rm GeV}$ (solid) and $2000\,{\rm GeV}$ (dotted).

preted as a signature of the decay of dark matter particles. We have shown that some decaying dark matter scenarios can indeed reproduce the energy spectra of the positron fraction and the total flux reasonably well, while being at the same time consistent with present measurements of the antiproton flux and the diffuse extragalactic gamma-ray flux. The most promising decay channels for fermionic and scalar dark matter particles are listed in Table 4.1, where we also show the approximate mass and lifetime which provide the best fit to the data. From the table it is apparent that direct decays of the dark matter into charged leptons are favored, as the e^+e^- spectra from the fragmentation of gauge bosons are generally too soft to match the steepness of the rising positron fraction. Furthermore, such decays necessarily produce antiprotons and are disfavored since the antiproton flux is consistent with secondary production by spallation. The total eletron + positron spectrum also yields some important information

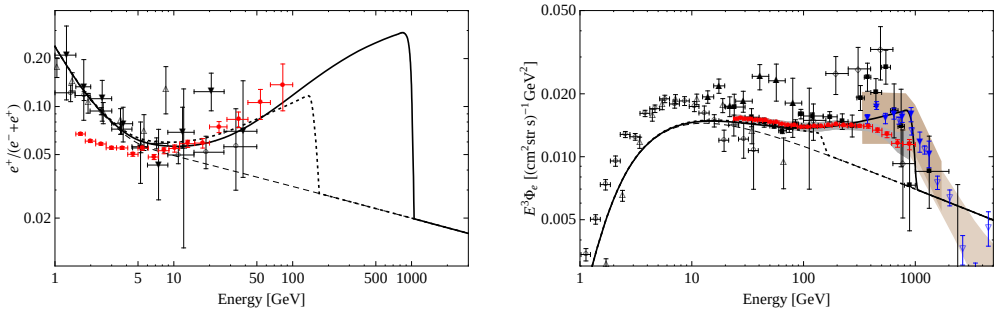

Figure 4.15: Same as Fig. 4.3, but for the flavor-democratic decay $\phi_{\rm DM} \to \ell^+\ell^-$ with equal branching ratios into the three charged lepton flavors, for $m_{\rm DM} = 2000\,{\rm GeV}$ (solid) and $300\,{\rm GeV}$ (dotted).

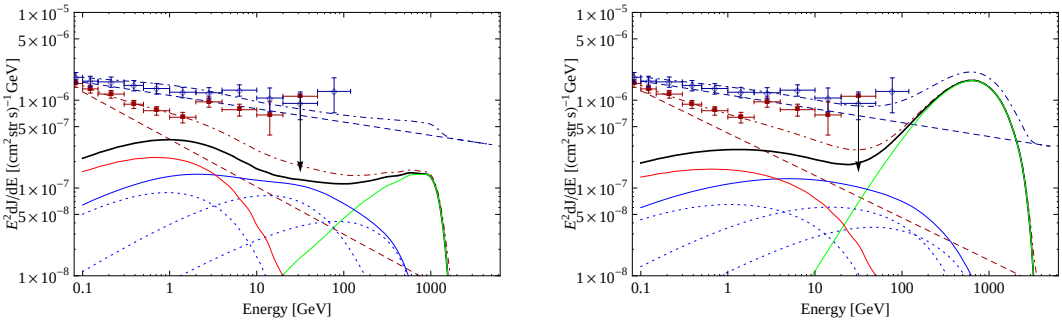

Figure 4.16: Same as Fig. 4.5, but for $\phi_{\rm DM} \to \mu^+\mu^-$ (*left panel*, with $m_{\rm DM} = 2500\,{\rm GeV}$), and for $\phi_{\rm DM} \to \tau^+\tau^-$ (*right panel*, with $m_{\rm DM} = 5000\,{\rm GeV}$).

about the preferred flavor of the leptonic decays. Namely, decays into electron flavor typically produce shoulder-like spectral features with a cutoff at the dark matter mass. While ATIC and PPB-BETS claim the observation of just such a feature, this claim is contradicted by Fermi LAT and H.E.S.S. Therefore, we tentatively conclude that decays into purely electron favor are disfavored, while decays into muons or democratic decays into all three flavors reproduce the observations well. Decays into pure tau flavor, on the other hand, typically yield too soft a spectrum.

Note that one of the largest uncertainties that enter in the determination of the dark matter lifetimes comes from the calculation of the local dark matter density (see [122] for a recent analysis) since this quantity is inversely proportional to the corresponding flux of cosmic rays. It should also be borne in mind that the astrophysical uncertainties in the propagation of cosmic rays and in the determination of the background fluxes of electrons and positrons are still large. At high energies, the propagation of electrons and positrons is dominated by energy losses, for which we have assumed the simplified form of Eq. (2.8), with some impact on the best-fit dark matter lifetime and mass. Besides, the existence of a potentially large primary component of electrons and positrons from astrophysical sources such as pulsars cannot be

precluded. Therefore, the precise values of the dark matter parameters are subject to these uncertainties. For this reason, we have not attempted to provide precise quantitative statements regarding the qualities of the fits. The present results can nevertheless be used as a guidance for building models with decaying dark matter as an explanation of the PAMELA and Fermi anomalies.

Decay channel	$m_{\rm DM}$ [GeV]	$\tau_{\rm DM}$ [10^{26} s]
$\psi_{\rm DM} \to \mu^+\mu^-\nu$	3500	1.1
$\psi_{\rm DM} \to \ell^+\ell^-\nu$	2500	1.5
$\phi_{\rm DM} \to \mu^+\mu^-$	2500	1.8
$\phi_{\rm DM} \to \tau^+\tau^-$	5000	0.9
$\psi_{\rm DM} \to W^\pm\mu^\mp$	3000	2.1

Table 4.1: Decay channels for fermionic and scalar dark matter, denoted $\psi_{\rm DM}$ and $\phi_{\rm DM}$, respectively, which best fit the Fermi LAT $e^+ + e^-$ and the PAMELA $e^+/(e^+ + e^-)$ data for the MED propagation model and the NFW halo profile. As discussed above, the dependence on the halo profile is negligible, while the dependence in the adopted propagation parameters is illustrated in Fig. 4.11 for the decay $\psi_{\rm DM} \to \mu^+\mu^-\nu$. The decay mode $\psi_{\rm DM} \to W^\pm\mu^\mp$ is in some tension with the PAMELA results on the antiproton-to-proton ratio as mentioned in the text.

Future measurements of the extragalactic diffuse gamma-ray flux by the Fermi LAT will provide important information about the decaying dark matter scenario. First, since the Earth is located far from the center of the Milky Way's dark matter halo, a dipole-like anisotropy in the diffuse extragalactic gamma-ray flux is expected, which could be observed by Fermi LAT. For a detailed analysis of this topic, see Chapter 6. Moreover, all scenarios in Table 4.1 predict a departure from a simple power law in the energy spectrum of the diffuse extragalactic gamma-ray background, the deviation depending on the spectrum of the genuinely extragalactic contribution originating presumably from AGN. The observation of such a deviation would provide support to the decaying dark matter scenario and may help discriminate between the different possibilities listed in Table 4.1.

Chapter 5

Antideuterons from Dark Matter Decay

The recent observations of a large excess of cosmic-ray positrons, as discussed in Chapter 4, have raised a lot of interest in leptonic decay modes of dark matter particles. Nevertheless, dark matter particles in the Milky Way halo could also decay hadronically, producing not only a flux of antiprotons, but also a flux of antideuterons. Searches for antideuteron are of particular interest for dark matter detection because the rate of secondary antideuteron production from cosmic-ray spallation is expected to lie significantly below observational sensitivities for the foreseeable future. Therefore, the detection of even a single cosmic antideuteron would be a compelling hint at a primary origin of such a particle.

In this chapter, which is based on the publication [6], we show that for certain choices of parameters the antideuteron flux from dark matter decay can be much larger than the purely seconday flux from spallation of cosmic rays on the interstellar medium, while the total antiproton flux remains consistent with present observations. We show that if the dark matter particle is sufficiently light, the antideuteron flux from dark matter decay could even be within the reach of planned experiments such as AMS-02 or GAPS. Furthermore, we discuss the prospects to observe the antideuteron flux in the near future if the steep rise in the positron fraction reported by the PAMELA collaboration is interpreted in terms of the decay of dark matter particles.

5.1 Introduction

As explained in Chapter 4, there is recent evidence for the existence of a primary component in the high energy electron and positron fluxes [169] which could be naturally accounted for by the decay of dark matter particles with a mass $m_{\rm DM} \gtrsim 300\,{\rm GeV}$, which decay preferentially into charged leptons with a lifetime $\tau_{\rm DM} \sim 10^{26}\,{\rm s}$ [4, 8]. The properties of the dark matter particles are further constrained from observations of the diffuse gamma-ray flux by EGRET [155], as well as from observations of the antiproton flux by PAMELA [129], BESS95 [182], BESS95/97 [183], CAPRICE94 [184], CAPRICE98 [185] and IMAX [186]. More concretely, the good agreement of the theoretical predictions for a purely secondary antiproton flux with the measurements indicates that the contribution to the total antiproton flux from dark matter matter can only be subdominant.

In this chapter we estimate the antideuteron flux from dark matter decay as a complementary way to search for indirect dark matter signatures that is essentially independent from the leptonic cosmic-ray anomalies. The importance of antideuteron searches for dark matter stems from the fact, as pointed out in [254, 255], that for energies smaller than $\sim 3\,\mathrm{GeV}$ the expectations for a purely secondary antideuteron flux due to spallation of cosmic rays on the interstellar medium lie well below the present BESS limit on the antideuteron flux [256], as well as the projected limits for AMS-02 [257, 258] and GAPS [259, 260]. Therefore, no detection of antideuterons should be expected by these instruments if the antideuteron flux is indeed of purely secondary origin. However, if the antideuterons are formed by the fusion of antiprotons and antineutrons originating from the same fragmentation process of a weak gauge boson or Higgs boson, as would be the case in many models of dark matter annihilation or decay, then the production rate can be significantly higher. Unlike the case of cosmic-ray antiprotons, the flux of antideuterons can therefore be of dominantly primary origin. Due to the low astrophysical background, a discovery of cosmic antideuterons in the upcoming generation of cosmic-ray instruments would therefore have to be interpreted as evidence for the existence of primary antideuterons, likely originating from the hadronic decay or annihilation of dark matter particles.

This chapter is organized as follows. In Section 5.2 we review the production of antideuterons from dark matter decay using the coalescence model, a simple phenomenological model to describe the fusion of antiprotons and antineutrons into antideuterons. Next, in Section 5.3 we briefly review the propagation of antideuterons from their production in the dark matter halo to the heliosphere. In Section 5.4 we will show our results for the antideuteron fluxes, and in Section 5.5 we will finally present our conclusions.

5.2 The Coalescence Model

One important complication in the determination of the source term for antideuteron production is that the energy spectrum of antideuterons is difficult to determine by Monte Carlo methods. Even when using a simple description of antideuteron formation in terms of a coalescence momentum, as explained below, the simultaneous production of an antiproton–antineutron pair with almost identical momenta is extremely rare, leading in practice to unfeasible running times on regular computers. Therefore, we derive the spectrum of antideuterons under the simplifying assumption that the production of antiprotons and antineutrons can be factorized, as well as by employing a simple model of antideuteron formation from antiprotons and antineutrons.[1]

We describe the formation of antideuterons in the fragmentation process of weak gauge bosons or Higgs bosons by using the so-called coalescence model. This is a purely phenomenological model that essentially posits that antideuteron is formed by fusion of an antiproton and an antineutron whenever they are found together within a sphere of radius p_0 in momentum space, the coalescence momentum. The model assumes that the probability of producing an antideuteron is simply proportional to the product of the probabilities of producing a single

[1] The production of antideuterons was discussed recently in [261].

antiproton and a single antineutron:

$$\left[\gamma_{\bar{d}}\frac{d^3N_{\bar{d}}}{d^3\vec{k}_{\bar{d}}}\right] = \int d^3\vec{k}_{\bar{p}}\, d^3\vec{k}_{\bar{n}}\, C\left(\vec{k}_{\bar{p}},\vec{k}_{\bar{n}}\right)\left[\gamma_{\bar{p}}\frac{d^3N_{\bar{p}}}{d^3\vec{k}_{\bar{p}}}\left(\vec{k}_{\bar{p}}\right)\right]\left[\gamma_{\bar{n}}\frac{d^3N_{\bar{n}}}{d^3\vec{k}_{\bar{n}}}\left(\vec{k}_{\bar{n}}\right)\right]\delta^3\left(\vec{k}_{\bar{p}}+\vec{k}_{\bar{n}}-\vec{k}_{\bar{d}}\right), \tag{5.1}$$

where γ is the relativistic Lorentz factor and $C(\vec{k}_{\bar{p}},\vec{k}_{\bar{n}})$ is the coalescence function, which can only depend on the relative momentum between antiproton and antineutron, $\vec{\Delta}\equiv\vec{k}_{\bar{p}}-\vec{k}_{\bar{n}}$. Using that $\vec{k}_{\bar{d}}=\vec{k}_{\bar{p}}+\vec{k}_{\bar{n}}$, one obtains

$$\left[\gamma_{\bar{d}}\frac{d^3N_{\bar{d}}}{d^3\vec{k}_{\bar{d}}}\right] = \int d^3\vec{\Delta}\, C\left(|\vec{\Delta}|\right)\left[\gamma_{\bar{p}}\frac{d^3N_{\bar{p}}}{d^3\vec{k}_{\bar{p}}}\left(\vec{k}_{\bar{p}}=\frac{\vec{k}_{\bar{d}}+\vec{\Delta}}{2}\right)\right]\left[\gamma_{\bar{n}}\frac{d^3N_{\bar{n}}}{d^3\vec{k}_{\bar{n}}}\left(\vec{k}_{\bar{n}}=\frac{\vec{k}_{\bar{d}}+\vec{\Delta}}{2}\right)\right]. \tag{5.2}$$

The coalescence function is strongly peaked at $|\vec{\Delta}|\simeq 0$ since the binding energy of the antideuteron, $B\simeq 2.2$ MeV, is much smaller than its rest mass, $m_{\bar{d}}\simeq 1.88\,\mathrm{GeV}$ [61]. Therefore, the previous equation can be approximated as

$$\left[\gamma_{\bar{d}}\frac{dN^3_{\bar{d}}}{d^3\vec{k}_{\bar{d}}}\right] \simeq \int d^3\vec{\Delta} C\left(|\vec{\Delta}|\right)\left[\gamma_{\bar{p}}\frac{d^3N_{\bar{p}}}{d^3\vec{k}_{\bar{p}}}\left(\vec{k}_{\bar{p}}=\frac{\vec{k}_{\bar{d}}}{2}\right)\right]\left[\gamma_{\bar{n}}\frac{d^3N_{\bar{n}}}{d^3\vec{k}_{\bar{n}}}\left(\vec{k}_{\bar{n}}=\frac{\vec{k}_{\bar{d}}}{2}\right)\right]. \tag{5.3}$$

It is useful to define the coalescence momentum p_0 as

$$\int d^3\vec{\Delta}\, C\left(|\vec{\Delta}|\right)\equiv\frac{4\pi}{3}p_0^3, \tag{5.4}$$

which can be interpreted as the maximum relative momentum between the antiproton and the antineutron for which an antideuteron will form by fusion of the two nucleons. The coalescence momentum can be determined experimentally from proton–nucleus collisions, yielding $p_0\simeq 79\,\mathrm{MeV}$,[2] or from e^+e^- collisions at the Z^0 resonance, yielding $p_0\simeq 71\pm 3.6$ MeV [262]. Since the decay of weak gauge bosons is precisely the source of antideuterons in the decaying dark matter scenario, we will adopt the latter value $p_0\simeq 71\pm 3.6$ MeV in the remainder of the chapter. Note that the measured coalescence momentum is not far from the estimate obtained by using the antideuteron binding energy, namely $\sqrt{m_{\bar{p}}B}\sim 46\,\mathrm{MeV}$, supporting the above physical interpretation of the coalescence momentum.

The dark matter decay produces antideuterons, antiprotons and antineutrons with an isotropic distribution,[3] and consequently

$$\left[\gamma\frac{d^3N}{d^3\vec{k}}\right]=\frac{1}{4\pi}\frac{1}{mk}\frac{dN}{dE}. \tag{5.5}$$

Therefore, Eq. (5.3) can be cast as

$$\frac{dN_{\bar{d}}}{dE_{\bar{d}}}\simeq\frac{4p_0^3}{3k_{\bar{d}}}\frac{m_{\bar{d}}}{m_{\bar{p}}m_{\bar{n}}}\left[\frac{dN_{\bar{p}}}{dE_{\bar{p}}}\left(E_{\bar{p}}=\frac{E_{\bar{d}}}{2}\right)\right]^2, \tag{5.6}$$

[2]The uncertainty in the measurement of the hadronic production cross sections translates into a range for the coalescence momentum that was estimated to be $p_0=79^{+26}_{-13}\,\mathrm{MeV}$ [255].

[3]Some authors have recently pointed out that the assumption of spherical symmetry is not entirely realistic and that including the full jet structure of the fragmentation can lead to an enhanced production rate of antideuterons [263]. This can lead to a more pronounced signal at higher antideuteron energies.

where on the basis of isospin invariance we have assumed that the probability of producing an antiproton with momentum $\vec{k}_{\bar{p}}$ in the fragmentation is the same as the probability of producing an antineutron.

5.3 Antideuteron Propagation

We will assume that the Milky Way dark matter halo is populated by dark matter particles with mass $m_{\rm DM}$, with their distribution following a density profile $\rho_{\rm DM}(\vec{r})$. We assume in this chapter a Navarro-Frenk-White profile as defined in Eq. (1.13), with a local dark matter density $\rho_\odot = 0.3\,\mathrm{GeV\,cm^{-3}}$. We treat the propagation of antideuterons in the Galaxy in the stationary two-zone diffusion model outlined in Chapter 2. The source term for antideuterons from dark matter decay in the transport equation, Eq. (2.14), is then given by

$$Q_{\bar{d}}(E_{\bar{d}}, \vec{r}) = \frac{1}{m_{\rm DM}\tau_{\rm DM}} \rho_{\rm DM}(\vec{r}) \frac{dN_{\bar{d}}}{dE_{\bar{d}}}\,, \tag{5.7}$$

where $dN_{\bar{d}}/dE_{\bar{d}}$ is the energy spectrum of antideuterons produced per decay, which we determine as described in the previous section. We treat the propagation of antideuterons as outlined in Chapter 2, where we also take into account a term describing the annihilation of antideuterons in the gaseous disk of the Milky Way.

No experimental data are available for the $\bar{d}p$ collisions, although measurements exist for the total cross-section of the charge-conjugated process $d\bar{p} \to X$. Since strong interactions preserve charge conjugation, it is reasonable to assume that $\sigma^{\rm tot}_{\bar{d}p} = \sigma^{\rm tot}_{d\bar{p}}$. However, it is not the total cross section that is required to compute the depletion of antideuterons during their propagation, but the annihilation cross section. Unfortunately, there is no experimental information about the annihilation cross-section, neither for $\bar{d}p$ nor for $d\bar{p}$ collisions. However, it was noted in [255] that the total cross section for $d\bar{p} \to X$ can be well approximated, within $\sim 10\%$, by $2\sigma^{\rm tot}_{p\bar{p}}$ and hence $\sigma_{\bar{d}p} \simeq 2\sigma^{\rm tot}_{p\bar{p}}$. Then, assuming that the same rule applies for the annihilation cross-section, one obtains $\sigma^{\rm ann}_{\bar{d}p} \simeq 2\sigma^{\rm tot}_{p\bar{p}}$. For our numerical analysis, we assume the proton–antiproton annihilation cross-section as given in Eq. (2.17).

For the antideuteron Green's function we perform a similar fit as in the case of antiprotons, see Chapter 2. We find that the Green's function can be numerically well approximated by the following interpolating function:

$$G_{\bar{d}}(T, T') \simeq 10^{14}\, e^{x + y \ln T + z \ln^2 T} \delta(T' - T)\,\mathrm{cm^{-3}\,s}\,. \tag{5.8}$$

The values for the parameters x, y and z can be found in Table 5.1 for the different sets of propagation parameters in Table 2.3. The dependence of the Green's function on the halo model is fairly weak. In this case the approximation is better than about 5% for $T_{\bar{d}}$ between 1 and 100 GeV/n and better than about 20% for $T_{\bar{d}}$ between 0.1 and 1 GeV/n. For the calculation of our numerical results, however, we used the analytical expressions given in Chapter 2.

Lastly, we take the effects of solar modulation on antiproton and antideuteron fluxes into account by using the spherically symmetric force-field approximation by using the prescription described in Section 2.3, where we choose a modulation potential $\phi_{\rm F} = 500$ MV.

Model	x	y	z
MIN	-0.3889	0.7532	-0.1788
MED	1.6023	0.4382	-0.1270
MAX	3.1992	-0.1098	-0.0374

Table 5.1: Coefficients of the interpolating function, Eq. (5.8), for the antideuteron Green's function for the NFW profile.

5.4 Antideuteron Flux from Dark Matter Decay

Using the injection spectrum of antideuterons from dark matter decay calculated in Section 5.2 and the propagation formalism described in Chapter 2, it is straightforward to calculate the antideuteron flux at Earth from dark matter decay.[4] We will pursue here a model-independent approach, calculating the expected antideuteron flux at Earth for various hadronic decay channels and different dark matter masses. To better compare the predictions for the different possibilities, we will first fix the dark matter lifetime to be $\tau_{\rm DM} = 10^{26}\,{\rm s}$, which is the order of magnitude which could explain the HEAT and PAMELA anomalies in the positron fraction [4, 8, 10, 198, 199, 99, 202, 266] and which saturates the EGRET constraints on the diffuse gamma-ray flux [11, 103, 198, 94]. Later on, we will discuss in more detail the predictions for the antideuteron flux in the light of the PAMELA anomaly.

In the case that the dark matter particle is a fermion $\psi_{\rm DM}$, the following hadronic decay channels are possible:

$$\begin{aligned} \psi_{\rm DM} &\to Z^0 \nu\,, \\ \psi_{\rm DM} &\to h^0 \nu\,, \\ \psi_{\rm DM} &\to W^{\pm} \ell^{\mp}\,. \end{aligned} \tag{5.9}$$

The fragmentation of the weak gauge bosons and the Standard Model Higgs boson produces a flux of antideuterons which we calculated using the coalescence model to simulate the nuclear fusion of an antiproton and an antineutron (*cf.* Section 5.2). To simulate the production of individual antiprotons and antineutrons we used the event generator `PYTHIA 6.4` [249].

Clearly, an exotic contribution to the antideuteron flux is closely correlated with an exotic contribution to the antiproton flux, which is severely constrained by a number of experiments. Namely, the measurements of the antiproton flux by PAMELA [129], BESS95 [182], BESS95/97 [183], CAPRICE94 [184], CAPRICE98 [185] and IMAX [186] do not show any significant deviation from the predictions by conventional astrophysical models of spallation of cosmic rays on the Milky Way disk. Therefore, in order to evaluate the prospects of observing the antideuteron flux in future experiments, one has to ensure that the prediction for the total antiproton flux does not exceed the observed flux. The antiproton flux from dark matter decay has been calculated following the analysis in [10], for the same propagation models as

[4] For calculations of the antideuteron flux from the annihilation of dark matter particles, see [254, 255, 264, 263, 265]

for the antideuteron flux.

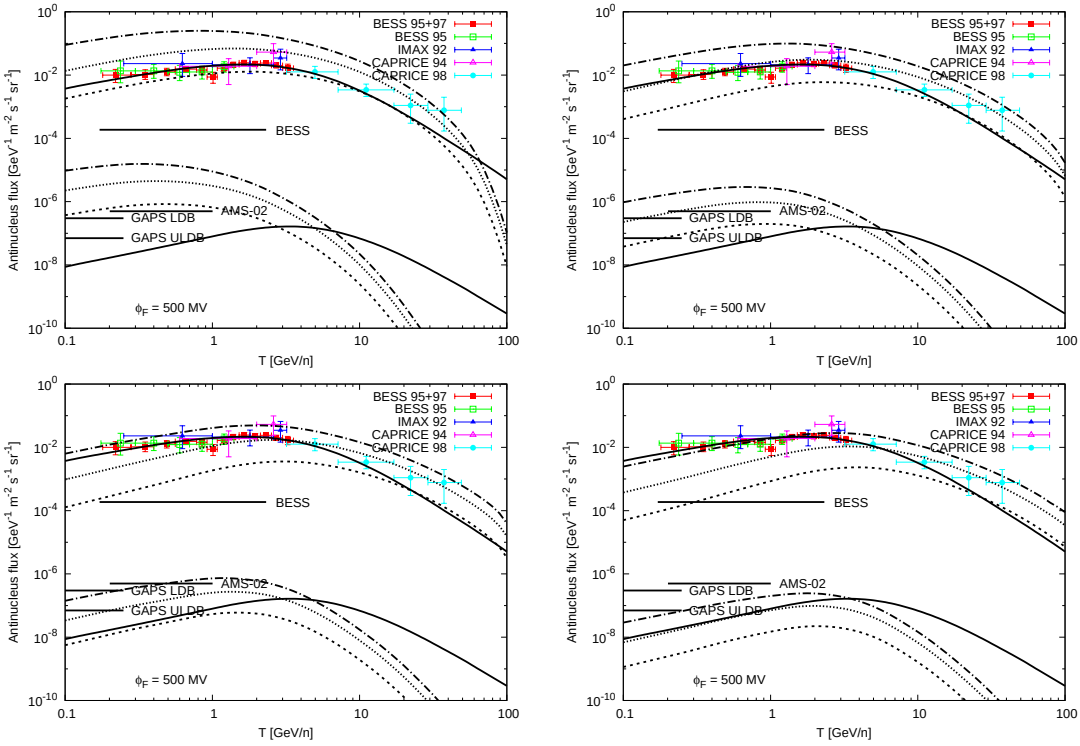

Figure 5.1: Fluxes of antiprotons (*upper curves*) and antideuterons (*lower curves*) from the decay of fermionic dark matter particles, assuming that the dark matter particle decays exclusively as $\psi_{\rm DM} \to Z^0\nu$ with a fixed lifetime $\tau_{\rm DM} = 10^{26}\,$s. The dark matter mass is 200 GeV (*top left panel*), 400 GeV (*top right*), 600 GeV (*bottom left*) and 800 GeV (*bottom right*). The dashed lines indicate the primary fluxes from dark matter decay for the MIN propagation model, the dotted lines for the MED propagation model, and the dash-dotted lines for the MAX propagation model (*cf.* Table 2.3). The solid lines indicate the secondary fluxes from cosmic-ray spallation.

We show in Figs. 5.1, 5.2, and 5.3 the antiproton and antideuteron fluxes from dark matter decay as a function of the kinetic energy per nucleon, assuming that the dark matter particle is a fermion $\psi_{\rm DM}$, which decays exclusively into $Z^0\nu$, $W^\pm\ell^\mp$ or $h^0\nu$, respectively. The lifetime has been fixed to $\tau_{\rm DM} = 10^{26}\,$s, while the dark matter mass has been chosen to be $m_{\rm DM} = 200$, 400, 600, 800 GeV. The predictions for the antiproton and antideuteron fluxes for a general model with a different dark matter lifetime and with arbitrary branching ratios can be straightforwardly derived from these figures. In each plot, we show the prediction for the antiproton and antideuteron fluxes at the top of the atmosphere for the MIN, MED and MAX propagation models (see Table 2.3), as well as the expected flux from spallation, taken from [188] in the case of the antiprotons and from [255] in the case of the antideuterons.[5] For the halo model, we adopt the Navarro-Frenk-White (NFW) profile; the results for other halo

[5]In these plots we only show the prediction for the secondary antiproton and antideuteron fluxes for the MED propagation model. Whereas the uncertainty on the propagation model is typically not very important

profiles are very similar to the ones presented here. We also show the present upper limit on the antideuteron flux from BESS [256], as well as the projected limits for AMS-02 for three years of data taking [257, 258], as well as for GAPS [259, 260] for a long duration balloon (LDB) flight (60 days total over three flights) and for an ultra-long duration balloon (ULDB) flight (300 days total).

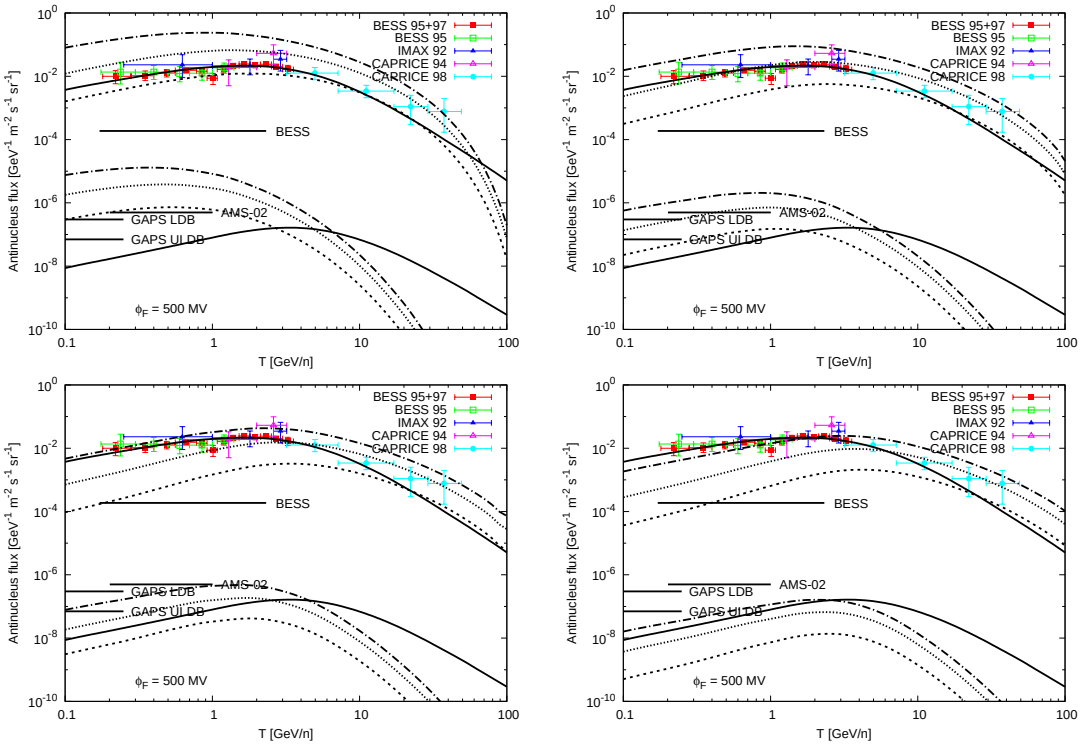

Figure 5.2: Same as Fig. 5.1, but for the decay mode $\psi_{\rm DM} \to W^{\pm}\ell^{\mp}$.

For this particular choice of the lifetime, $\tau_{\rm DM} = 10^{26}\,$s, we find wide ranges of diffusion parameters yielding a total antiproton flux consistent with the observations. Besides, the total antideuteron flux always lies well below the present BESS bound. We also find that for dark matter masses below $\sim 1\,$TeV, the antideuteron flux from dark matter decay can be, at energies below 3 GeV, significantly larger than the secondary antideuteron flux from spallation. Furthermore, the primary antideuteron flux from dark matter decay could be large enough to be observable at the projected experiments AMS-02 and GAPS. Therefore, since the purely secondary antideuteron flux is expected to be below the sensitivity of projected experiments, the observation of an antideuteron flux in the near future could be interpreted as a signature of dark matter particles which decay hadronically.

When the decaying dark matter particle is a scalar, the following hadronic decay modes

for the prediction of the secondary fluxes, there exists a more important source of uncertainty stemming from the nuclear and hadronic cross sections, which can be as large as 25% for antiprotons [188] and 100% for antideuterons [255].

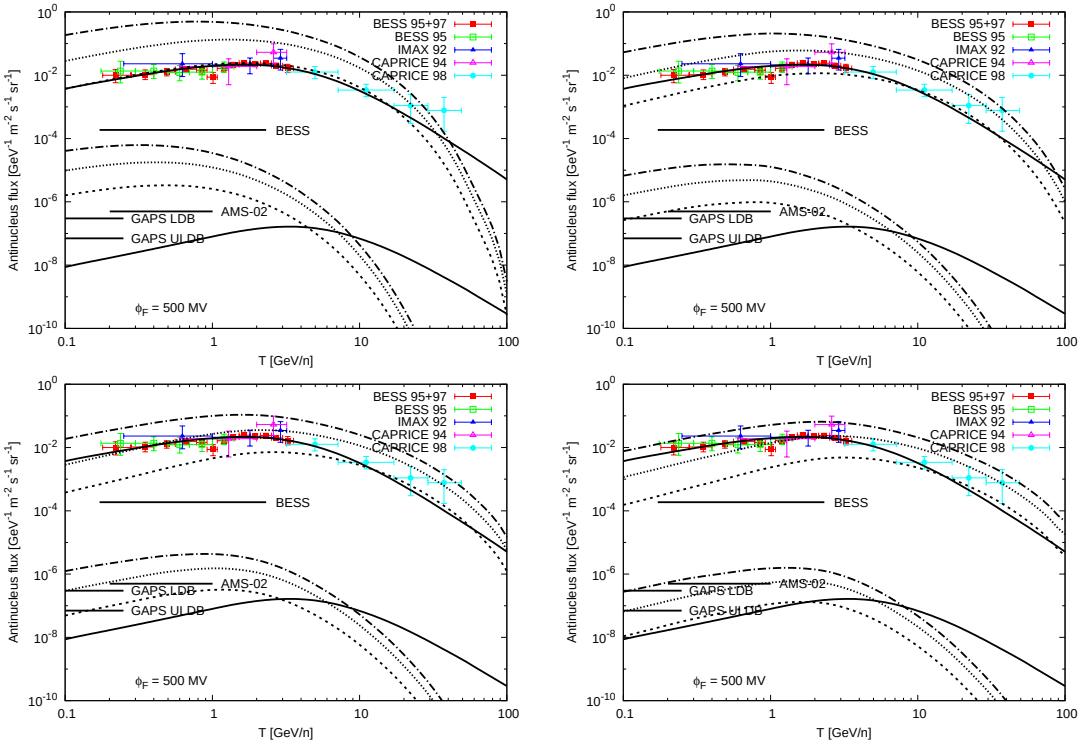

Figure 5.3: Same as Fig. 5.1, but for the decay mode $\psi_{\rm DM} \to h^0 \nu$.

are possible:

$$\begin{aligned} \phi_{\rm DM} &\to Z^0 Z^0 \,, \\ \phi_{\rm DM} &\to W^+ W^- \,, \\ \phi_{\rm DM} &\to h^0 h^0 \,. \end{aligned} \tag{5.10}$$

In these cases, the produced antideuteron flux is approximately twice as large as in the fermionic channels, $\psi_{\rm DM} \to Z^0 \nu$, $\psi_{\rm DM} \to W^\pm \ell^\mp$, $\psi_{\rm DM} \to h^0 \nu$, respectively, and will not be discussed further.

Let us now discuss the prospects for the detection of an antideuteron flux in projected experiments, assuming that dark matter decay is the explanation of the positron excess reported by the PAMELA and HEAT collaborations. As discussed in [8], the steep rise of the positron fraction measured by PAMELA can be explained by the decay of a dark matter particle into hard electrons and positrons. Namely, in the case that the dark matter particle is a fermion, the decay modes $\psi_{\rm DM} \to e^+ e^- \nu$ and $\psi_{\rm DM} \to W^\pm e^\mp$ (and the analogous decay modes into muon flavor) are favored by the data. On the other hand, when the dark matter particle is a scalar, the decay modes $\phi_{\rm DM} \to e^+ e^-$, $\mu^+ \mu^-$ are favored. Purely leptonic decay modes, such as $\psi_{\rm DM} \to \ell^+ \ell^- \nu$ or $\phi_{\rm DM} \to \ell^+ \ell^-$ do not produce antideuterons. However, as discussed above, the decay of a fermionic dark matter particle into $W^\pm$ bosons and charged leptons could produce an observable antideuteron flux.

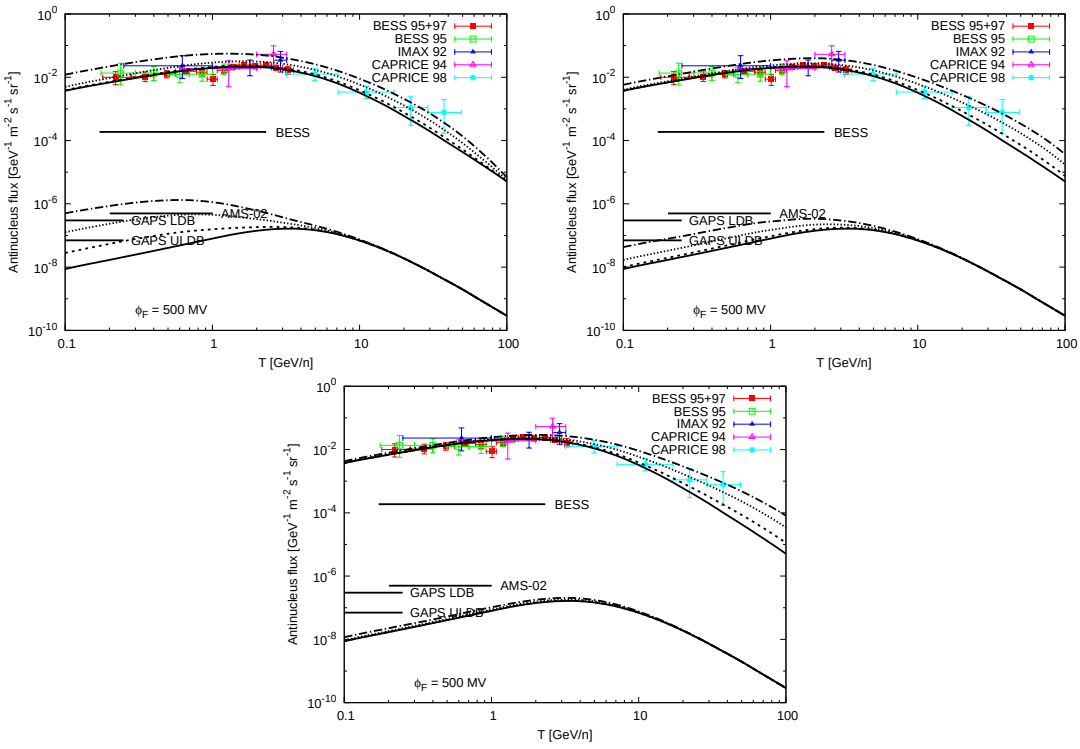

Figure 5.4: Total antiproton and antideuteron fluxes including a primary contribution to the flux from the decay of a fermionic dark matter particle in the channel $\psi_{\rm DM} \to W^{\pm}e^{\mp}$. The lifetime has been chosen, for each dark matter mass, to reproduce the steep rise in the positron fraction observed by the PAMELA collaboration. When the dark matter mass is 300 GeV (*top left panel*), 600 GeV (*top right panel*) and 1000 GeV (*bottom panel*), the corresponding lifetimes are $\tau_{\rm DM} = 4.0,\ 2.3,\ 1.6\ \times 10^{26}$ sec, respectively. The dashed lines indicate the total fluxes for the MIN propagation model, the dotted lines for the MED propagation model, and the dash-dotted lines for the MAX propagation model (*cf.* Table 2.3). We also show the purely secondary fluxes as solid lines.

We show in Fig. 4 the total antiproton and antideuteron fluxes from the decay of a fermionic dark matter particle in the channel $\psi_{\rm DM} \to W^{\pm}e^{\mp}$, fixing for each dark matter mass the lifetime in order to account for the steep rise in the positron fraction observed by PAMELA. For a dark matter mass $m_{\rm DM} = 300,\ 600,\ 1000$ GeV, the corresponding lifetimes are $\tau_{\rm DM} = 4.0,\ 2.3,\ 1.6 \times 10^{26}$ s, respectively. For these particularly interesting decaying dark matter scenarios, we find that the antideuteron flux could be within the reach of the planned experiments AMS-02 and GAPS, provided the dark matter particle is not too heavy. The discovery of antideuterons would thus favor the decay mode $\psi_{\rm DM} \to W^{\pm}e^{\mp}$ as a possible origin of the PAMELA positron excess over the purely leptonic decay modes such as $\psi_{\rm DM} \to e^{+}e^{-}\nu$.[6] It is important to emphasize that this conclusion holds for ranges of propagation parameters which not only reproduce the positron excess observed by PAMELA, but also yield a total antiproton flux consistent with present measurements.

[6]The decay mode $\psi_{\rm DM} \to W^{\pm}e^{\mp}$ may also yield signatures in the diffuse gamma-ray background.

5.5 Conclusions

We have calculated the antideuteron fluxes at Earth from the decay of dark matter particles in the Milky Way halo and discussed the prospects of observing cosmic antideuterons in the projected experiments AMS-02 and GAPS. We have adopted a model-independent approach, analyzing possible hadronic decay modes for the dark matter particles. The nuclear fusion of an antiproton and an antineutron to form an antideuteron was simulated employing the coalescence model, while the propagation of antideuterons in the Galaxy was described by a stationary two-zone diffusion model with cylindrical boundary conditions. The hadronic showers also produce a flux of antiprotons, which is severely constrained by observations. Therefore, we have simultaneously calculated the predicted antiproton flux to verify whether the chosen parameters and decay modes are consistent with present observations.

We have shown that there are choices of parameters where the antideuteron flux from dark matter decay can be much larger than the purely secondary component from spallation of cosmic rays on the interstellar medium, while at the same time the total antiproton flux remains consistent with observations. We have also shown that if the dark matter particle is sufficiently light, the antideuteron flux from dark matter decay could be within the reach of the planned experiments AMS-02 or GAPS, while the secondary component is expected to lie below the projected sensitivities. Therefore, the observation of cosmic antideuterons in the near future could be interpreted as an indication of hadronic decays of dark matter particles. In particular, this conclusion holds for a fermionic dark matter particle which decays preferentially via $\psi_{\mathrm{DM}} \to W^{\pm} e^{\mp}$, which has been proposed as an explanation for the steep rise in the positron fraction observed by the PAMELA collaboration.

Chapter 6

Large-Scale Gamma-Ray Anisotropies

As discussed in Chapter 3, decaying dark matter particles could be indirectly detected as an excess over a simple power law in the energy spectrum of the diffuse extragalactic gamma-ray background. Furthermore, since the Earth is not located at the center of the Galactic dark matter halo, the exotic contribution from dark matter decay to the diffuse gamma-ray flux is expected to be anisotropic, offering a complementary method for the indirect search for decaying dark matter particles. In this chapter, which is based on the publication [3], we discuss in detail the expected dipole-like anisotropies in the dark matter signal, also taking into account the radiation from inverse Compton scattering of electrons and positrons from dark matter decay. As an application, we calculate the expected anisotropies for the decaying dark matter scenarios that can reproduce the electron/positron excesses reported by PAMELA and the Fermi LAT, and we estimate the prospects for detecting the predicted gamma-ray anisotropy in the near future.

6.1 Introduction

The full-sky observations of gamma rays undertaken in the 1990s by the Energetic Gamma Ray Experiment Telescope (EGRET) revealed a map which is highly anisotropic, containing resolved sources as well as diffuse emission, mostly produced by cosmic-ray interactions in the Galaxy. As mentioned in Chapter 3, the diffuse part of the emission is well understood in terms of microscopic processes, although the intensity of the individual contributions depends on various astrophysical uncertainties. Interestingly, once the Galactic disk (at low latitudes in the range $-10^\circ < b < 10^\circ$) is masked, the remaining diffuse emission is remarkably isotropic, typically of order 10% or less.

On the other hand, over the last years a picture of cosmic-ray propagation has emerged which can account for the observed abundances of almost all secondary cosmic-ray species. Remarkably, this same propagation model can reproduce, using the interstellar gas and radiation field distributions and a Galactic magnetic field inferred from observations, the full-sky gamma-ray map with rather good accuracy. However, this requires the introduction of an additional, a priori undetermined, diffuse component which is postulated to be of extragalactic

origin and thus isotropic. Its energy spectrum is determined by observations at high Galactic latitudes.

As discussed at length in Chapter 4, it has recently become apparent that the state-of-the-art propagation models fail to reproduce the measurements of the positron fraction at energies larger than 10 GeV, which has been tentatively interpreted as a dark matter signature. A great deal of effort has been made to study the prospects and predictions of cosmic-ray signatures from annihilating dark matter, see, for example [267, 268, 136]. However, as we have stressed, the decay of dark matter is a viable alternative scenario for indirect dark matter detection. Among the different probes for such indirect signatures, the gamma-ray channel is probably the most important to study, due to its sensitivity to far-distant sources and its potential to discriminate between signals from annihilating or decaying dark matter and astrophysical sources (recently some efforts have been made to distinguish dark matter annihilation from dark matter decay by the morphology of the associated gamma-ray emission [269, 270]).

In this chapter we will present a detailed study of the peculiar predictions for gamma rays from decaying dark matter. We will concentrate on their angular anisotropies on large and small scales. These can be used to discriminate this component from other contributions to the extragalactic diffuse emission. It turns out that the predictions for decaying dark matter are much more robust than the ones for annihilation, which makes this scenario very predictive and easier to confirm or falsify [103]. Second, we will discuss the prospects to see such signals in the upcoming Fermi LAT gamma-ray data, and we will apply our results to the decaying dark matter explanation of the electron/positron excess.

This chapter is organized as follows. In Section 6.2 we will review the basic concepts about production, propagation and absorption of gamma rays from dark matter decay. In Section 6.3 we will calculate the gamma-ray anisotropy expected from the decay of dark matter particles on large angular scales. We will show in particular the expected anisotropy in scenarios which can explain the electron/positron excesses observed by PAMELA and the Fermi LAT, and we will argue that this anisotropy should be seen by the Fermi LAT. Lastly, in Section 6.5, we will present our conclusions. We also present two sections in which we discuss statistical properties of the large-scale anisotropy and the general observational strategy for gamma rays from dark matter decay.

6.2 Gamma Rays from Dark Matter Decay

To calculate the gamma-ray flux dark matter decay both in the Galactic halo and and extragalactic distances we follow the procedure outlined in Chapter 3. Aside from the prompt radiation produced in dark matter decay, the electrons and positrons that may also arise as decay products, and which may be the origin of the PAMELA and Fermi LAT anomalies, also generate a contribution to the gamma-ray flux through their inverse Compton scattering on the interstellar radiation field, which includes the CMB, thermal dust radiation, and starlight. Recently, inverse Compton scattering was discussed in connection with the PAMELA excess in [192, 193, 196, 197, 271, 272]. Furthermore, the interactions of energetic electrons and positrons with the Galactic magnetic field produces synchrotron radiation in the radio band

with frequencies $\mathcal{O}(0.1\,\mathrm{GHz} - 100\,\mathrm{GHz})$, which may also be observable (see, *e.g.* [165, 195]).

Throughout this chapter we will assume the Einasto dark matter halo profile as defined in Eq. (1.14), with $\alpha = 0.17$ and $r_\mathrm{s} = 20\,\mathrm{kpc}$, unless stated otherwise. For the local dark matter density we use the value $\rho_\odot = 0.39\,\mathrm{GeV\,cm^{-3}}$, as determined in [122], to normalize the profiles at the position of the Sun. Related uncertainties and their impact on our results will be discussed below. For the size of the diffusive halo in which the electrons and positrons propagate, we assume a cylinder of radius $R = 20\,\mathrm{kpc}$ and half-height $L = 3\,\mathrm{kpc}$.[1] The impact of a variation of the height of the diffusive halo on our results will be discussed below.

6.3 Large-Scale Anisotropies from Dark Matter Decay

As discussed in Chapter 3, the decay of dark matter particles in the Galactic halo can produce gamma rays that could be detected as an exotic contribution to the diffuse extragalactic gamma-ray background (EGBG). The diffuse extragalactic background at high energies is believed to be dominated by the emission from unresolved active galactic nuclei (AGN) and is expected to follow a power law, with an intensity and an index that have to be determined by fitting to the data [155, 157, 251]. Thus, if the dark matter particles decay at a sufficiently high rate, one generically expects to observe a deviation from a simple power law in the gamma-ray energy spectrum, which could show up in observatories like Fermi LAT.

A complementary signature of dark matter decay is the observation of anisotropies in the EGBG. It is well known that the offset between the Sun and the Galactic center causes a peculiar angular dependence in the gamma-ray signal from dark matter decaying [103] or annihilating [273, 274] in the Milky Way halo, even when the halo profile itself is isotropic. From our vantage point, the halo signal is largest in the direction of the Galactic center and smallest in the direction of the Galactic anticenter due to the differing amounts of dark matter in the respective hemispheres. On the other hand, some anisotropy would be expected between the North ($b > 0$) and South ($b < 0$) hemispheres. The observation of an anisotropy that is aligned in this way would be a strong signal for a contribution from dark matter and, on the other hand, its non-observation would provide constraints on this scenario. Gamma rays from the decay of dark matter particles at cosmological distances are isotropic and therefore tend to reduce the anisotropy of the overall flux. This attenuation effect is small, however, due to the relative weakness of the extragalactic contribution.

To compare the sizes of the halo and the extragalactic component of gamma rays from decaying dark matter (neglecting ICS radiation for simplicity), we show in Fig. 6.1 the total flux of photons, integrated over all energies, as a function of the angular distance from the Galactic center, for a dark matter particle which decays producing a monoenergetic photon with an energy in the range $E'_\gamma \simeq 10\,\mathrm{GeV} - 1\,\mathrm{TeV}$. As apparent from the figure, the cosmological contributions decrease with the energy due to the attenuation described above, while the radiation profile from decaying particles in the halo is independent of energy. The halo

[1] For some sample decay channels we have cross-checked with `GALPROP V50P`, using appropriately modified versions of the model 50p_599278 (which adopts a diffusive halo height $L = 4\,\mathrm{kpc}$) and of the annihilation package, that our approximations give correct ICS gamma-ray sky maps at the 30% level everywhere in the sky for gamma-ray energies above 1 GeV.

contribution typically dominates the total flux independently of the halo profile, except at low energies $E'_\gamma \lesssim 10\,\mathrm{GeV}$ in the direction of the Galactic anticenter. The differences in the two dark matter profiles become only relevant near the Galactic center when $\psi \lesssim 10^\circ$ and at the Galactic center the flux predicted for the Einasto profile is almost one order of magnitude larger than the corresponding flux from the isothermal profile.

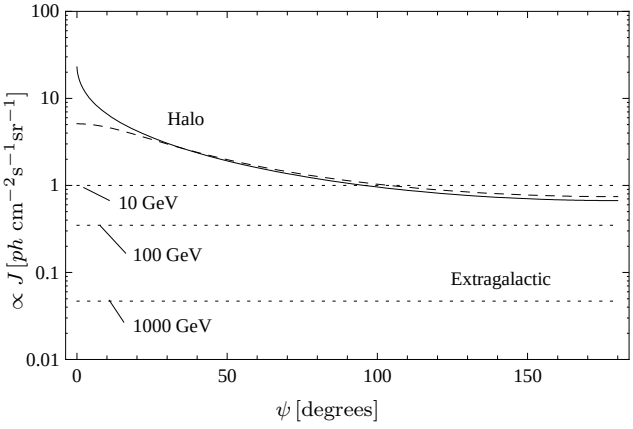

Figure 6.1: Angular profile of the gamma-ray signal from dark matter decay as a function of the angle ψ to the center of the galaxy. The *solid* (*dashed*) line shows the contribution from decay in the Milky Way halo, assuming the Einasto (isothermal) profile. Extragalactic contributions are shown in *dotted* lines for the case that dark matter decay produces a monoenergetic line with energies between $E'_\gamma = 10$ and $1000\,\mathrm{GeV}$. The fluxes are integrated over energy and normalized to the size of the extragalactic component when absorption is neglected.

To analyze the prospects of detecting a gamma-ray anisotropy from dark matter decay at the Fermi LAT, it is convenient to define the quantity

$$A_{b_0:b_1} = \frac{\bar{J}_{\mathrm{GC}} - \bar{J}_{\mathrm{GAC}}}{\bar{J}_{\mathrm{GC}} + \bar{J}_{\mathrm{GAC}}}\,, \tag{6.1}$$

where $\bar{J}_{\mathrm{GC}}$ and $\bar{J}_{\mathrm{GAC}}$ in general denote the total diffuse gamma-ray flux (the sum of conventional astrophysical emission and the putative dark matter signal), integrated over the photon energy E_γ in some energy range and appropriately average over the hemisphere in the direction of the Galactic center (GC) and anticenter (GAC), respectively. Regions of the sky at low ($|b| < b_0$) or high ($|b| > b_1$) Galactic latitudes are excluded from the average.

As an example, we calculate the anisotropy parameter A in different regions of the sky for the decay $\psi_{\mathrm{DM}} \to \gamma\nu$ of a fermionic dark matter particle ψ_{DM}, after subtracting astrophysical sources (the Galactic foreground and the extragalactic gamma-ray background), in order to compare the anisotropy expected purely from dark matter decay to the anisotropy expected from the Galactic models (in the rest of the chapter, however, we will consider both sources of gamma rays simultaneously, calculating the anisotropy of the total flux). In this case, the energy spectrum of gamma rays has two components: a monoenergetic line from the decay of

dark matter particles in the halo and a redshifted line from decays at cosmological distances (note that in this decay channel there is no contribution from ICS). We show in Table 6.1 the values of A for dark matter particles with masses between 20 GeV and 2 TeV, producing monoenergetic photons with energies 10 GeV and 1 TeV, respectively. It is interesting that the anisotropy parameter can be as large as 0.5 for large energies and relatively low latitudes. In the region defined by $b_0 = 10^\circ$ and $b_1 = 90^\circ$ (on which we will concentrate below), the anisotropy of the "pure" dark matter signal ranges between 0.20 and 0.36, with only little dependence on the profile of the dark matter halo. These values have to be compared with the anisotropies of the Galactic foreground as predicted by `GALPROP` (see below), which are considerably smaller, and typically $A \lesssim 0.10$ in all the regions that are shown in Table 6.1, up to energies above 300 GeV. Furthermore, the anisotropies measured by EGRET for energies below 10 GeV are consistent with the predictions for the Galactic foreground [153].

Sky Patch	Anisotropy $A_{b_0:b_1}$	
$b_0 : b_1$	Einasto	Isothermal
$10^\circ : 90^\circ$	$0.21 - 0.36$	$0.20 - 0.33$
$10^\circ : 20^\circ$	$0.32 - 0.50$	$0.29 - 0.45$
$20^\circ : 60^\circ$	$0.21 - 0.35$	$0.20 - 0.33$
$60^\circ : 90^\circ$	$0.07 - 0.13$	$0.07 - 0.13$

Table 6.1: Anisotropy of the gamma-ray signal from the decay $\psi_{\rm DM} \to \gamma\nu$ of a fermionic dark matter particle $\psi_{\rm DM}$, after subtracting astrophysical contributions. The ranges correspond to the anisotropies from gamma-ray lines with energies between 10 GeV and 1000 GeV in different regions of the sky, see Eq. (6.1)

From the theoretical point of view, the search for anisotropies in the gamma-ray flux is a cleaner method for the indirect detection of dark matter than the search for an excess in the spectrum of the EGBG. As mentioned above, the genuinely extragalactic flux from active galactic nuclei and other extragalactic sources is poorly understood. Thus, it is difficult to make firm predictions for the total gamma-ray flux in scenarios with decaying dark matter, even when the particle physics model is specified (namely, the dark matter mass, lifetime and decay modes). Moreover, there are other potentially important isotropic contributions to the total flux with an intensity that cannot be predicted theoretically. For instance, interactions of high-energy cosmic rays with debris in the hypothetical Oort cloud could produce a sizable gamma-ray flux, provided that the column density is larger than 10^{-3} g cm^{-2} [275]. Since all these contributions to the total flux are perfectly isotropic, they cancel out when calculating the difference of fluxes between the Galactic center and Galactic anticenter regions.

To illustrate the large-scale anisotropy A that could be produced by dark matter decay, we will show predictions for different dark matter decay channels and masses, including Galactic foreground radiation and the astrophysical extragalactic background. As Galactic foreground, we assume the predictions of the conventional `GALPROP` model [276] (model 44__500180). For the extragalactic background we will use the following parametrization, which agrees with

preliminary results from Fermi LAT [277],

$$\frac{dJ}{dE_\gamma} = 5.8 \times 10^{-7} (\mathrm{GeV\,cm\,s\,sr})^{-1} \left(\frac{E_\gamma}{1\,\mathrm{GeV}} \right)^{-2.45} . \tag{6.2}$$

For illustration, we show in the left panels of Fig. 6.2 the predicted anisotropy of the total gamma-ray flux that would be measurable in the different regions in the sky if the dark matter particles decay exclusively into $\tau^+\tau^-$ pairs. The anisotropy is calculated taking into account the Galactic foreground emission and the extragalactic background as discussed above. We choose a dark matter mass $m_{\rm DM} = 600\,\mathrm{GeV}$ and set the lifetime to $\tau_{\rm DM} = 3.5 \times 10^{27}\,\mathrm{s}$. The energy spectra $dN_{\gamma,e}/dE_{\gamma,e}$ of photons, electrons and positrons generated in the $\tau^\pm$ decays are generated using `PYTHIA 6.4` [249]. The lifetime is chosen such that the gamma-ray fluxes are below and compatible with the EGBG, as demonstrated in the right panels of Fig. 6.2, where we also show preliminary results from Fermi LAT for comparison.[2]

Furthermore, we note that the contribution to the total electron and positron fluxes from dark matter decay is negligible in this scenario (*cf.* Chapter 4). Interestingly, for the adopted choice of parameters, an anisotropy is predicted that is significantly different from the one expected from the diffuse Galactic emission in the conventional `GALPROP` model. Statistically, such an anisotropy should be within the reach of Fermi LAT, as illustrated by the boxes in the figure, which correspond to our estimates of the one-year and five-year statistical errors of Fermi LAT, assuming exposures of $\varepsilon = 3 \times 10^{10}\,\mathrm{cm^2\,s}$ [277] and $\varepsilon = 2 \times 10^{11}\,\mathrm{cm^2\,s}$ [278], respectively. For a discussion of our calculation of the statistical error, see below and Appendix A. As expected, the size of the anisotropy is largest at low latitudes $b \lesssim 20^\circ$, and decreases slowly when observing higher latitudes. On the other hand, the statistical error is smallest in the patch of the sky shown in the upper panels of Fig. 6.2, where the whole sky with $|b| > 10^\circ$ is included. The effects of inverse Compton radiation are negligible in the present case of decays into $\tau^+\tau^-$ pairs since the electrons and positrons produced in the subsequent decays of the tau leptons have only relatively small energies.

To illustrate the impact of inverse Compton radiation, on the anisotropy parameter A, we show in Fig. 6.3 the anisotropy of the gamma-ray flux assuming that the dark matter decays exclusively into e^+e^- pairs, where we choose $m_{\rm DM} = 1000\,\mathrm{GeV}$ and $\tau_{\rm DM} = 2 \times 10^{27}\,\mathrm{s}$. In this case the dominant source of gamma rays is inverse Compton scattering (Note that we assumed that the dark matter particle has spin 1; for scalar dark matter particles, helicity-suppression leads to an enhanced rate of production of final-state radiation [279], suppressing the relative contribution of inverse Compton). For comparison, we also show the anisotropy that would be present if inverse Compton radiation were absent (dashed lines in the left panels of Fig. 6.3). Note that in this scenario electrons and positrons produced in dark matter decay yield a significant contribution to the local cosmic-ray fluxes, without being in conflict with the PAMELA and Fermi LAT data. Again, we find that a sizable anisotropy is expected in several patches of the sky. In this case, however, the gamma rays relevant for our predictions are mainly produced close to the Galactic center, above and below the Galactic disk. Hence, the anisotropies are relatively small at higher latitudes, $|b| \gtrsim 20^\circ$. A more detailed discussion

[2] Fitting the preliminary Fermi LAT results with a Galactic foreground model is well beyond the scope of this work. Hence, there is a mismatch between the total fluxes and the data, which does not affect our conclusions, however.

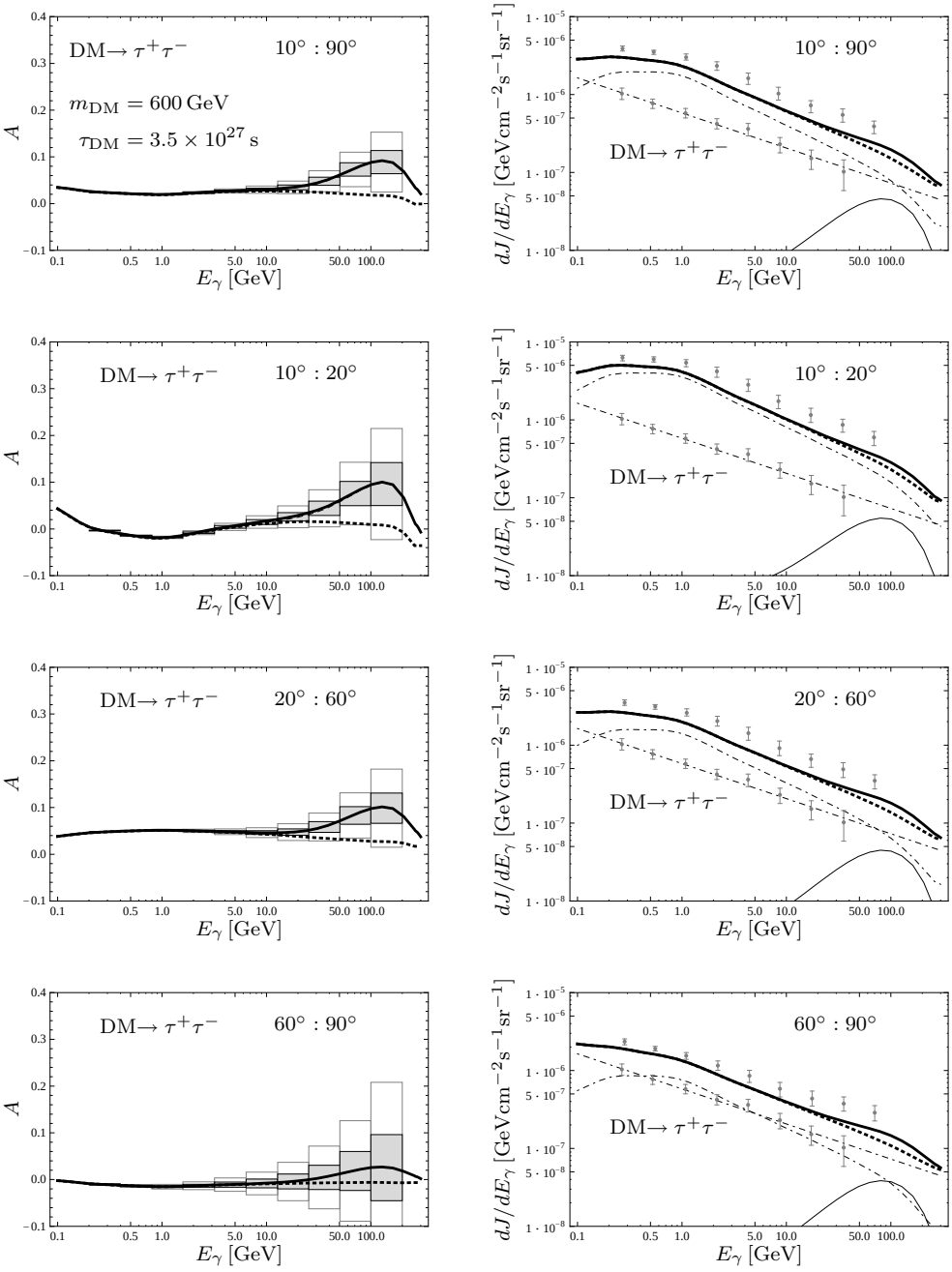

Figure 6.2: *Left panels:* Anisotropy of the gamma-ray flux from dark matter decay into $\tau^+\tau^-$ pairs as a function of energy. The dotted line shows the background anisotropy as expected from the Galactic foreground, while the solid line shows the anisotropy of signal + background. We also show the signal + background anisotropy neglecting gamma rays from inverse Compton scattering (dashed, overlapping with solid line). *Right panels:* Gamma-ray fluxes averaged over all Galactic longitudes as a function of energy. The thin solid line shows the gamma rays from dark matter decay. The two dash-dotted lines show the astrophysical EGBG and the Galactic foreground separately. The thick solid line shows the sum of all contributions, whereas the dotted line shows the sum without contributions from dark matter. From top to bottom the different panels show predictions for different patches of the sky.

of the morphological differences between prompt and inverse Compton radiation from dark matter decay can be found in Section 6.4.

If dark matter decay is the origin of the excess in the positron fraction observed by PAMELA and in the total electron + positron flux observed by Fermi LAT, the predicted anisotropies can be rather large. This is to be expected, since any explanation of these anomalies requires the injection of hard electrons and positrons. In Fig. 6.4 we show our results for the anistropy parameter A, which is expected if the dark matter particles decay via one of the decay modes that we identified in Chapter 4 to fit the electron and positron data well.[3] To minimize the statistical errors, we concentrate on the region defined by $b_0 = 10^\circ$ and $b_1 = 90^\circ$ (see Section 6.4). As is apparent from the plots, the predictions for some of the decay channels, the predictions for some decay channels (in particular the decay $\psi_{\rm DM} \to W^\pm \mu^\mp$) are already in conflict with the preliminary results of the Fermi LAT collaboration for the EGBG, whereas other decay channels are marginally consistent (*e.g.*, the decay into $\mu^+\mu^-$ pairs). However, even for those channels which are compatible with the data, sizable anisotropies, around $A \simeq 0.2 - 0.3$, are predicted at energies $E_\gamma \simeq 100\,\mathrm{GeV}$. This is significantly different from the anisotropy expected for the astrophysical foreground. As indicated by our estimates of the statistical error bars for one year of Fermi LAT data taking, this deviation should be clearly visible in the upcoming results for the diffuse gamma-ray sky. On the other hand, its non-observation would impose strong constraints on the decaying dark matter interpretation of the positron excess observed by PAMELA/Fermi LAT.

Uncertainties in the determination of the above large-scale anisotropy come from different sources. When neglecting ICS radiation, the prediction of an anisotropy between 0.2 and 0.3 in the dark matter signal at latitudes $|b| > 10^\circ$ is relatively robust. The main sources of uncertainty are the profile of the Milky Way dark matter halo and its normalization. As discussed above, the dependence on the profile is rather weak (*cf.* Table 6.1). Only in case of a much lower value for the local dark matter density, say $\rho_\odot = 0.2\,\mathrm{GeV\,cm^{-3}}$, and only for gamma rays with energies $E'_\gamma \lesssim 10\,\mathrm{GeV}$ the anisotropy can become as small as $A \simeq 0.15$. On the other hand, the size and anisotropy of the ICS radiation from electrons and positrons originating from dark matter decay is plagued by many uncertainties like the exact height of the diffusion zone, the distribution of the ISRF and the size of the Galactic magnetic field. In general the ICS radiation, and hence the overall anisotropy of the observed flux, becomes stronger if the height of the diffusive halo is increased, but a detailed study of these uncertainties is beyond the scope of this work. Note, however, that the large scale anisotropies predicted for the decay channels shown in Fig. 6.4 are sizable even if ICS radiation is neglected (dashed lines in the left panels).

Finally, we will discuss in a more quantitative way the main prospects for the Fermi LAT to detect gamma rays from dark matter decay through the observations of large-scale anisotropies. To this end we will neglect inverse Compton radiation for the electrons and positrons produced in the decay of the dark matter particles, and we will assume perfect subtraction of the Galactic foreground. The remaining flux is then expected to be constituted by the isotropic EGBG, which is possibly contaminated by anisotropic radiation from dark

[3] We use slightly larger lifetimes here than in Chapter 4 to compensate for the slightly larger local dark matter density used here.

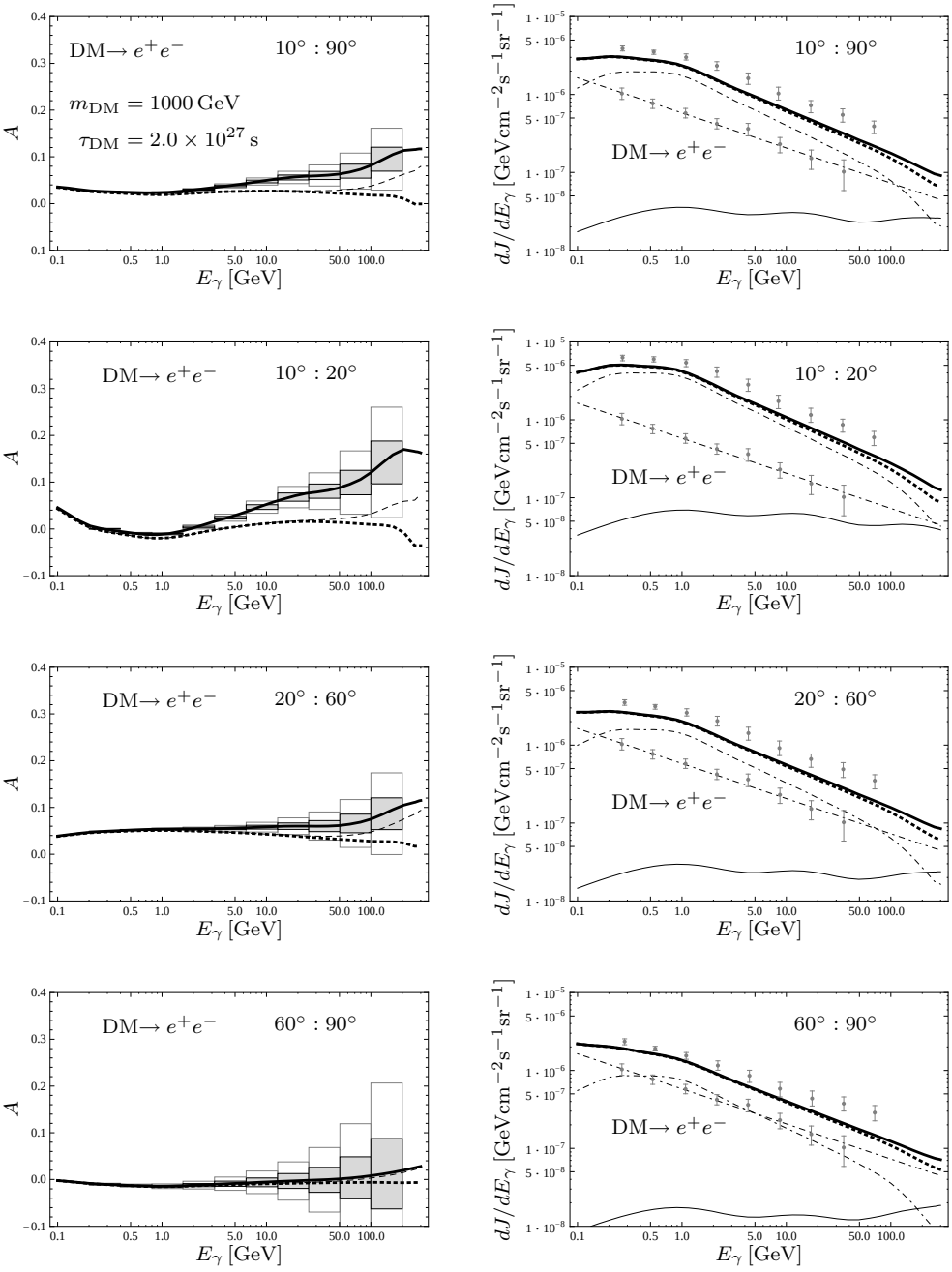

Figure 6.3: Same as Fig. 6.2, but for the decay into e^+e^- pairs. Here, in the left panels the difference in the predictions for the anisotropy when including inverse Compton radiation (solid line) and neglecting inverse Compton radiation (dashed line) is clearly visible.

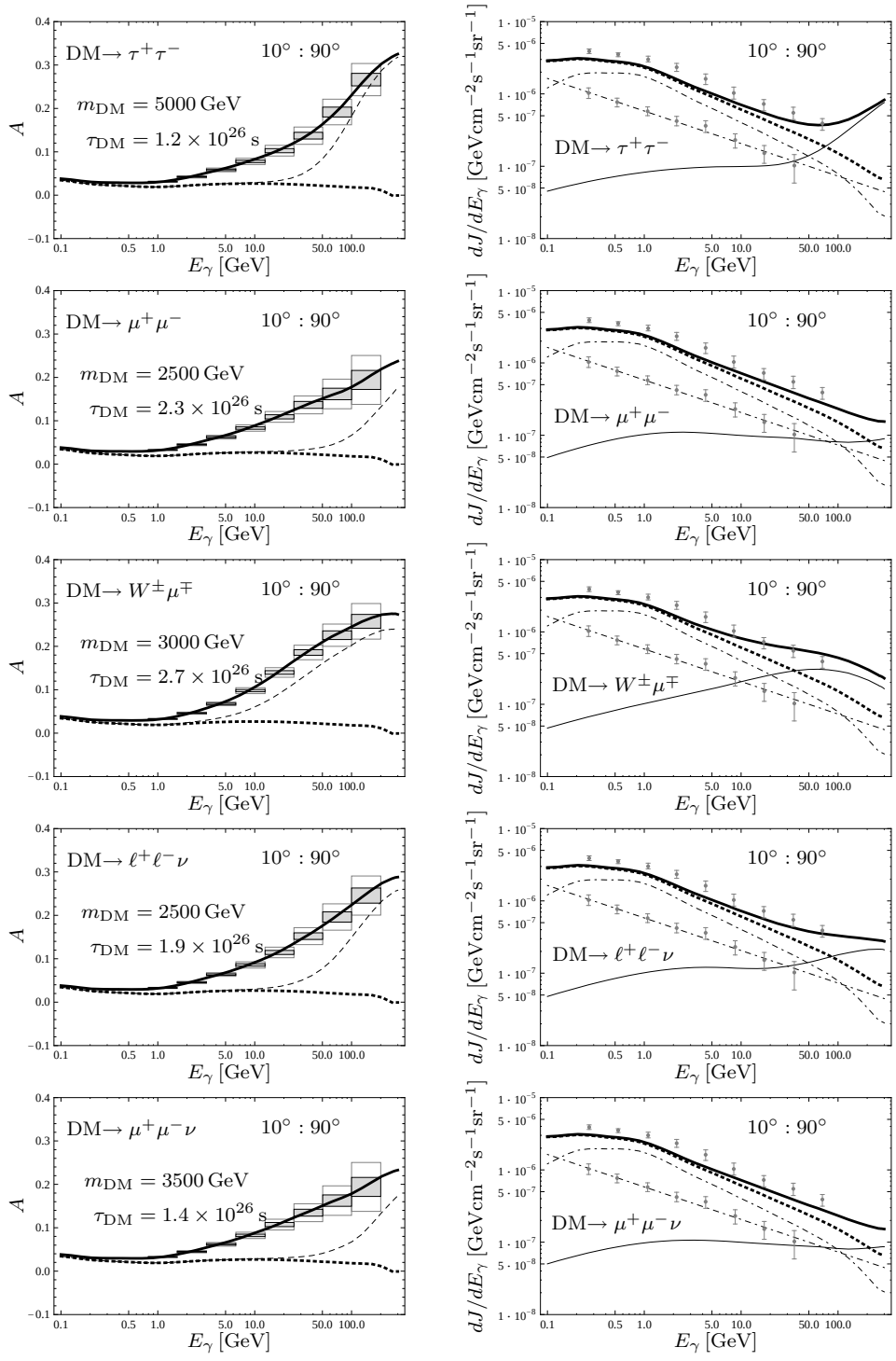

Figure 6.4: Predictions for the five dark matter decay channels that were found to fit the positron excess as observed by PAMELA/Fermi LAT. The left panels show predictions for the total measurable anisotropy at latitudes $|b| > 10°$ (solid line) and estimates of the corresponding 1-year and 5-year statistical error bars of the Fermi LAT measurements. The dotted line is the anisotropy predicted by the conventional `GALPROP` model. In the right panels we show predictions for the averaged fluxes in the same sky region. Line coding is the same as in Fig. 6.2.

matter decay. For definiteness, we will assume that the remaining flux follows the power law in Eq. (6.2).

Provided that a fraction $f_{\rm sig}$ of the considered gamma-ray photons in a given energy range is due to decaying dark matter, the measured anisotropy A is given by

$$A = f_{\rm sig} A_{\rm sig} + (1 - f_{\rm sig}) A_{\rm bkg} \,. \tag{6.3}$$

Here, $A_{\rm sig}$ and $A_{\rm bkg}$ denote, respectively, the anisotropy of the dark matter signal, which can be read off from Table 6.1, and the anistropy of the astrophysical background, which is $A_{\rm bkg} = 0$ as per our assumptions. A possible detection at the 3σ level requires that

$$f_{\rm sig} > \frac{3\sigma_A}{A_{\rm sig} - A_{\rm bkg}} \,, \tag{6.4}$$

where σ_A denotes the standard deviation of the anistropy A. It depends on the total number of measured photons N_γ and can be approximated by $\sigma_A \simeq N^{-1/2}$. The adopted approximation for σ_A is better than 10% as long as $|A| \lesssim 0.3$ and $\sigma_A \lesssim 0.2$. See Appendix A for a short discussion. The photon number density is given by

$$N_\gamma = \varepsilon \cdot \Omega_{\rm sky} \int_{E_0}^{E_1} dE_\gamma \frac{dJ}{dE_\gamma} \,, \tag{6.5}$$

where ε denotes the observationally given exposure (see above) and $\Omega_{\rm sky}$ is the solid angle of the sky under observation, which is given by $\Omega_{\rm sky} \approx 4\pi \cdot 0.83$ if the Galactic disk with $|b| < 10^\circ$ is excluded. Following Eq. (6.2), the Fermi LAT will detect $N_\gamma \simeq 3.0 \times 10^4$ ($N_\gamma \simeq 1.1 \times 10^3$) photons with energies $E_\gamma \geq 10\,{\rm GeV}$ ($E_\gamma \geq 100\,{\rm GeV}$) after five years of data taking. Taking for definiteness $A_{\rm sig} = 0.3$, this allows in principle a 3σ detection of a dark matter contamination down to $f_{\rm sig} \simeq 6\%$ ($f_{\rm sig} \simeq 30\%$). Note, however, that additional statistical noise and systematic uncertainties from point source subtraction and the determination of the Galactic foreground are neglected in this estimation and can reduce the sensitivity to $f_{\rm s}$ by factors of order one.

6.4 Morphology of Prompt and Inverse Compton Radiation

In this section we will briefly discuss the differences between observing ICS radiation from positrons and electrons from dark matter decay and observing the gamma rays that come directly from the decay itself (prompt radiation like "internal bremsstrahlung") by means of signal-to-noise and signal-to-background ratios.

Signal-to-noise ratios quantify the significance of a signal against random statistical noise. The signal-to-noise ratio S/N of a dark matter signal with respect to the background is given by

$$\frac{S}{N} = \frac{N_\gamma^{\rm sig}}{\sqrt{N_\gamma^{\rm sig} + N_\gamma^{\rm bkg}}}, \tag{6.6}$$

where $N_\gamma^{\rm sig}$ and $N_\gamma^{\rm bkg}$ denote the number of detected signal and background photons, respectively, that are observed in a given sky region $\Delta\Omega$ and energy band $E_0 \ldots E_1$. Signal photons

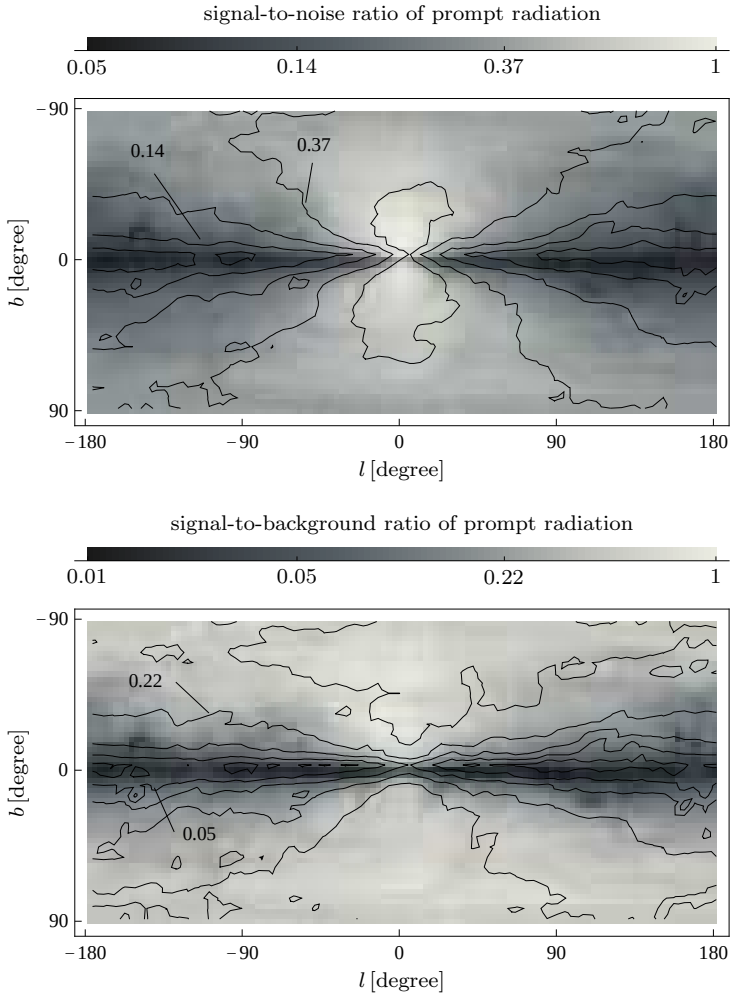

Figure 6.5: Upper panel: Sky map of the relative signal-to-noise ratio of the gamma-ray signal from dark matter decay as a function of Galactic longitude l and latitude b, normalized to unity at the Galactic center. Lower panel: Sky map of the relative signal-to-background ratio for the same process. Extragalactic and ICS radiation is neglected, and for the background we assume the predictions of the conventional `GALPROP` model at 100 GeV.

are all photons from dark matter decay; background photons are in principle all other observed photons, including the astrophysical part of the EGBG and the Galactic foreground. Since the number of detected photons scales like

$$N_\gamma^i \propto \int_{\Delta\Omega} d\Omega \int_{E_0}^{E_1} dE \, \frac{dJ^i}{dE_\gamma} \equiv \Delta\Omega \bar{J}_i \,, \tag{6.7}$$

the signal-to-noise ratio in the limit $\Delta\Omega \to 0$ has the proportionality

$$\frac{S}{N} \propto \frac{\bar{J}^{\rm sig}}{\sqrt{\bar{J}^{\rm sig} + \bar{J}^{\rm bkg}}} \,, \tag{6.8}$$

where $\bar{J}^{\rm sig}$ and $\bar{J}^{\rm bkg}$ denote the appropriately averaged and integrated signal and background gamma-ray fluxes, respectively. In the upper panel of Fig. 6.5 we plot the relative signal-to-noise ratio (with arbitrary normalization), assuming that the background completely dominates the signal, $\bar{J}^{\rm sig} \ll \bar{J}^{\rm bkg}$, and neglecting ICS and extragalactic radiation. As background we take the predictions of the conventional `GALPROP` model at $E_\gamma = 100\,\text{GeV}$ (from [276], see above), but the results do not change qualitatively for other energies. The anisotropy of the dark matter signal as a function of l is clearly recognizable in the plot. Furthermore, it is apparent that, from the perspective of statistical noise, the sky regions that are most sensitive to decaying dark matter signals lie closely above and below the Galactic center, with $|l| \lesssim 25^\circ$ and $5^\circ \lesssim |b| \lesssim 35^\circ$.

To determine the best observational strategy in light of the systematics that are related to the determination of the Galactic foreground, it is more convenient to consider the signal-to-background ratio $J^{\rm sig}/J^{\rm bkg}$ (we assume that systematic uncertainties scale roughly like $\sim J^{\rm bkg}$). We show the signal-to-background ratio as a function of the Galactic coordinates in the lower panel of Fig. 6.5. Again, the large-scale anisotropy of the dark matter flux is clearly visible in the plot. Furthermore, it is apparent that concerning systematics, the best strategy is to avoid regions near the Galactic plane and to observe fluxes only at higher latitudes, $|b| \gtrsim 20^\circ$. However, as a compromise between statistical and systematic uncertainties we choose to consider the whole region $10^\circ \leq |b| \leq 90^\circ$ in most of the present analysis.

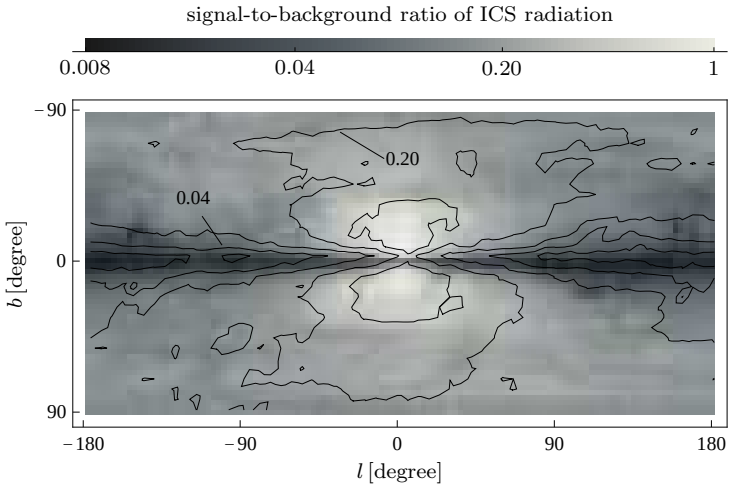

Figure 6.6: Sky map of the relative signal-to-background ratio of pure ICS radiation from dark matter decay at the energy $E_\gamma = 10\,\text{GeV}$. We assume that $m_{\rm DM} = 1\,\text{TeV}$ and that the dark matter is decaying into e^+e^- pairs. For the background we assume the fluxes from the conventional `GALPROP` model.

In contrast to gamma rays that come directly from decay of dark matter, the gamma rays that originate in inverse Compton scattering of positrons or electrons from dark matter on the ISRF are mostly coming from the region near the Galactic center. This can be seen in Fig. 6.6, where we plot the signal-to-background ratio of the pure ICS signal caused by dark matter

decaying into e^+e^- pairs (with $m_{\rm DM} = 1\,\text{TeV}$) as a function of the Galactic coordinates. The gamma-ray energy is $E_\gamma = 10\,\text{GeV}$ in this plot. As background we again use the predictions from the conventional `GALPROP` model. From the figure it is apparent that the relative size of the signal peaks at regions very closely above and below the Galactic center, with $|l| \lesssim 20^\circ$ and $5^\circ \lesssim |b| \lesssim 30^\circ$. This suggests that concentrating the observation on these regions is most promising for the search for ICS radiation from dark mattter decay. However, in light of the large underlying uncertainties related to the predictions of ICS radiation we will neglect these subtleties, and we consider ICS radiation only in so far as it affects the anisotropies and fluxes in the sky regions that are most promising for the search for gamma rays coming from dark matter decay itself.

6.5 Conclusions

Dark matter particles could decay into gamma rays at a rate which is sufficiently large as to allow the indirect detection of the dark matter through an excess over the expected power law in the energy spectrum of the diffuse extragalactic gamma-ray background. In this chapter we have discussed a complementary way of indirectly detecting unstable dark matter particles by exploiting the fact that the Earth is not located at the center of the dark matter halo, leading to a dipole-like asymmetry in the gamma radiation from dark matter. We have discussed the relative size of the extragalactic and the halo component of the gamma rays from dark matter decay, incorporating the attenuation effects from pair production on the intergalactic background light, and we have calculated the dipole-like anisotropy between the high-latitude gamma-ray flux coming from the Galactic center and anticenter regions for different dark matter decay channels. We have furthermore demonstrated the strong impact of gamma rays from inverse Compton scattering of electrons and positrons from dark matter decay on the anisotropy signal. We have found that if dark matter decay is the correct explanation of the excesses in the positron fraction and the electron + positron flux reported by the PAMELA and Fermi LAT collaborations, based on the statistical errors we have estimated such an anisotropy in the gamma-ray flux should be observable by Fermi LAT (see Fig. 6.4).

Chapter 7

Gamma-Ray Lines from Radiative Dark Matter Decay

The decay of dark matter particles which are coupled predominantly to charged leptons has been proposed as a possible origin of excess high-energy positrons and electrons observed by cosmic-ray telescopes PAMELA and Fermi LAT. Even though the dark matter itself is electrically neutral, the tree-level decay of dark matter into charged lepton pairs will generically induce radiative two-body decays of dark matter at the quantum level. In this chapter, which is based on the publication [1], we calculate the rates of radiative two-body decays for scalar and fermionic dark matter particles using an effective theory of leptophilic dark matter decay. Due to the absence of astrophysical sources of monochromatic gamma rays, the observation of a line in the diffuse gamma-ray spectrum would constitute a strong indication of a particle physics origin of these photons. We estimate the intensity of the gamma-ray line that may be present in the energy range of a few TeV if the dark matter decay interpretation of the leptonic cosmic-ray anomalies is correct and comment on observational prospects of present and future Imaging Cherenkov Telescopes, in particular the CTA.

7.1 Introduction

There exists the possibility that the excess of positrons and electrons is due to the annihilation or decay of dark matter particles. However, measurements of cosmic-ray antiprotons, in particular measurements of the antiproton-to-proton ratio by PAMELA [129, 280], yield stringent constraints on the fraction of dark matter decays or annihilations into hadronic final states. This has lead some authors to consider "leptophilic" models of dark matter [7, 281, 282, 283, 284, 285, 286, 287, 288, 289], where the dark matter is coupled predominantly or exclusively to charged leptons. In the following, we consider the possibility that the dark matter particles decay leptonically with extremely long lifetimes. More precisely, the interpretation of the leptonic cosmic-ray anomalies observed by PAMELA and Fermi LAT in terms of dark matter decay suggests a lifetime of the dark matter on the order of 10^{26} seconds (see Chapter 4).

In this chapter, we examine some of the effects of leptophilic models of decaying dark matter which arise at next-to-leading order in perturbation theory and show that they can have relevance to indirect dark matter searches. We will not speculate on the precise nature

of the particle physics that could give rise to leptophilic dark matter decay. Instead, our approach will be to examine simple models where we assume effective interactions that describe the desired leptophilic coupling of dark matter particles to charged leptons. The salient point for us here is that even if one assumes an exclusive coupling of the dark matter to charged leptons at tree level, this behavior is only valid at leading order, while at next-to-leading order other particles, including photons and weak gauge bosons, will be produced. Indeed, these higher-order corrections have been analyzed in the past for the case of annihilating dark matter [290, 291, 292, 293, 294, 295]. It is well known that the higher-order corrections in the form of internal bremsstrahlung or from final-state radiation of weak gauge bosons can even dominate under certain conditions [291, 294].

The decay modes induced by higher-order corrections are usually suppressed by powers of the couplings and possibly loop factors, as opposed to the leading-order decay modes. This means that the resulting decay products will be difficult to detect unless they possess some distinct features. Weak gauge bosons can be produced, for instance, via final-state radiation off the charged leptons [296]. By their subsequent hadronization, the massive gauge bosons will then generate hadronic particles, including antiprotons [295]. Therefore, every leptophilic dark matter model that aims to explain the leptonic cosmic-ray anomalies also serves as a source of antiprotons. In this chapter, however, we will focus on complementary constraints arising from a different decay channel induced by higher-order effects. Namely, we will study radiative two-body decays involving photons. These are particularly interesting, since they give rise to monochromatic lines in the diffuse gamma-ray spectrum or in extragalactic sources. Such lines are of utmost importance because astrophysical processes generally generate continuous gamma-ray spectra. Thus, the observation of a gamma-ray line would be a compelling signature of an underlying particle physics process. In some cases, a gamma-ray line can be produced already in tree level decays [11]. In the present work, we demonstrate that for leptophilic models of dark matter, the ratio between leading-order and next-to-leading-order decay modes can be large enough to produce a potentially observable gamma-ray line signal.

This chapter is organized as follows. In Section 7.2, we discuss the production of monochromatic photons from radiative two-body decays induced at the one-loop level for fermionic dark matter particles in a simple leptophilic toy model. In Section 7.3, we examine the corresponding case for a scalar dark matter particle. Next, in Section 7.4, we discuss observational constraints on gamma-ray lines in the GeV to TeV region and compare existing bounds with the expected signal from dark matter decay. We also comment on future observational prospects, in particular for the proposed Cherenkov Telescope Array. Finally, we present our conclusions in Section 7.5.

7.2 Radiative Decay of Fermionic Dark Matter

We first regard the case that the particles comprising the dark matter are fermions which we denote by $\psi_{\rm DM}$. We require that the dark matter decays with a large branching fraction into pairs of charged leptons in order to explain the excess of such leptons in high-energy cosmic rays, and we assume that this is the only channel in which the dark matter decays at leading order. If the dark matter carries spin 1/2, Lorentz invariance requires the decay to

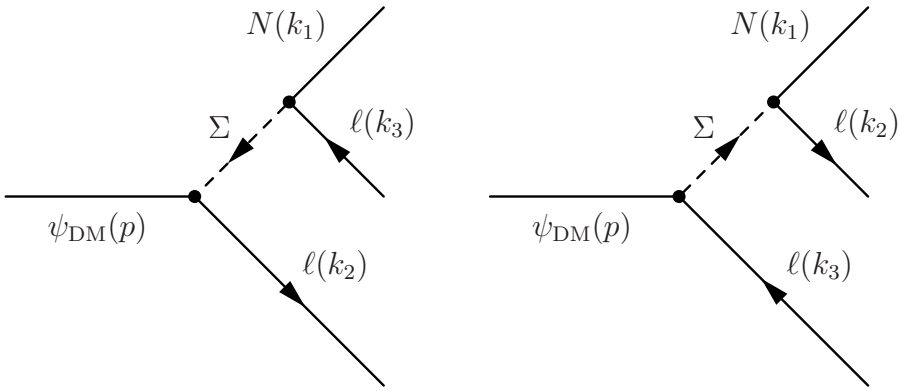

Figure 7.1: Tree-level diagrams contributing to the three-body decay $\psi_{\rm DM} \to \ell^+\ell^- N$ of fermionic dark matter, mediated by a heavy charged scalar Σ. Instead of the intermediate scalar Σ, the decay can also be mediated by a vector V.

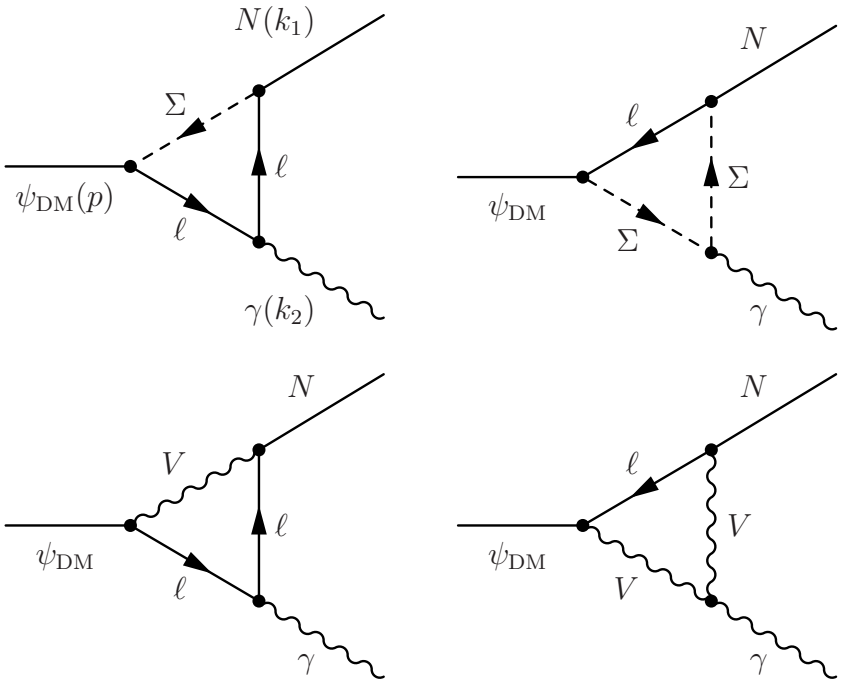

Figure 7.2: Diagrams contributing at one loop to the radiative two-body decay $\psi_{\rm DM} \to \gamma N$, induced by a charged scalar Σ (top row) and a vector particle V (bottom row), respectively. There are two additional diagrams in each case which differ only by the direction of the charge flow.

be (at least) a three-body decay involving a third, electrically neutral fermion N for angular momentum conservation. Thus, the decay $\psi_{\rm DM} \to \ell^+\ell^- N$ is the simplest one allowed by gauge and Lorentz invariance. Here, N could be a neutrino, a neutralino or a gravitino, for instance. The decays may be mediated by a virtual charged scalar particle Σ or by a charged

vector boson V, with masses m_Σ and m_V, respectively, which are assumed to be larger than the mass of the dark matter particle. We regard the two cases separately.

In the case of an intermediate scalar, the effective Lagrangian that we use is given as the sum of a term coupling the dark matter, which we take to be a metastable Majorana fermion, to a charged lepton and a Σ particle, as well as a term coupling the neutral fermion to the Σ and a lepton field. We decompose the couplings into left- and right-handed components to allow for chiral couplings. Then the Lagrangian has the form

$$\mathcal{L}_{\text{eff}}^{\Sigma} = -\bar{\psi}_{\text{DM}} \left[\lambda_{\ell\psi}^{L} P_L + \lambda_{\ell\psi}^{R} P_R\right] \ell\, \Sigma^\dagger - \bar{N} \left[\lambda_{\ell N}^{L} P_L + \lambda_{\ell N}^{R} P_R\right] \ell\, \Sigma^\dagger + \text{h.c.}\,, \tag{7.1}$$

where $P_L = (1-\gamma^5)/2$ and $P_R = (1+\gamma^5)/2$ are the left- and right-handed chirality projectors, respectively. The λ-couplings can in general be complex. To obtain the required cosmological lifetime for the dark matter, the couplings have to be super-weak or the mass m_Σ of the mediator has to be super-heavy. The operators of the effective Lagrangian induce three-body decays of the dark matter into a pair of charged leptons and a neutral fermion at tree level, $\psi_{\text{DM}} \to \ell^+\ell^- N$. The corresponding diagram is shown in Fig. 7.1.

In the case of a vector interaction, on the other hand, we assume an effective Lagrangian of the form

$$\mathcal{L}_{\text{eff}}^{V} = -\bar{\psi}_{\text{DM}}\gamma^\mu \left[\lambda_{\ell\psi}^{L} P_L + \lambda_{\ell\psi}^{R} P_R\right] \ell\, V_\mu^\dagger - \bar{N}\gamma^\mu \left[\lambda_{\ell N}^{L} P_L + \lambda_{\ell N}^{R} P_R\right] \ell\, V_\mu^\dagger + \text{h.c.}\,. \tag{7.2}$$

The case of mediation by a vector boson is more involved than the previous case of mediation by a scalar. In choosing a Lagrangian of this form, we assume that the essence of the gauge interaction giving rise to this Lagrangian is captured by the effective charged-vector interaction. In general, one expects neutral currents in association with the charged currents, which introduces a high degree of model dependence. For simplicity, we assume here that the decay is dominated by the charged-current interaction.

7.2.1 Decay Widths

In the following we examine decay modes of the dark matter at the tree- and one-loop level and summarize the relevant decay widths.[1]

Tree-level decay: $\psi_{\text{DM}} \to \ell^+\ell^- N$

The leading-order decay induced by the effective Lagrangian is the three-body decay $\psi_{\text{DM}} \to \ell^+\ell^- N$. If the dark matter decays in this way, it constitutes a possible explanation for the observed cosmic-ray anomalies under certain conditions [4]. We present the relevant expressions for the decay widths in the following.

Mediation by a Scalar. In the plausible limit $m_\ell \ll m_{\psi_{\text{DM}}} \ll m_\Sigma$, the partial decay width for the decay $\psi_{\text{DM}} \to \ell^+\ell^- N$ is given by (see Appendix B.1 and [299])

$$\Gamma(\psi_{\text{DM}} \to \ell^+\ell^- N) = \frac{1}{64(2\pi)^3} \frac{m_{\psi_{\text{DM}}}^5}{6 m_\Sigma^4} \left\{C_1^\Sigma F_1(m_N^2/m_{\psi_{\text{DM}}}^2) + C_2^\Sigma F_2(m_N^2/m_{\psi_{\text{DM}}}^2)\right\}\,. \tag{7.3}$$

[1] We have cross-checked the matrix elements for the three-body decays and the decay rates in the following sections by comparing them to the results from `FeynArts` [297] and `FormCalc` [298].

The constants C_1^Σ, C_2^Σ are determined by the couplings as

$$C_1^\Sigma \equiv \left(|\lambda_{\ell\psi}^L|^2 + |\lambda_{\ell\psi}^R|^2\right)\left(|\lambda_{\ell N}^L|^2 + |\lambda_{\ell N}^R|^2\right) - \eta\,\mathrm{Re}\left(\lambda_{\ell\psi}^L \lambda_{\ell N}^{L*} \lambda_{\ell\psi}^R \lambda_{\ell N}^{R*}\right), \tag{7.4}$$

$$C_2^\Sigma \equiv 2\eta\,\mathrm{Re}\left[\left(\lambda_{\ell\psi}^L \lambda_{\ell N}^{L*}\right)^2 + \left(\lambda_{\ell\psi}^R \lambda_{\ell N}^{R*}\right)^2\right]. \tag{7.5}$$

Here, $\eta \equiv \eta_{\psi_{\rm DM}}\eta_N = \pm 1$ depending on the CP eigenvalues of $\psi_{\rm DM}$ and N. The kinematical functions, on the other hand, are given by

$$F_1(x) \equiv (1-x^2)(1+x^2-8x) - 12x^2\ln(x)\,, \tag{7.6}$$

$$F_2(x) \equiv \sqrt{x}[(1-x)(1+10x+x^2) + 6x(1+x)\ln(x)]\,. \tag{7.7}$$

In the hierarchical limit $m_N/m_{\psi_{\rm DM}} \to 0$, the kinematical functions satisfy

$$F_1(x) \simeq 1\,, \quad F_2(x) \simeq \sqrt{x} \quad \text{for} \quad x \to 0\,, \tag{7.8}$$

whereas in the degenerate limit $m_N/m_{\psi_{\rm DM}} \to 1$, one gets

$$F_1(x) \simeq \frac{2}{5}(1-x)^5, \quad F_2(x) \simeq \frac{1}{10}(1-x)^5 \quad \text{for} \quad x \to 1\,. \tag{7.9}$$

In the limit $m_N \ll m_{\psi_{\rm DM}}$ the decay rate (7.3) corresponds to a lifetime

$$\tau_{\psi_{\rm DM}\to\ell^+\ell^-N} \simeq 6\times 10^{26}\,\mathrm{s}\left(\frac{0.1}{C_1^\Sigma}\right)\left(\frac{1\ \mathrm{TeV}}{m_{\psi_{\rm DM}}}\right)^5\left(\frac{m_\Sigma}{10^{15}\ \mathrm{GeV}}\right)^4. \tag{7.10}$$

In the case where $m_{\psi_{\rm DM}}$ and m_N are quasi-degenerate, the decay rate scales approximately like $(m_{\psi_{\rm DM}} - m_N)^5$.

Mediation by a vector. For the vector-mediated decay we find for the three-body decay rate in the limit $m_\ell \ll m_{\psi_{\rm DM}} \ll m_V$

$$\Gamma(\psi_{\rm DM} \to \ell^+\ell^- N) = \frac{1}{64(2\pi)^3}\frac{4m_{\psi_{\rm DM}}^5}{6m_V^4}\left\{C_1^V F_1(m_N^2/m_{\psi_{\rm DM}}^2) + C_2^V F_2(m_N^2/m_{\psi_{\rm DM}}^2)\right\}, \tag{7.11}$$

where the functions F_1 and F_2 are the same as in Eqs. (7.6), (7.7) and

$$C_1^V \equiv \left(|\lambda_{\ell\psi}^L|^2 + |\lambda_{\ell\psi}^R|^2\right)\left(|\lambda_{\ell N}^L|^2 + |\lambda_{\ell N}^R|^2\right) + 2\eta\,\mathrm{Re}\left(\lambda_{\ell\psi}^L \lambda_{\ell N}^{L*} \lambda_{\ell\psi}^R \lambda_{\ell N}^{R*}\right), \tag{7.12}$$

$$C_2^V \equiv 2\eta\,\mathrm{Re}\left[\left(\lambda_{\ell\psi}^L \lambda_{\ell N}^{L*}\right)^2 + \left(\lambda_{\ell\psi}^R \lambda_{\ell N}^{R*}\right)^2\right] = C_2^\Sigma\,. \tag{7.13}$$

For $m_N \ll m_{\psi_{\rm DM}}$ and an analogous choice of parameters, the lifetime is smaller by a factor of four compared to Eq. (7.10),

$$\tau_{\psi_{\rm DM}\to\ell^+\ell^-N} \simeq 1.5\times 10^{26}\,\mathrm{s}\left(\frac{0.1}{C_1^V}\right)\left(\frac{1\ \mathrm{TeV}}{m_{\psi_{\rm DM}}}\right)^5\left(\frac{m_V}{10^{15}\ \mathrm{GeV}}\right)^4. \tag{7.14}$$

One-loop decay: $\psi_{\rm DM} \to \gamma N$

By combining the external charged lepton lines from the tree-level diagrams into a loop, we obtain diagrams contributing to the two-body decay $\psi_{\rm DM} \to \gamma N$ (see Fig. 7.2). This decay mode will be suppressed with respect to the tree-level three-body decay by a loop factor and an additional power of the electromagnetic coupling. This is partially compensated by phase-space factors, however. More importantly, the two-body decay gives rise to monochromatic photons at an energy

$$E_\gamma = \frac{m_{\psi_{\rm DM}}}{2}\left(1 - \frac{m_N^2}{m_{\psi_{\rm DM}}^2}\right), \tag{7.15}$$

which can result in a distinct observational signature at gamma-ray telescopes, as will be discussed in some detail in Section 7.4. Interestingly, the experimental constraints on the parameters of decaying dark matter stemming from the non-observation of energetic gamma-ray lines could, despite the loop-suppression, be more stringent than the ones stemming from measurements of cosmic-ray electrons and positrons.

Based on gauge invariance, and irrespective of whether the decay is mediated by a scalar or a vector particle, the matrix element for the sum of all diagrams contributing to the radiative two-body decay can be written in the following form, introducing an effective coupling $g_{N\gamma\psi}$ [300],

$$\begin{aligned}\mathcal{M} &= \frac{i g_{N\gamma\psi}}{m_{\psi_{\rm DM}}}\bar{u}(k_1)(P_R - \eta_N \eta_{\psi_{\rm DM}} P_L)\sigma^{\mu\nu} k_{2\mu} \epsilon^*_\nu u(p) \\ &= -\frac{g_{N\gamma\psi}}{m_{\psi_{\rm DM}}}\bar{u}(k_1)(P_R - \eta_N \eta_{\psi_{\rm DM}} P_L)\not{k}_2 \not{\epsilon}^* u(p)\,,\end{aligned} \tag{7.16}$$

where $\sigma^{\mu\nu} = i[\gamma^\mu, \gamma^\nu]/2$ and $\eta_{\psi_{\rm DM}}$, η_N are the CP eigenvalues of $\psi_{\rm DM}$ and N, respectively. The partial decay width for $\psi_{\rm DM} \to \gamma N$ can then be easily calculated to be

$$\Gamma(\psi_{\rm DM} \to \gamma N) = \frac{g_{N\gamma\psi}^2}{8\pi} m_{\psi_{\rm DM}} \left(1 - \frac{m_N^2}{m_{\psi_{\rm DM}}^2}\right)^3. \tag{7.17}$$

The effective coupling $g_{N\gamma\psi}$ encodes all the information about the interaction between dark matter and the decay products. We give explicit expressions for this coupling in the following.

Mediation by a scalar. We first examine the case of mediation by a charged scalar particle Σ (top row of Fig. 7.2). Assuming that CP is conserved in the interactions of $\psi_{\rm DM}$ and N, *i.e.*, when the λ-couplings are assumed to be real, the explicit form of the effective coupling $g^\Sigma_{N\gamma\psi}$ can be expressed as follows,

$$\begin{aligned}g^\Sigma_{N\gamma\psi} = &-\frac{e\,\eta_N m_{\psi_{\rm DM}}}{16\pi^2}\sum_{\ell,\Sigma} Q_\ell C_\ell \Big\{ m_f(\eta_{\psi_{\rm DM}}\lambda^L_{\ell N}\lambda^R_{\ell\psi} - \eta_N \lambda^R_{\ell N}\lambda^L_{\ell\psi}) I \\ &+ (\lambda^L_{\ell N}\lambda^L_{\ell\psi} - \eta\,\lambda^R_{\ell N}\lambda^R_{\ell\psi})[\eta_{\psi_{\rm DM}} m_{\psi_{\rm DM}}(I^2 - K) - \eta_N m_N K]\Big\},\end{aligned} \tag{7.18}$$

where the loop integrals I, I^2 and K are defined in Appendix B.1.[2] The sum runs over all lepton flavors $\ell \in \{e, \mu, \tau\}$, for which $Q_\ell = C_\ell = 1$. If multiple mediator particles (like left-

[2]Note that the superscript '2' in the integral I^2 is an index, not a square.

and right-handed sleptons, $\Sigma = \widetilde{\ell}_L, \widetilde{\ell}_R$) are present, one also has to sum over their contributions. In principle, there can also be contributions from quarks in the loop. Then, the sum runs over quarks and leptons with electric charge Q_q and color charge $C_q = 3$. However, tree-level decays into quarks can potentially lead to an overproduction of antiprotons if the relative size of the effective coupling to quarks compared to the coupling to leptons is too large. The requirement of avoiding antiproton overproduction then leads to the assumption of a leptophilic structure. For this reason, we assume throughout this work that the dark matter decays only into leptons at tree level.

If the mass of the intermediate particle Σ is much larger than the other masses, the loop integrals take on a very simple form. The effective coupling is then given approximately by

$$g^{\Sigma}_{N\gamma\psi} \simeq \frac{e\,\eta}{64\pi^2} m^2_{\psi_{\rm DM}} \left(1 - \frac{\eta\, m_N}{m_{\psi_{\rm DM}}}\right) \sum_{\ell,\Sigma} \frac{Q_\ell C_\ell}{m^2_\Sigma} \left\{ \left(\lambda^L_{\ell N}\lambda^L_{\ell\psi} - \eta\,\lambda^R_{\ell N}\lambda^R_{\ell\psi}\right)\right\} . \tag{7.19}$$

For the concrete case where there is only one mediator Σ, which couples exclusively to leptons, the decay rate reads

$$\begin{aligned}\Gamma(\psi_{\rm DM} \to \gamma N) = \frac{e^2}{8\pi\,(64\pi^2)^2} \frac{m^5_{\psi_{\rm DM}}}{m^4_\Sigma} \left(1 - \frac{m^2_N}{m^2_{\psi_{\rm DM}}}\right)^3 \left(1 - \frac{\eta\, m_N}{m_{\psi_{\rm DM}}}\right)^2 \\ \times \left[\sum_\ell \left(\lambda^L_{\ell N}\lambda^L_{\ell\psi} - \eta\,\lambda^R_{\ell N}\lambda^R_{\ell\psi}\right)\right]^2 .\end{aligned} \tag{7.20}$$

For $m_N \ll m_{\psi_{\rm DM}}$, this decay width corresponds to a partial lifetime

$$\tau_{\psi_{\rm DM}\to\gamma N} \simeq 7\times 10^{29}\ {\rm s}\ \frac{0.1}{\left[\left(\lambda^L_{\ell N}\lambda^L_{\ell\psi} - \eta\,\lambda^R_{\ell N}\lambda^R_{\ell\psi}\right)\right]^2} \left(\frac{1\ {\rm TeV}}{m_{\psi_{\rm DM}}}\right)^5 \left(\frac{m_\Sigma}{10^{15}\ {\rm GeV}}\right)^4 . \tag{7.21}$$

Mediation by a vector. In the case of mediation by a charged vector boson (bottom row of Fig. 7.2) we obtain the following expression for the effective coupling [300],

$$\begin{aligned} g^V_{N\gamma\psi} = \frac{e\,\eta_N m_{\psi_{\rm DM}}}{8\pi^2} \sum_\ell \Big\{ &(\eta_{\psi_{\rm DM}}\eta_N \lambda^L_{\ell N}\lambda^L_{\ell\psi} - \lambda^R_{\ell N}\lambda^R_{\ell\psi})\big[\eta_{\psi_{\rm DM}} m_{\psi_{\rm DM}}(I^2 - J - K) \\ &+ \eta_N m_N (J-K)\big] + 2m_\ell(\eta_{\psi_{\rm DM}}\lambda^L_{\ell N}\lambda^R_{\ell\psi} - \eta_N \lambda^R_{\ell N}\lambda^L_{\ell\psi})J\Big\} , \end{aligned} \tag{7.22}$$

where we encounter an additional loop integral J, which is defined in Appendix B.1. Again, it is possible to include quarks by the replacement $\sum_\ell \to \sum_f Q_f C_f$. However, as discussed above, this would not correspond to a leptophilic model. In the limit $m_\ell \to 0$, $m_{\psi_{\rm DM}} \ll m_V$, the above expression simplifies to

$$g^V_{N\gamma\psi} \simeq \frac{3e\,\eta}{32\pi^2} \frac{m^2_{\psi_{\rm DM}}}{m^2_V} \left(1 - \frac{\eta\, m_N}{m_{\psi_{\rm DM}}}\right) \sum_\ell \left(\lambda^L_{\ell N}\lambda^L_{\ell\psi} - \eta\,\lambda^R_{\ell N}\lambda^R_{\ell\psi}\right) . \tag{7.23}$$

Thus, in the limit $m_\ell \ll m_N$ and $m_{\psi_{\rm DM}} \ll m_V$ we obtain for the decay width

$$\Gamma(\psi_{\rm DM} \to \gamma N) = \frac{9e^2}{8\pi\,(32\pi^2)^2}\frac{m_{\psi_{\rm DM}}^5}{m_V^4}\left(1-\frac{m_N^2}{m_{\psi_{\rm DM}}^2}\right)^3\left(1-\frac{\eta\, m_N}{m_{\psi_{\rm DM}}}\right)^2 \times\left[\sum_\ell\left(\lambda_{\ell N}^L\lambda_{\ell\psi}^L-\eta\,\lambda_{\ell N}^R\lambda_{\ell\psi}^R\right)\right]^2 . \tag{7.24}$$

For $m_N \ll m_{\psi_{\rm DM}}$, this yields a partial lifetime

$$\tau_{\psi_{\rm DM}\to\gamma N} \simeq 2\times 10^{28}\ {\rm s}\ \frac{0.1}{\left[\sum_\ell\left(\eta\,\lambda_{\ell N}^L\lambda_{\ell\psi}^L-\lambda_{\ell N}^R\lambda_{\ell\psi}^R\right)\right]^2}\left(\frac{1\ {\rm TeV}}{m_{\psi_{\rm DM}}}\right)^5\left(\frac{m_V}{10^{15}\ {\rm GeV}}\right)^4 . \tag{7.25}$$

7.2.2 Intermediate Scalar: Intensity of the Gamma-ray Line

The detectability of a loop-induced gamma-ray line will depend crucially on the ratio between the three-body decays at tree level and the two-body decays at the loop level. We examine the general expressions first and then evaluate them for some specific examples.

General Expressions

In the intermediate scalar case, the ratio between two- and three-body decay widths reads, neglecting the charged lepton masses,

$$\frac{\Gamma(\psi_{\rm DM}\to\gamma N)}{\sum_\ell\Gamma(\psi_{\rm DM}\to\ell^+\ell^- N)} \simeq \frac{3\alpha_{\rm em}}{8\pi}\frac{\left[\sum_\ell\left(\lambda_{\ell N}^L\lambda_{\ell\psi}^L-\eta\,\lambda_{\ell N}^R\lambda_{\ell\psi}^R\right)\right]^2(1-x)^3(1-\eta\sqrt{x})^2}{\sum_\ell C_1^\Sigma F_1(x)+C_2^\Sigma F_2(x)}, \tag{7.26}$$

where $x \equiv m_N^2/m_{\psi_{\rm DM}}^2$ and the kinematical functions F_1 and F_2 were defined in Eqs. (7.6), (7.7). This general expression can be used to study the intensity of the one-loop induced gamma-ray line in different scenarios. The numerical value of the prefactor is $3\alpha_{\rm em}/(8\pi) \simeq 1/1148$.

In general, the fraction depends on the chiral and flavor structure of the couplings, the mass ratio $m_N/m_{\psi_{\rm DM}}$ of the decay product and the dark matter particle, and the relative CP parities $\eta = \pm 1$ of N and $\psi_{\rm DM}$. For many practical purposes, it turns out that the dependence on the couplings $\lambda_{\ell N/\psi}$ and on kinematics, *i.e.* on $x = m_N^2/m_{\psi_{\rm DM}}^2$, can be factored according to

$$\frac{\Gamma(\psi_{\rm DM}\to\gamma N)}{\sum_\ell\Gamma(\psi_{\rm DM}\to\ell^+\ell^- N)} \simeq \frac{3\alpha_{\rm em}}{8\pi}\times R_\eta^\Sigma(\lambda_{\ell N}^L,\lambda_{\ell\psi}^L,\lambda_{\ell N}^R,\lambda_{\ell\psi}^R)\times S_\eta(m_N/m_{\psi_{\rm DM}})\,. \tag{7.27}$$

In this parametrization R_η^Σ captures the model-dependence, whereas S_η is determined entirely by kinematics.

It is interesting to consider the two limiting cases of hierachical masses, $m_N/m_{\psi_{\rm DM}} \to 0$, and degenerate masses, $m_N/m_{\psi_{\rm DM}} \to 1$. In the hierarchical limit, and assuming for simplicity

real couplings, one explicitly obtains $S_\eta^{\rm hier} = 1$ and

$$R_\eta^{\Sigma,\rm hier}(\lambda_{\ell N}^L, \lambda_{\ell\psi}^L, \lambda_{\ell N}^R, \lambda_{\ell\psi}^R) = \frac{\left[\sum_\ell \left(\lambda_{\ell N}^L \lambda_{\ell\psi}^L - \eta\, \lambda_{\ell N}^R \lambda_{\ell\psi}^R\right)\right]^2}{\sum_\ell \left[\left(\lambda_{\ell\psi}^{L2} + \lambda_{\ell\psi}^{R2}\right)\left(\lambda_{\ell N}^{L2} + \lambda_{\ell N}^{R2}\right) - \eta\, \lambda_{\ell\psi}^L \lambda_{\ell N}^L \lambda_{\ell\psi}^R \lambda_{\ell N}^R\right]}\,. \tag{7.28}$$

For generic couplings, $R_\eta^{\Sigma,\rm hier}$ is roughly of order one, unless for some special cases where cancellations or chirality suppressions occur. It follows that in the hierarchical limit the two-body decays into γN are typically suppressed roughly by a factor 10^{-3} compared to the tree-level decays into $\ell^+\ell^- N$. In the next subsection we will examine the model-dependent factor R_η^Σ for some specific cases.

On the other hand, in the degenerate limit $m_N/m_{\psi_{\rm DM}} \to 1$, and again assuming real couplings, one finds

$$R_\eta^{\Sigma,\rm deg}(\lambda_{\ell N}^L, \lambda_{\ell\psi}^L, \lambda_{\ell N}^R, \lambda_{\ell\psi}^R) = \frac{\left[\sum_\ell \left(\lambda_{\ell N}^L \lambda_{\ell\psi}^L - \eta\, \lambda_{\ell N}^R \lambda_{\ell\psi}^R\right)\right]^2}{\sum_\ell \left[\frac{2}{2+\eta}\left(\lambda_{\ell\psi}^{L2} + \lambda_{\ell\psi}^{R2}\right)\left(\lambda_{\ell N}^{L2} + \lambda_{\ell N}^{R2}\right) + \frac{\eta}{2+\eta}\left(\lambda_{\ell\psi}^L \lambda_{\ell N}^L - \lambda_{\ell\psi}^R \lambda_{\ell N}^R\right)^2\right]}\,, \tag{7.29}$$

which is also roughly of order one for generic couplings, $R_\eta^{\Sigma,\rm deg} \sim \mathcal{O}(1)$, and

$$S_\eta^{\rm deg}(m_N/m_{\psi_{\rm DM}}) \simeq \begin{cases} 5/12 & \text{for} \quad \eta = +1 \\ 20/(1 - m_N^2/m_{\psi_{\rm DM}}^2)^2 & \text{for} \quad \eta = -1\,. \end{cases} \tag{7.30}$$

Thus, for the case $\eta = +1$, *i.e.* when $\psi_{\rm DM}$ and N have the same CP parities, we again find a typical suppression factor of the order of 10^{-3} for the two-body relative to the tree-level decay rate, as in the hierarchical case. Interestingly, however, when $\psi_{\rm DM}$ and N have opposite CP parities, $\eta = -1$, the two-body rate can be enhanced significantly even for a relatively mild degeneracy, as is shown in Fig. 7.3. This enhancement is due to the fact that the decay rate $\Gamma(\psi_{\rm DM} \to \gamma N)$ is proportional to $(m_N - m_{\psi_{\rm DM}})^3$, whereas the decay into leptons is suppressed like $(m_N - m_{\psi_{\rm DM}})^5$ [300]. Most interestingly, due to this enhancement the decay rate into γN can be rather large in some cases, yielding potentially very intense gamma-ray lines. As a side remark, we note that in addition to the decay channel $\psi_{\rm DM} \to \gamma N$ into photons, there can exist a decay mode $\psi_{\rm DM} \to Z^0 N$ into Z-bosons, which can naively be expected to be of similar size. Thus, for situations where the gamma-ray line signal is strongly enhanced, an equally enhanced decay into Z-bosons can yield additional constraints from the antiproton flux produced by the subsequent fragmentation of the Z-bosons. We leave a more detailed discussion for the future [301].

For concreteness, we consider the case of purely chiral, say left-handed, couplings, and that only one mediator species is present. Then the fraction of decay rates is given by

$$\frac{\Gamma(\psi_{\rm DM} \to \gamma N)}{\sum_\ell \Gamma(\psi_{\rm DM} \to \ell^+\ell^- N)} \simeq \frac{3\alpha_{\rm em}}{8\pi} R^{\rm chir} \begin{cases} 1 & \text{for } m_N \to 0,\ \eta = \pm 1 \\ \frac{5}{12} & \text{for } m_N \to m_{\psi_{\rm DM}},\ \eta = +1 \\ \frac{20}{(1 - m_N^2/m_{\psi_{\rm DM}}^2)^2} & \text{for } m_N \to m_{\psi_{\rm DM}},\ \eta = -1 \end{cases}\,. \tag{7.31}$$

In this case the model-dependent factor for the hierarchical and degenerate regimes coincides, $R^{\Sigma,\mathrm{hier}} = R^{\Sigma,\mathrm{deg}} \equiv R^{\mathrm{chir}}$, and is furthermore independent of η. Explicitly, one has

$$R^{\mathrm{chir}} = \frac{\left[\sum_\ell \lambda^L_{\ell N}\lambda^L_{\ell\psi}\right]^2}{\sum_\ell \left(\lambda^L_{\ell N}\lambda^L_{\ell\psi}\right)^2}\,. \tag{7.32}$$

The result for purely right-handed couplings is analogous. For a generic choice of couplings, one expects $R^{\mathrm{chir}} \sim \mathcal{O}(1)$. Note that $R^{\mathrm{chir}} \leq N_\ell$, where N_ℓ is the number of flavors participating in the decay.

For example, consider two particular cases for the flavor composition of the lepton pairs produced in the decay:

(A) Decay into a single lepton flavor: $\mu^+\mu^-$,

(B) Flavor-democratic decay into e^+e^-, $\mu^+\mu^-$, $\tau^+\tau^-$.

Then one has $R^{\mathrm{chir}} = 1$ in case (A) and $R^{\mathrm{chir}} = 3$ in case (B). The dependence of the ratio of decay rates on the mass ratio $m_N/m_{\psi_{\mathrm{DM}}}$ is shown in Fig. 7.3 for the two cases (A) and (B), and for $\eta = \pm 1$. This dependence is in fact a rather generic feature, which is independent of the details of the couplings. We emphasize again that, in the case when ψ_{DM} and N have opposite CP parities, $\eta = -1$, even a rather mild degeneracy between m_N and $m_{\psi_{\mathrm{DM}}}$ can lead to a considerable enhancement of the gamma-ray line signal relative to the electron/positron flux.

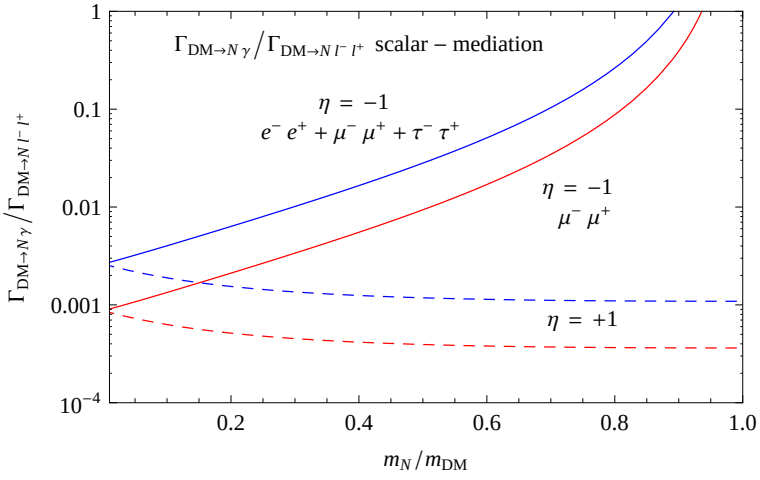

Figure 7.3: Ratio of the decay rates $\Gamma(\psi_{\mathrm{DM}} \to \gamma N)/\sum_\ell \Gamma(\psi_{\mathrm{DM}} \to \ell^+\ell^- N)$ when the decay is mediated by a scalar. The four cases correspond to single-flavor decay (red) and democratic decay into all flavors (blue), as well as ψ_{DM}/N having the same CP parity (dashed, $\eta = +1$) or opposite CP parity (solid, $\eta = -1$). See Eq. (7.31).

Examples

Next, we will discuss the branching ratio into monochromatic photons for several specific scenarios. Namely, we consider the case where N corresponds to left-handed neutrinos ν_L, as well as the scenario of kinetically mixed hidden $U(1)$ gauginos, where N corresponds to a neutralino.

Decay into left-handed neutrinos.

As a basic example for the scalar-mediated decay described in the previous subsection, we consider the case where the neutral fermion is a left-handed neutrino, $N \equiv \nu_L$. Then one can set $\lambda^L_{\ell\nu} = 0$ and $m_\nu = 0$.

From Eq. (7.26) it directly follows, that in the limit $m_\ell \ll m_{\psi_{\rm DM}} \ll m_\Sigma$ the ratio reads

$$\frac{\Gamma(\psi_{\rm DM} \to \gamma\nu)}{\sum_\ell \Gamma(\psi_{\rm DM} \to \ell^+\ell^-\nu)} \simeq \frac{3\alpha_{\rm em}}{8\pi} \frac{\left[\sum_\ell \lambda^R_{\ell\nu}\lambda^R_{\ell\psi}\right]^2}{\sum_\ell \left(\left|\lambda^L_{\ell\psi}\right|^2 + \left|\lambda^R_{\ell\psi}\right|^2\right)\left|\lambda^R_{\ell\nu}\right|^2}. \tag{7.33}$$

As long as only one virtual scalar particle is relevant for the three-body decay, the last factor in this expression is bounded from above by the number of lepton flavors N_ℓ that contribute to the decay. For $N_\ell = 3$, this corresponds to a branching ratio into monochromatic photons smaller than 3×10^{-3}.

Hidden-gaugino dark matter.

In this section, we consider a scenario where a portion of the dark matter is made of the gauginos of an unbroken hidden-sector $U(1)_X$ which interact with the visible sector only through a tiny kinetic mixing. See Chapter 10 for a detailed discussion of the cosmic-ray signatures of this scenario.

In supersymmetric scenarios with an extra unbroken $U(1)_X$ gauge group in the hidden sector, which kinetically mixes with the Standard Model $U(1)_Y$, the particles $\psi_{\rm DM}$ and N could be associated with the hidden gaugino and the lightest MSSM neutralino, respectively. If the kinetic mixing parameter θ is extremely small, the hidden gaugino could constitute decaying dark matter [100]. For a bino-like lightest neutralino and $\Sigma \equiv \widetilde{\ell}_L$ being a left-handed slepton, the couplings are approximately given by

$$\lambda^L_{\ell\psi} \simeq \frac{g'}{\sqrt{2}} Y^L_\ell \theta, \tag{7.34}$$

$$\lambda^L_{\ell N} \simeq \frac{g'}{\sqrt{2}} Y^L_\ell, \tag{7.35}$$

where $\theta \sim 10^{-24}$ is the mixing angle of hidden gaugino and bino, fixed by the requirement of a lifetime of the order of 10^{26} s, and $Y^L_\ell = +1$.

For a hidden gaugino that decays into a bino-like neutralino, the decay rates are given in appendix A of [100]. One can also obtain these rates using the expressions derived above. In particular, we have to sum over two "mediators" Σ for each flavor:

- $\Sigma = \widetilde{\ell}_L$: $\lambda^L_{\ell\psi} = \frac{g'}{\sqrt{2}} Y^L_\ell \theta$, $\lambda^L_{\ell N} = \frac{g'}{\sqrt{2}} Y^L_\ell$, $\lambda^R_{\ell\psi} \simeq 0$, $\lambda^R_{\ell N} \simeq 0$.
- $\Sigma = \widetilde{\ell}_R$: $\lambda^R_{\ell\psi} = \frac{g'}{\sqrt{2}} Y^R_\ell \theta$, $\lambda^R_{\ell N} = \frac{g'}{\sqrt{2}} Y^R_\ell$, $\lambda^L_{\ell\psi} \simeq 0$, $\lambda^L_{\ell N} \simeq 0$.

In addition, there are corresponding contributions from (s)quarks. We assume $m_{\widetilde{f}} \gg m_{\psi_{\rm DM}}$, and neglect the mixing of $\widetilde{f}_{L,R}$ for simplicity. Note that there are additional contributions from chargino loops [300] that are suppressed by the fourth power of the inverse chargino mass. We assume that the squarks are much heavier than the sleptons, and we furthermore assume that all slepton masses are degenerate. Finally, if we take the limit $m_\ell \to 0$, we get

$$\begin{aligned}\Gamma(\psi_{\rm DM} \to \gamma N) &\simeq \frac{e^2 g'^4 \theta^2}{8\pi\,(32\pi^2)^2} \frac{m^5_{\psi_{\rm DM}}}{16 m^4_{\widetilde{\ell}}} \left(1 - \frac{m_N^2}{m^2_{\psi_{\rm DM}}}\right)^3 \left(1 - \eta\,\frac{m_N}{m_{\psi_{\rm DM}}}\right)^2 \\ &\quad \times \left[3\,(1-4\eta)\right]^2 . \end{aligned} \tag{7.36}$$

If the bino and the hidden gaugino have the same *CP* eigenvalue, one has $\eta = +1$, otherwise $\eta = -1$.

The three-body decay rate can be obtained from Eq. (7.3), which can be easily generalized to also account for neutrinos and quarks in the final state. Note that in general, one has to add the matrix elements for the decays mediated by $\Sigma = \widetilde{l}_L$ and $\Sigma = \widetilde{l}_R$, and compute the decay rate from the square of the summed matrix elements. However, it turns out that all "interference" terms are suppressed by the bino–higgsino mixing,[3] which we neglect here. Thus, it is possible to add the decay rates directly. Note that there is an additional contribution from a Z^0 on the intermediate line [299], which is subdominant for the parameter range considered in [100]. Therefore, we also neglect it here for simplicity. We assume, as above, degenerate sleptons. The decay rate summed over three generations of charged leptons and neutrinos is thus (assuming $m_{\widetilde{\nu}} \simeq m_{\widetilde{l}}$)

$$\sum_{\ell,\nu} \Gamma(\psi_{\rm DM} \to \ell\bar{\ell}N) \simeq \frac{g'^4\theta^2}{64(2\pi)^3} \frac{m^5_{\psi_{\rm DM}}}{24 m^4_{\widetilde{l}}} \times 3 \times 18 \times (F_1 + 2\eta F_2) . \tag{7.37}$$

In the hierarchical limit $m_N \ll m_{\psi_{\rm DM}}$, the kinematical factor approaches unity, $F_1 + 2\eta F_2 \to 1$. In the degenerate limit $m_N \to m_{\psi_{\rm DM}}$, one finds $F_1 + 2\eta F_2 \to (2+\eta)(1 - m_N^2/m^2_{\psi_{\rm DM}})^5/5$.

The ratio of decays into γN to the decays into *charged* leptons is thus given by

$$\frac{\Gamma(\psi_{\rm DM} \to \gamma N)}{\sum_\ell \Gamma(\psi_{\rm DM} \to \ell^+\ell^- N)} \simeq \frac{3\alpha_{\rm em}}{8\pi} \underbrace{\frac{[3(1-4\eta)]^2}{51}}_{\equiv R_\eta} \underbrace{\frac{(1-x)^3\,(1-\eta\sqrt{x})^2}{F_1(x) + 2\eta F_2(x)}}_{\equiv S_\eta} , \tag{7.38}$$

with $x = m_N^2/m^2_{\psi_{\rm DM}}$. For the hidden gaugino, the decays $\psi_{\rm DM} \to Z^0 N$ and $\psi_{\rm DM} \to h^0 N$ can also be important since they occur at tree level. Their rates are given in Eqs. (A.1) and (A.3) of [100].

[3] The reason is the following: If we consider a pure bino-slepton-lepton interaction, the slepton $\widetilde{l}_L$ couples only to left-handed leptons and the slepton $\widetilde{l}_R$ only to right-handed ones. Thus both channels are "orthogonal" in the limit where neutralino and slepton mixing are neglected.

According to Eq. (7.38), the model-dependent factor R_η is here given by $R_+ = 1.6$ for $\eta = +1$ and $R_- = 4.4$ for $\eta = -1$, respectively, and hence of order one. The kinematical factor S_η is precisely of the form that was discussed in section 7.2.2, where we found that the two-body decay rate may gain significantly in importance relative to the three-body decay rate if the masses of the hidden gaugino $\psi_{\rm DM}$ and the neutralino N are near-degenerate and the two particles have opposite CP parities.

7.2.3 Intermediate Vector: Intensity of the Gamma-Ray Line

In the case of mediation by a vector, the ratio between two- and three-body decay rates is

$$\frac{\Gamma(\psi_{\rm DM} \to N\gamma)}{\sum_\ell \Gamma(\psi_{\rm DM} \to \ell^+\ell^- N)} \simeq \frac{27\alpha_{\rm em}}{8\pi} \frac{\left[\sum_\ell \left(\lambda^L_{\ell N}\lambda^L_{\ell\psi} - \eta\,\lambda^R_{\ell N}\lambda^R_{\ell\psi}\right)\right]^2 (1-x)^3(1-\eta\sqrt{x})^2}{\sum_\ell (C_1^V F_1(x) + C_2^V F_2(x))}, \quad (7.39)$$

where $x \equiv m_N^2/m^2_{\psi_{\rm DM}}$. As before, it is useful to consider the hierarchical limit $m_N/m_{\psi_{\rm DM}} \to 0$, and the degenerate limit $m_N/m_{\psi_{\rm DM}} \to 1$, for which it is possible to capture the dependence on the couplings in a factor R_η^V and on kinematics in a model-independent factor S_η,

$$\frac{\Gamma(\psi_{\rm DM} \to N\gamma)}{\sum_\ell \Gamma(\psi_{\rm DM} \to \ell^+\ell^- N)} \simeq \frac{27\alpha_{\rm em}}{8\pi} \times R_\eta^V(\lambda^L_{\ell N}, \lambda^L_{\ell\psi}, \lambda^R_{\ell N}, \lambda^R_{\ell\psi}) \times S_\eta(m_N/m_{\psi_{\rm DM}})\,. \quad (7.40)$$

The kinematical factors S_η are identical to the case of scalar mediation, see Eq. (7.30). For the model-dependent factors, one finds

$$R_\eta^{V,\rm hier}(\lambda^L_{\ell N}, \lambda^L_{\ell\psi}, \lambda^R_{\ell N}, \lambda^R_{\ell\psi}) = \frac{\left[\sum_\ell \left(\lambda^L_{\ell N}\lambda^L_{\ell\psi} - \eta\,\lambda^R_{\ell N}\lambda^R_{\ell\psi}\right)\right]^2}{\sum_\ell \left[\left(\lambda^{L2}_{\ell\psi} + \lambda^{R2}_{\ell\psi}\right)\left(\lambda^{L2}_{\ell N} + \lambda^{R2}_{\ell N}\right) + 2\eta\,\lambda^L_{\ell\psi}\lambda^L_{\ell N}\lambda^R_{\ell\psi}\lambda^R_{\ell N}\right]} \quad (7.41)$$

in the hierarchical case, and

$$R_\eta^{V,\rm deg}(\lambda^L_{\ell N}, \lambda^L_{\ell\psi}, \lambda^R_{\ell N}, \lambda^R_{\ell\psi}) = \quad (7.42)$$
$$\frac{\left[\sum_\ell \left(\lambda^L_{\ell N}\lambda^L_{\ell\psi} - \eta\,\lambda^R_{\ell N}\lambda^R_{\ell\psi}\right)\right]^2}{\sum_\ell \left[(\lambda^{L2}_{\ell\psi}\lambda^{L2}_{\ell N} + \lambda^{R2}_{\ell\psi}\lambda^{R2}_{\ell N}) + \frac{2}{2+\eta}(\lambda^{L2}_{\ell\psi}\lambda^{R2}_{\ell N} + \lambda^{R2}_{\ell\psi}\lambda^{L2}_{\ell N}) + \frac{4\eta}{2+\eta}\lambda^L_{\ell\psi}\lambda^R_{\ell\psi}\lambda^L_{\ell N}\lambda^R_{\ell N}\right]}$$

in the degenerate case. For purely chiral, *e.g.* left-handed, couplings one finds that $R_\eta^{V,\rm hier} = R_\eta^{V,\rm deg} = R^{\rm chir}$ coincides with the expression (7.32) for the scalar case, as does the kinematical factor. For a generic set of couplings, R_η^V is roughly of order one.

Note that the prefactor of the ratio of decay rates, Eq. (7.40), for mediation by a vector is larger by a factor of nine compared to mediation by a scalar, Eq. (7.27). Thus, in the hierarchical case $m_N/m_{\psi_{\rm DM}} \to 0$ as well as in the degenerate case with $\eta = +1$ one finds a ratio between two-body and tree-level decay of the order of 10^{-2}, one order of magnitude larger than for the scalar case. In addition, when $\eta = -1$ the gamma-ray line is further enhanced for $m_N/m_{\psi_{\rm DM}} \to 1$ by the kinematic effect discussed in Section 7.2.2. The ratio for some specific examples is shown in Fig. 7.4. Therefore, there are scenarios with dark matter decay mediated by heavy vectors where a gamma-ray line can be fairly intense, despite being loop-suppressed, while at the same time being in agreement with the electron/positron measurements.

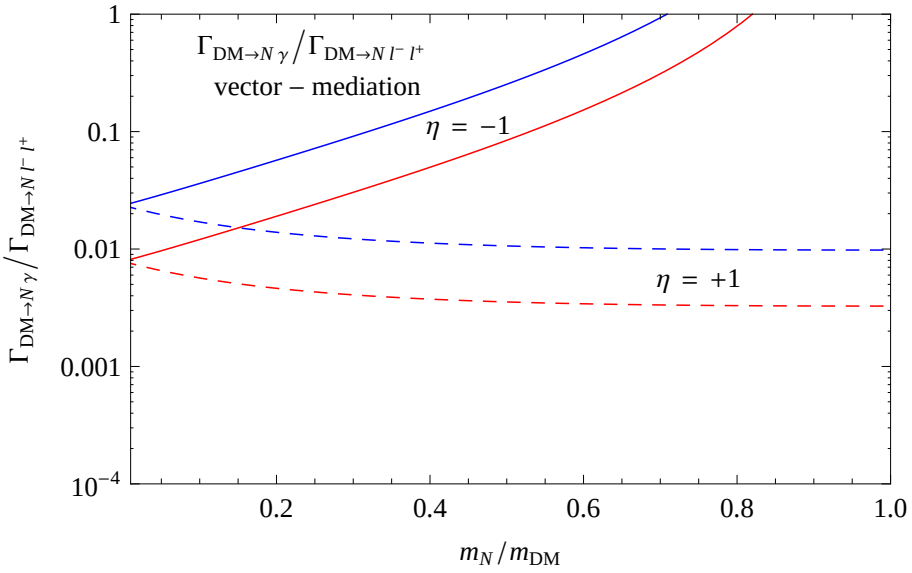

Figure 7.4: Ratio of the decay rates $\Gamma(\psi_{\rm DM} \to \gamma N)/\sum_\ell \Gamma(\psi_{\rm DM} \to \ell^+\ell^- N)$ for decay mediated by a heavy vector. Otherwise, the four cases are identical to the ones shown in Fig. 7.3.

7.3 Radiative Decay of Scalar Dark Matter

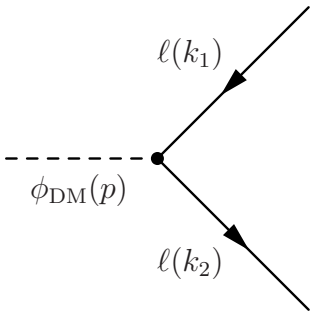

Figure 7.5: Tree-level decay of scalar dark matter.

We now consider the case that the dark matter particle is a (pseudo-)scalar which we denote by $\phi_{\rm DM}$. In this case, the symmetries allow for the decay into a pair of charged leptons at tree level, $\phi_{\rm DM} \to \ell^+\ell^-$. We describe this by an effective Lagrangian that describes a direct interaction between dark matter and charged leptons,

$$\mathcal{L}_{\rm eff} = -\bar{\ell}\left[\lambda^L_{\ell\phi} P_L + \lambda^R_{\ell\phi} P_R\right] \ell\, \phi_{\rm DM} + \text{h.c.}\,. \tag{7.43}$$

If the dark matter particle is a parity eigenstate, one has $\lambda^L_{\ell\phi} = \lambda^R_{\ell\phi}$ for a scalar and $\lambda^L_{\ell\phi} = -\lambda^R_{\ell\phi}$ for a pseudo-scalar.

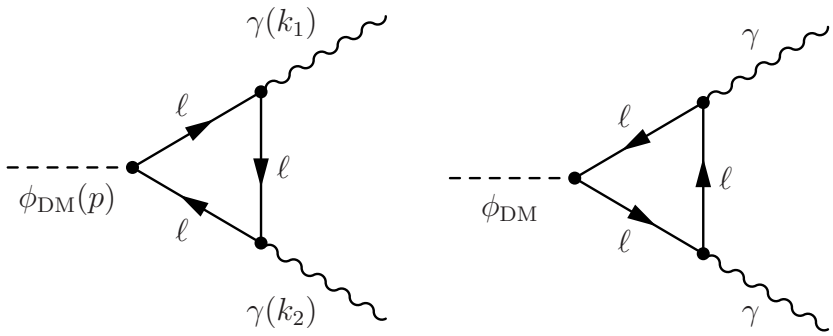

Figure 7.6: Diagrams contributing to the two-body decay of scalar dark matter into two photons at the one-loop level.

7.3.1 The Decay $\phi_{\rm DM} \to \ell^+\ell^-$

The effective Lagrangian (7.43) will give rise to the tree-level decay shown in Fig. 7.5. The corresponding decay width is

$$\Gamma\left(\phi_{\rm DM} \to \ell^+\ell^-\right) = \frac{1}{16\pi\, m_{\phi_{\rm DM}}} \left|\mathcal{M}\right|^2 \sqrt{1 - \frac{4m_\ell^2}{m_{\phi_{\rm DM}}^2}}, \tag{7.44}$$

where $m_{\phi_{\rm DM}}$ and m_ℓ are the mass of the dark matter and the charged leptons, respectively, and the amplitude is given by

$$\left|\mathcal{M}\right|^2 = m_{\phi_{\rm DM}}^2 \left(\left|\lambda_{\ell\phi}^L\right|^2 + \left|\lambda_{\ell\phi}^R\right|^2\right) - 2m_\ell^2 \left|\lambda_{\ell\phi}^L + \lambda_{\ell\phi}^R\right|^2 . \tag{7.45}$$

Thus, in the case of equal left- and right-handed couplings, $\lambda_{\ell\phi}^L = \lambda_{\ell\phi}^R \equiv \lambda_{\ell\phi}$, one gets

$$\Gamma\left(\phi_{\rm DM} \to \ell^+\ell^-\right) = \frac{|\lambda_{\ell\phi}|^2}{8\pi} m_{\phi_{\rm DM}} \left(1 - \frac{4m_\ell^2}{m_{\phi_{\rm DM}}^2}\right)^{3/2} . \tag{7.46}$$

For $m_\ell \ll m_{\phi_{\rm DM}}$ this corresponds to a lifetime

$$\tau_{\phi_{\rm DM}\to\ell^+\ell^-} \simeq 2 \times 10^{26}\,{\rm s} \left(\frac{10^{-26}}{|\lambda_{\ell\phi}|}\right)^2 \left(\frac{1\,{\rm TeV}}{m_{\phi_{\rm DM}}}\right) . \tag{7.47}$$

7.3.2 The Decay $\phi_{\rm DM} \to \gamma\gamma$

By combining the external lepton lines into a loop, decays into two monochromatic photons radiated off the charged lepton loop are induced at the quantum level (see Fig. 7.6).

For equal left- and right-handed couplings, $\lambda_{\ell\phi}^L = \lambda_{\ell\phi}^R \equiv \lambda_{\ell\phi}$, and in the limit $m_\ell \ll m_{\phi_{\rm DM}}$ (see Appendix B.2 and [302, 303]),

$$\Gamma(\phi_{\rm DM} \to \gamma\gamma) = \frac{m_{\phi_{\rm DM}}^3}{16\pi} \left(\frac{e^2}{16\pi^2}\right)^2 \left|\sum_\ell \frac{\lambda_{\ell\phi}}{m_\ell} A_f(\tau_\ell)\right|^2 , \tag{7.48}$$

where for the relevant limit $\tau \gg 1$ one has

$$A_f(\tau) \simeq \frac{1}{\tau}\left\{2 - \frac{1}{2}\left(\ln(4\tau) - i\pi\right)\right\}. \tag{7.49}$$

Thus, when taking only one lepton species into account, we obtain for the ratio between the decay into photons and charged leptons

$$\begin{aligned}\frac{\Gamma(\phi_{\rm DM} \to \gamma\gamma)}{\Gamma(\phi_{\rm DM} \to \ell^+\ell^-)} &\simeq \frac{\alpha_{\rm em}^2}{2\pi^2}\frac{m_\ell^2}{m_{\phi_{\rm DM}}^2}\left|2 - \frac{1}{2}\left(\ln(4\tau_\ell) - i\pi\right)^2\right|^2 \\ &\simeq 10^{-9}\left(\frac{m_\ell}{106\ \text{MeV}}\right)^2\left(\frac{1\ \text{TeV}}{m_{\phi_{\rm DM}}}\right)^2 .\end{aligned} \tag{7.50}$$

We see that for scalar dark matter, the decay into two photons is highly suppressed by the factor $m_\ell^2/m_{\phi_{\rm DM}}^2$ compared to the decay into a pair of charged leptons. In addition to this helicity-suppression factor, there appears a factor $\alpha_{\rm em}^2/\pi^2$ as opposed to $\alpha_{\rm em}/\pi$ for fermionic dark matter, since the loop contains two photon vertices, and both the tree-level and one-loop decays are two-body decays. The same suppression factors occur for pseudo-scalar dark matter and for the decay into massive gauge bosons. Thus, there appears to be no hope of detecting a gamma-ray line in this case. For more general expressions for the decay rates, see Appendix B.2.

7.4 Observational Constraints

The observation of a cosmic gamma-ray line at TeV energies would be a strong hint for the dark matter interpretation of the PAMELA/Fermi LAT $e^\pm$ anomalies. On the other hand, the non-observation of gamma-ray lines can be used to constrain the above leptophilic models, which induce these lines at one loop, as discussed above. The gamma-ray lines that originate from dark matter decay inside the Milky Way halo could be observed in the isotropic diffuse gamma-ray flux. Furthermore, lines may be observable in the flux from nearby galaxies and galaxy clusters.

At intermediate energies, satellite instruments such as Fermi LAT are a very sensitive probe for gamma-ray lines in the Galactic flux. At higher energies, Imaging Air Cherenkov Telescopes (IACTs) provide important information. For the future, the proposed Cherenkov Telescope Array (CTA) is expected to improve the flux sensitivity of current IACTs (MAGIC, H.E.S.S., VERITAS) by an order of magnitude. We put some emphasis on IACTs, since these instruments are capable of probing the high energy ranges relevant to the dark matter interpretation of PAMELA/Fermi LAT.

7.4.1 Fermi LAT Line Searches

The flux of monochromatic gamma rays from the decay of dark matter in the Milky Way halo is given by a line-of-sight integral over the dark matter distribution [103]. This component of the gamma-ray flux is explicitly given by

$$\frac{dJ_{\rm DM}^{\rm halo}}{dE} = \frac{\Gamma(\psi_{\rm DM} \to \gamma N)}{4\pi m_{\psi_{\rm DM}}}\,\delta\left(E_\gamma - E\right)\int_{\rm l.o.s.} d\vec{l}\,\rho_{\rm DM}^{\rm MW}(\vec{l})\,, \tag{7.51}$$

where $\Gamma(\psi_{\rm DM} \to \gamma N)$ denotes the partial decay width of dark matter particles for two-body decays involving a photon and a neutral particle N. When the neutral particle is massless, we will write ν instead of N in the following. Furthermore, $m_{\psi_{\rm DM}}$ is the mass of the dark matter particle, E_γ is the energy of the produced gamma-ray line as given by Eq. (7.15), while $\rho_{\rm DM}^{\rm MW}$ is the Milky Way's dark matter halo density profile. We adopt the Navarro-Frenk-White (NFW) profile here (see Eq. (1.13) and Table 1.1), with a local dark matter density of 0.4 GeV/cm^3 [122]. The gamma-ray flux from dark matter decay inside the Galactic halo has only a mild angular dependence and can be considered as isotropic for our purposes (for details on anisotropies in the Galactic gamma-ray flux from dark matter decay, see [103, 3]). The extragalactic contribution stemming from the decay of dark matter at cosmological distances is generally fainter than the Galactic flux, and we will neglect this component here.

The Fermi LAT collaboration has conducted a negative search for Galactic gamma-ray lines in the diffuse flux in the energy range from 30 to 200 GeV [304]. For the NFW halo profile we plot the resulting 2σ limits on the partial decay width corresponding to $\psi_{\rm DM} \to \gamma\nu$ in Fig. 7.7. Most interestingly, the Fermi LAT observations can constrain the dark matter decay into photons at the one-loop level if the total dark matter lifetime is of the order 10^{26} seconds. Thus, the Fermi LAT bounds on gamma-ray lines can be relevant for dark matter scenarios with $m_{\psi_{\rm DM}} \simeq 300$ – 400 GeV, which can provide a possible explanation for the rise in the positron fraction observed by PAMELA (see, *e.g.* [8]).

7.4.2 Imaging Air Cherenkov Telescopes

IACTs are important tools to constrain scenarios with dark matter masses in the multi-TeV range. One property of these instruments is that the atmospheric showers induced by cosmic-ray electrons or gamma rays cannot be distinguished easily, since both particle species initiate similar electro-magnetic cascades in the atmosphere. The large cosmic-ray electron flux hence comprises an irreducible background for high energy gamma-ray observations. Since the electron background, in contrast to the gamma rays, is expected to be very isotropic, it can be removed by calculating differences between fluxes that are observed in different neighboring regions of the sky. As a result, IACTs are best suited to observe localized sources, whereas diffuse signals such as those resulting from dark matter decay are more difficult to discern from the background unless they exhibit sharp spectral features. Constraints on the gamma-rays from decaying dark matter can be derived in two different ways. First, one can observe point-like sources like M31. Second, by using the observed electron + gamma-ray flux (potentially also contaminated by unrejected protons), one can derive upper limits on the Galactic halo signal from dark matter decay. If the statistics are good enough, one could even hope to see spectral features in the electron+gamma-ray flux, or translate their non-observation into bounds on the corresponding dark matter decay width. This will be described in the context of the CTA below.

The HEGRA collaboration has published constraints on the gamma-ray line flux from M31 [305]. These bounds can be converted into 99% C.L. limits on the decay width of dark matter into gamma-ray lines. HEGRA observed a region with an opening-angle of $\theta_{\rm obs} = 0.105^\circ$, corresponding to the inner 1.4 kpc region of M31. The expected flux of gamma rays from dark matter decay from M31 can be derived as follows. We define θ to be the angle between the line of sight and the ray that passes through our position and the center of M31. Each angle θ then corresponds to an "impact parameter" R. If D is the distance to the target

($D = 770$ kpc in case of M31), we have $R \simeq D\,\theta$. The gamma-ray flux from dark matter decay in M31 within the opening angle $\theta_{\rm obs}$ is then

$$\frac{dJ_{\rm DM}^{\rm M31}}{dE} = \frac{\Gamma(\psi \to \gamma N)}{4\pi m_{\rm DM}}\,\delta(E_\gamma - E)\,2\pi \int_0^{\theta_{\rm obs}} d\theta\,\sin\theta \int_{-\infty}^{\infty} ds\,\rho_{\rm DM}^{\rm M31}(\sqrt{s^2+R^2})\,, \qquad (7.52)$$

where the first integral is over the solid angle, whereas the second integral is over the line of sight. For the dark matter density profile of M31 we adopt the NFW profile with values given in [306], $\rho_{\rm c} = 2.0\,{\rm GeV}/\,{\rm cm}^3$ and $r_{\rm c} = 8.31$ kpc. The other profiles listed in [306] lead to similar constraints. The signal from decaying dark matter has a relatively large angular extent due to the linear dependence on the halo profile, and can leak into the off-region which is used to estimate the background fluxes of the IACT. The details of this effect depend on the details of the adopted off-region and are different for each observation. Here and below, we incorporate this effect simply by subtracting from Eq. (7.52) a flux corresponding to the dark matter-induced flux emitted at $\theta = 2\,\theta_{\rm obs}$. This should lead to correct bounds within a factor of two. Our results are shown in Fig. 7.7.

Upper limits on the gamma-ray flux from the Perseus galaxy cluster were presented by the MAGIC collaboration in [307]. For the density profile of the Perseus cluster we take the NFW profile with $r_{\rm c} = 384$ kpc and $\rho_{\rm c} = 0.04\,{\rm GeV\,cm}^{-3}$. The observational angle is $\theta_{\rm obs} = 0.15^\circ$, and the distance to the Perseus cluster is 78 Mpc [308]. The resulting 95% C.L. bounds are shown in Fig. 7.7.[4] Since the energy threshold of the MAGIC telescope is very low, we can constrain gamma-ray lines with energies down to 100 GeV.

#	Channel	η	$m_{\rm DM}$ [GeV]	E_γ [GeV]	m_N [GeV]	$\Gamma^{-1}_{\ell^+\ell^- N}$ [s]	$\frac{m_{\rm DM}}{\Gamma_{\psi\to\gamma N}}$ [s TeV]
1	$e_L^- e_L^+ N$	-1	1000	170	812.4	2.5×10^{26}	2.47×10^{27}
2	$e_L^- e_L^+ N$	$+1$	500	170	282.8	5×10^{26}	6.51×10^{29}
3	$e_L^- e_L^+ N$	-1	400	170	154.9	6.3×10^{26}	4.83×10^{28}
4	$\mu_L^- \mu_L^+ N$	-1	100000	5000	94868	4.5×10^{24}	2.87×10^{26}
5	$\mu_L^- \mu_L^+ N$	$+1$	15000	5000	8660	3×10^{25}	1.18×10^{30}
6	$\mu_L^- \mu_L^+ N$	-1	15000	5000	8660	3×10^{25}	3.06×10^{28}
7	$\mu_L \mu_R N$	$+1$	15000	5000	8660	3×10^{25}	3.42×10^{34}

Table 7.1: Benchmark scenarios. In the first three cases, the three-body decay produces only electrons. In the last four cases, the three-body decay produces muons. The gamma-ray line intensity of these scenarios is illustrated in Fig. 7.12.

The H.E.S.S. collaboration has published measurements of the electron flux at TeV energies [175, 217]. The measured electron flux may be contaminated with diffuse gamma rays by no more than $\approx 50\%$ [175]. This fact alllows the translation of the electron flux into upper bounds on gamma-ray lines from dark matter decay in the Galactic halo. For energies above 1 TeV, we derived $2\,\sigma$-bounds from the fluxes shown in Fig. 3 of [175]. For energies below 1 TeV, where the H.E.S.S. results overlap with the Fermi LAT measurements of the electron flux, 1σ-upper limits on the amount of diffuse gamma rays were derived by comparing the H.E.S.S. and the Fermi LAT electron fluxes in [309]. These upper limits can also be used as bounds on gamma-ray lines. Our results are shown in Fig. 7.7.

[4] We take the limits corresponding to $\Gamma = -2.5$ from Table 4 in [307].

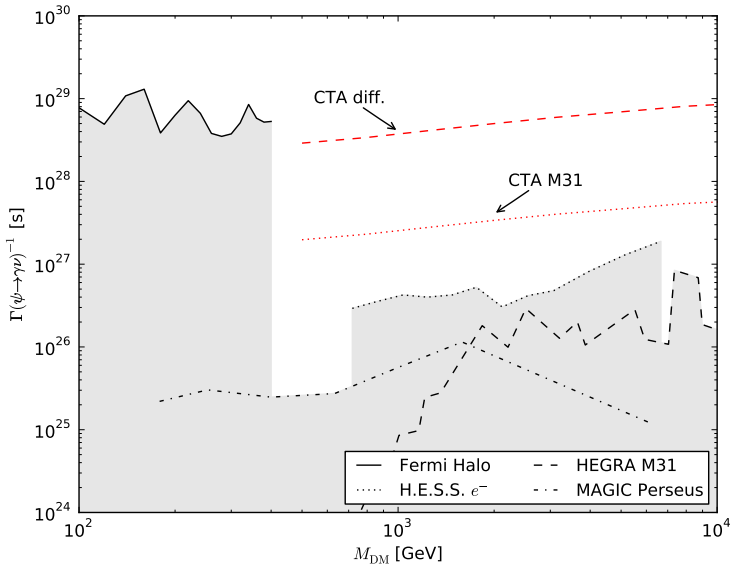

Figure 7.7: Lower bounds on the inverse decay width of dark matter decaying into gamma-ray lines via $\psi_{\rm DM} \to \gamma\nu$ are shown as black lines. The bounds on this decay channel come from line searches in M31 by HEGRA, from line searches in the diffuse flux by Fermi LAT and from observations of the Perseus cluster by MAGIC. Further bounds can be derived from the $(\gamma+)e^-$ observations of H.E.S.S. Our estimates of the reach of the future CTA in measurements of the flux from M31 or spectral variations in the diffuse $\gamma + e^-$ flux are shown as red lines.

Prospects for the CTA. We will now briefly discuss observational prospects for the future Cherenkov Telescope Array (CTA, see [310] for a recent discussion). The expected $2\,\sigma$-limit from M31 that the CTA could produce can be roughly estimated by

$$\langle J^{\rm M31}_{\rm DM}\rangle_{\rm on} \lesssim \frac{\max(2\sqrt{N_{\rm on}}, 3.1)}{T A_{\rm eff}}\,, \tag{7.53}$$

where $N_{\rm on}$ denotes the number of measured events in the on-region, T is the measurement time, $A_{\rm eff}$ denotes the effective area of the instrument (we take $A_{\rm eff} \approx 2\,{\rm km}^2$ at 5 TeV, and let it scale with the energy as in [311], Fig. 17a), and $\langle J^{\rm M31}_{\rm DM}\rangle_{\rm on}$ is the gamma-ray flux from M31 averaged over the on-region. As on-region, we take a circle with 1.0° radius around the center of M31, and for the off-region we assume that the solid-angle of the off-region is much larger than the on-region, $\Omega_{\rm off} \gg \Omega_{\rm on}$. If we assume that only the background is observed, and no signal is coming from M31, $N_{\rm on}$ can be estimated by

$$\bar{N}_{\rm on} = \Omega_{\rm on} T A_{\rm eff} (J_{e^-} + \varepsilon_{\rm r} J_p)\,. \tag{7.54}$$

Here, J_{e^-} and J_p denote the cosmic-ray electron and proton fluxes, respectively, and $\varepsilon_{\rm r}$ is the rejection factor of protons. Fluxes have to be integrated over an energy range that corresponds to the energy resolution of the detector (around 10%, taken from [310], Fig. 23, scenario E).

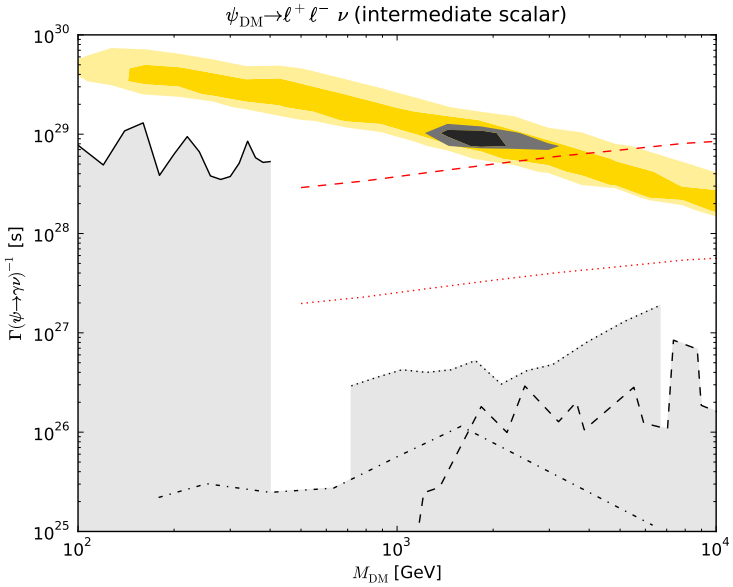

Figure 7.8: Same as Fig. 7.7. In addition, the orange and gray shaded regions show the parts of the parameter space that are relevant for the dark matter explanation of the PAMELA/Fermi $e^{\pm}$ anomalies with the flavor-democratic decay channel $\psi_{\rm DM} \to \ell^+\ell^-\nu$. The intermediate particle is assumed to be a scalar, in which case the branching ratio into monochromatic photons can be as large as $\mathrm{BR}(\psi_{\rm DM} \to \gamma\nu) \simeq 3 \times 3\alpha_{\rm em}/(8\pi)$, which we assume here.

For the cosmic-ray electron and proton fluxes at high energies we take

$$\frac{dJ_{e^-}}{dE} = 1.17 \times 10^{-11} \left(\frac{E}{\mathrm{TeV}}\right)^{-3.9} \mathrm{cm}^{-2}\,\mathrm{s}^{-1}\,\mathrm{sr}^{-1}\,\mathrm{GeV}^{-1}\,, \tag{7.55}$$

from [175], and

$$\frac{dJ_p}{dE} = 8.73 \times 10^{-9} \left(\frac{E}{\mathrm{TeV}}\right)^{-2.7} \mathrm{cm}^{-2}\,\mathrm{s}^{-1}\,\mathrm{sr}^{-1}\,\mathrm{GeV}^{-1}\,, \tag{7.56}$$

from [311], respectively, in agreement with the cosmic-ray measurements. Furthermore, at energies below 1 TeV, the electron flux becomes somewhat harder with a spectral index of $\simeq -3.1$, and we replace Eq. (7.55) with a flux fitting the results of [216] in this energy regime. Taking into account also other cosmic-ray species beside the protons would only have minor impact on our results. The proton rejection factor is set to $\varepsilon_{\rm r} \approx 10^{-2}$ [310, 311], and we use as observational time of M31 the value $T = 20\,\mathrm{h}$. Our estimates for the limits that the CTA could produce from M31 observations in the future are shown in Fig. 7.7 by the lower dashed line. They are almost two orders of magnitude better than the limits derived from the HEGRA observation. This is mainly due to the increased effective area of CTA, but also due to the larger on-region that we adopted in our estimates. For decaying dark matter it is not optimal to search for point-source signals, as was done in the HEGRA analysis, for example. Using a larger on-region typically leads to better results.

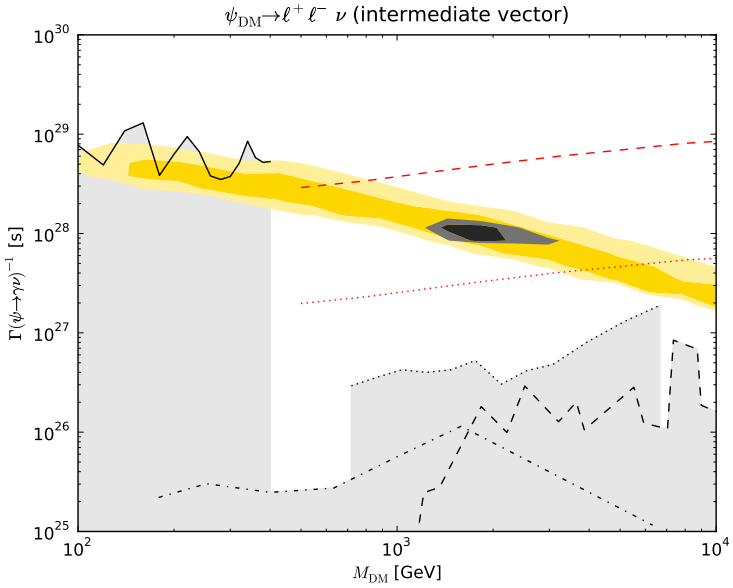

Figure 7.9: Same as Fig. 7.8, but assuming that the intermediate particle is a vector, in which case the branching ratio into monochromatic photons can be as large as $\mathrm{BR}(\psi_{\rm DM} \to \gamma\nu) \simeq 3 \times 27\alpha_{\rm em}/(8\pi)$, which we assume here.

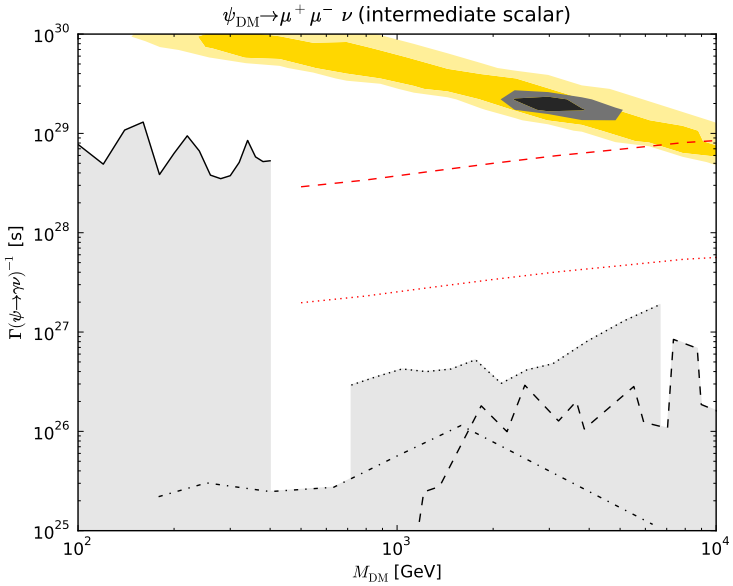

Figure 7.10: Same as Fig. 7.8, but for decay into $\psi_{\rm DM} \to \mu^+\mu^-\nu$. The intermediate particle is assumed to be a scalar, leading to a maximal branching ratio of $\mathrm{BR}(\psi_{\rm DM} \to \gamma\nu) \simeq 3\alpha_{\rm em}/(8\pi)$, which we assume here.

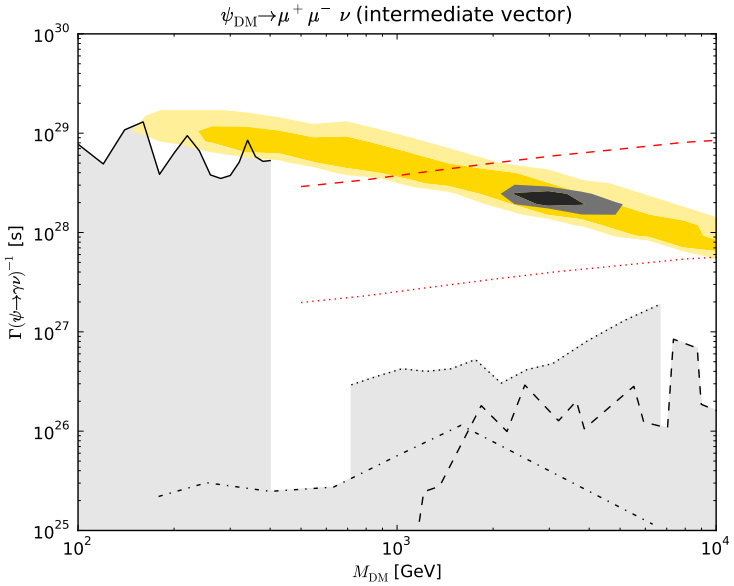

Figure 7.11: Same as Fig. 7.8, but for decay into $\psi_{\rm DM} \to \mu^+\mu^-\nu$. The intermediate particle is assumed to be a vector, leading to a maximal branching ratio of $\mathrm{BR}(\psi_{\rm DM} \to \gamma\nu) \simeq 27\alpha_{\rm em}/(8\pi)$, which we assume here.

Instead of using the spatial variations of the observed cosmic-ray flux to derive constraints on dark matter decay in extragalactic sources, one can also derive constraints from the non-observation of spectral line features in the diffuse flux, which could come from dark matter decaying into gamma-ray lines in the Galactic halo. In this case it is best to consider data from large fractions of the sky, to maximize the statistics. The expected "halo"-bound that the CTA will presumably reach then follows from

$$\langle J_{\rm DM}^{\rm halo} \rangle_{\rm sky} \leq \frac{2\sqrt{N}}{T A_{\rm eff} \Omega}\,, \tag{7.57}$$

where $\langle J_{\rm DM}^{\rm halo} \rangle_{\rm sky}$ denotes the gamma-ray flux coming from dark matter decaying in our Galactic halo, averaged over all angles. We assume that the data will be good enough to estimate the background by fitting a power-law to the observed flux at energies close to the line, similar to the analysis in [304], and we neglect the statistical uncertainties in the background estimate.[5] In Eq. (7.57), N is the total number of observed events, including electrons, gamma-rays and protons that pass the cuts. The region Ω is taken to be as large as possible to maximize the statistics (we assume $\Omega = \pi(3^\circ)^2$), and as observational time we take $T = 1000$ h. As above, we integrate over energy bands which correspond to the anticipated energy resolution of CTA. Our resulting estimates for the bounds that CTA could obtain observing the diffuse flux are shown in Fig. 7.7 by the upper dashed line. As can be seen from this figure, the bounds on gamma-ray lines from dark matter decay that can be put by looking at spectral variations in

[5]Note that this is different from our treatment of the H.E.S.S. electron flux, where we only required that the predicted line signal is below the observed fluxes, without any attempt to subtract a power-law background.

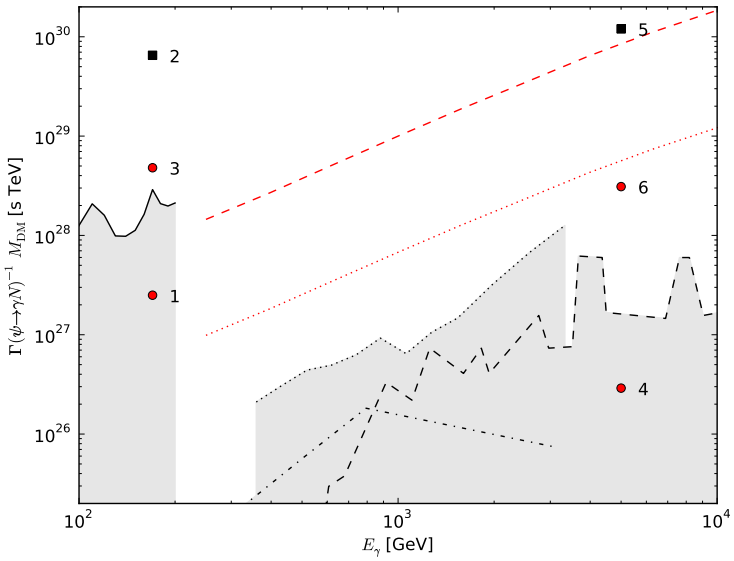

Figure 7.12: Same as Fig. 7.7, but with different scaling of the axes to allow for non-vanishing m_N. The black squares and red dots show the predictions for the different benchmark scenarios summarized in Table 7.1. Black squares correspond to scenarios with $\eta = +1$, while red dots correspond to $\eta = -1$. The last benchmark point in Table 7.1 lies outside of the shown parameter region.

the observed diffuse fluxes can be even stronger than the ones that can be derived from flux limits on point-like sources like M31.

7.4.3 Discussion

The case $m_N \to 0$. We first discuss the case where dark matter decays into a photon and a massless particle. In Fig. 7.7 we present a collection of the lower bounds on the inverse decay width for two-body decays into a monochromatic photon and a massless particle as determined by the methods described in the previous subsection. For dark matter masses between 100 and 400 GeV, the line searches in the diffuse Galactic flux by the Fermi LAT constitute the strongest constraints. At higher energies, Cherenkov telescopes provide important information. As far as constraints from particular sources are concerned, we show the constraints from HEGRA observations of M31 and MAGIC observations of the Perseus cluster. We also plot the constraints from the diffuse electron flux observed by H.E.S.S. Lastly, we show our estimates for the reach of the future CTA which could improve current limits by almost two orders of magnitude at energies above a few hundred GeV.

In Fig. 7.8 we show the same constraints together with shaded regions indicating the part of the parameter space relevant to PAMELA and Fermi for the gamma-ray lines induced by the decay $\psi_{\rm DM} \to \ell^+\ell^-\nu$. The orange regions correspond to the fit to the positron fraction as measured by PAMELA, whereas the dark gray regions correspond to the fit to the total $e^\pm$

flux as measured by Fermi LAT. In both cases, the lighter shades indicate the 5σ confidence level around the best-fit point, while the darker shades indicates the 3σ confidence level. We only regard the data points above 10 GeV, which are not significantly affected by solar modulation. For the background fluxes of secondary electrons and positrons, we assume the "model 0" backgrounds [218] as parametrized in Chapter 4. In the energy range of interest, we assume that the primary electron flux is given by a simple power law. At each point in the $(m_{\rm DM}, \tau_{\rm DM})$-plane, we then allow the power-law index of the primary electron flux to vary between -3.0 and -3.3, whereas the normalization is fitted to the data. We find that the relevant parameter space is not constrained by current instruments, but could be constrained by CTA in the future. The same plot is shown in Fig. 7.9, but assuming that the decay is mediated by an intermediate vector particle, in which case the branching ratio can be as large as $3 \times 27\alpha_{\rm em}/(8\pi)$, which we assume in the figure. This is about an order of magnitude larger than in the case of mediation by a scalar, and one can see that in this case the CTA can indeed constrain a significant part of the parameter space relevant to the dark matter interpretations of PAMELA and Fermi. Analogously, in Figs. 7.10, 7.11 we show the corresponding plots for the lines induced by the decay $\psi_{\rm DM} \to \mu^+\mu^-\nu$, in the cases of an intermediate scalar and an intermediate vector particle, respectively. In these scenarios the expected line signal is somewhat weaker.

The case $m_N \sim m_{\psi_{\rm DM}}$. Let us now turn to the case where the mass m_N of the neutral fermion produced in the tree-level decay $\psi_{\rm DM} \to \ell^+\ell^- N$ is comparable in size to the dark matter mass itself. This possibility can occur, for example, within the leptophilic model discussed in Section 7.2.2, where $\psi_{\rm DM}$ is the hidden gaugino of an unbroken $U(1)$-symmetry, and N is a neutralino [100]. As we showed in Section 7.2.2, the decay channel $\psi_{\rm DM} \to \gamma N$ is kinematically enhanced compared to the three-body decay when $m_N \sim m_{\psi_{\rm DM}}$, provided that $\psi_{\rm DM}$ and N have opposite CP parities ($\eta = -1$). Thus, such scenarios can be tested particularly well via the loop-induced gamma-ray line signal. In order to infer the observational constraints, it is convenient to consider the ratio $m_{\psi_{\rm DM}}/\Gamma(\psi_{\rm DM} \to \gamma N)$, which determines the magnitude of the observable flux. For the case of scalar-mediated decay, and purely chiral couplings, it is given by (see Eq. (7.31))

$$\Gamma(\psi_{\rm DM} \to \gamma N)^{-1} m_{\psi_{\rm DM}} \;\approx\; \frac{1}{R^{\rm chir}} \left(\frac{\Gamma(\psi_{\rm DM} \to \ell^+\ell^-)^{-1} m_{\psi_{\rm DM}}}{10^{26}\,{\rm s} \times 2.5\,{\rm TeV}} \right) \times \\ \times \begin{cases} 3 \times 10^{29}\,{\rm s\,TeV} & \text{for } m_N \to 0,\ \eta = \pm 1 \\ 7 \times 10^{29}\,{\rm s\,TeV} & \text{for } m_N \to m_{\psi_{\rm DM}},\ \eta = +1 \\ 1.4 \times 10^{28}\,{\rm s\,TeV} \left(\frac{2E_\gamma}{m_{\psi_{\rm DM}}}\right)^2 & \text{for } m_N \to m_{\psi_{\rm DM}},\ \eta = -1 \end{cases} , \tag{7.58}$$

where $R^{\rm chir} = 1$ for three-body decays into a single lepton flavor, and $R^{\rm chir} = 3$ for flavor-democratic three-body decays. In the case of an intermediate vector, the right-hand side is smaller by a factor of nine, implying a nine times larger gamma-ray flux. From the last line, it is apparent that in the case of opposite CP parities, the monochromatic gamma-ray flux is enhanced for large values of $m_{\psi_{\rm DM}}$, when keeping the photon energy E_γ fixed. Note that a similar enhancement of the decay channel $\psi_{\rm DM} \to Z^0 N$, which may also be induced at the loop-level, could lead to complementary constraints from the antiproton flux produced by the fragmentation of the Z-boson, which we do not discuss here. In order to illustrate this result, we consider a number of benchmark scenarios for which $m_{\psi_{\rm DM}}$ and m_N are of comparable size,

with parameters chosen as shown in Table 7.1. All the benchmark scenarios reproduce the PAMELA positron data, and all except scenarios 1, 2 and 3 additionally reproduce the electron spectrum measured by Fermi. Note that the maximum lepton energy in the three-body decay $\psi_{\rm DM} \to \ell^+\ell^- N$ coincides with the energy of the monochromatic photons, $E_{\rm max} = E_\gamma$.

The gamma-ray line signal induced by the one-loop decay $\psi_{\rm DM} \to \gamma N$ is shown in Fig. 7.12 for the various benchmark scenarios. Clearly, the scenarios 1 and 4 are in conflict with the gamma-ray line searches performed by Fermi and HEGRA, respectively. Thus, despite the fact that the dark matter couples only to leptons at tree-level, the gamma-ray line signal induced by one-loop corrections has an intensity that is detectable by present gamma-ray telescopes. In other words, scenarios 1 and 4 can be ruled out as possible explanations of the high-energy positron excess, because the loop-induced radiative decay produces a gamma-ray line that should have been already detected. This shows that the higher-order corrections are indeed relevant and have to be taken into account. In contrast, the other benchmarks are in agreement with present bounds on gamma-ray lines. For example, in scenario 3 the partial lifetime for the radiative decay is larger compared to scenario 1, and lies slightly above the current Fermi bounds. Scenario 6 can be tested in the future by the CTA. Since there is no kinematic enhancement of the decay $\psi_{\rm DM} \to \gamma N$ in the case $\eta = +1$, the intensity of the gamma-ray line is comparably weak in scenarios 2 and 5. For example, scenario 5 differs from 6 just by the sign of η, but is much more difficult to probe by the CTA. Finally, for benchmark point 7, we assume that the couplings of the leptons to $\psi_{\rm DM}$ and to N have opposite chirality, in which case the loop is strongly suppressed and there is no hope of detecting a gamma-ray line signal.

7.5 Conclusions

We have analyzed the radiative decay of dark matter particles in view of the leptonic cosmic-ray anomalies reported by PAMELA and Fermi LAT. Assuming an effective description of leptophilic dark matter decay, we have pointed out that the lines induced at the quantum level may be observable and can be used to constrain models of decaying dark matter. In the case of scalar dark matter, two-body decays into photons are strongly helicity-suppressed and thus unobservable. In the case that the dark matter particles carry spin 1/2, however, the radiative decay rate is typically suppressed compared to the tree-level decays by some two to three orders of magnitude. Interestingly, the corresponding partial lifetimes for decays into monochromatic photons can then be in the observable range, in particular for dark matter masses of a few hundred GeV, where stringent constraints from Fermi LAT apply. Thus, in some cases the loop-induced gamma-ray line yields constraints that can be competitive with the constraints on charged cosmic rays. At higher energies, constraints from Cherenkov telescopes exist. At present, these constraints are only relevant for certain scenarios for which the radiative two-body decay is kinematically enhanced compared to the three-body decay channel. However, we have pointed out that the proposed CTA should be able to improve on the existing bounds significantly and probe a relevant part of the parameter space which is presently unconstrained.

Chapter 8

Neutrino Signals from Decaying Dark Matter

In this chapter, which is based on the publication [2], we investigate different neutrino signals from the decay of dark matter particles to determine the prospects for their detection, and more specifically if any spectral signatures can be disentangled from the background in present and future neutrino observatories. If detected, such a signal could bring an independent confirmation of the dark matter interpretation of the dramatic rise in the positron fraction above 10 GeV recently observed by the PAMELA satellite experiment and offer the possibility of distinguishing between astrophysical sources and dark matter decay or annihilation. In combination with other signals, it may also be possible to distinguish among different dark matter decay channels.

8.1 Introduction

As explained in Chapter 4 the decay of dark matter particles in the Galactic halo is a viable explanation of the observed electron anomalies, and it is worthwhile trying to confirm or exclude this possibility by a complementary examination of other indirect detection channels, including neutrinos [9, 105, 106, 107, 209, 281, 312]. Neutrinos in this context have two clear advantages. First, they are unaffected by magnetic fields and thus, like photons, allow to reconstruct the direction of their origin; therefore they would offer a way to distinguish between the cases of annihilating and decaying dark matter, as well as pulsar interpretations of the signal (even assuming that the pulsars produce also neutrinos in the energy range considered). Second, they are typically produced along with or from the decay of the charged leptons in many "leptophilic" decaying dark matter models [7, 202, 210, 283, 313, 314]. In such cases, therefore, the flux of neutrinos is correlated with the other cosmic-ray signals, and their spectrum may give direct information on the dark matter decay channel. In particular, choosing the mass and lifetime of the dark matter particle such as to yield a good agreement with the PAMELA positron excess, one can directly predict the rates for the corresponding neutrino signal and look for it in present and future experiments. These are the two advantages we will try to exploit in this chapter.

Nevertheless, neutrinos also suffer from some clear disadvantages with respect to other indirect detection channels: The large atmospheric neutrino background makes it difficult

to disentangle any signal up to TeV energies for the lifetimes indicated by the cosmic-ray anomalies mentioned above. A further disadvantage is the necessity of very large detectors to measure the comparably small neutrino fluxes expected from dark matter decay. Fortunately, new large neutrino detectors, namely IceCube and possibly KM3NeT, will become fully operational in the near future and may allow to detect even the small signals we discuss here.

This chapter is organized as follows. In Section 8.2 we will discuss the neutrino flux expected from decaying dark matter in our Galaxy and compare it with the one from dark matter annihilation in order to discuss the best strategy for the detection of the signal in these two cases. In Section 8.3, we will present the spectral signatures for a number of different dark matter decay modes. In Section 8.4 we will give the present bounds from neutrino experiments and the expected rates for present and future neutrino detectors. We will also discuss the prospects for distinguishing between different neutrino spectra in case a signal is detected. We will finally present our conclusions in Section 8.5.

8.2 Neutrino Fluxes

We concentrate in this section on the neutrino flux expected from the dark matter in the Milky Way halo, since on one hand it is the dominant source, and on the other hand it has a nontrivial directionality that may be exploited, as in the case of gamma rays [103, 3], to disentangle the different hypotheses of dark matter decay versus annihilation. In addition, an isotropic extragalactic component is expected from unresolved cosmological sources, which in the case of decaying dark matter is of the same order of magnitude as the halo contribution, so that it may increase the overall signal by a factor of two or so. This extragalactic component is expected to be negligible in the case of dark matter annihilation.

The differential flux of neutrinos from decaying dark matter is given by the following integral along the line of sight:

$$\frac{dJ_{\rm halo}}{dE} = \frac{1}{4\pi\,\tau_{\rm DM} m_{\rm DM}}\,\frac{dN_\nu}{dE}\int_{\rm l.o.s.}\rho_{\rm DM}(\vec{l})\,d\vec{l}\,, \tag{8.1}$$

where $\tau_{\rm DM}$ and $m_{\rm DM}$ are the lifetime and the mass of the decaying particle, dN_ν/dE is the neutrino energy spectrum from the decay and $\rho_{\rm DM}$ is the dark matter density in the halo. Adopting for $\rho_{\rm DM}$ the NFW density profile, as defined in Eq. (1.13) and Table 1.1, we obtain for the averaged full-sky flux

$$\left\langle\frac{dJ_{\rm halo}}{dE}\right\rangle = 1.3\times10^{-8}\,({\rm cm^2\,s\,sr})^{-1}\left(\frac{10^{26}\,{\rm s}}{\tau_{\rm DM}}\right)\left(\frac{1\,{\rm TeV}}{m_{\rm DM}}\right)\frac{dN_\nu}{dE}\,, \tag{8.2}$$

assuming a local halo density $\rho_\odot = 0.3\,{\rm GeV\,cm^{-3}}$ and a solar distance from the Galactic center $R_\odot = 8.5\,{\rm kpc}$. The numerical result is only weakly dependent on the halo parameters and the profile. The flux is inversely proportional to the product of the dark matter particle mass and lifetime. Thus, for a fixed lifetime the flux is inversely proportional to the dark matter mass $m_{\rm DM}$ due to the lower number density of dark matter particles for higher masses.

After the neutrinos are produced in the decay or annihilation of dark matter particles, they travel in straight lines through the Galaxy, essentially without any interactions. The only

modifications to the fluxes during this time are due to flavor oscillations [315]. In fact, using the experimental best-fit values for the neutrino mixing angles, $\sin^2\theta_{12} = 0.304$, $\sin^2\theta_{23} = 0.5$ and $\sin^2\theta_{13} = 0.01$ [316], and neglecting possible CP-violating effects, the neutrino oscillation probabilities in vacuum are given by

$$\begin{aligned} P(\nu_e \leftrightarrow \nu_e) &= 0.56\,, \\ P(\nu_e \leftrightarrow \nu_\mu) = P(\nu_e \leftrightarrow \nu_\tau) &= 0.22\,, \\ P(\nu_\mu \leftrightarrow \nu_\mu) = P(\nu_\mu \leftrightarrow \nu_\tau) = P(\nu_\tau \leftrightarrow \nu_\tau) &= 0.39\,. \end{aligned} \tag{8.3}$$

Thus, a primary neutrino flux in a specific flavor is redistributed almost equally into all neutrino flavors during propagation and any flavor information is lost. On the other hand, this means that nearly the same signal is present in any flavor and may allow to choose the best channel for discovery according to the background and efficiency of the detector.

8.2.1 Background Fluxes

Let us now discuss the background for our neutrino signal. The main background for the observation of neutrinos in the GeV to TeV range are neutrinos produced in cosmic-ray interactions with the Earth's atmosphere. Here we use the atmospheric neutrino fluxes calculated by Honda *et al.* [317]. The theoretical uncertainty of these fluxes is estimated to be better than 25 % in the GeV to TeV range, while the uncertainty in the ratio of the different flavors is significantly smaller. We extend the atmospheric neutrino fluxes to energies above 10 TeV using the slopes given by Volkova *et al.* [318].

Conventional electron and muon neutrinos are directly produced from pion and kaon decays. While electron neutrinos are practically unaffected by neutrino oscillations due to the large oscillation length, muon neutrinos, particularly at low energies, can be converted into tau neutrinos and provide the dominant tau neutrino background at energies below 1 TeV. The conversion probability of muon neutrinos into tau neutrinos is given by

$$P(\nu_\mu \to \nu_\tau) \simeq \sin^2\left(3.05 \times 10^{-3}\,\frac{L\,(\mathrm{km})}{E_\nu\,(\mathrm{GeV})}\right). \tag{8.4}$$

In this expression, E_ν is the neutrino energy and L is their propagation length after being produced in the atmosphere, which is given by

$$L(\theta) = \sqrt{(R_\oplus \cos\theta)^2 + 2R_\oplus h + h^2} - R_\oplus \cos\theta\,, \tag{8.5}$$

with $R_\oplus \simeq 6.4 \times 10^3$ km being the Earth's radius and $h \simeq 15$ km the mean altitude at which atmospheric neutrinos are produced.

In addition to the conventional atmospheric neutrino flux from pion and kaon decays there is a prompt neutrino flux from the decay of charmed particles that are also produced in cosmic-ray collisions with the atmosphere. The prompt neutrinos have a harder spectrum than the conventional ones and therefore dominate at higher energies (roughly above 10 TeV for electron neutrinos and above 100 TeV for muon neutrinos). Since these contributions are not well understood and in any case subdominant in the energy range that is of interest here, we neglect them in the present study. On the other hand, the prompt tau neutrinos start

to dominate around 1 TeV (and at even smaller energies for downgoing neutrinos). Thus we include this contribution using the parametrization [319]

$$\log_{10}\left[E^3\,\frac{dJ_{\nu_\tau}}{dE}\,\Big/\left(\frac{\mathrm{GeV}^2}{\mathrm{cm}^2\,\mathrm{s}\,\mathrm{sr}}\right)\right] = -A + Bx - Cx^2 - Dx^3, \tag{8.6}$$

where $x = \log_{10}(E\,(\mathrm{GeV}))$, $A = 6.69$, $B = 1.05$, $C = 0.150$ and $D = -0.00820$. This parametrization is valid in the energy range of 100 GeV up to 1 PeV. However, we point out that compared to the conventional atmospheric neutrino flux, the prompt flux suffers from larger uncertainties.

Other neutrino backgrounds in the considered energy range are neutrinos produced in cosmic-ray interactions with the solar corona [320] and those produced in cosmic-ray interactions with the interstellar medium in the Milky Way [321]. While the former is subdominant in diffuse searches for all flavors [9] and can be excluded from the analysis by excluding neutrinos from the direction of the Sun, the latter represents an irreducible, ill-understood neutrino background for searches in the Galactic disc direction. In fact, the flux of Galactic neutrinos is expected to become comparable to the atmospheric electron neutrino background for the Galactic disc direction and energies in the TeV range.

8.2.2 General Detection Strategy and Use of Directionality

In view of the subdominant neutrino signals from dark matter decays it is important to devise strategies that reduce the background. In [9] it was proposed to use directionality in order to reduce the background in the tau neutrino channel. This is possible since the tau neutrino background at low energies comes mainly from the muon neutrino oscillation and is therefore strongly suppressed in the zenith direction. Some of the authors of [105, 106, 209, 107] propose instead to search for an enhanced muon neutrino signal only in the direction of the Galactic center. However, taking into account the typically low neutrino event rates, it is not always the best strategy to optimize the signal-to-background ratio. Instead, the statistical significance $\sigma = S/\sqrt{B}$ (number of signal events divided by the square root of the number of background events) is a better measure for comparing different detection strategies.

In Fig. 8.1 we show the significance of the signal as a function of the cone half angle around the Galactic center normalized to the significance of the full-sky observation. Here we assume a background that (practically) does not depend on Galactic coordinates like atmospheric neutrinos and neglect the contribution of Galactic neutrinos, which is subdominant in the case of muon neutrinos. We see clearly that for annihilating dark matter the best way to detect the signal is indeed looking towards the Galactic center: The cone half angle offering the best signal-to-square root of background ratio varies depending on the cuspiness of the profile, but it is always between $\sim 0^\circ$ (NFW) and 30° (isothermal). Note that in any case the gain of looking at the Galactic center is not very large for a cored profile like the isothermal one.

For the case of decaying dark matter on the other hand, the best strategy is to measure the full-sky signal and not concentrate on the region around the Galactic center. In fact the gain coming from the enhanced dark matter density is counteracted by the smallness of the collecting area and so the significance of the signal goes quickly to zero as a function of the

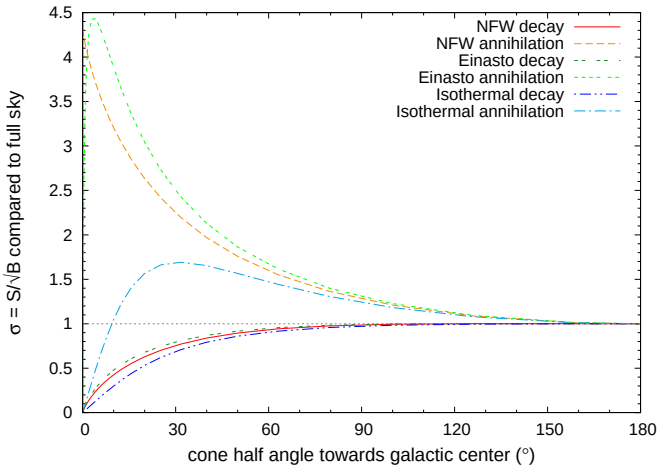

Figure 8.1: Significance of the signal as a function of the cone half angle towards the Galactic center normalized to the significance of the full-sky signal for annihilating/decaying dark matter depending on the different density profiles.

angle for any profile, even for cuspy profiles like the NFW profile. The observation of only a fraction of the sky around the Galactic center direction leads to an increase in the signal-to-background ratio, but not of the significance. We therefore conclude that for decaying dark matter there is no advantage in looking only at the Galactic center. The full-sky signal offers not only better statistics, but also a higher significance. Considering the directionality of the atmospheric background instead of the signal, another good strategy might be to exploit the fact that the flux from the zenith direction is (dependent on the energy) a few times smaller than from the horizontal direction. Assuming a signal that does not depend on the zenith angle, the observation of only a fraction of the sky around the zenith direction is again clearly leading to an increase in the signal-to-background ratio. Also in this case though, it turns out that the best value for the significance is achieved for a full-sky observation.

We can therefore conclude that exploiting the directionality of the signal or background, apart from the case of specific flavors like the tau neutrino discussed in [9], is not promising for the first detection of decaying dark matter. The largest rate and significance is achieved for a full-sky search, and this is the option we will discuss in the following. On the other hand, directionality offers a clear way to disentangle decaying dark matter from either annihilating dark matter, where looking into the Galactic center should give an increase in significance, or from point sources like dwarf galaxies, pulsars and supernova remnants.

8.3 Neutrino and Muon Spectra

The neutrino spectra depend on the decay channel of the dark matter particle. The simplest possibility is a direct decay into two neutrinos for a scalar particle or into $Z^0\nu$ for a fermion. Then the resulting spectrum is just a monochromatic line for the Galactic signal and an integral of the redshifted line from the extragalactic signal (and a continuum contribution from the fragmentation of the Z^0 boson in the case of decay into $Z^0\nu$). So for this case we

have the simple spectra

$$\frac{dN_\nu}{dE}\,(\mathrm{DM}\to X\nu) \propto \delta\left(E-\frac{m_{\mathrm{DM}}}{2}\right) + C_{\mathrm{l.o.s.}}\left(1+\frac{\Omega_\Lambda}{\Omega_{\mathrm{M}}}\left(\frac{2\,E}{m_{\mathrm{DM}}}\right)^3\right)^{-1/2}\left(\frac{2\,E}{m_{\mathrm{DM}}}\right)^{1/2}\Theta\left(E-\frac{m_{\mathrm{DM}}}{2}\right) \quad (8.7)$$
$$(+\ \text{continuum})\,,$$

where $X = Z^0, \gamma, \nu$ and we have assumed here that the mass of X is negligible. $C_{\mathrm{l.o.s.}}$ is the ratio of the extragalactic and the Galactic signal, which is a number of order one given by

$$C_{\mathrm{l.o.s.}} = \frac{\Omega_{\mathrm{DM}}\,\rho_c}{H_0\,\Omega_M^{1/2}}\left(\int_{\mathrm{l.o.s.}}\rho_{\mathrm{DM}}(\vec{l}\,)\,d\vec{l}\right)^{-1} \quad (8.8)$$

Another characteristic spectrum is that obtained from a three-body decay into three leptons $\ell^+\ell^-\nu$, which has the familiar triangular shape when plotted on a logarithmic axis.[1] In this case the expression for the extragalactic signal is more involved, but it still appears as a softer triangular shape which dominates at low energies, as can be seen from the change in slope for the three-body spectra in Figs. 8.2 and 8.3. We show here as an example the spectrum of the decay of a fermionic dark matter particle mediated by a heavy scalar particle, corresponding to a scalar-type 4-fermion interaction. Finally, a continuous neutrino spectrum is generated by any heavy particle that decays into neutrinos, like the muon, or fragments into charged pions, like the electroweak gauge bosons or the tau lepton. We use here as examples of continuum neutrino spectra, the spectra arising from the decay of a scalar particle into longitudinal gauge bosons similar to the Higgs decay and from the decay of a fermionic chiral lepton into $W^\pm\ell^\mp, Z^0\nu$. We use `PYTHIA 6.4` [249] to simulate the gauge boson fragmentation and the heavy leptonic decays.

The corresponding neutrino fluxes for these different types of spectra are shown in Figs. 8.2 and 8.3 for a scalar and a fermionic dark matter candidate, respectively, together with the expected atmospheric background and the data measured by the Fréjus [322], Super-Kamiokande [323], AMANDA-II [324, 325] and IceCube [326] experiments. We see that for a lifetime of the order of 10^{26} s, which is the order of magnitude suggested by the PAMELA excess, as explained in Chapter 4, the signal always lies below the measured background of muon neutrinos. The best signal-to-background ratio is achieved for the high-energy end of the spectrum, which gives information about the mass scale of the decaying particle. The neutrino spectra shown in Figs. 8.2 and 8.3 look rather distinctive, and an interesting question is whether they can be disentangled in a neutrino detector. We have to consider that neutrino detectors do not measure neutrinos directly, but the corresponding charged leptons or showers produced in the interactions of neutrinos with the intervening matter.

8.3.1 Neutrino Interactions

Since we are interested in neutrino energies much larger than nucleon masses, we only take into account deep inelastic neutrino–nucleon scattering. Neutrino–electron elastic scattering is subdominant in this energy range and will be neglected.

[1] This holds for the most common scenarios, where the decay is mediated by a heavy scalar or a heavy vector boson. In both cases the Michel parameter ρ is equal to 3/4, yielding the same neutrino energy spectrum.

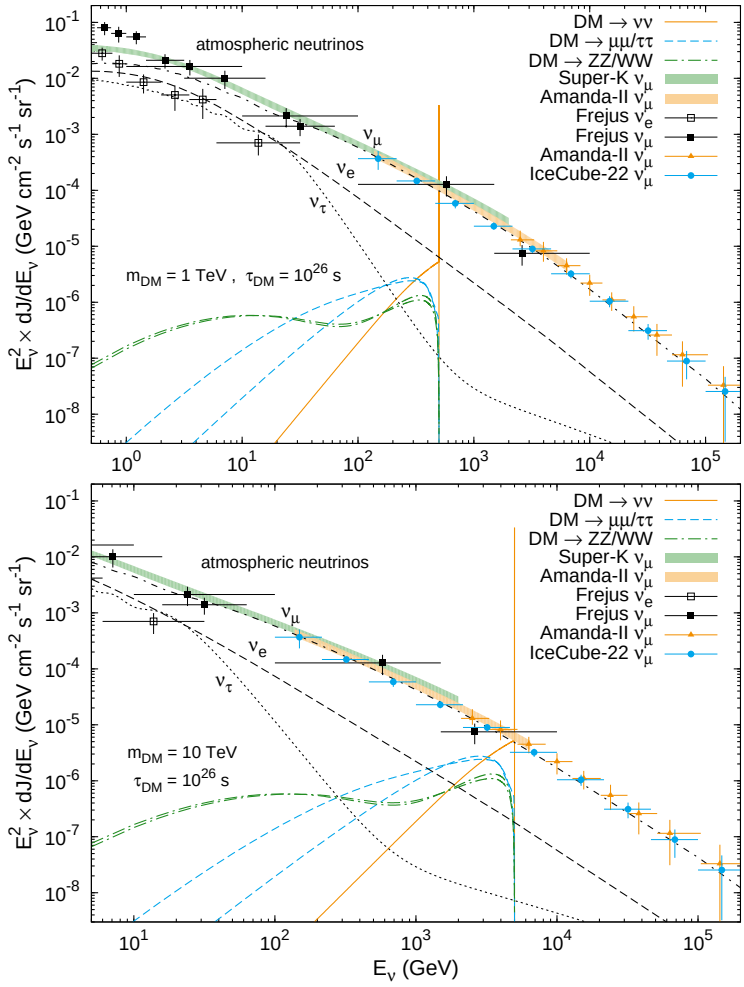

Figure 8.2: Neutrino spectra for different decay channels of a scalar dark matter candidate compared to the expected background of atmospheric neutrinos from Honda *et al.* [317] and the data of Fréjus [322], Super-Kamiokande [323], Amanda-II [324, 325] and IceCube [326]. The flux is computed for a dark matter mass of 1 TeV (*top*) or 10 TeV (*bottom*) and a lifetime of 10^{26} s. The line from the two-body decay into $\nu\bar{\nu}$ and the extragalactic contribution to this decay spectrum is easy to distinguish. The spectra from the decays of a dark matter candidate into $\mu^+\mu^-$, $\tau^+\tau^-$, Z^0Z^0 or $W^\pm W^\mp$ are softer at the endpoint. The low-energy tail of these decay channels is due to the muon/tau decay and $Z^0/W^\pm$ fragmentation. Due to the steeply falling atmospheric background the signal-to-background ratio at the endpoint of the decay spectra increases significantly for larger dark matter masses.

The cross-sections for deep inelastic scattering of (anti)neutrinos off nucleons at rest are given by

$$\begin{aligned}\frac{d\sigma^{\nu\,p,n}_{\mathrm{CC/NC}}(E_\nu, y)}{dy} &\simeq \frac{2\, m_{p,n}\, G_\mathrm{F}^2}{\pi}\, E_\nu \left(a^{\nu\,p,n}_{\mathrm{CC/NC}} + b^{\nu\,p,n}_{\mathrm{CC/NC}}\,(1-y)^2\right) \\ &\simeq 3.2\times 10^{-38}\,\frac{\mathrm{cm}^2}{\mathrm{GeV}}\, E_\nu \left(a^{\nu\,p,n}_{\mathrm{CC/NC}} + b^{\nu\,p,n}_{\mathrm{CC/NC}}\,(1-y)^2\right)\end{aligned} \tag{8.9}$$

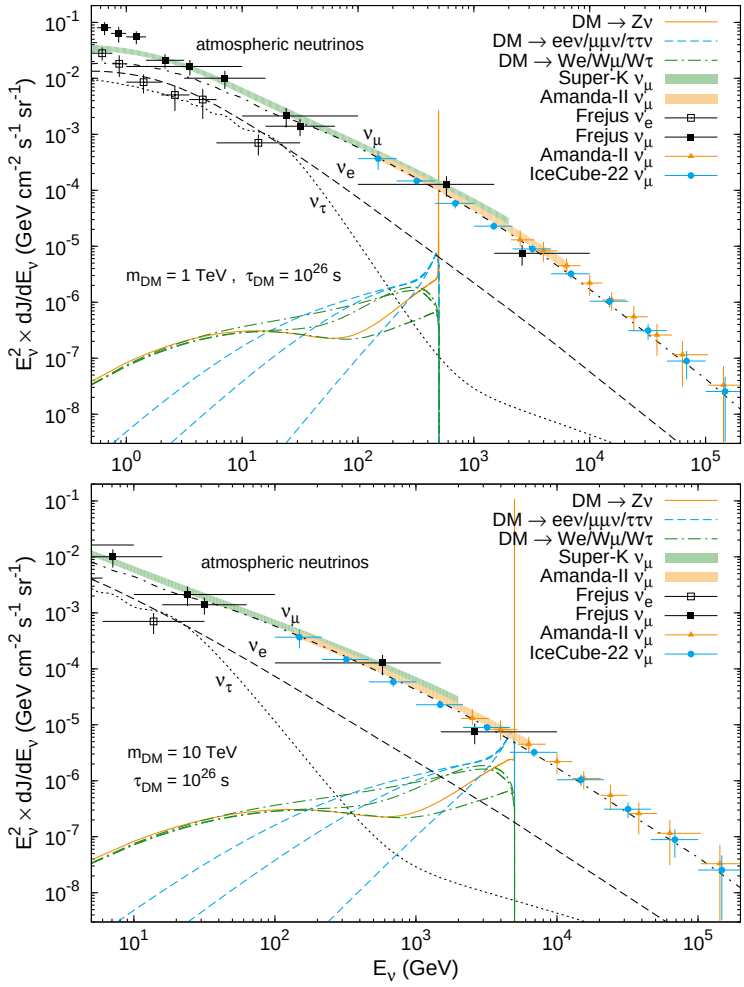

Figure 8.3: Neutrino spectra for different decay channels of a fermionic dark matter candidate compared to the expected background of atmospheric neutrinos from Honda *et al.* [317] and the data of Fréjus [322], Super-Kamiokande [323], Amanda-II [324, 325] and IceCube [326]. The flux is computed for a dark matter mass of 1 TeV (*top*) or 10 TeV (*bottom*) and a lifetime of 10^{26} s. The pure line and three-body decays are easy to distinguish and correspond to the line contained in $Z^0\nu$ and the decay into $e^+e^-\nu$. Note that the low-energy tail of $Z^0\nu$ and of the other leptonic three-body decays is due to the Z^0 fragmentation and muon/tau decay. Also shown are the cases of a pure continuum spectrum coming from the decay into $W^\pm\ell^\mp$. Due to the steeply falling atmospheric background the signal-to-background ratio at the endpoint of the decay spectra increases significantly for larger dark matter masses.

with $a_{\mathrm{CC}}^{\nu\,p,n} = 0.15,\, 0.25$, $b_{\mathrm{CC}}^{\nu\,p,n} = 0.04,\, 0.06$ and $a_{\mathrm{CC}}^{\bar{\nu}\,p,n} = b_{\mathrm{CC}}^{\nu\,n,p}$, $b_{\mathrm{CC}}^{\bar{\nu}\,p,n} = a_{\mathrm{CC}}^{\nu\,n,p}$ for charged-current interactions, and $a_{\mathrm{NC}}^{\nu\,p,n} = 0.058,\, 0.064$, $b_{\mathrm{NC}}^{\nu\,p,n} = 0.022,\, 0.019$ and $a_{\mathrm{NC}}^{\bar{\nu}\,p,n} = b_{\mathrm{NC}}^{\nu\,p,n}$, $b_{\mathrm{NC}}^{\bar{\nu}\,p,n} = a_{\mathrm{NC}}^{\nu\,p,n}$ for neutral-current interactions [315, 327]. The inelasticity y is given by

$$y = 1 - \frac{E_\ell}{E_\nu} \qquad \text{or} \qquad y \simeq \frac{E_{\mathrm{had}}}{E_\nu}\,, \tag{8.10}$$

where E_ℓ is the energy of the generated lepton and E_{had} is the energy of the generated hadronic shower. Eq. (8.9) holds only for neutrino energies up to the TeV region when the effect of

the massive gauge boson propagators cannot be neglected anymore. For higher energies the cross-sections are overestimated.

For the total neutrino–nucleon cross-sections one obtains

$$\sigma^{\nu\,p,n}_{\mathrm{CC/NC}}(E_\nu) \simeq \frac{2\,m_{p,n}G_{\mathrm{F}}^2}{\pi}\,E_\nu\left(a^{\nu\,p,n}_{\mathrm{CC/NC}} + \frac{1}{3}\,b^{\nu\,p,n}_{\mathrm{CC/NC}}\right). \tag{8.11}$$

As one can see, the total cross-section is proportional to the energy of the incoming neutrino in the considered energy range.

8.3.2 Muon Neutrinos

The charged-current deep inelastic scattering of a muon neutrino off a nucleus produces a hadronic shower and a muon. These track-like events can be clearly identified in Cherenkov detectors via the Cherenkov light cone of the relativistic muon.

Through-going Muons

Since muons are rather long-lived ($c\tau_\mu = 658.650\,\mathrm{m}$), their range is only limited by energy loss during their passage through matter and not by their lifetime. Therefore Cherenkov detectors can also observe muons that are generated in the surrounding material of the detector. This effect enhances the effective detector area for high-energy muon neutrinos.

The average rate of muon energy loss can be written as

$$-\frac{dE_\mu}{dx} = \alpha(E_\mu) + \beta(E_\mu)\,E_\mu\,, \tag{8.12}$$

where $\alpha(E_\mu)$ describes the ionization energy loss and $\beta(E_\mu)$ takes into account the energy loss due to radiative processes: e^+e^- pair production, bremsstrahlung and photonuclear contributions. Both $\alpha(E_\mu)$ and $\beta(E_\mu)$ are slowly varying functions of the muon energy. As long as we can approximate α and β as energy-independent, the average range after which the muon energy drops below a threshold energy E_μ^{th} is given by

$$R_\mu(E_\mu, E_\mu^{\mathrm{th}}) = \frac{1}{\rho\,\beta}\,\ln\left[\frac{\alpha+\beta E_\mu}{\alpha+\beta E_\mu^{\mathrm{th}}}\right], \tag{8.13}$$

where ρ is the density of the medium. The relevant parameters for standard rock, water and ice are given in Table 8.1. The values of the density and the average proton-number-to-mass-number ratio are taken from [328]. The muon energy loss parameters given in the table are best-fit values from the fit of Eq. (8.13) to the tabulated data in [328]. From Eq. (8.13) we can determine the initial muon energy as a function of the final muon energy and the muon range:

$$E_\mu^0(E_\mu) = E_\mu e^{\beta\rho r} + \frac{\alpha}{\beta}\left(e^{\beta\rho r} - 1\right). \tag{8.14}$$

In fact, Eq. (8.12) does not account for the stochastic nature of radiative muon energy losses which start to dominate at TeV energies ($E > \alpha/\beta$), and therefore Eq. (8.13) overestimates the muon range for large energies.

material	density (g/cm^3)	$\langle Z/A \rangle$	α (GeV cm^2/g)	β (cm^2/g)
standard rock	2.650	0.5	2.3×10^{-3}	4.4×10^{-6}
water	1.000	0.55509	2.7×10^{-3}	3.3×10^{-6}
ice	0.918	0.55509	2.7×10^{-3}	3.3×10^{-6}

Table 8.1: Density, proton-number-to-mass-number ratio and approximate muon energy loss parameters for the materials of interest in Cherenkov detectors.

The rate of muon neutrino induced through-going muon events is given by

$$\begin{aligned}\frac{dN}{dt} &= \int d\Omega \int_0^\infty dE_{\nu_\mu} \frac{dJ_{\nu_\mu}(E_{\nu_\mu},\theta,\phi)}{dE_{\nu_\mu}} A_{\nu_\mu}^{\text{eff}}(E_{\nu_\mu},\theta,\phi) \\ &= \int d\Omega \int_{E_\mu^{\text{th}}}^\infty dE_{\nu_\mu} \int_{E_\mu^{\text{th}}}^{E_\nu} dE_\mu \frac{dJ_{\nu_\mu}(E_{\nu_\mu},\theta,\phi)}{dE_{\nu_\mu}} \left[\frac{d\sigma_{\text{CC}}^{\nu p}(E_{\nu_\mu},E_\mu)}{dE_\mu} n_p + (p \to n)\right] \\ &\quad \times R_\mu(E_\mu, E_\mu^{\text{th}})\, A_\mu^{\text{eff}}(E_\mu,\theta,\phi)\, e^{-\sigma^{\nu N}(E_{\nu_\mu})\, n_N\, L(\theta)} + (\nu \to \bar{\nu})\,,\end{aligned} \tag{8.15}$$

where the number density of protons is given by $n_p = \rho N_A \langle Z/A \rangle$ and the density of neutrons by $n_n = \rho N_A (1 - \langle Z/A \rangle)$. $N_A = 6.022 \times 10^{23}\,\text{mol}^{-1}$ is the Avogadro constant, ρ is the density of the material and $\langle Z/A \rangle$ is the average ratio of the proton number and the mass number of the material as given in Table 8.1. Due to the small neutrino–nucleon cross-section the attenuation term that accounts for the absorption of part of the signal and background neutrino fluxes during the passage of the Earth is negligible in the considered energy range. However, since the neutrino–nucleon cross-section rises with increasing neutrino energy, this effect becomes non-negligible at neutrino energies above 10 TeV.

The neutrino effective area $A_{\nu_\mu}^{\text{eff}}$ is defined as the ratio of the rate of reconstructed events and the incident neutrino flux. It is calculated using Monte Carlo methods and incorporates the attenuation of the neutrino flux during the passage of the Earth, the neutrino–nucleon cross-section, the range of the generated muon and the reconstruction and selection efficiencies. This effective area is usually provided by the experimental collaborations. The energy dependence of the neutrino effective area comes mainly from the energy dependence of the cross-section (roughly $\propto E_\nu$) and the increase of the muon range. Note that the muon effective area A_μ^{eff}, on the other hand, is defined as the ratio of the rate of reconstructed events and the incident muon flux. This area incorporates only the geometry of the detector and the detection efficiency. It is roughly equal to the geometrical area but might have a slight energy dependence.

For the calculation of the spectrum of muon neutrino induced muons at the detector position we have to take into account the shift to lower energies due to the energy loss during muon propagation through matter [329]:

$$\begin{aligned}\frac{d\phi_\mu}{dE_\mu} &= \int d\Omega \int_{E_\mu}^\infty dE_{\nu_\mu} \int_0^{R_\mu(E_{\nu_\mu},E_\mu)} dr\, e^{\beta\varrho r} \frac{dJ(E_{\nu_\mu},\theta,\phi)}{dE_{\nu_\mu}} \\ &\quad \times \left[\frac{d\sigma_{\text{CC}}^{\nu p}(E_{\nu_\mu},E_\mu^0)}{dE_\mu^0} n_p + (p \to n)\right]_{E_\mu^0 = E_\mu^0(E_\mu)} + (\nu \to \bar{\nu})\,,\end{aligned} \tag{8.16}$$

where we neglected the attenuation term. In this expression the initial muon energy enters as an explicit function of the final muon energy as given by Eq. (8.14).

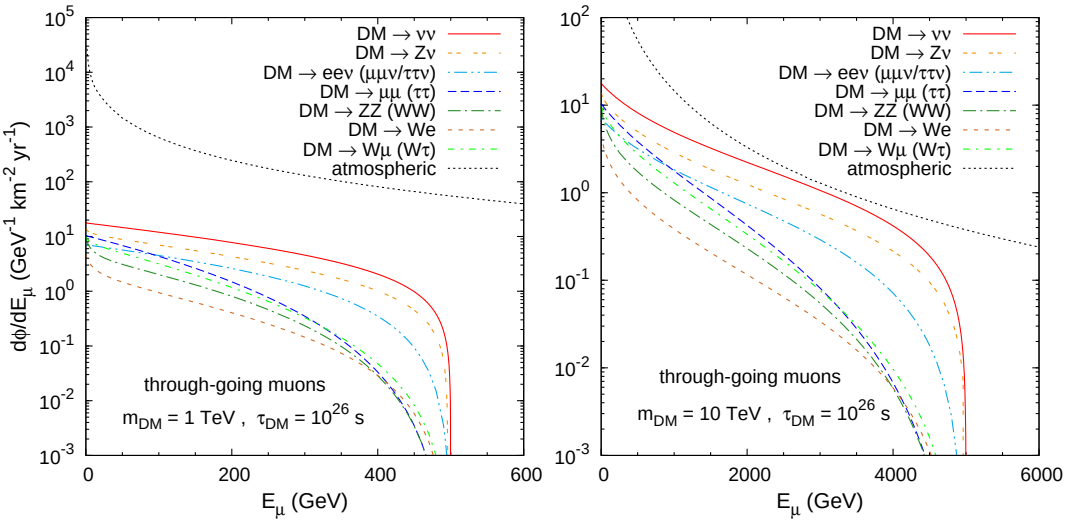

Figure 8.4: Muon fluxes for the different decay channels of a dark matter candidate compared to the atmospheric background for upward through-going muons in standard rock. The flux is computed for a dark matter mass of 1 TeV (*left*) or 10 TeV (*right*) and a lifetime of 10^{26} s, for the neutrino spectra in Figs. 8.2 and 8.3. In this case the muons lose energy on their way to the detector, smoothing out the spectral edges.

Using Eq. (8.16) we calculate the flux of through-going muons induced by neutrinos from various dark matter decay channels and show the results in Fig. 8.4 for the case of a detector surrounded by standard rock. However, the result is also applicable for the case of detectors surrounded by water or ice since the dependence on the density cancels in Eq. (8.16) and the muon energy loss parameters are roughly similar for the different materials (*cf.* Table 8.1). Since there is no possibility to veto for the overwhelming background of atmospheric muons, only upgoing events and therefore a solid angle of 2π can be used for the analysis. We see that the deep inelastic scattering transforms the monochromatic neutrino lines into a continuous muon spectrum. In addition, the energy loss in the muon propagation smooths out all the spectra making the edge corresponding to half the dark matter particle mass less clear. Still the spectrum for a line signal remains steeper than the others at the endpoint.

Contained Muons

These events are similar to through-going muons but in this case the neutrino–nucleon interaction takes place inside the instrumented volume. If the muon track ends inside the detector the events are called contained. If the muon track leaves the detector one speaks of a partially contained event. The rate of muon neutrino induced (partially) contained track-like events per unit detector volume is given by

$$\frac{dN}{dE_\mu\, dV\, dt} = \int d\Omega \int_{E_\mu}^{\infty} dE_{\nu_\mu}\, \frac{dJ_{\nu_\mu}(E_{\nu_\mu},\theta,\phi)}{dE_{\nu_\mu}} \left[\frac{d\sigma_{\rm CC}^{\nu p}(E_{\nu_\mu},E_\mu)}{dE_\mu}\, n_p + (p \to n)\right] + (\nu \to \bar{\nu})\,, \tag{8.17}$$

where we also neglected the attenuation term. In this case also the hadronic cascade is contained in the detector volume and therefore, by measuring the energy of the muon as well as of the hadronic cascade, it is in principle possible to reconstruct the total energy of the incident muon neutrino. In this case, however, one has to rely on the detection also of the hadronic cascade which, as we will discuss later, seems to be challenging.

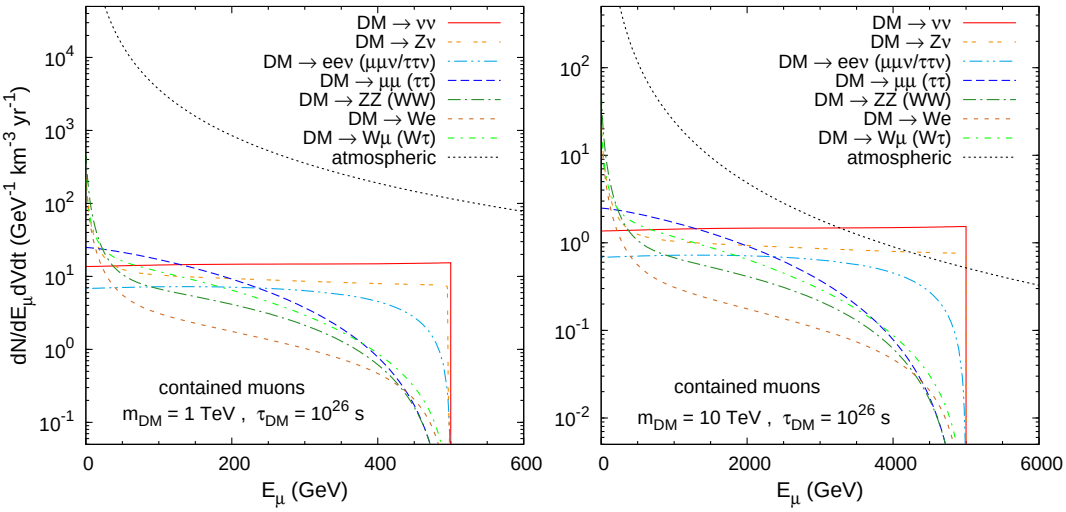

Figure 8.5: Spectra of contained muons for the different decay channels of a dark matter candidate compared to the atmospheric background. The event rate per km^3 of detector volume (filled with ice) is computed for a dark matter mass of 1 TeV (*left*) or 10 TeV (*right*) and a lifetime of 10^{26} s, for the neutrino spectra in Figs. 8.2 and 8.3. The line signal is changed into a muon continuum due to deep inelastic scattering, but it retains a hard edge at half the decaying particle mass. Also the other spectra are softer than the original neutrino ones, with the continuum neutrino spectra producing a rise at low energy, unfortunately well below the background.

The effective volume of the detector for contained events corresponds roughly to the geometrical volume (apart from boundary effects and reconstruction efficiency) and it is not enhanced by the muon range, which as we have seen, grows as E_ν. Therefore, the statistics for contained events is much lower than for through-going events at large energies. For instance in the case of Super-Kamiokande the event rate above roughly 10 GeV is dominated by through-going muons. On the other hand, in the energy range of interest for dark matter searches the muon range is of the order of one kilometer and therefore the expected rate of contained muons is comparable to the rate of through-going muons in detectors of cubic kilometer size. Thus, these contained events might be equally important for dark matter searches at the new generation of neutrino telescopes. In addition, for downgoing contained muon events there is the interesting possibility to reduce the background of atmospheric muon neutrinos by the detection of a coincident muon that was produced in the same parent meson decay [330]. This strategy could be used to increase the signal-to-background ratio for this channel, especially at large energies. However, we will not discuss this strategy quantitatively in this work.

In Fig. 8.5 we show the muon spectra for contained events calculated using Eq. (8.17)

for the case of a detector volume filled with ice. The result for a volume of water can easily be obtained rescaling the rate with the slightly different density. In this case there is no smoothing due to muon energy loss as in the case of through-going muons and the edges of the spectra are clearer, in particular for the case of a two-body decay. We only discussed the case where solely the muon is measured since this is what can be done by the experiments at the moment. If the hadronic shower is also measured, the combined reconstructed spectra would be as in Figs. 8.2 and 8.3. This is similar to the case of electron and tau neutrinos that is discussed in the next section. However, as will be discussed there, that channel offers a better signal-to-background ratio and a better energy resolution and will therefore be of more interest once the showers can be measured and used for analyses.

8.3.3 Electron and Tau Neutrinos

The charged-current deep inelastic scattering of an electron neutrino off a nucleus produces a hadronic shower and an electron that immediately causes an electromagnetic shower. The charged-current deep inelastic scattering of a tau neutrino off a nucleus produces a hadronic shower and a tau lepton. Due to the short lifetime of the tau lepton ($c\tau_\tau = 87.11\,\mu$m), at these energies it decays almost instantly and produces another shower at the interaction point. Thus, at energies below many TeV, detectors like IceCube cannot distinguish electron neutrino from tau neutrino events since both types produce similar showers in the detector [331]. In these cases, however, the whole neutrino energy is deposited in the detector, and therefore it may be possible in principle to reconstruct better the initial neutrino spectrum. On the other hand, the analysis for cascade-like events is much more difficult than the analysis for muon tracks. No cascade events from atmospheric neutrinos have been identified yet and there are only first studies on this topic *e.g.* by the IceCube collaboration [332]. For this reason there is no effective area for this type of events available yet and therefore it is difficult to estimate realistically the sensitivity in shower events.

Shower-like events are also characteristic of the neutrino–nucleon neutral-current interaction and for this reason probably only a combined analysis of neutral-current interactions for all neutrino flavors and charged-current interactions for tau and electron neutrinos will be feasible. In this case the total rate of neutrino-induced shower-like events is given by

$$\begin{aligned}\frac{dN}{dE_{\rm shower}\,dV\,dt} = \int d\Omega \Bigg\{ & \sum_{\ell=e,\tau} \left(\frac{dJ_{\nu_\ell}(E_{\nu_\ell},\theta,\phi)}{dE_{\nu_\ell}} \left[\sigma^{\nu p}_{\rm CC}(E_{\nu_\ell})\, n_p + (p \to n)\right] \right)_{E_{\nu_\ell}=E_{\rm shower}} \\ & + \sum_{\ell=e,\mu,\tau} \int_{E_{\rm shower}}^{\infty} dE_{\nu_\ell}\, \frac{dJ_{\nu_\ell}(E_{\nu_\ell},\theta,\phi)}{dE_{\nu_\ell}} \left[\frac{d\sigma^{\nu p}_{\rm NC}(E_{\nu_\ell}, E_{\rm shower})}{dE_{\rm shower}}\, n_p + (p \to n) \right] \Bigg\} \\ & + (\nu \to \bar{\nu})\,. \end{aligned} \tag{8.18}$$

We give in Fig. 8.6 the signal and atmospheric background spectra calculated from Eq. (8.18) for the case of a detector volume filled with ice. Note that in this case the muon neutrinos contribute only via neutral-current interactions which are weaker by a factor of about three compared to charged-current interactions (*cf.* Eq. (8.11)). Still, since the atmospheric muon neutrino flux is a factor of 20 larger than the electron neutrino flux at TeV energies, the atmospheric muon neutrinos provide the dominant background. At the same

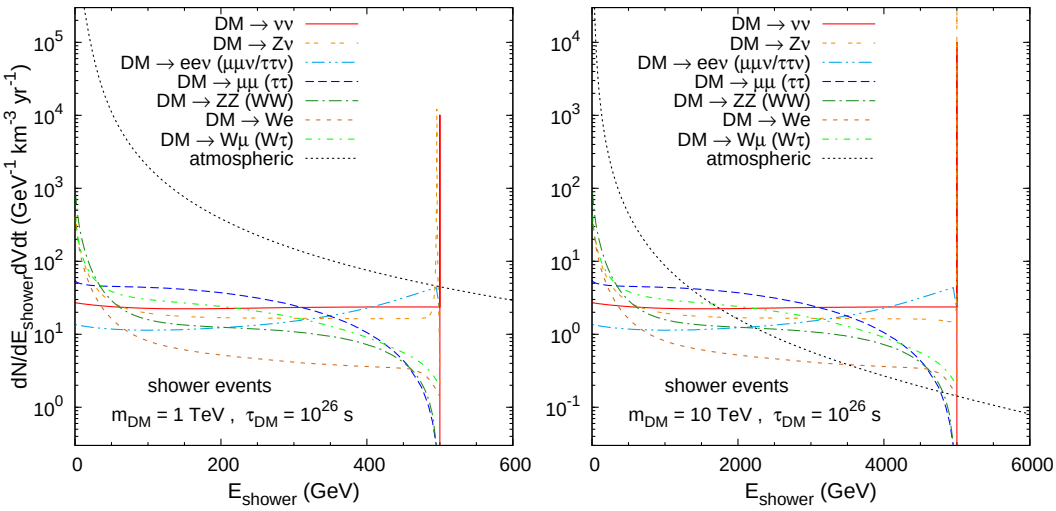

Figure 8.6: Spectra of cascade-like events for the different decay channels of a dark matter candidate compared to the atmospheric background. The event rate per km^3 of detector volume (filled with ice) is computed for a dark matter mass of 1 TeV (*left*) or 10 TeV (*right*) and a lifetime of 10^{26} s, for the neutrino spectra in Figs. 8.2 and 8.3.

time the signal is increased by roughly a factor of three. This is because due to neutrino oscillations, the signal is roughly equal in all neutrino flavors and, therefore, the signal rate from the charged-current interactions of electron and tau neutrinos is the same as for the muon neutrinos. In addition, the combined neutral-current signal of all flavors contributes at the same level as the charged-current signal of one flavor. In summary, cascade-like events will offer a signal-to-background ratio that is roughly one order of magnitude larger than in the muon case and, therefore, they appear to be a very promising channel, if they are measured. We see also that in this case, assuming that the total shower energy can be reconstructed, the line-feature is preserved and clearly visible.

8.4 Rates and Bounds

8.4.1 Super-Kamiokande

Super-Kamiokande is a 50 kt water Cherenkov detector with a fiducial mass of 22.5 kt and a muon effective area of $1200\,\mathrm{m}^2$ (with a slight zenith angle dependence due to the cylindrical shape of the detector). The muon effective area is identical to the geometrical area since the reconstruction and selection efficiencies are virtually 100%. Super-Kamiokande has been looking for a neutrino signal, mostly from dark matter annihilation in the center of the Sun, the center of the Earth and in the Galactic center. No excess has been found so far, and this fact can be used to put a constraint on the decaying dark matter case. We compare the flux of upward through-going muons from dark matter decay (integrated over energies above the threshold at 1.6 GeV) with the 90 % C.L. flux limit of excess neutrino-induced upward through-going muons provided by the Super-Kamiokande collaboration for the Galactic center (the limits from the Sun and Earth flux are weaker) [333]. As discussed in Section 8.2.2, the strongest bounds are obtained for the largest field of view. The exclusion region in the de-

caying dark matter parameter space derived from the limit in the 30° half-angle cone around the Galactic center is given in Fig. 8.7.

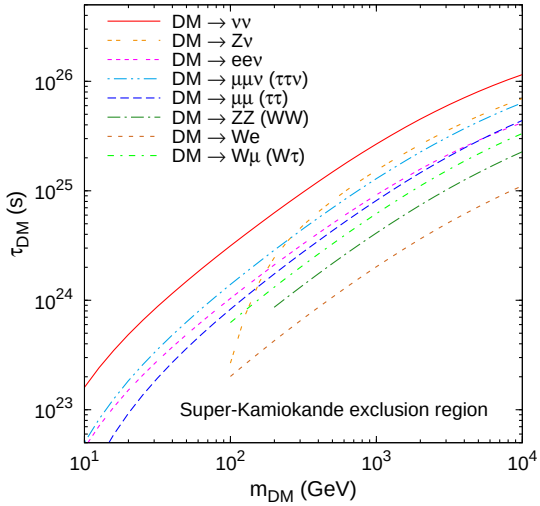

Figure 8.7: 90 % C.L. exclusion region in the lifetime vs. mass plane for a decaying dark matter candidate from the non-observation of an excess in the Super-K data. The bound is stronger for a line signal, since the spectrum there is harder, resulting in a larger muon flux due to the increasing neutrino–nucleon cross-section and muon range. For the channels that contain Z^0 or $W^\pm$ bosons in the final state the exclusion range is cut at the threshold for their production.

The bounds obtained here become stronger for larger masses although the neutrino flux is proportional to $1/m_{\rm DM}$ for constant lifetime. This is due to the increasing neutrino–nucleon cross-section and the increasing muon range. The bounds are stronger for the two-body decay signal compared to the other cases since there the signal is concentrated at the end of the spectrum and benefits from the larger neutrino–nucleon cross-section and muon range. Note that these present bounds do not have sensitivity to the parameter region preferred by the PAMELA excess yet, which corresponds to a lifetime of the order of 10^{26} s and masses larger than 200 GeV.

8.4.2 Rates and Bounds for Present and Future Experiments

Assuming decaying dark matter with a lifetime of 10^{26} s, we can now compute the expected signal rates for present and future experiments. These results can be easily generalized to arbitrary lifetimes sice the flux is simply proportional to $1/\tau_{\rm DM}$. We give the rates for some typical detectors of different sizes, *i.e.*, Super-Kamiokande, ANTARES/AMANDA and IceCube. The results for Super-K can be easily scaled up to the Hyper-Kamiokande/UNO size by multiplying by a factor 10 or 20 (for a Hyper-K mass of 500 kt and Hyper-K/UNO mass of 1 Mt, respectively). The result for KM3NeT will be very similar to that expected for IceCube. We would like to stress here that Super-K is still taking data, and that the full ANTARES detector was completed in summer 2008 and is also operational. The AMANDA detector was decommissioned in summer 2009, but has since been substituted by the IceCube detector, which already had 59 strings deployed in the ice in early 2009. The other experiments

are still in the planning phase: KM3NeT is a proposed cubic-kilometer sized underwater neutrino telescope in the Mediterranean Sea, which will probably have an effective volume comparable to IceCube, but will be able to look at the Galactic center, while the proposed Hyper-Kamiokande and Underwater Neutrino Observatory (UNO) are water Cherenkov detectors similar to Super-Kamiokande but of megaton scale.

For the case of IceCube we also take into account the DeepCore subdetector, which was completed in 2010. It is designed to lower the energy threshold of the experiment to roughly 30 GeV and to increase the sensitivity at low energies. This detector consists of six additional strings with less spacing between the digital optical modules compared to IceCube. The first of these strings was deployed in December 2008, while the other five were deployed a year later. The six strings were later complemented by two infill strings, while the entire IceCube detector was finally completed in December 2010. The combination of IceCube and DeepCore can use the outer layers of IceCube as a veto to atmospheric muons and therefore has a 4π sensitivity for fully and partially contained events, but a considerably smaller effective volume.

For the calculation of rates of upward through-going muon events we use the neutrino effective areas for AMANDA, ANTARES and the IceCube 80 strings configuration from [334] and integrate over the muon spectrum. For the combined IceCube + DeepCore detector we amend the effective area in the low-energy range using the neutrino effective area given in [335]. In the case of Super-Kamiokande we calculate the rate using Eq. (8.15) with standard rock as surrounding material, a muon effective area of $1200\,\mathrm{m}^2$ and a threshold muon energy of 1.6 GeV.

decay channel	Super-K	AMANDA	ANTARES	IceCube	IC+DeepCore
atmospheric ν_μ	4.3×10^2	1.5×10^3	1.8×10^3	3.0×10^5	3.5×10^5
$DM \to \nu\bar{\nu}$	1.4×10^0	5.0×10^0	6.4×10^0	1.4×10^3	1.6×10^3
$DM \to \mu^+\mu^-$	4.1×10^{-1}	6.3×10^{-1}	1.0×10^0	2.7×10^2	3.5×10^2
$DM \to \tau^+\tau^-$	4.1×10^{-1}	6.0×10^{-1}	9.6×10^{-1}	2.6×10^2	3.5×10^2
$DM \to Z^0Z^0$	2.4×10^{-1}	3.6×10^{-1}	5.4×10^{-1}	1.4×10^2	1.8×10^2
$DM \to W^+W^-$	1.8×10^{-1}	3.0×10^{-1}	4.5×10^{-1}	1.2×10^2	1.5×10^2
$DM \to Z^0\nu$	7.1×10^{-1}	2.1×10^0	2.8×10^0	6.4×10^2	7.3×10^2
$DM \to e^+e^-\nu$	4.8×10^{-1}	1.4×10^0	1.9×10^0	4.4×10^2	5.0×10^2
$DM \to \mu^+\mu^-\nu$	6.7×10^{-1}	1.6×10^0	2.2×10^0	5.4×10^2	6.4×10^2
$DM \to \tau^+\tau^-\nu$	6.8×10^{-1}	1.6×10^0	2.2×10^0	5.3×10^2	6.4×10^2
$DM \to W^\pm e^\mp$	1.0×10^{-1}	2.0×10^{-1}	2.8×10^{-1}	7.1×10^1	8.9×10^1
$DM \to W^\pm \mu^\mp$	3.1×10^{-1}	5.2×10^{-1}	8.0×10^{-1}	2.1×10^2	2.7×10^2
$DM \to W^\pm \tau^\mp$	2.9×10^{-1}	4.4×10^{-1}	7.0×10^{-1}	1.9×10^2	2.4×10^2

Table 8.2: Number of upward through-going muon events per year from the atmospheric neutrino background and different dark matter decay channels at several neutrino experiments. The signals are given for a dark matter lifetime of 10^{26} s and a dark matter mass of 300 GeV.

We see from Tables 8.2 and 8.3 that a sizable number of events is expected for a lifetime of 10^{26} s, especially for experiments of cubic kilometer scale, such as to become significant above the atmospheric background even for a dark matter particle mass of 300 GeV. Of course for larger masses the significance becomes greater due to the increasing signal rate. Note that

decay channel	Super-K	AMANDA	ANTARES	IceCube	IC+DeepCore
atmospheric ν_μ	4.3×10^2	1.5×10^3	1.8×10^3	3.0×10^5	3.5×10^5
$DM \to \nu\bar{\nu}$	4.1×10^0	2.4×10^1	2.8×10^1	4.6×10^3	4.6×10^3
$DM \to \mu^+\mu^-$	1.3×10^0	6.0×10^0	7.2×10^0	1.4×10^3	1.4×10^3
$DM \to \tau^+\tau^-$	1.3×10^0	5.8×10^0	7.0×10^0	1.3×10^3	1.4×10^3
$DM \to Z^0Z^0$	7.3×10^{-1}	2.9×10^0	3.5×10^0	6.6×10^2	6.8×10^2
$DM \to W^+W^-$	5.7×10^{-1}	2.5×10^0	3.1×10^0	5.8×10^2	6.0×10^2
$DM \to Z^0\nu$	2.4×10^0	1.3×10^1	1.6×10^1	2.6×10^3	2.6×10^3
$DM \to e^+e^-\nu$	1.4×10^0	7.8×10^0	9.3×10^0	1.6×10^3	1.6×10^3
$DM \to \mu^+\mu^-\nu$	2.0×10^0	1.0×10^1	1.2×10^1	2.2×10^3	2.2×10^3
$DM \to \tau^+\tau^-\nu$	2.0×10^0	1.0×10^1	1.2×10^1	2.2×10^3	2.2×10^3
$DM \to W^\pm e^\mp$	3.1×10^{-1}	1.4×10^0	1.7×10^0	3.2×10^2	3.3×10^2
$DM \to W^\pm \mu^\mp$	9.6×10^{-1}	4.5×10^0	5.4×10^0	1.0×10^3	1.0×10^3
$DM \to W^\pm \tau^\mp$	9.1×10^{-1}	4.0×10^0	4.9×10^0	9.3×10^2	9.8×10^3
$DM \to \nu\bar{\nu}$	1.8×10^1	1.7×10^2	1.7×10^2	1.3×10^4	1.3×10^4
$DM \to \mu^+\mu^-$	6.8×10^0	5.5×10^1	6.0×10^1	5.5×10^3	5.5×10^3
$DM \to \tau^+\tau^-$	7.2×10^0	5.7×10^1	6.2×10^1	6.0×10^3	6.0×10^3
$DM \to Z^0Z^0$	3.8×10^0	2.7×10^1	3.0×10^1	2.9×10^3	2.9×10^3
$DM \to W^+W^-$	3.2×10^0	2.5×10^1	2.7×10^1	2.6×10^3	2.7×10^3
$DM \to Z^0\nu$	1.1×10^1	9.8×10^1	1.0×10^2	8.1×10^3	8.1×10^3
$DM \to e^+e^-\nu$	6.5×10^0	5.8×10^1	6.0×10^1	4.8×10^3	4.8×10^3
$DM \to \mu^+\mu^-\nu$	9.9×10^0	8.4×10^1	8.9×10^1	7.7×10^3	7.7×10^3
$DM \to \tau^+\tau^-\nu$	1.0×10^1	8.6×10^1	9.2×10^1	8.1×10^3	8.1×10^3
$DM \to W^\pm e^\mp$	1.7×10^0	1.3×10^1	1.5×10^1	1.4×10^3	1.4×10^3
$DM \to W^\pm \mu^\mp$	5.2×10^0	4.1×10^1	4.5×10^1	4.2×10^3	4.2×10^3
$DM \to W^\pm \tau^\mp$	5.1×10^0	4.0×10^1	4.3×10^1	4.2×10^3	4.2×10^3

Table 8.3: Number of upward through-going muon events per year from the atmospheric neutrino background and different dark matter decay channels at several neutrino experiments. The signals are given for a dark matter lifetime of 10^{26} s and dark matter masses of 1 TeV *(top)* and 10 TeV *(bottom)*.

here we did not make use of any spectral information. In that case larger dark matter masses would also benefit from the falling background.

Requiring the combined number of signal and background events not to exceed the background above the 90 % C.L. (in the Gaussian approximation this corresponds to $\sigma = S/\sqrt{B} < 1.28$), similar to the case of Super-K in Fig. 8.7, we can then give in Fig. 8.8 a forecast of the exclusion region which may be obtained from kilometer-cubed experiments using one year of data. The larger statistics of the future experiments will improve the Super-K bounds by more than an order of magnitude and explore the region of lifetimes above 10^{25} s, for masses larger than 200 GeV. Note that for ten years of data, the lifetime limit will become stronger approximately by a factor of three. For lower masses the bounds will remain weaker, but in that parameter region a very important role will be played by DeepCore, which will considerably improve the IceCube performance for masses between 30 and 100 GeV, as can be seen in the right panel of Fig. 8.8, and also by the megaton water detectors which are expected to

strengthen the Super-K bounds by an order of magnitude down to masses of a few GeV. This low-mass region does not provide an explanation of the PAMELA excess and is plagued by a stronger atmospheric background. Nevertheless, it is remarkable that even there lifetimes larger than 10^{24} s will be probed in future experiments.

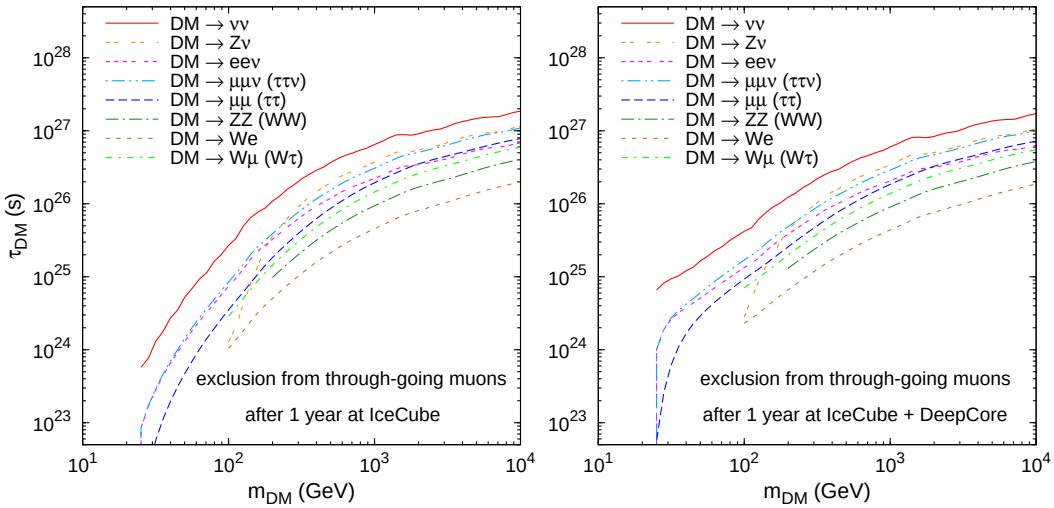

Figure 8.8: 90 % C.L. exclusion prospects in the lifetime vs. mass plane for a decaying dark matter candidate from the non-observation of a significant excess in the total rate of neutrino induced upward through-going muons observed at IceCube (*left*) or IceCube + DeepCore (*right*) in one year. Clearly visible is the enhanced sensitivity of the DeepCore extension in the low-mass region.

8.4.3 Energy Resolution and Reconstructed Spectra

Once a signal has been detected, the question arises if it will also be possible to reconstruct the neutrino spectra and extract some information on the dark matter decay channel. For this purpose one important factor is the energy resolution of the neutrino detectors. We will take here for reference the IceCube detector, for which the energy resolution is $\log_{10}(E_{\max}/E_{\min}) = 0.3$–$0.4$ for track-like events and $\log_{10}(E_{\max}/E_{\min}) = 0.18$ for cascade-like events [336].

We show in Figs. 8.9–8.14 the histograms for the signal and the atmospheric background using an energy resolution of 0.3 in $\log_{10} E$ and three bins per decade for upward through-going and contained muons, and an energy resolution of 0.18 in $\log_{10} E$ and five bins per decade for shower events. These figures can be compared to Figs. 8.4–8.6 which show the spectra unbinned and without finite energy resolution. Also shown is the significance of the signal over the background in different bins for a lifetime of 10^{26} s for the different channels using one year of data with an effective area of $1\,\mathrm{km}^2$ for upward through-going muons and an effective volume of $1\,\mathrm{km}^3$ for contained muons and cascades. All plots are available for both scalar and fermionic dark matter candidates.

We see that for nearly any of the spectra, the signal will appear with large statistical significance in more than one single bin, and it will be clear that the neutrino signal is not

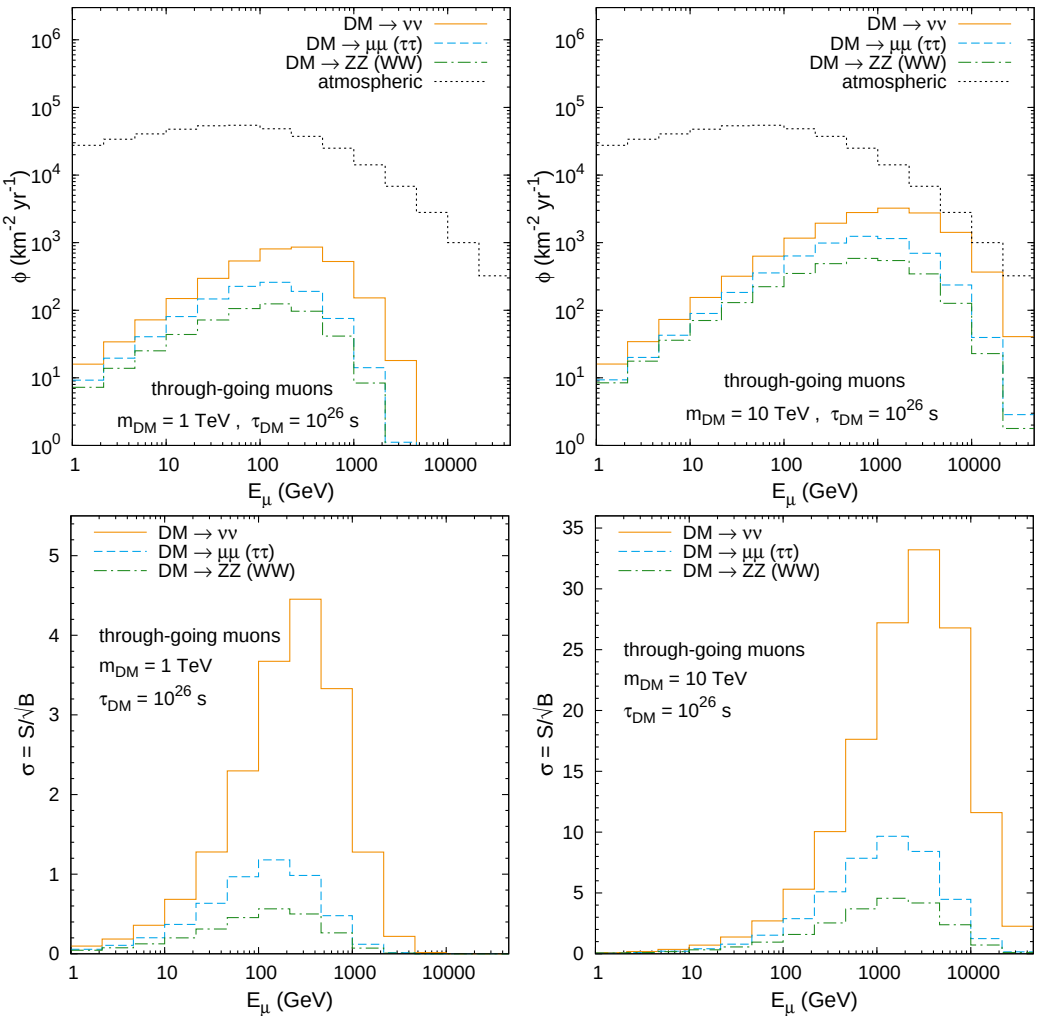

Figure 8.9: *Top:* Muon fluxes for the different decay channels of a scalar dark matter candidate compared to the atmospheric background for upward through-going muons. The flux is computed for a dark matter mass of 1 TeV (*left*) or 10 TeV (*right*) and a lifetime of 10^{26} s using an energy resolution of 0.3 in $\log_{10} E$ and three bins per decade. *Bottom:* Statistical significance of the signal of through-going muons shown above calculated for every single energy bin using one year of data with an effective area of 1 km^2.

following a power law, unlike the atmospheric flux. Thus, it is clear that by using spectral information it will be possible to set much stricter limits on the decaying dark matter parameter space than shown in Fig. 8.8. In order to give an idea of the sensitivities that can be obtained using spectral information, we show in Table 8.4 the values of the dark matter lifetime for several decay channels that correspond to a $5\,\sigma$ signal in the most significant energy bin after one year of observation for an idealized detector with an effective muon area of 1 km^2 and an effective volume of 1 km^3 for contained muons and shower events. We see there that the limits from through-going and contained muons are better but not far from those shown in Fig. 8.8, while the shower events in principle allow to reach even one order of magnitude larger lifetimes. Using not only the dominant energy bin from Figs. 8.9–8.14 but

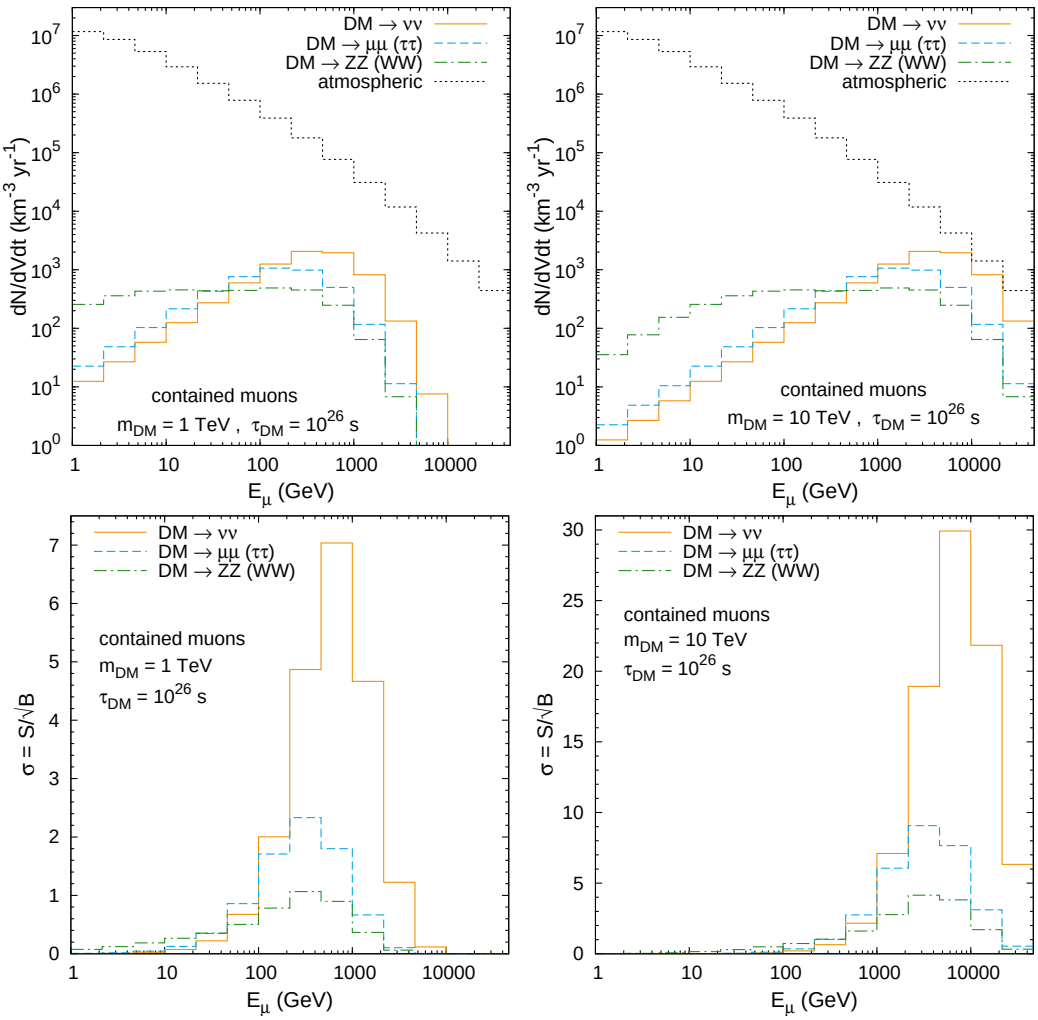

Figure 8.10: *Top:* Muon rates per km^3 of detector volume for the different decay channels of a scalar dark matter candidate compared to the atmospheric background for contained muons. The flux is computed for a dark matter mass of 1 TeV (*left*) or 10 TeV (*right*) and a lifetime of 10^{26} s using an energy resolution of 0.3 in $\log_{10} E$ and three bins per decade. *Bottom:* Statistical significance of the contained muon signal shown above calculated for every single energy bin using one year of data with an effective volume of 1 km^3.

a combination of several energy bins optimized for each individual decay channel it will be possible to set even stronger constraints on the dark matter lifetime. Therefore, a signal in the region preferred by PAMELA should be in the detectable range.

On the other hand, discriminating between the spectra for the different channels will not be so straightforward, especially if the mass of the decaying particle is unknown. After convolution with the energy resolution, the two-body, three-body or continuum spectra appear quite similar, especially within their statistical error, but their significance peaks at slightly different values for the same dark matter mass. Note, though, that the signal from a neutrino line remains steeper than the other ones at the edge and it may be possible to distinguish it

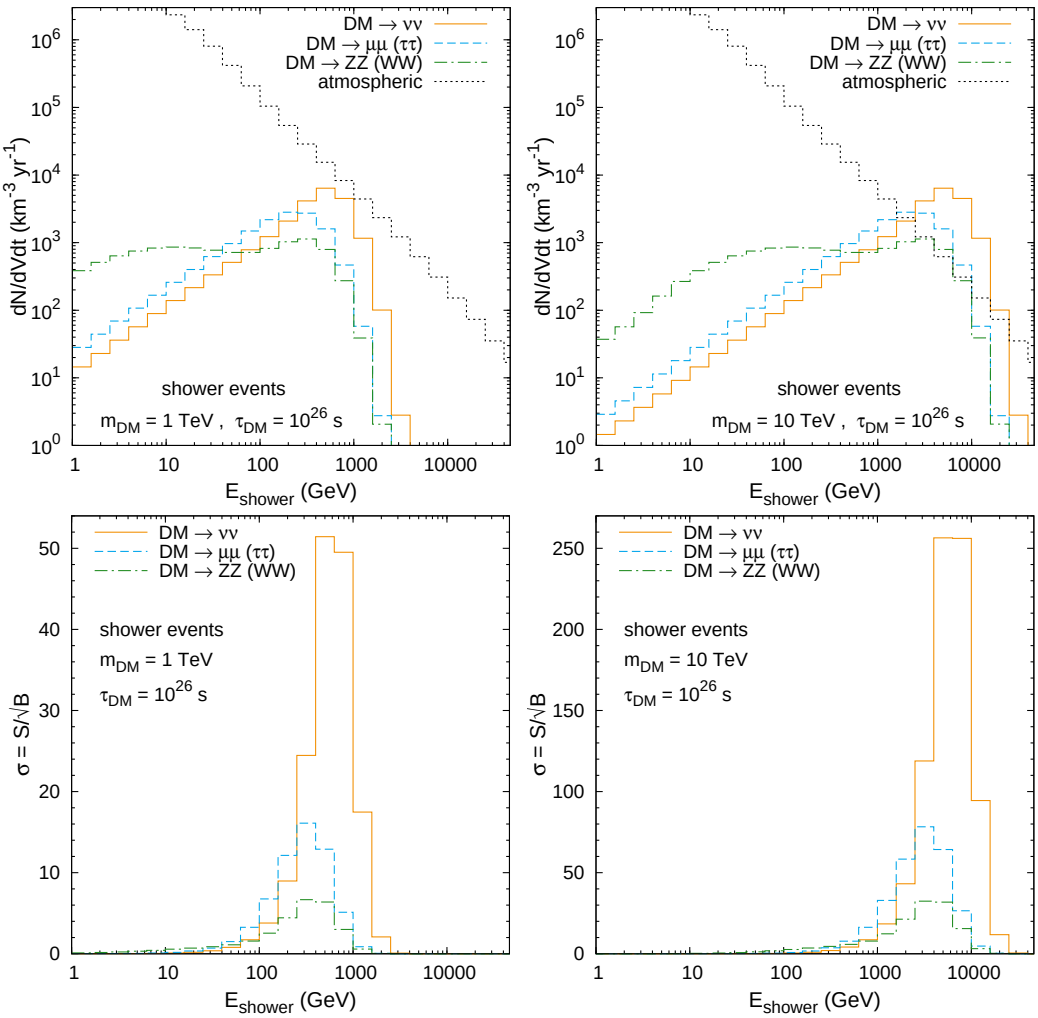

Figure 8.11: *Top:* Shower rates per km^3 of detector volume for the different decay channels of a scalar dark matter candidate compared to the atmospheric background for electromagnetic and hadronic showers. The flux is computed for a dark matter mass of 1 TeV (*left*) or 10 TeV (*right*) and a lifetime of 10^{26} s using an energy resolution of 0.18 in $\log_{10} E$ and five bins per decade. *Bottom:* Statistical significance of the shower signal shown above calculated for every single energy bin using one year of data with an effective volume of 1 km^3.

with sufficient statistics. In this respect the more promising strategy is probably exploiting the better energy resolution of the shower events, if they can be detected. In general a comparison between the different types of events, through-going, contained and cascade-like, will make disentangling the shape of the spectra easier. Moreover, if the dark matter mass is measured via another channel, like gamma-rays, it may be possible to exploit this information in the neutrino fit and compare the position of the neutrino signal "peak" in the data with the expectation. This should help in disentangling at least a continuum spectrum from the two- and perhaps also three-body decay cases. For this specific strategy probably one of the most promising dark matter candidates would be a fermion, which may decay into a leptonic three-body final state and subdominantly into $\gamma\nu$, as *e.g.* gravitino dark matter

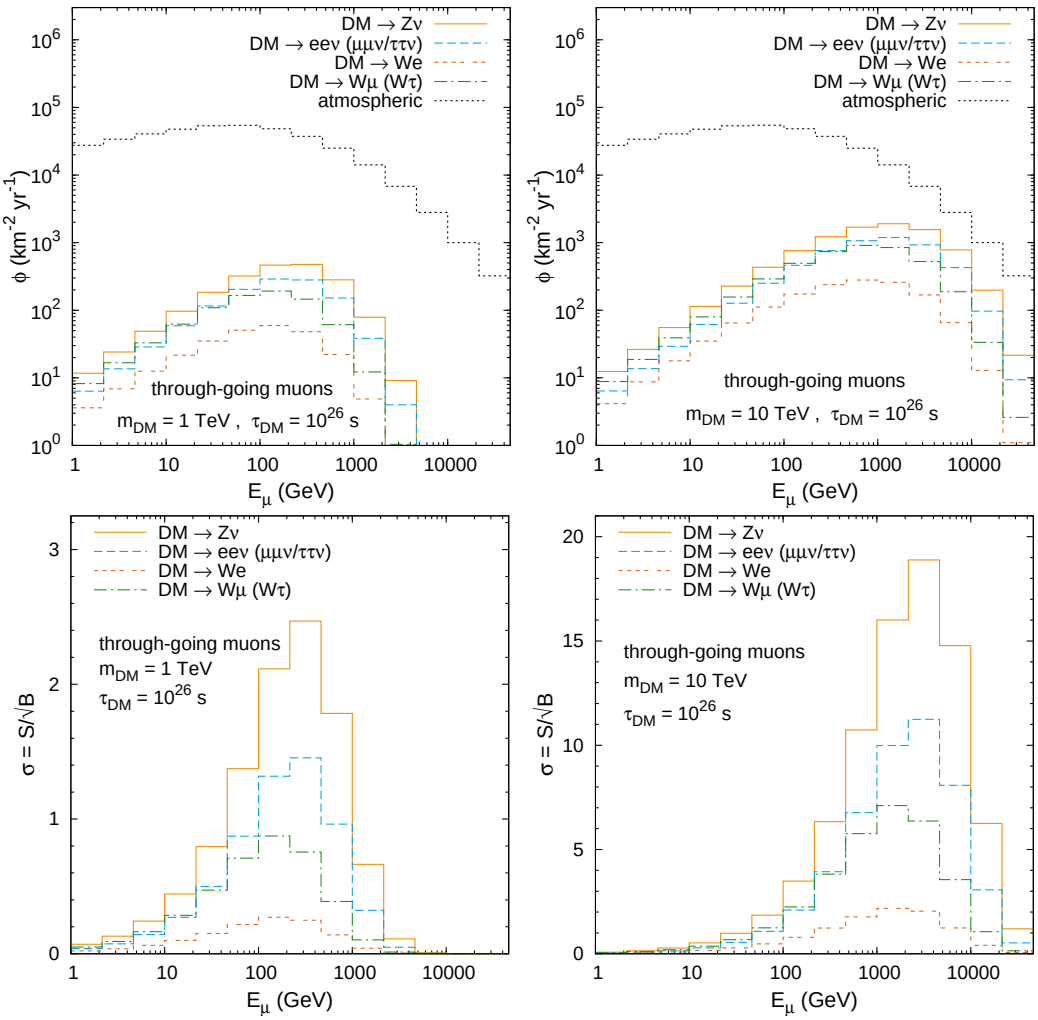

Figure 8.12: *Top:* Muon fluxes for the different decay channels of a fermionic dark matter candidate compared to the atmospheric background for upward through-going muons. The flux is computed for a dark matter mass of 1 TeV (*left*) or 10 TeV (*right*) and a lifetime of 10^{26} s using an energy resolution of 0.3 in $\log_{10} E$ and three bins per decade. *Bottom:* Statistical significance of the signal of through-going muons shown above calculated for every single energy bin using one year of data with an effective area of 1 km^2.

with trilinear R-parity breaking [337]. Then, if the γ-channel is suppressed by 2 to 3 orders of magnitude compared to a leptonic three-body decay, the gamma-ray and neutrino experiments will actually be exploring the same range of lifetimes. In this case an observation of a gamma line by Fermi will provide the dark matter mass measurement and the neutrino signal with a much shorter lifetime will point at a three-body or $Z^0\nu$ dominant decay. In case both signals in gamma-rays and neutrinos are measured, it may be possible to disentangle also between a scalar and a fermionic dark matter candidate, which seems to be very difficult from neutrino measurements alone, since the two types of particles produce very similar spectra within the energy resolution of the detectors, as can be seen comparing Figs. 8.9, 8.10 and 8.11 with Figs. 8.12, 8.13 and 8.14.

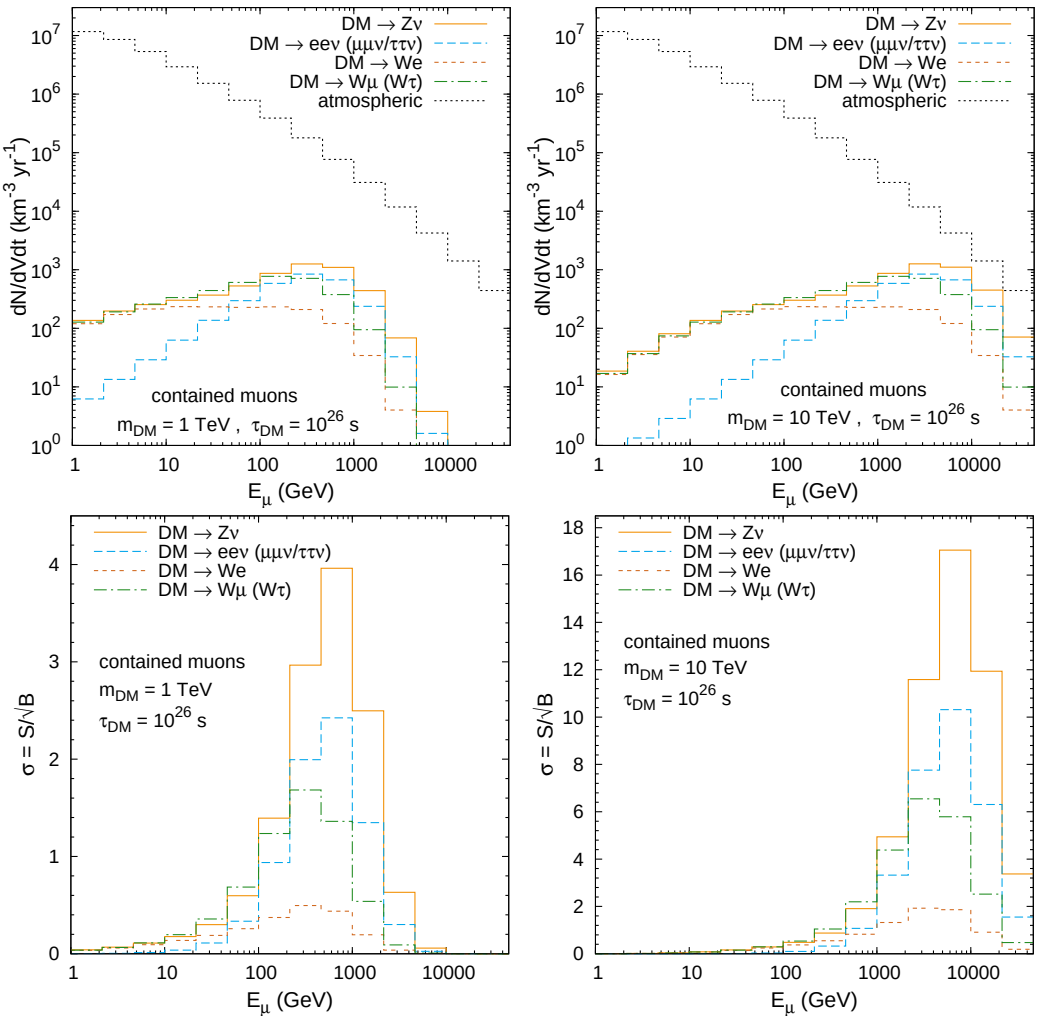

Figure 8.13: *Top:* Muon rates per km^3 of detector volume for the different decay channels of a fermionic dark matter candidate compared to the atmospheric background for contained muons. The flux is computed for a dark matter mass of 1 TeV (*left*) or 10 TeV (*right*) and a lifetime of 10^{26} s using an energy resolution of 0.3 in $\log_{10} E$ and three bins per decade. *Bottom:* Statistical significance of the contained muon signal shown above calculated for every single energy bin using one year of data with an effective volume of 1 km^3.

8.5 Conclusions

We have studied in this chapter the possible neutrino signals from decaying dark matter, considering different decay channels and spectra, both for a scalar and a fermionic candidate. We have concentrated here on the region of parameter space that is preferred in order to explain the PAMELA positron excess and shown that in this case a signal may soon be visible at neutrino observatories. The non-observation of such a signal will put rather strong constraints on the leptophilic decaying dark matter explanation of the excess, except for the decay into e^+e^- where no signal in neutrinos is expected. In this sense neutrino observations are complementary to other astrophysical constraints coming from radio frequencies and in-

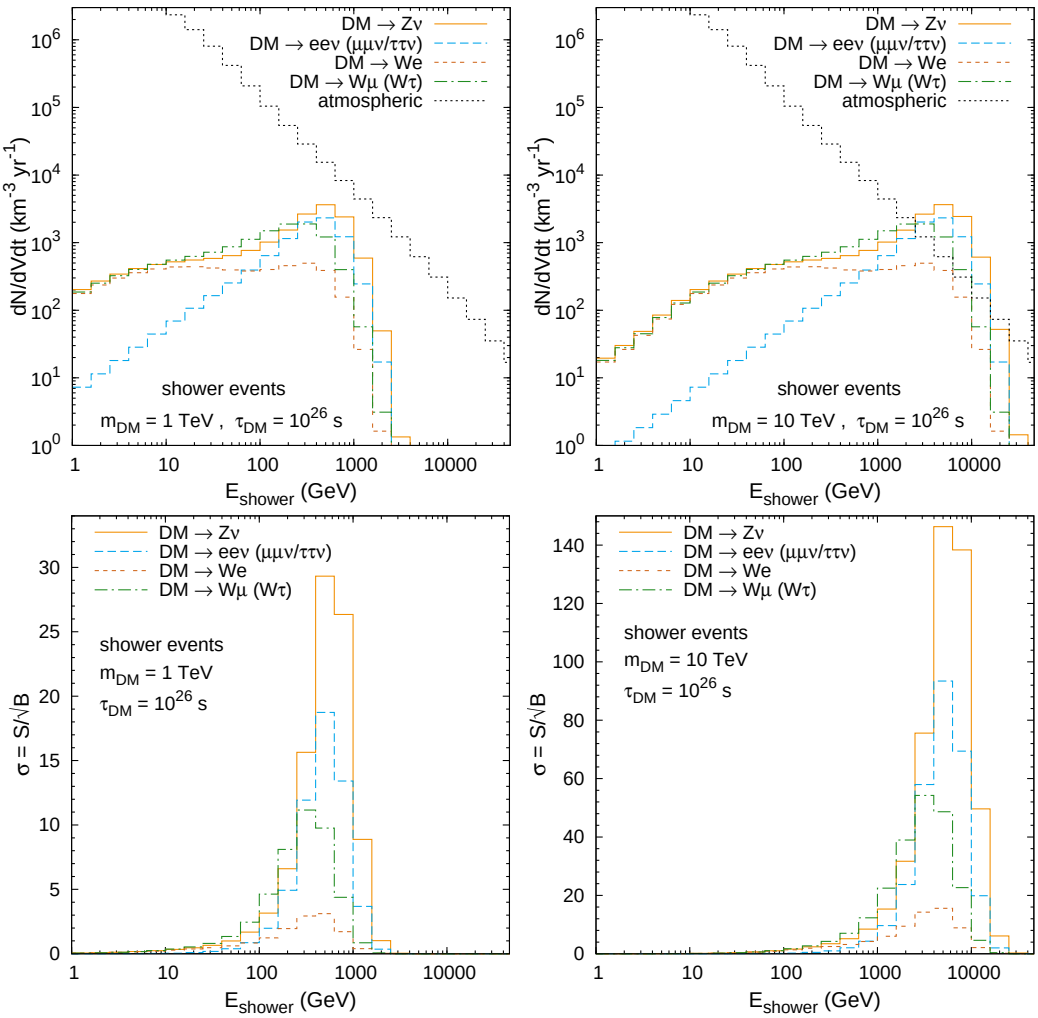

Figure 8.14: *Top:* Shower rates per km^3 of detector volume for the different decay channels of a fermionic dark matter candidate compared to the atmospheric background for electromagnetic and hadronic showers. The flux is computed for a dark matter mass of 1 TeV (*left*) or 10 TeV (*right*) and a lifetime of 10^{26} s using an energy resolution of 0.18 in $\log_{10} E$ and five bins per decade. *Bottom:* Statistical significance of the shower signal shown above calculated for every single energy bin using one year of data with an effective volume of 1 km^3.

verse Compton emission, which are more sensitive to the electron channel. A neutrino signal will allow to disentangle between decaying and annihilating dark matter, by comparing the signal towards and away from the Galactic center [3, 103], and also between dark matter and astrophysical sources.

More difficult is the identification of the dark matter decay channels, since all neutrino spectra finally result in a broad peak in the muon spectrum. However, the analysis of cascade-like events, which contain in principle all the neutrino energy and have the advantage of a better energy resolution, may improve the situation and allow with sufficient statistics to disentangle at least a line-like feature. Furthermore, the neutrino signal alone cannot be used to

decay channel	through-going muons	contained muons	shower events
$DM \to \nu\bar{\nu}$	$8.9 \times 10^{25}\,\mathrm{s}$	$1.4 \times 10^{26}\,\mathrm{s}$	$1.0 \times 10^{27}\,\mathrm{s}$
$DM \to \mu^+\mu^-$	$2.4 \times 10^{25}\,\mathrm{s}$	$4.7 \times 10^{25}\,\mathrm{s}$	$3.2 \times 10^{26}\,\mathrm{s}$
$DM \to Z^0 Z^0$	$1.1 \times 10^{25}\,\mathrm{s}$	$2.1 \times 10^{25}\,\mathrm{s}$	$1.3 \times 10^{26}\,\mathrm{s}$
$DM \to Z^0\nu$	$4.9 \times 10^{25}\,\mathrm{s}$	$7.9 \times 10^{25}\,\mathrm{s}$	$5.9 \times 10^{26}\,\mathrm{s}$
$DM \to e^+e^-\nu$	$2.9 \times 10^{25}\,\mathrm{s}$	$4.8 \times 10^{25}\,\mathrm{s}$	$3.7 \times 10^{26}\,\mathrm{s}$
$DM \to W^\pm e^\mp$	$5.4 \times 10^{24}\,\mathrm{s}$	$9.9 \times 10^{24}\,\mathrm{s}$	$6.2 \times 10^{25}\,\mathrm{s}$
$DM \to W^\pm \mu^\mp$	$1.7 \times 10^{25}\,\mathrm{s}$	$3.4 \times 10^{25}\,\mathrm{s}$	$2.2 \times 10^{26}\,\mathrm{s}$
$DM \to \nu\bar{\nu}$	$6.6 \times 10^{26}\,\mathrm{s}$	$6.0 \times 10^{26}\,\mathrm{s}$	$5.1 \times 10^{27}\,\mathrm{s}$
$DM \to \mu^+\mu^-$	$1.9 \times 10^{26}\,\mathrm{s}$	$1.8 \times 10^{26}\,\mathrm{s}$	$1.6 \times 10^{27}\,\mathrm{s}$
$DM \to Z^0 Z^0$	$9.1 \times 10^{25}\,\mathrm{s}$	$8.3 \times 10^{25}\,\mathrm{s}$	$6.5 \times 10^{26}\,\mathrm{s}$
$DM \to Z^0\nu$	$3.8 \times 10^{26}\,\mathrm{s}$	$3.4 \times 10^{26}\,\mathrm{s}$	$2.9 \times 10^{27}\,\mathrm{s}$
$DM \to e^+e^-\nu$	$2.2 \times 10^{26}\,\mathrm{s}$	$2.1 \times 10^{26}\,\mathrm{s}$	$1.9 \times 10^{27}\,\mathrm{s}$
$DM \to W^\pm e^\mp$	$4.4 \times 10^{25}\,\mathrm{s}$	$3.9 \times 10^{25}\,\mathrm{s}$	$3.1 \times 10^{26}\,\mathrm{s}$
$DM \to W^\pm \mu^\mp$	$1.4 \times 10^{26}\,\mathrm{s}$	$1.3 \times 10^{26}\,\mathrm{s}$	$1.1 \times 10^{27}\,\mathrm{s}$

Table 8.4: Dark matter lifetimes corresponding to a $5\,\sigma$ significance in the most significant energy bin after one year of observation in an idealized detector with an effective muon area of $1\,\mathrm{km}^2$ and an effective volume for contained muons and showers of $1\,\mathrm{km}^3$. The numbers are given for dark matter masses of 1 TeV (*top*) and 10 TeV (*bottom*). Note that the sensitivity obtained with through-going and contained muons is similar. At larger masses the bound from through-going muons is stronger since the statistics increase due to the longer muon range at higher energies. However, neglecting reconstruction efficiencies the strongest constraint is obtained from shower events since that channel offers the best signal-to-background ratio (see discussion in Section 8.3.3).

distinguish between scalar and fermionic dark matter candidates since the resulting spectra are very similar in the two cases.

On the other hand, for some of the decay channels discussed here, like the ones with a $Z^0/W^\pm$ gauge boson in the final state, corresponding signals are also expected in gamma rays and antiprotons and may provide additional information on the model parameters and a cross-check of the decay channel. Even for the pure leptophilic channels, gamma rays from final state radiation or from subdominant decays may play an important role in discriminating between models due to the better sensitivity in the gamma-ray channel. In general, neutrino observations offer complementary information and can be used to also test models where the gamma-ray signal is strongly suppressed compared to the leptonic one. The next generation of neutrino experiments can therefore be expected to yield some very interesting results.

Part III

Models of Decaying Dark Matter

Chapter 9

Gravitino Dark Matter

In this chapter, which is based on the publication [5], we discuss a particulary interesting example of a decaying dark matter scenario, namely gravitino dark matter in models with broken R-parity. We analyze the cosmic-ray signatures of decaying gravitino dark matter in a model-independent way based on an operator analysis. We do this regarding a rather narrow window of gravitino masses with a view of the leptonic cosmic rays anomalies observed by PAMELA and Fermi LAT on the one side and an upper bound on the gravitino mass from the requirement of thermal leptogenesis and universal boundary conditions at the Grand Unification scale on the other. From an analysis of the maximally allowed contribution of gravitino dark matter to the antiproton flux, we estimate the possible gamma-ray signatures of gravitino decay, which include a line at the end of the spectrum at an energy below 300 GeV. Future measurements of the gamma-ray flux will provide important constraints on possible signatures of decaying gravitino dark matter at the LHC.

9.1 Introduction

An unequivocal prediction of locally supersymmetric extensions of the Standard Model is the existence of the gravitino, the gauge fermion of supergravity [338, 339]. Depending on the mechanism of supersymmetry breaking, it can be the lightest superparticle, which makes it a natural dark matter candidate [340]. In connection with thermal leptogenesis [341], gravitino dark matter has been discussed as an alternative [342] to the standard WIMP scenario [343].

In a class of models with small R-parity and lepton number breaking the gravitino is no longer stable, but its decays into Standard Model particles are doubly suppressed by the Planck mass and the small R-parity breaking parameter. Hence, its lifetime can exceed the lifetime of the Universe by many orders of magnitude, and the gravitino remains a viable dark matter candidate [109]. Recently, it has been shown that such models yield a consistent cosmology incorporating nucleosynthesis, leptogenesis and supersymmetric dark matter [94]. Small R-parity breaking can arise from spontaneous $B - L$ breaking [94] or from left–right symmetry breaking [95]. Alternatively, explicity R-parity violating couplings of heavy Majorana neutrinos can lead to suppressed R-parity breaking interactions in the low-energy effective theory via the seesaw mechanism [344]. In the simplest supergravity models with universal gaugino masses at the Grand Unification (GUT) scale, thermal leptogenesis implies an upper bound of 600 GeV on the gravitino mass [345]. By relaxing the boundary conditions

at the GUT scale, gravitino masses up to 1.4 TeV are possible [346].

Gravitino decays may lead to characteristic signatures in high-energy cosmic rays. The produced flux of gamma rays [11, 94, 198, 109, 347, 103] and positrons [10, 198] has been found to potentially account for the extragalactic component of the excess in the EGRET [251, 276] and HEAT [170] data, respectively. Furthermore, a neutrino flux from gravitino decays is predicted [9] as well as a possibly observable antideuteron flux [6]. As discussed in detail in Chapter 4, a steep rise in the cosmic-ray positron fraction above 10 GeV has recently been discovered by the PAMELA collaboration [169] whereas the observed antiproton-to-proton ratio [129] is consistent with previous measurements of the antiproton flux by BESS [182, 183], IMAX [186] and WiZard/CAPRICE [184, 185]. A possible explanation of this exotic positron source is annihilating or decaying dark matter (see [348] for a recent review and references), including decaying gravitinos [10, 199, 349]. Equally important are the recent measurements of the total electron + positron flux by ATIC [173], H.E.S.S. [175] and Fermi LAT [216].

In this chapter we analyze the cosmic-ray signatures of decaying gravitino dark matter in a model-independent way based on an operator analysis. Consistency with the observed antiproton flux yields a lower bound on the gravitino lifetime. As we shall see, this determines an upper bound on the continuous gamma-ray spectrum. Following a previous analysis of supergravity models and leptogensis, we only consider gravitino masses below 600 GeV. Hence, gravitino decays cannot be the cause of the anomaly observed by the ATIC and Fermi LAT collaborations. An interpretation of the PAMELA positron anomaly as the result of gravitino dark matter decay, on the other hand, requires gravitino masses above 200 GeV.

This chapter is organized as follows. In Section 9.2 we present a general operator analysis of gravitino decays and study the implications for the different branching ratios. In particular we discuss the strength of the predicted monochromatic line in the gamma-ray spectrum. Section 9.3 deals with the electron, positron and antiproton flux from gravitino decays and the implications for the gravitino lifetime. The results for the gamma-ray spectrum are discussed in Section 9.4, followed by our conclusions in Section 9.5.

9.2 Operator Analysis

R-parity violating gravitino decays are conveniently described in terms of effective operators. The spinor ψ_ν of a gravitino with mass $m_{3/2}$ (*cf.* [350, 351]) satisfies the Dirac equation

$$\left(i\gamma^\mu\partial_\mu - m_{3/2}\right)\psi_\nu = 0\,, \tag{9.1}$$

together with the constraints

$$\gamma^\mu\psi_\mu = 0, \quad \partial^\mu\psi_\mu = 0\,. \tag{9.2}$$

Using the above two equations, one can verify that the dimension-five and dimension-six operators for R-parity violating couplings of the gravitino to the Standard Model are given by

$$\mathcal{L}_{\rm eff} = \frac{i\kappa}{\sqrt{2}M_{\rm Pl}}\left\{\bar{l}\gamma^\lambda\gamma^\nu D_\nu\phi\,\psi_\lambda + \frac{i}{2}\bar{l}\gamma^\lambda\left(\xi_1\,g'YB_{\mu\nu} + \xi_2\,gW_{\mu\nu}\right)\sigma^{\mu\nu}\phi\,\psi_\lambda\right\} + \text{h.c.}\,, \tag{9.3}$$

where we have suppressed flavor indices for simplicity. Typically $\xi_{1,2} = \mathcal{O}(1/m_{3/2})$. The covariant derivative involves the $U(1)_Y$ and $SU(2)_L$ gauge fields B_μ and W_μ, respectively,

$$D_\mu = \partial_\mu + ig'YB_\mu + igW_\mu, \quad Y[\phi] = -\frac{1}{2}, \quad W_\mu = \frac{1}{2}\sigma^I W_\mu^I, \tag{9.4}$$

with the corresponding gauge field strengths

$$B_{\mu\nu} = \partial_\mu B_\nu - \partial_\nu B_\mu, \quad W_{\mu\nu} = \partial_\mu W_\nu - \partial_\nu W_\mu - i\,[W_\mu, W_\nu]\ . \tag{9.5}$$

In the unitary gauge, the Higgs and lepton doublets read

$$\phi = \begin{pmatrix} v + \frac{1}{\sqrt{2}}h \\ 0 \end{pmatrix}, \quad l = \begin{pmatrix} \nu \\ e \end{pmatrix}\ , \tag{9.6}$$

where h, ν and e denote Higgs boson, neutrino and charged lepton fields, respectively. From Eq. (9.3) one then obtains the couplings of leptons and gravitinos to Higgs bosons and gauge bosons which are responsible for the two-body gravitino decays,

$$\begin{aligned} \mathcal{L}_3 \supset \frac{i\kappa}{\sqrt{2}M_{\rm Pl}}\Big\{ & (\partial_\mu h + iM_Z Z_\mu)\,\bar\nu\gamma^\nu\gamma^\mu\psi_\nu + i\sqrt{2}M_W W_\mu^-\,\bar e\gamma^\nu\gamma^\mu\psi_\nu \\ & + iM_Z(\xi_Z\partial_\mu Z_\nu + \xi_\gamma\partial_\mu A_\nu)\bar\nu\gamma^\lambda\sigma^{\mu\nu}\psi_\lambda \\ & + i\sqrt{2}M_W\xi_W\partial_\mu W_\nu^-\,\bar e\gamma^\lambda\sigma^{\mu\nu}\psi_\lambda\Big\} + \text{h.c.}\,, \end{aligned} \tag{9.7}$$

with the following relations in terms of the Weinberg angle $\theta_{\rm W}$,

$$\xi_Z = \sin^2\theta_{\rm W}\xi_1 + \cos^2\theta_{\rm W}\xi_2\,, \tag{9.8}$$

$$\xi_W = \xi_2\,, \tag{9.9}$$

$$\xi_\gamma = \sin\theta_{\rm W}\cos\theta_{\rm W}(\xi_2 - \xi_1)\,, \tag{9.10}$$

$$\sin\theta_{\rm W} = \frac{g'}{\sqrt{g'^2 + g^2}}\,. \tag{9.11}$$

Note that the gauge boson couplings satisfy the relation

$$\xi_Z + \tan\theta_{\rm W}\xi_\gamma = \xi_W. \tag{9.12}$$

For $\xi_1 = \xi_2$ one has $\xi_\gamma = 0$ and $\xi_Z = \xi_W$.

The interaction Lagrangian, Eq. (9.7), coincides with the one from bilinear R-parity breaking if parameters are properly matched.[1]

[1]The relations are $\kappa_i = \langle\widetilde\nu_i\rangle/v$, $U_{\widetilde Z\widetilde Z} = -M_Z\xi_Z$, $U_{\widetilde W\widetilde W} = -M_W\xi_W$, $U_{\widetilde\gamma\widetilde Z} = -M_Z\xi_\gamma$, $U_{\widetilde H_u\widetilde Z}\sin\beta + U_{\widetilde H_d\widetilde Z}\cos\beta + m_{\widetilde\nu_\tau^2}/(m_{\widetilde\nu_\tau^2} - m_h^2) = 1$.

Using the results of [9, 352] we then obtain the following partial gravitino decay widths:

$$\Gamma(\psi_{3/2} \to h\nu_i) = \frac{\kappa_i m_{3/2}^3}{384\pi M_{\rm Pl}^2}\beta_h^4\,, \tag{9.13}$$

$$\Gamma(\psi_{3/2} \to \gamma\nu_i) = \frac{\kappa_i |\xi_{\gamma i}|^2 M_Z^2 m_{3/2}^3}{64\pi M_{\rm Pl}^2}\,, \tag{9.14}$$

$$\Gamma(\psi_{3/2} \to Z\nu_i) = \frac{\kappa_i m_{3/2}^3}{384\pi M_{\rm Pl}^2}\beta_Z^2\left(H_Z + 16\frac{M_Z^2 {\rm Re}(\xi_{Zi})}{m_{3/2}}G_Z + 6M_Z^2|\xi_{Zi}|^2 F_Z\right)\,, \tag{9.15}$$

$$\Gamma(\psi_{3/2} \to W^\pm e_i^\mp) = \frac{\kappa_i m_{3/2}^3}{192\pi M_{\rm Pl}^2}\beta_W^2\left(H_W + 16\frac{M_W^2 {\rm Re}(\xi_{Wi})}{m_{3/2}}G_W + 6M_W^2|\xi_{Wi}|^2 F_W\right)\,, \tag{9.16}$$

where the subscript i denotes the generation index. The functions β_a, H_a, G_a and F_a (where $a = h, Z, W$) are given by

$$\beta_a = 1 - \frac{M_a^2}{m_{3/2}^2}\,, \tag{9.17}$$

$$H_a = 1 + 10\frac{M_a^2}{m_{3/2}^2} + \frac{M_a^4}{m_{3/2}^4}\,, \tag{9.18}$$

$$G_a = 1 + \frac{1}{2}\frac{M_a^2}{m_{3/2}^2}\,, \tag{9.19}$$

$$F_a = 1 + \frac{2}{3}\frac{M_a^2}{m_{3/2}^2} + \frac{1}{3}\frac{M_a^4}{m_{3/2}^4}\,. \tag{9.20}$$

As expected, one has for $m_a\xi_a \sim m_a/m_{3/2} \ll 1$,

$$\Gamma(\psi_{3/2} \to h\nu_i) \simeq \Gamma(\psi_{3/2} \to Z\nu_i) \simeq \frac{1}{2}\Gamma(\psi_{3/2} \to W^\pm e_i^\mp)\,. \tag{9.21}$$

The decay width $\Gamma(\psi_{3/2} \to \gamma\nu)$ is of particular interest since it determines the strength of the gamma-ray line at the end of the continous spectrum. As discussed above, this decay width is model-dependent. Contrary to the continuous part it can vanish, which is the case for $\xi_1 - \xi_2 = 0$. Generically, without such a cancellation, one obtains for the branching ratio using Eqs. (9.8) – (9.11) and Eqs. (9.13) – (9.16):

$${\rm BR}(\psi_{3/2} \to \gamma\nu) \sim 0.3\sin^2\theta_{\rm W}\left(\frac{M_Z}{m_{3/2}}\right)^2 \sim 0.02\left(\frac{200\,{\rm GeV}}{m_{3/2}}\right)^2 \tag{9.22}$$

This estimate will be used in Section 9.4 where the gamma-ray spectrum is discussed.

Another phenomenologically important issue is the flavor structure of gravitino decays, *i.e.*, the dependence of the parameters $\xi_{\gamma i}$, ξ_{Zi} and ξ_{Wi} on the generation index. In models of bilinear R-parity breaking, for instance, this information is encoded in the mixing parameters μ_i,

$$\Delta\mathcal{L} = \mu_i H_u L_i\,, \tag{9.23}$$

where H_u and L_i are the Higgs and lepton doublet superfields, respectively. In models of flavor the ratios of the parameters μ_i are related to the structure of the Majorana neutrino mass matrix,

$$M_\nu = c_{ij}(l_i\phi)(l_j\phi)\,. \tag{9.24}$$

An interesting example, which can account for the large mixing angles in the neutrino sector, is "anarchy" [353] where $c_{ij} = \mathcal{O}(1)$. In this case on also has

$$\frac{\mu_i}{\mu_j} = \mathcal{O}(1) \tag{9.25}$$

For the purpose of illustration we shall use in the following sections the "democratic" case $\mu_1 = \mu_2 = \mu_3$, where the parameters $\xi_{\gamma i}$, ξ_{Zi} and ξ_{Wi} have no flavor dependence. Alternatively, one may consider "semi-anarchy" (*cf.* [94]). Other examples can be found in [354].

In the following we shall consider gravitino masses between 100 GeV and 600 GeV, for which the assumed hierarchy $m_{\rm SM}^2 \ll m_{3/2}^2 \ll m_{\rm soft}^2$ can only be a rough approximation. A more detailed treatment would have to incorporate mixings with heavy particles of the supersymmetric Standard Model. However, we find the operator analysis useful to illustrate the main qualitative features of gravitino decays.

9.3 Antimatter from Gravitino Decays

The scenario of decaying gravitino dark matter provides, for a wide range of gravitino masses and liftimes, a consistent thermal history of the Universe, incorporating successful primordial nucleosynthesis and successful baryogenesis through leptogenesis. Furthermore, if dark matter gravitinos decay at a sufficiently large rate, the decay products could be observed through an anomalous contribution to the high-energy cosmic-ray fluxes. In this section we shall discuss the constraints on the gravitino parameters which follow from the observations of the positron fraction by HEAT and PAMELA and of the antiproton flux by BESS, IMAX and WiZard/CAPRICE.

The rate of antimatter production per unit energy and unit volume at the posititon $\vec{r}$ with respect to the center of the Milky Way is given by

$$Q(E,\vec{r}) = \frac{\rho_{\rm DM}(r)}{m_{3/2}\tau_{3/2}}\frac{dN}{dE} \tag{9.26}$$

where dN/dE is the energy spectrum of antiparticles produced in the decay, which we determine using the event generator `PYTHIA 6.4` [249]. On the other hand, $\rho_{\rm DM}(r)$ is the dark matter halo profile, for which we assume a Navarro-Frenk-White profile, as defined in Eq. (1.13) with the parameters listed in Table 1.1, although our conclusions are not very sensitive to the choice of halo profile. For the local dark matter density we assume $\rho_\odot = 0.3\,{\rm GeV}/\,{\rm cm}^3$. As in previous chapters, we model the propagation of antimatter in the Galaxy using the stationary two-zone diffusion model described in Chapter 2. We use the semi-analytical solutions of the Green's functions given there to compute the local fluxes of positrons and antiprotons. We take solar modulation into account using the prescription of Eq. (2.23) and a value of $\phi_{\rm F} = 500\,{\rm MV}$ for the modulation potential.

The calculation of the high-energy cosmic-ray fluxes from gravitino decay is hindered by a large number of uncertainties stemming both from astrophysics, encoded in the Green's functions, and from particle physics. However, as we shall show below, present observations of the positron fraction and the antiproton flux constrain the parameters of the model well enough to make definite predictions for the diffuse gamma-ray flux. These predictions will be tested by the Fermi LAT, thus providing a crucial test of the scenario of decaying gravitino dark matter.

From the particle-physics point of view, the solution to the transport equation depends on the following uncertainties: the energy spectrum of positrons or antiprotons produced in the decay, the gravitino mass, and the gravitino lifetime. The energy spectrum of positrons and antiprotons depends crucially on the R-parity breaking interactions of the gravitino. For definiteness, we assume throughout this chapter a Standard Model-like Higgs boson with a mass of $m_h = 115\,\mathrm{GeV}$. It was shown in Section 9.2 that when the gravitino mass is relatively large, the branching ratios for the dominant decay channels are predicted to be

$$\sum_i \mathrm{BR}(\psi_{3/2} \to h^0 \nu_i) \simeq 1/4\,, \tag{9.27}$$

$$\sum_i \mathrm{BR}(\psi_{3/2} \to Z^0 \nu_i) \simeq 1/4\,, \tag{9.28}$$

$$\sum_i \mathrm{BR}(\psi_{3/2} \to W^{\pm} e_i^{\mp}) \simeq 1/2\,, \tag{9.29}$$

while the model-dependent branching ratio $\mathrm{BR}(\psi_{3/2} \to \gamma\nu)$ is generally predicted to be much smaller. Therefore, in this limit the injection spectrum of antiprotons from gravitino decay is fairly model-independent, being a function of only the gravitino mass. This is not the case, however, for the energy spectrum of positrons, since the flavor composition of the final state depends on the flavor structure of the R-parity breaking couplings, which cannot be predicted without choosing a particular flavor model.

The observation by PAMELA of an excess in the positron fraction at energies extending up to at least 100 GeV implies a lower bound on the gravitino mass of $\sim 200\,\mathrm{GeV}$ if the positron excess is interpreted in terms of gravitino decay. Besides, as shown in [345], there exists a theoretical upper bound on the gravitino mass of $\sim 600\,\mathrm{GeV}$ in supergravity models with universal gaugino masses at the GUT scale, stemming from the requirement of successful thermal leptogenesis. This leaves a relatively narrow range for the gravitino mass in this setup, $m_{3/2} \simeq 200 - 600\,\mathrm{GeV}$. If the positron excess observed by PAMELA is unrelated to gravitino decay, the gravitino mass can be as low as $\sim 5\,\mathrm{GeV}$ without resulting in overclosure of the Universe [94].

9.3.1 Constraints from the Antiproton Flux

As discussed in Chapter 2, the calculation of the antiproton flux from dark matter decay suffers from uncertainties in the determination of the physical parameters in the propagation of charged cosmic rays in the diffusive halo, leading to uncertainties in the magnitude of fluxes as large as two orders of magnitude at energies relevant for present antiproton experiments. The requirement that the antiproton flux from gravitino decay be consistent with existing measurements yields a lower bound on the gravitino mass which strongly depends on

the choice of the propagation model. In the following we shall adopt the MED propagation model parameters (see Table 2.3), which provides the best fit to the B/C ratio and measurements of the flux ratios of radioactive cosmic-ray species [137]. It is worth noting, however, that there is a degeneracy in the determination of the diffusion coefficient and the height of the diffusive halo, which can be used to reduce the antiproton flux relative to the flux from spallation when different transport parameters are assumed [144].

In order to determine the maximally allowed exotic contribution to the total antiproton flux, a precise knowledge of the secondary flux of antiprotons from spallation of high-energy cosmic rays on the Hydrogen and Helium nuclei in the interstellar medium is necessary. Unfortunately, the determination of this secondary flux is also subject to uncertainties. First, the choice of the propagation model parameters can change the prediction of the secondary flux by $10 - 20\%$. More importantly, the uncertainty in the nuclear cross-sections for p–p, p–He, He–p and He–He collisions can change the prediction of the secondary flux by $22 - 25\%$ above or below the central value [188].

A conservative upper bound on the antiproton flux from gravitinos is obtained by demanding that the total flux not be larger than the theoretical uncertainty band of the MED propagation model. This means that a "minimal" dark matter lifetime for the MED model can be defined by a scenario where the secondary antiproton flux from spallation is 25% smaller than the central value, due to a putative overestimation of the nuclear cross-sections, and where the total antiproton flux saturates the upper limit of the uncertainty band which stems from the astrophysical uncertainties discussed above. This amounts to the requirement that the antiproton flux should not exceed $\sim 50\%$ of the central value of secondary flux from spallation.

We find the following minimum gravitino lifetimes that are compatible with antiproton constraints using the above prescription,

$$\tau_{3/2}^{\rm min}(200) \simeq 7 \times 10^{26}\,{\rm s}, \quad \tau_{3/2}^{\rm min}(400) \simeq 3 \times 10^{26}\,{\rm s}, \quad \tau_{3/2}^{\rm min}(600) \simeq 1.5 \times 10^{26}\,{\rm s}\,, \tag{9.30}$$

where the numbers in parentheses correspond to the gravitino masses $m_{3/2} = 200$, 400 and 600 GeV, respectively. The corresponding antiproton fluxes from gravitino decay are shown in Fig. 9.1 together with the experimental measurements by BESS, IMAX and WiZARD/CAPRICE, and the uncertainty band from the nuclear cross-sections in the MED propagation model. The minimal lifetimes listed in Eq. (9.30) can be compared with the gravitino lifetimes needed to explain the PAMELA positron excess, which will be discussed in the next section.

9.3.2 Comparison with the Electron/Positron Fluxes

Using the procedure outlined in the previous subsection, it is straightforward to calculate the positron flux from gravitino dark matter decay at the position of the Earth. We will adopt for definiteness the MED propagation model (see Table 2.1), characterized by the parameters $\delta = 0.70$, $K_0 = 0.0112\,{\rm kpc}^2/{\rm Myr}$, $L = 4\,{\rm kpc}$ and $V_{\rm c} = 12\,{\rm km/s}$. Note that the sensitivity of the positron fraction to the choice of propagation parameters is fairly mild at the energies where the excess is observed since the high-energy positrons are produced within a few kilo-

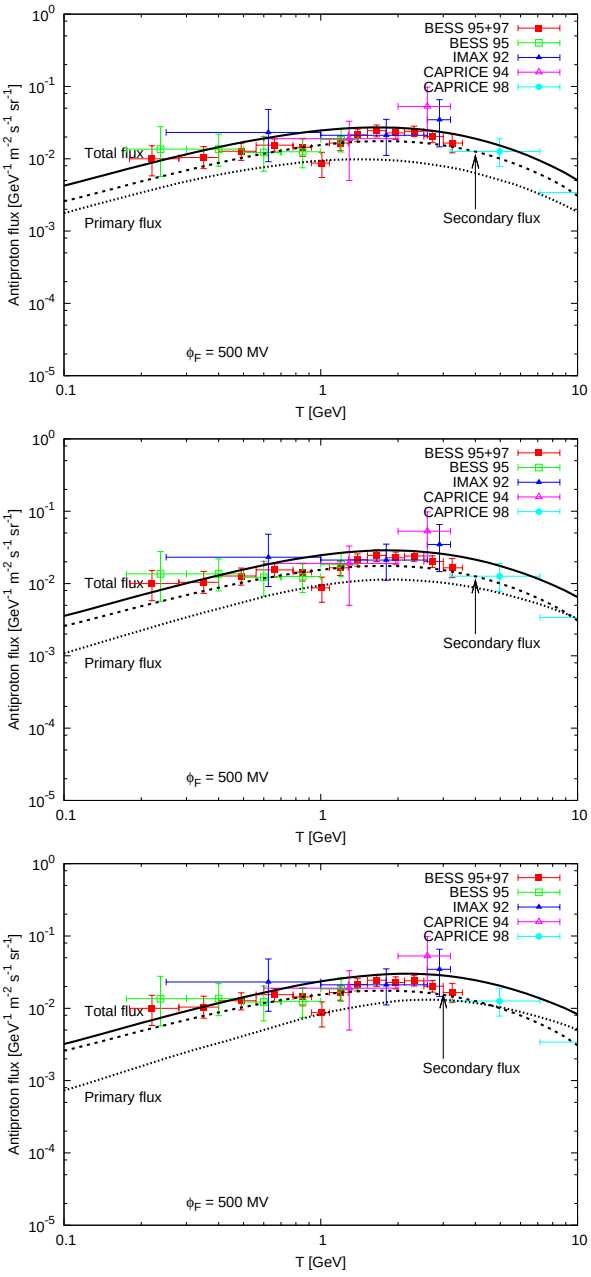

Figure 9.1: Antiproton fluxes for $m_{3/2} = 200$, 400, 600 GeV in the MED set of propagation parameters that saturate the antiproton overproduction bound (see text). Dotted lines: antiproton flux from gravitino decays, dashed lines: secondary antiproton flux from spallation in the case of minimal nuclear cross-sections, solid lines: total antiproton flux. The gravitino lifetimes are $\tau_{3/2} = 7 \times 10^{26}$ s, 3×10^{26} s and 1.5×10^{26} s, respectively.

parsecs from our position in the Milky Way and barely suffer the effects of diffusion.

To compare the predictions to the PAMELA results, we shall calculate the positron frac-

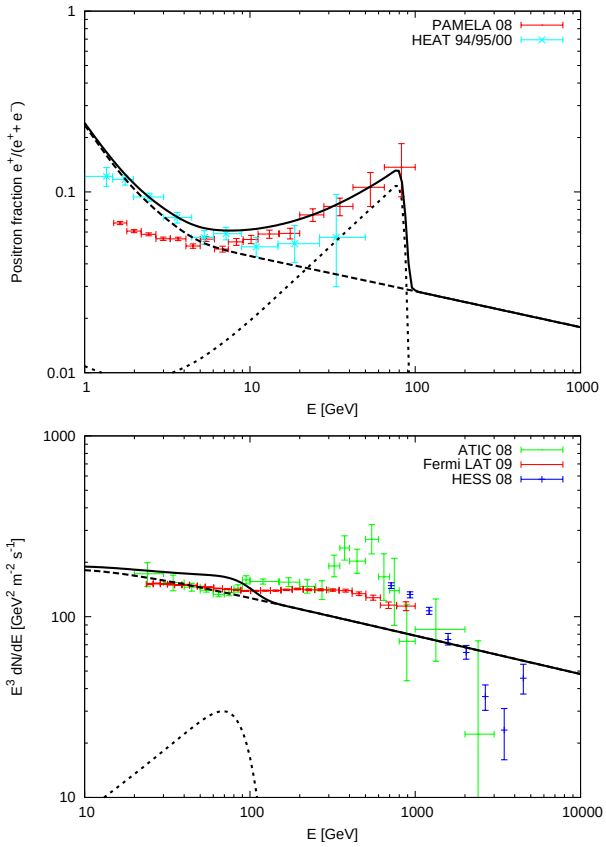

Figure 9.2: Contribution from dark matter decay to the positron fraction and the total electrom + positron flux, compared with data from PAMELA and HEAT, and ATIC, Fermi LAT and H.E.S.S., respectively; $m_{3/2} = 200$ GeV, $\tau_{3/2} = 3.2 \times 10^{26}$ s; for $W^{\pm}l^{\mp}$ decays pure electron flavor is assumed. The "model 0" background is used, and for comparison with Fermi LAT data a 25% energy resolution is taken into account.

tion, as defined in Eq. 4.1. For the background fluxes of primary and secondary electrons, as well as secondary positrons, we adopt the fluxes corresponding to "model 0," as presented by the Fermi LAT collaboration [218], which fits well the low-energy data points of the total electron + positron flux and the positron fraction, and is similar to the MED model for energies above a few GeV [139]. See Chapter 4 for an explicit parametrization of these fluxes. We also allow for a variable normalization of the primary electron flux, as discussed there. The positron fraction then assumes the form given in Eq. (4.4).

We now discuss the hypothesis that the PAMELA positron excess is due to gravitino dark matter decay. For this to be the case, the gravitino mass must be at least $\sim 200\,\text{GeV}$. As discussed above, the branching ratios for decays into Standard Model particles will be essentially fixed for gravitino masses of a few hundred GeV. The decay $\psi_{3/2} \to W^{\pm}\ell^{\mp}$ then has a branching ratio of $\sim 50\%$, and the hard leptons that are directly produced in these two-body decays may account for the rise in the positron fraction if a significant fraction of these decays has electron or muon flavor, as discussed in Chapter 4.

Consider first the extreme case that the decays proceed purely into electron flavor. For $m_{3/2} = 200\,\mathrm{GeV}$, the PAMELA excess can then be explained for the gravitino lifetime $\tau^e_{3/2}(200) \simeq 3.2 \times 10^{26}\,\mathrm{s}$, as illustrated in Fig. 9.2. Note that this lifetime is a factor 2 smaller than the minimum lifetime given in Eq. (9.30), which we obtained from the antiproton overproduction constraint. In other words, an interpretation of the PAMELA excess in terms of gravitino decay is incompatible with the MED set of propagation parameters when antiprotons are taken into account. Nevertheless, the MIN model and other sets of propagation parameters that yield intermediate values for the antiproton flux can be compatible with both the positron fraction and the antiproton-to-proton ratio observed by PAMELA. The situation is very similar for $m_{3/2} = 400$ and $600\,\mathrm{GeV}$.

Fig. 9.2 also shows the predicted total electron + positron flux together with the results from Fermi and ATIC. Obviously, the "model 0" presented by the Fermi collaboration cannot account for the present data, and the contribution from gravitino decays makes the discrepancy even worse. In particular, the data show no spectral feature as would be expected for decaying dark matter. On the other hand, gravitino decays may very well be consistent with the measured total electron + positron flux once the background is appropriately adjusted. This is evident from Fig. 9.3, where the contribution from gravitino decays is shown in the theoretically well motivated case of flavor-democratic decays. The figure also illustrates that, depending on the gravitino mass, the dark matter contribution to the PAMELA excess can still be significant.

An obvious possibility is that both the total electron + positron flux and the positron fraction are dominated by astrophysical sources. For instance, for the gravitino mass $m_{3/2} = 100\,\mathrm{GeV}$ we obtain from the antiproton overproduction constraint a minimum lifetime

$$\tau^{\mathrm{min}}_{3/2}(100) \simeq 1.0 \times 10^{27}\,\mathrm{s}\,. \tag{9.31}$$

As Fig. 9.4 demonstrates, the contribution from gravitino decays to the total electron + positron flux and the positron fraction is indeed negligible for lifetimes above this bound. Nonetheless, as we shall see in the following section, the dark matter contribution to the gamma-ray flux can be sizable.

9.4 Predictions for the Diffuse Gamma-Ray Flux

Once the gravitino mass and lifetime, as well as the flavor structure of the decays are fixed, one can make the corresponding predictions for the contribution to the diffuse gamma-ray flux from gravitino decay. This flux is composed of two components; the first one stems from the decay of gravitinos in the Milky Way halo, whereas the second one is due to the decay of gravitinos at cosmological distances. For explicit expressions for these fluxes, see Chapter 3. For the extragalactic fluxes, we assume a standard flat ΛCDM cosmology with parameters as given in Chapter 1. The cosmological contribution is fainter than the halo contribution. Moreover, the flux of gamma rays of extragalactic origin is attenuated by electron–positron pair production on the extragalactic background light emitted by galaxies in the ultraviolet, optical and infrared frequencies [355, 356]. However, the flux of gamma rays originating from the decay of dark matter particles in the halo is barely attenuated by pair production on the

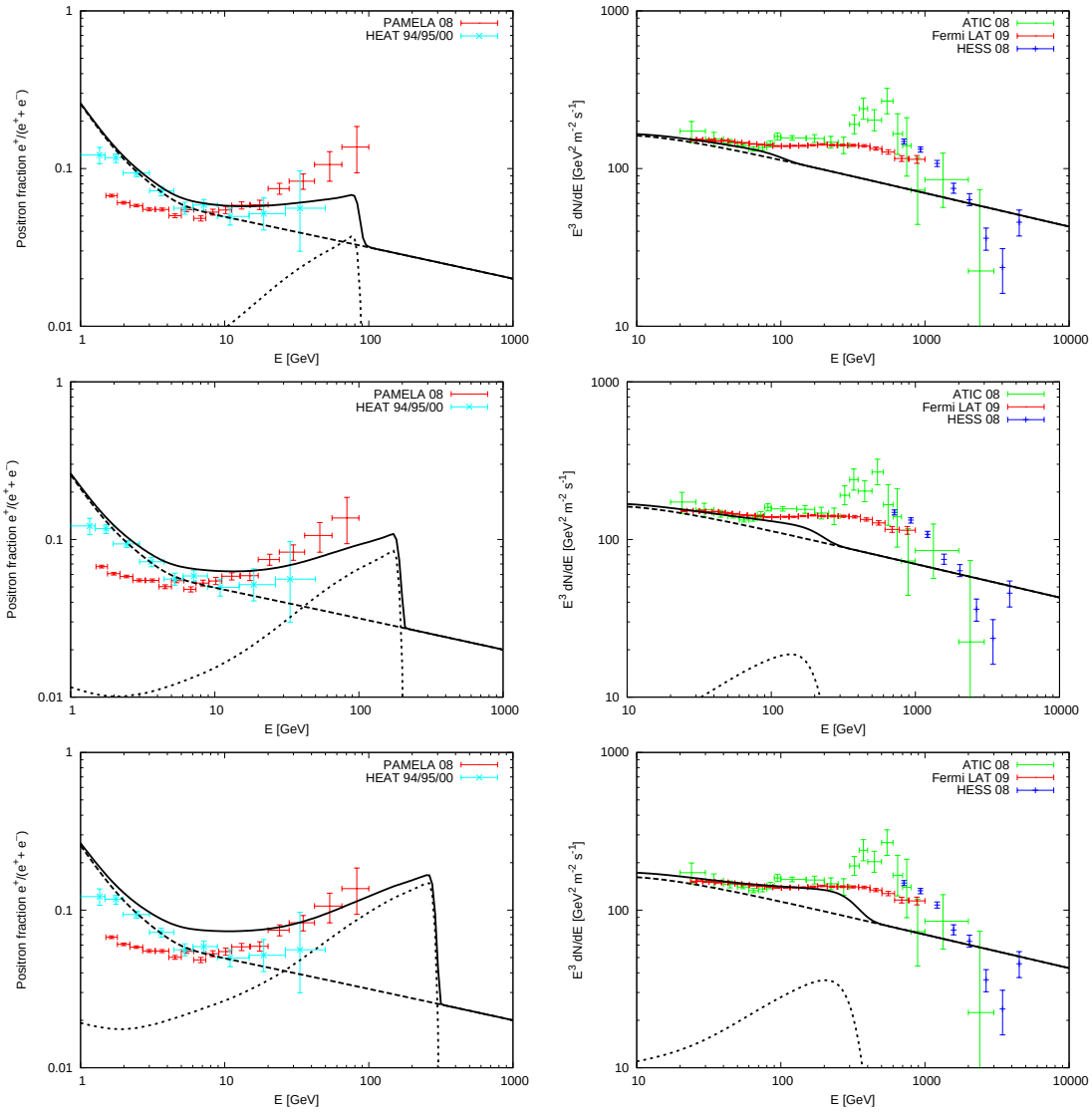

Figure 9.3: Contribution from dark matter decay to the positron fraction and the total electron + positron flux, compared with data from PAMELA and HEAT, and ATIC, Fermi LAT and H.E.S.S., respectively; $m_{3/2} = 200$ GeV, 400 , 600 GeV with the minimal lifetimes; for $W^{\pm}l^{\mp}$ decays democratic flavor dependence is assumed. The "model 0" background is used, and for comparison with Fermi LAT data a 25% energy resolution is taken into account.

Galactic interstellar radiation field at energies below 10 TeV [159]. Thus, the total flux is dominated by the halo component, yielding a slightly anisotropic gamma-ray flux [103] which is compatible with the EGRET observations [11]. For a detailed study of the prospects of detecting this anisotropy with the Fermi LAT, see Chapter 6.

The decay of gravitinos produces a continous spectrum of gamma rays which is determined by the fragmentation of the Higgs boson and the weak gauge bosons. Furthermore, there exists

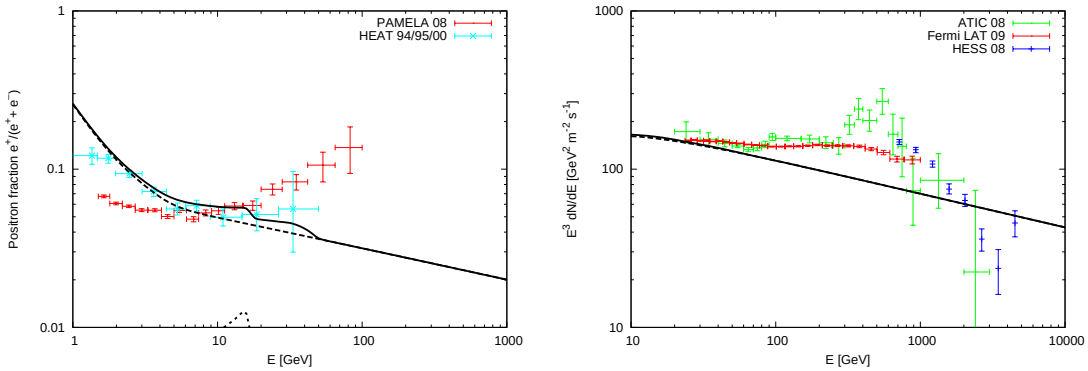

Figure 9.4: Contribution of gravitino decays to positron fraction and total electron + positron flux for $m_{3/2} = 100$ GeV and $\tau_{3/2} = 1 \times 10^{27}$ s.

a distinct spectral feature in the form of a gamma-ray line at the endpoint of the spectrum at $E_\gamma = m_{3/2}/2$ with an intensity that is model-dependent.[2] For our numerical analysis we shall use the typical branching ratio in this channel derived in Section 9.2,

$$\mathrm{BR}(\psi_{3/2} \to \gamma\nu) = 0.02 \left(\frac{200\,\mathrm{GeV}}{m_{3/2}} \right)^2 , \tag{9.32}$$

for gravitino masses in the range $m_{3/2} = 100 - 600\,\mathrm{GeV}$. In Fig. 9.5 we show the predicted diffuse gamma-ray flux for $m_{3/2} = 200,\ 400,\ 600\,\mathrm{GeV}$ and the respective lower bounds on the gravitino lifetime, as in Eq. (9.30). Therefore, the spectra shown correspond to upper bounds on the signal in gamma rays that can be expected from gravitino dark matter decay when taking the antiproton constraints into account.

For comparison, we show two sets of data points obtained from the EGRET measurements of the diffuse extragalactic gamma-ray background using different models of the Galactic foreground emission. An analysis by Strong, Moskalenko and Reimer using a model optimized to better simulate the the Galactic diffuse emission revealed a power law below 1 GeV, with an intriguing deviation from the power law above 1 GeV, which is precisely the kind of signature one might expect from a dark matter contribution (see, for example, [11] for an interpretation of the EGRET GeV excess in terms of gravitino decay). This deviation has not been confirmed by Fermi LAT, however, and was most likely of instrumental nature [357].

For our present analysis we will show both sets of data as extracted by Sreekumar *et al.* [155] and by Strong, Moskalenko and Reimer [251], as the status of the extragalactic background is presently unclear. For comparison with the data points, we have averaged the slightly anisotropic halo signal [103] over the whole sky, excluding a band of $\pm 10^\circ$ around the

[2] We neglect in our analysis the contribution to the gamma-ray flux from inverse Compton scattering of high-energy electrons and positrons on the interstellar radiation field. We estimate that this contribution is peaked at energies smaller than 0.1 GeV and has an intensity $E^2 dJ/dE \lesssim \mathcal{O}(10^{-7})\,\mathrm{GeV}\,(\mathrm{cm}^2\ \mathrm{sr\,s})^{-1}$ [197], thus giving a negligible contribution to the total flux, which is constrained by EGRET to be $E^2 dJ/dE \sim 10^{-6}\,\mathrm{GeV}\,(\mathrm{cm}^2\ \mathrm{sr\,s})^{-1}$ at $E_\gamma = 0.1\,\mathrm{GeV}$. However, the inverse Compton contribution can be sizable for larger dark matter masses [3, 197]. See Chapters 3 and 6 for a detailed discussion.

Galactic disk.[3] We have conservatively used an energy resolution $\sigma(E)/E = 15\%$ as quoted by the Fermi LAT collaboration [358].

It is noteworthy that for both choices of the extragalactic background, the antiproton constraint allows for a sizable deviation from a power-law background if the gravitino mass is above 200 GeV. Therefore, if such a deviation with the proper angular dependence were observed by Fermi LAT, the scenario of gravitino dark matter would gain support. Furthermore, the existence of a gamma-ray line at the endpoint of the spectrum is predicted, with an intensity that depends on the model of R-parity breaking, as discussed in Section 9.2. The observation of such a line would be a smoking-gun signature for the presence of a particle-physics process. This line could also be observed by Fermi LAT in the diffuse gamma-ray background, but also by the ground-based Cherenkov telescopes MAGIC, H.E.S.S., or VERITAS in galaxies such as M31 [1, 103] (see Chapter 7 for a detailed discussion). For smaller gravitino masses the gamma-ray line becomes more prominent, whereas the contribution to the continuous part of the spectrum decreases. This is illustrated in Fig. 9.6 for $m_{3/2} = 100\,\mathrm{GeV}$.

The observation of the discussed features in the diffuse gamma-ray spectrum might, if interpreted as the result of gravitino decay, open the exciting possibility of constraining the reheating temperature of the Universe. Namely, the thermal relic abundance of gravitinos is given by [83, 345, 359]

$$\Omega_{3/2}^{\mathrm{th}} h^2 \simeq 0.5 \left(\frac{T_{\mathrm{R}}}{10^{10}\,\mathrm{GeV}}\right) \left(\frac{100\,\mathrm{GeV}}{m_{3/2}}\right) \left(\frac{m_{\tilde{g}}}{1\,\mathrm{TeV}}\right)^2 . \tag{9.33}$$

Therefore, imposing that the thermal abundance of gravitinos should not be larger than the total dark matter abundance, the measurement of the gravitino mass by Fermi LAT and the measurement of the gluino mass at the LHC would imply the following upper bound on the reheating temperature of the Universe:

$$T_{\mathrm{R}} \lesssim 2 \times 10^9\,\mathrm{GeV} \left(\frac{\Omega_{3/2} h^2}{0.1}\right) \left(\frac{100\,\mathrm{GeV}}{m_{3/2}}\right)^{-1} \left(\frac{m_{\tilde{g}}}{1\,\mathrm{TeV}}\right)^{-2} , \tag{9.34}$$

which is saturated when all the dark matter gravitinos are of thermal origin. This bound has important implications for the scenario of thermal leptogenesis, which requires $T_{\mathrm{R}} \gtrsim 10^9\,\mathrm{GeV}$ [360, 361], as well as for many inflationary scenarios.

9.5 Conclusions

In supersymmetric theories with small R-parity breaking thermally produced gravitinos can account for the observed dark matter, consistent with leptogenesis and nucleosynthesis. Gravitino decays then contribute to the antimatter component of cosmic rays as well as to the gamma-ray flux. We consider gravitino masses below 600 GeV, which are consistent with

[3] The halo signal would have a larger degree of anisotropy if the dark matter halo is not completely uniform but present substructures, as suggested by N-body simulations of Milky Way-size galaxies. In the present calculation we are interested in the average flux in the whole sky excluding the Galactic disk, which depends on the total amount of dark matter in this region and not on the way in which it is distributed. Therefore, for our purposes it is a good approximation to neglect substructures and to assume a smooth dark matter halo profile.

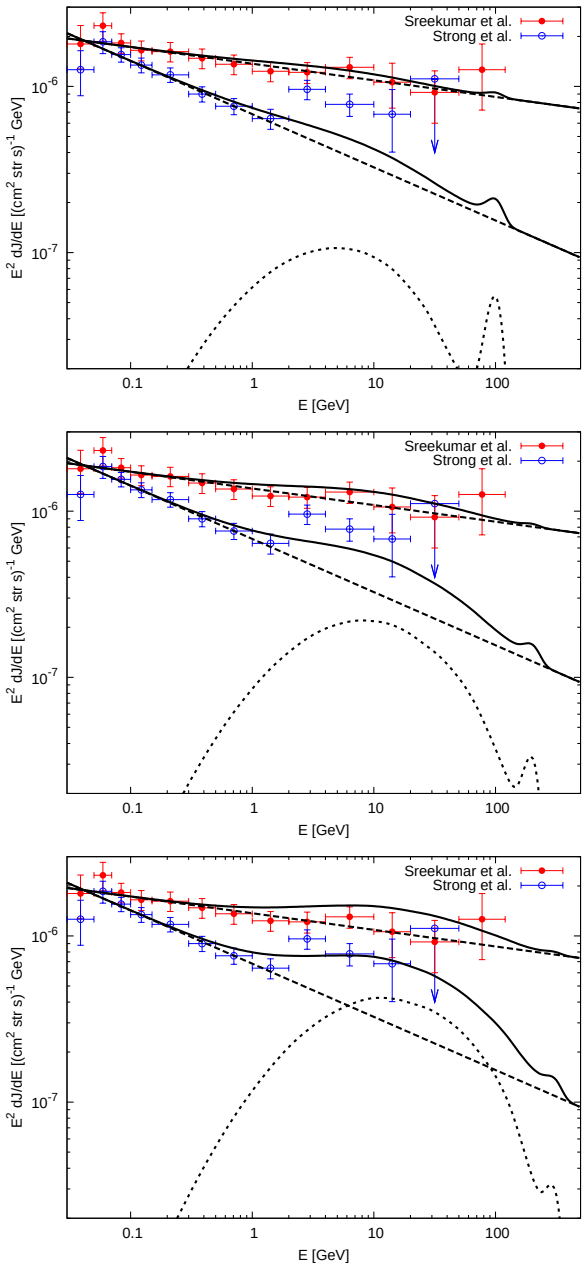

Figure 9.5: Predicted gamma-ray flux for $m_{3/2} = 200, 400, 600\,\text{GeV}$ for the minimal lifetimes compatible with antiproton constraints, Eq. (9.30). We assume decays purely into electron flavor here. We show both the extragalactic gamma-ray background obtained by Sreekumar *et al.* as well as the background obtained by Strong, Moskalenko and Reimer.

universal boundary conditions at the GUT scale.

Gravitino decays into Standard Model particles can be studied in a model-independent way by means of an operator analysis. For sufficiently large gravitino masses the dimension-

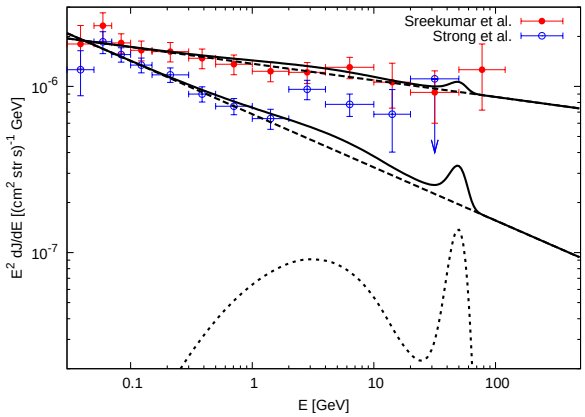

Figure 9.6: Predicted gamma-ray flux for $m_{3/2} = 100\,\text{GeV}$ and $\tau_{3/2} = 1 \times 10^{27}\,\text{s}$. We show both the extragalactic gamma-ray background obtained by Sreekumar *et al.* as well as the background obtained by Strong, Moskalenko and Reimer.

five operator dominates. This means that the branching ratios into $h^0\nu$, $Z^0\nu$ and $W^{\pm}l^{\mp}$ are fixed, except for the dependence on lepton flavor. As a consequence, the gamma-ray flux is essentially determined once the antiproton flux is known. The positron flux, on the other hand, is model-dependent. The intensity of the gamma-ray line from the decay $\psi_{3/2} \to \gamma\nu$ is controlled by the dimension-six operator. Hence, it is suppressed compared to the continous gamma-ray spectrum. Its intensity is model-dependent and decreases with increasing gravitino mass. Therefore, the presence of this spectral feature is not a generic prediction of this scenario.

Electron and positron fluxes from gravitino decays, together with the standard `GALPROP` background, cannot account for both the PAMELA positron fraction and the electron + positron flux measured by Fermi LAT due to the upper bound we have imposed on the gravitino mass, which restricts the contribution to energies below 300 GeV. For gravitino dark matter, the hard high-energy e^+e^- flux therefore requires additional astrophysical sources. However, depending on the gravitino mass and the background, the dark matter contribution to the electron and positron fluxes can be non-negligible.

Present data on charged cosmic rays allow for a sizable contribution of gravitino dark matter to the gamma-ray spectrum, in particular a line at an energy below 300 GeV. The non-observation of such a line would place an upper bound on the gravitino lifetime, and therefore on the strength of R-parity breaking, restricting possible signatures at the LHC.

Chapter 10

Hidden-Gaugino Dark Matter

If interpreted in terms of decaying dark matter, the steep rise in the positron fraction of cosmic rays above 10 GeV, as observed by the PAMELA experiment, suggests an underlying production mechanism that favors leptophilic channels. In this chapter, which is based on the publication [7], we consider a scenario where a portion of the dark matter is made of the gauginos of an unbroken hidden-sector $U(1)_X$, which interact with the visible sector only via a tiny kinetic mixing. The second component of the dark matter is made of neutralinos, and depending on the mass spectrum, either the lighest neutralino or the hidden gaugino becomes unstable and subject to decay. We analyze the cosmic rays, namely the contributions to the positron, the extragalactic gamma-ray and the antiproton flux, which potentially result from these decays and demonstrate that the production of antiprotons can be naturally suppressed. Therefore, this model is a realization of a leptophilic decaying dark matter scenario favored by the model-independent analysis in Chapter 4. We also briefly discuss in this chapter the apparent double-peak structure in the ATIC data in light of cascade-decaying hidden gauginos, even though the existence of this feature has not been confirmed by later Fermi LAT measurements.

10.1 Introduction

We will speculate in this scenario that a tiny kinetic mixing $\mathcal{O}(10^{-24})$ induces the decay of the dark matter particles into lighter supersymmetric particles and positrons, thus providing a potential explanation to the excess observed by PAMELA. Assuming exact R-parity conservation, two possibilities may arise. First, we will study the case that the hidden gaugino mass is smaller than the lightest neutralino mass. We will show that the neutralino mostly decays into two charged leptons and the hidden gaugino. The hard positrons produced in the decay can then potentially explain the steep rise in the positron fraction observed by PAMELA and the absence of an excess in the antiproton flux. Second, we will study the case that the lightest neutralino mass is smaller than the hidden gaugino mass. If this is the case, it is the hidden gaugino which decays into the lightest neutralino, either directly or in a cascade decay, when there are supersymmetric particles with masses between the hidden gaugino mass and the lightest neutralino mass. Either particle could be the dominant component of dark matter. However, we will focus in this work on the possibility that the dominant component of dark matter is the lightest neutralino, which may allow direct dark matter detection.

This chapter is organized as follows. In Section 10.2 we will briefly review the main features and possible origins of scenarios with a hidden Abelian gauge group and kinetic mixing. In Section 10.3 we will present our results for the decaying neutralino case and the decaying hidden gaugino case. Lastly, in Section 10.4 we will present our conclusions.

10.2 The Model

Many extensions of the Minimal Supersymmetric Standard Model (MSSM) contemplate the possibility of a hidden sector, consisting of superfields which are singlets under the Standard Model gauge group. Hidden-sector superfields usually couple very weakly to our observable sector, thus constituting a very natural arena for finding dark matter candidates. We consider an extension of the MSSM by a hidden Abelian gauge group $U(1)_X$ (for details about the model and a discussion of its phenomenology and cosmological constraints see [100]). This gauge group is assumed to remain unbroken at low energies and couples to the MSSM only through a tiny kinetic mixing χ with the hypercharge $U(1)_Y$,

$$G = SU(3)_C \times SU(2)_L \times \underbrace{U(1)_Y \times U(1)_X}_{\text{kinetic mixing} \sim \chi} . \tag{10.1}$$

For simplicity, we assume that all states that are charged under the hidden-sector gauge group are heavy and therefore decouple from the observable sector. However, as shown in [100], a non-zero mass mixing of the order $\delta M \sim \mathcal{O}(\chi \cdot M_X)$ between hidden gaugino and Bino generally remains. More precisely, in the basis where the kinetic terms are canonical, the extended (5×5) neutralino mass matrix reads, to lowest order in χ,

$$\mathcal{M}_N = \begin{pmatrix} M_X & \delta M & 0 & 0 & 0 \\ \delta M & M_1 & 0 & -M_Z c_\beta s_\mathrm{W} & M_Z s_\beta s_\mathrm{W} \\ 0 & 0 & M_2 & M_Z c_\beta c_\mathrm{W} & -M_Z s_\beta c_\mathrm{W} \\ 0 & -M_Z c_\beta s_\mathrm{W} & M_Z c_\beta c_\mathrm{W} & 0 & -\mu \\ 0 & M_Z s_\beta s_\mathrm{W} & -M_Z s_\beta c_\mathrm{W} & -\mu & 0 \end{pmatrix} \tag{10.2}$$

where M_Z is the Z boson mass, μ is the MSSM μ-parameter, $s_\mathrm{W} \equiv \sin\theta_\mathrm{W}$, $c_\mathrm{W} \equiv \cos\theta_\mathrm{W}$ are the sine and cosine of the Weinberg angle, and $s_\beta \equiv \sin\beta$, $c_\beta \equiv \cos\beta$ are the sine and cosine of $\beta \equiv \arctan(\langle v_u \rangle / \langle v_d \rangle)$. M_X denotes the mass of the $U(1)_X$ gaugino, whereas M_1 and M_2 are the $U(1)_Y$ and $SU(2)_L$ gaugino masses.

Below we will concentrate on the case where the lightest supersymmetric particle in the visible sector is a bino-like neutralino χ_1^0. Then, depending on the masses of the hidden gaugino and the neutralino, one of the particles becomes unstable with a lifetime that is roughly given by

$$\tau_{X,\chi_1^0} \sim \mathcal{O}(10^{-2} - 10^{1}) \times 10^{26}\,\mathrm{s} \left(\frac{M_{X,\chi_1^0}}{100\,\mathrm{GeV}}\right)^{-1} \left(\frac{\theta}{10^{-24}}\right)^{-2} , \tag{10.3}$$

where we made use of the mixing angle $\theta \simeq \delta M / |M_{\chi_1^0} - M_X| \sim \mathcal{O}(\chi)$. The exact prefactor depends on the dominant decay modes and on the mass spectrum of the supersymmetric particles. However, it is apparent that a lifetime around $10^{26}\,\mathrm{s}$, as required to fit the PAMELA excess with decaying dark matter particles, implies an extremely small mixing on the order of

$\chi \sim 10^{-24}$. Note that the mixing must be somewhat larger when the decaying particle is only a subdominant component of the dark matter, but an upper bound of roughly $\sim 10^{-20}$ holds from the requirement that the relic abundance has not already decayed before the present day.

The thermal production of hidden gauginos by oscillations between Bino and hidden gaugino, which generally takes place in the primeval MSSM plasma, is irrelevant for the mixing parameters that we are looking at here [100]. However, the hidden gaugino may be produced non-thermally, *e.g.* in the decay of a heavy gravitino, or it may be a thermal relic of the hidden sector [362]. In the latter case one requires additional particles that are charged under the hidden $U(1)_X$ with masses around M_X, however. For simplicity, we will assume throughout this chapter that the lightest neutralino in the visible sector has the right relic energy density to make up the dominant part of the observed dark matter abundance, whereas the abundance of the hidden gaugino is subdominant, $\rho_X \ll \rho_{\chi_1^0} \simeq \rho_{\rm DM}$.

The actual mass scale of the hidden gaugino depends on how the breaking of supersymmetry is mediated to the visible sector and the hidden $U(1)_X$. If the soft masses $\sim m_{\rm soft}$ in the visible sector arise from gauge mediation, whereas the $U(1)_X$ couples to the supersymmetry-breaking sector only gravitationally, the predicted mass hierarchy is $m_{\rm soft} \gg m_{3/2} \sim M_X$, where $m_{3/2}$ denotes the mass of the gravitino. In this scenario the lightest neutralino cannot be the dark matter because it would decay into the gravitino in the early Universe. However, if we assume gravity mediation to the visible sector and anomaly mediation [363] to the $U(1)_X$, one expects $m_{\rm soft} \sim m_{3/2} \gg M_X$. If the soft masses of both the visible sector and the $U(1)_X$ arise from gravity mediation, one in general expects that all masses are of the same order, $m_{\rm soft} \sim m_{3/2} \sim M_X$. Below we will assume that the gravitino is heavy enough to have no impact on the decay modes, $m_{3/2} > \max(M_X, M_{\chi_1^0})$.

Neutralino/hidden gaugino decay modes	
$M_{\chi_1^0} > M_X$	$M_{\chi_1^0} < M_X$
$\chi_1^0 \to \begin{cases} f\bar{f}\tilde{\bar{f}}^*_{R/L} \to f\bar{f}X \\ Xh^0 \\ XZ^0 \end{cases}$	$X \to \begin{cases} f\bar{f}\tilde{\bar{f}}^{(*)}_{R/L} \to f\bar{f}\chi_i^0 \\ \chi_i^0 h^0 \\ \chi_i^0 Z^0 \\ \chi_j^\pm W^\mp \end{cases}$

Table 10.1: Dominant decay modes of the neutralino and the hidden gaugino, respectively. Depending on the masses M_X of the hidden gaugino and $M_{\chi_1^0}$ of the lightest neutralino, one of the two particles becomes unstable with a lifetime roughly given by Eq. (10.3). Since the three-body decay into fermion pair $f\bar{f}$ is mainly mediated by virtual sfermions, $\tilde{f}^*$, we show this explicitly. Furthermore, when a sfermion is lighter than the decaying particle, the corresponding three-body decay crosses over to a cascade decay. The subsequent decay and fragmentation of the Higgs and gauge bosons, charginos and neutralinos is not indicated. Note that the symbol f represents any lepton or quark.

Additional $U(1)$ gauge factors are a generic feature of string compactifications. For example, in the "mini-landscape" of orbifold compactifications of the heterotic string [364] one encounters, at the compactification scale, a breaking of the gauge symmetry to a theory involving many hidden $U(1)$s, *e.g.* $E_8 \times E_8 \to G_{\rm SM} \times U(1)^4 \times \left[SO(8) \times SU(2) \times U(1)^3\right]$ and the like. Similarly, type-II compactifications generically invoke hidden-sector $U(1)$s, often also for global consistency requirements. Some of these hidden $U(1)$s may remain unbroken down to very small scales [365].

Kinetic mixing is generated by the exchange of heavy messengers that couple both to the hypercharge $U(1)_Y$ and the hidden $U(1)_X$. Correspondingly, it is loop suppressed, $\chi = g_Y g_X C/(16\pi^2)$, where g_Y and g_X are the Abelian gauge couplings and C is a dimensionless constant. In field-theoretic setups, the latter is naturally of order one [366] and thus way too large for our purposes. However, it can be much smaller if there are additional gauge or global symmetries (*cf.* [100, 266]). Moreover, in models arising from string compactifications rather small mixings seem to be generic [365, 367, 368, 369]. In the context of compactifications of the heterotic string, the mixing can be quite small, but is generally still too large for our purposes. However, a sufficiently strong suppression of the coupling could be achieved in models with multiple $U(1)$s [100]. The required small mixing may also be obtained in scenarios with significant warping, such as KKLT [370], where the standard model stack of branes, notably the brane featuring the hypercharge $U(1)$, is placed at a special position – at the tip of a warped throat – while the hidden brane is separated from it by a distance d along the throat. In this case the kinetic mixing may be exponentially suppressed [369]. If a sufficiently strong suppression of the kinetic mixing can be achieved, the NLSP can be sufficiently stable to constitute the dark matter.

As mentioned above, depending on the mass spectrum of the supersymmetric particles, either the lightest neutralino χ_1^0 or the hidden gaugino X then becomes unstable. The relevant decay modes are shown in Table 10.1. These decays may be detectable as anomalous contributions to the cosmic-ray fluxes observed at Earth. We will discuss this in some detail in the next section.

10.3 Cosmic Rays from Leptophilic Dark Matter Decay

Below we will present our results for the cosmic-ray signatures of decaying neutralinos and decaying hidden gauginos.[1] In both cases we will start with an analysis of the predictions that follow when assuming that the visible sector is described by an exemplary point in the coannihilation region of the mSUGRA parameter space. This ensures a consistent cosmology in the visible sector and that all free parameters of the MSSM are fixed. After that we will go beyond this mSUGRA scenario and discuss how the comsic-ray signatures can change in more generic cases. This will include a discussion about cascade decays in light of the apparent double-peak structure in the ATIC data.

[1] For a short discussion of our model in light of the new Fermi LAT electron data [216] see the below.

10.3.1 Decaying Neutralinos

The potentially relevant decay modes for the case $M_X < M_{\chi_1^0}$, where the lightest neutralino can decay into the hidden gaugino, are summarized in Table 10.1. Beside the three-body decays, which produce fermion-antifermion pairs, we also have to take into account the decay into Higgs and Z^0 bosons. Throughout the analysis we will assume that the lightest neutralino χ_1^0 makes up the dominant part of the dark matter, $\rho_{\chi_1^0} \simeq \rho_{\rm DM}$.

mSUGRA point. As stated above, our exemplary mSUGRA model lies in the coannihilation region. The defining parameters of the model are $m_0 = 150\,\text{GeV}$, $m_{1/2} = 720\,\text{GeV}$, $A_0 = 0$, $\tan\beta = 10$ and sign $\mu = +1$. In this model the lightest neutralino has a mass of 301 GeV and the correct relic density to be the dark matter, $\Omega h^2 = 0.104$, where we calculated the mass spectrum and relic abundance with the aid of `DarkSUSY 5.0.4` [371]. As is typical for models in the coannihilation region, the three right-handed sleptons have masses around $304 - 307\,\text{GeV}$, which is similar to the mass of the lightest neutralino. The left-handed sleptons have masses around 500 GeV. Furthermore, this particular mSUGRA point, which features a spin-independent cross-section per proton of $2 \times 10^{-46}\,\text{cm}^2$, can be probed with the next-to-next generation direct dark matter detection experiments like XENON1T and LUX/ZEP.

We calculated the dominant branching ratios for the decay of the lightest neutralino using `FeynArts 3.4` [297] and `FormCalc 5.4` [298]. They are summarized in Table 10.2 for different masses of the hidden gaugino between 1 and 200 GeV. Most interestingly, the fraction of decays into charged leptonic final states is never below $\sim 65\%$. Beside the small masses of the right-handed sleptons, the underlying reason is the large μ-term, $\mu = 865\,\text{GeV}$, which suppresses the mixing between the Bino-like lightest neutralino χ_1^0, the hidden gaugino and the Higgsinos like $\mathcal{O}(M_Z/\mu)$. Furthermore, for large enough masses of the hidden gaugino, the decay into $h^0 X$ becomes kinematically forbidden. Note that although we present a concrete mSUGRA model for definiteness, the branching ratios shown here are typical for mSUGRA models in the coannihilation region, provided that the μ-term is large enough. If the latter is the case, three-body decays into charged leptons dominate over two-body decays into Higgs and gauge bosons.

To obtain the energy spectra of gamma rays, positrons and antiprotons that are produced in the neutralino decay we used the event generator `PYTHIA 6.4` [249]. From these spectra, the contribution to the cosmic-ray fluxes that are observed locally can be derived as described in Chapter 2. Throughout this Chapter we assume for the dark matter density the Navarro-Frenk-White halo profile as defined in Eq. (1.13) and Table 1.1 with a local dark matter density $\rho_\odot = 0.3\,\text{GeV}\,\text{cm}^{-3}$. Solar modulation is taken into account using the force field model described in Chapter 2.3 with a potential $\phi_{\rm F} = 500$ MV. The lifetime of the neutralino is always fixed by requiring a qualitatively good agreement with the positron fraction as measured by PAMELA. Note that due to the relatively light mass of the neutralino at our mSUGRA point it is not possible to reproduce the hard electron spectrum as measured by Fermi LAT and H.E.S.S. which extends up to 1 TeV. We will discuss the case of heavier dark matter particles below. As a complementary signature we also compute the corresponding gamma-ray fluxes from dark matter decay as explained in Chapter 3, where we neglect here the contribution from inverse Compton scattering of electrons and positrons.

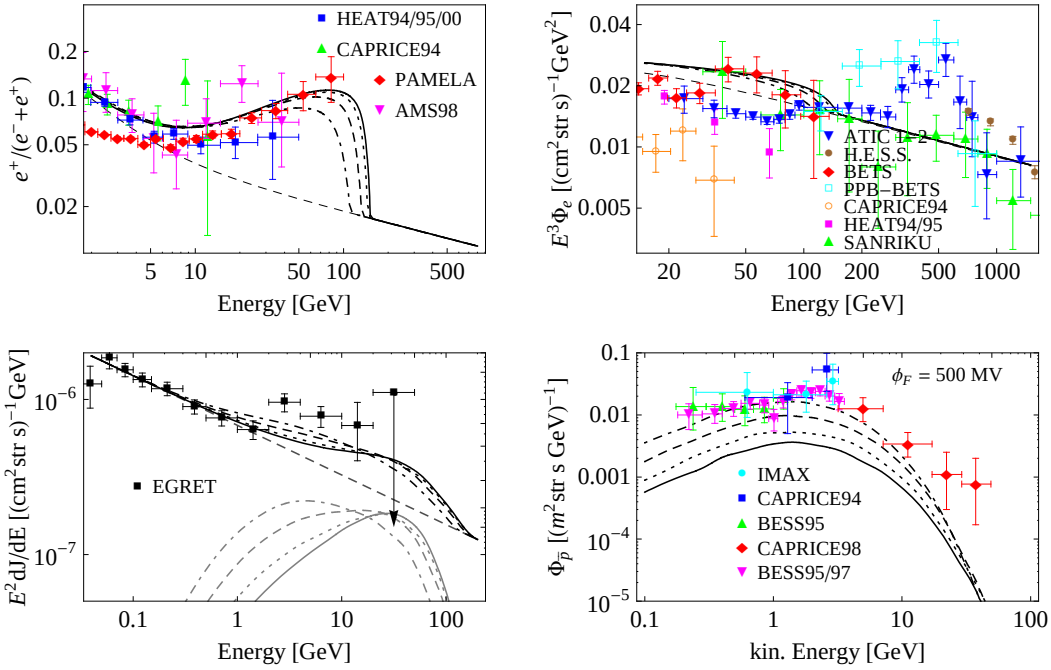

Figure 10.1: Positron fraction, total electron + positron flux, extragalactic gamma-ray flux and antiproton flux of a decaying neutralino χ_1^0 as predicted for our exemplary mSUGRA scenario. The branching ratios used are shown in Table 10.2. The mass of the decaying neutralino is 301 GeV, the hidden gaugino mass varies between 1 GeV (solid), 50 GeV (dotted), 100 GeV (dashed) and 150 GeV (dot-dashed). We use the MED propagation model. In the lower left plot, the grey lines indicate the flux without the extragalactic background, where we have averaged the signal over the whole sky, excluding the Galactic disk. In the lower right plot, we only show the primary antiproton flux without the background.

Our results are shown in Fig. 10.1. We find that in principle, the model can account for the observed excess in the positron fraction around $10 - 100$ GeV if the hidden gaugino is light, with a mass $M_X \lesssim 50$ GeV, although the predicted peak seems to rise too slowly to fully match the PAMELA data. This slow rise is due to the two-body decay into Higgs bosons whose subsequent fragmentation produces relatively soft positrons. From the lower plots of Fig. 10.1 it is apparent that the model is compatible with the EGRET measurements of the extragalactic gamma-ray background. Gamma rays with energies below ~ 10 GeV stem from the fragmentation of the Higgs boson whereas gamma rays at higher energies mainly come from $\tau^\pm$ decay. The contribution to the antiproton flux generally compatible with existing measurements, but can become problematic for hidden gaugino masses above ~ 100 GeV. Note that the uncertainty in the antiproton flux at Earth from dark matter decay can be as large as one order of magnitude in both directions [10, 145] due to our ignorance of the propagation parameters (*cf.* Chapter 2 and Fig. 4.6). Of course, the peak in the ATIC data around $300 - 800$ GeV cannot be reproduced in this setup.[2]

[2]In Fig. 10.1 we aimed to fit the PAMELA data. Since we restricted ourselves to using the background

Idealized three-body decay of a heavy neutralino. For different parameters of the underlying MSSM model, the above plots can mainly change in two ways. First, a larger value of the μ-parameter would reduce the branching ratio into Higgs and Z^0 bosons.[3] As a result, the rise in the positron fraction would be steeper and the contribution to the antiproton flux smaller. Second, a higher mass of the decaying neutralino would shift the peak to higher energies, as suggested by the ATIC data.

M_X	e^+e^-X	$\mu^+\mu^-X$	$\tau^+\tau^-X$	h^0X	Z^0X	$\tau_{\chi_1^0}[10^{26}\,\mathrm{s}]$
1	0.28	0.28	0.32	0.088	0.026	1.8
50	0.27	0.27	0.30	0.13	0.024	1.7
100	0.24	0.24	0.28	0.21	0.024	1.5
150	0.21	0.21	0.24	0.32	0.026	1.3
200	0.30	0.30	0.36	—	0.037	

Table 10.2: Branching ratios for the decay of a neutralino χ_1^0 into a lighter hidden gaugino X for different hidden gaugino masses M_X. In the visible sector, masses and mixing parameters are fixed by an mSUGRA scenario in the coannihilation region, as described in the text. The lightest neutralino has a mass of 301 GeV. Branching ratios of three-body decays into neutrinos, $\chi_1^0 \to \nu\bar{\nu}X$, and into quarks, $\chi_1^0 \to q\bar{q}X$, are smaller than 0.3% and 0.02%, respectively. The two-body decay into photons, $\chi_1^0 \to \gamma X$, is one-loop suppressed and neglected here. We also indicate the lifetime of the neutralino which gives the best fit to the data.

In Fig. 10.2 we show our results for the cosmic-ray fluxes in the idealized case where a Bino-like neutralino decays only via right-handed sleptons. This resembles scenarios with a large μ-term and large masses for the left-handed sleptons. The masses of the hidden gaugino and the neutralino χ_1^0 are 150 GeV and 500 GeV (solid lines) or 300 GeV and 1850 GeV (dotted lines), respectively. Note that the thick lines correspond to the standard case where the neutralino decays democratically into all three flavors. As expected, the rise in the positron fraction is now steeper and can easily accommodate the PAMELA data. Furthermore, a very heavy neutralino around 1.8 TeV allows to also account for the ATIC excess. In any case we find a clear excess in the extragalactic gamma-ray flux at energies above 10 GeV.

The gamma rays come mainly from $\tau^\pm$ decays and bremsstrahlung, but the latter is a subdominant effect as long as the three-body decay into charged leptons is democratic. However, the decay into taus can be suppressed in cases where the stau mixing angle is large, since the correspondingly larger left-handed component of the lighter stau weakens the coupling to the Bino-like neutralino and the hidden gaugino. For example, if the lighter stau is equally

fluxes from [372], as described above, this results in an electron + positron flux that lies above the ATIC data points at energies below 100 GeV. A lower normalization of the background flux of primary electrons would increase the agreement with ATIC, while at the same time flattening the positron fraction somewhat. Note that this behavior is common to all simultaneous fits to ATIC and PAMELA when using the above backgrounds. The same reasoning holds for Figs. 10.2, 10.3 and 10.4.

[3] A concrete lower bound on the μ-parameter is extremely model-dependent. However, in the concrete scenario with a Bino-like lightest neutralino where we take $\tan\beta = 10$, $\alpha_h = -0.1$ and assume that the right-handed sleptons have a mass around $1.02 \times M_{\chi_1^0}$, the lower bound $\mu \gtrsim \mathcal{O}(2M_{\chi_1^0})$ turns out to be sufficient to suppress the branching ratio into Higgs bosons below 20%.

left- and right-handed, the three-body decay into taus would be suppressed by a factor of ~ 0.5. To obtain a lower bound on the predicted gamma-ray signal, we also show the case where the neutralino decays into the first two generations only (see thin lines in Fig. 10.2). The gamma-ray flux is much smaller in this case and comes mainly from bremsstrahlung of the electrons produced in the three-body decay $\chi_1^0 \to e^+e^-X$. Note that in any case, we obtain a tight correlation between the contributions to the positron flux and the extragalactic gamma-ray flux where the latter comes mostly from $\tau^\pm$ decays in most cases.

Heavy Bino-like neutralinos with masses above a few hundred GeV are problematic for cosmology since they are typically overproduced, even when coannihilation with sleptons is taken into account. At the same time, Wino- and Higgsino-like lightest neutralinos do not exhibit the desired leptophilic decay.[4] However, these problems are absent if one considers scenarios where the hidden gaugino is heavier than the lightest neutralino, $M_X > M_{\chi_1^0}$. First, due to the mixing with the Bino, the interactions of the hidden gaugino are automatically "Bino-like." Second, for the small mixings that we consider bounds from overproduction arguments are irrelevant [7]. Note that the results from this paragraph can also hold in that case, provided one exchanges the roles of the hidden gaugino and the lightest neutralino. However, this requires that all sparticles, apart from the lightest neutralino, are heavier than the hidden gaugino. Generically, this will not be the case and the hidden gaugino will cascade-decay though the different sparticles down into the lightest neutralino. We will consider this in detail in the next subsection.

M_X [GeV]	$\nu\bar{\nu}$	$l\bar{l}$	$q\bar{q}$	$h^0\chi_i^0$	$Z^0\chi_i^0$	$W^\pm\chi_i^\mp$	$\tau_X[10^{23}\,\mathrm{s}]$
600	0.018	0.982	—	0.001	0.000	—	1.1
700	0.056	0.929	—	0.006	0.000	0.009	
800	0.056	0.846	—	0.035	0.002	0.061	1.0
850	0.007	0.498	—	0.173	0.012	0.310	
900	0.153	0.537	—	0.107	0.009	0.194	0.8
1000	0.141	0.811	—	0.014	0.010	0.024	
1200	0.133	0.768	—	0.027	0.025	0.047	0.7
1400	0.132	0.741	0.016	0.029	0.028	0.054	
1600	0.125	0.685	0.084	0.027	0.027	0.052	

Table 10.3: Branching ratios of the dominant decay modes of a hidden gaugino that cascade-decays into MSSM particles. The underlying scenario is our chosen mSUGRA reference point as described in the text. The decay into neutrinos and charged leptons is essentially democratic in all three flavors. We also indicate the lifetime of the hidden gaugino that gives the best fit to the PAMELA data, assuming an energy density of $\rho_X = 10^{-3}\rho_{\mathrm{DM}}$.

10.3.2 Decaying Hidden Gauginos

A hidden gaugino that is heavier than the lightest neutralino, $M_X > M_{\chi_1^0}$, turns out to be more appealing from the phenomenological point of view. In this case, the mass of the lightest

[4] Winos only couple to left-handed sleptons, which are typically heavier than the right-handed ones, whereas Higgsinos can easily decay to the Higgs boson.

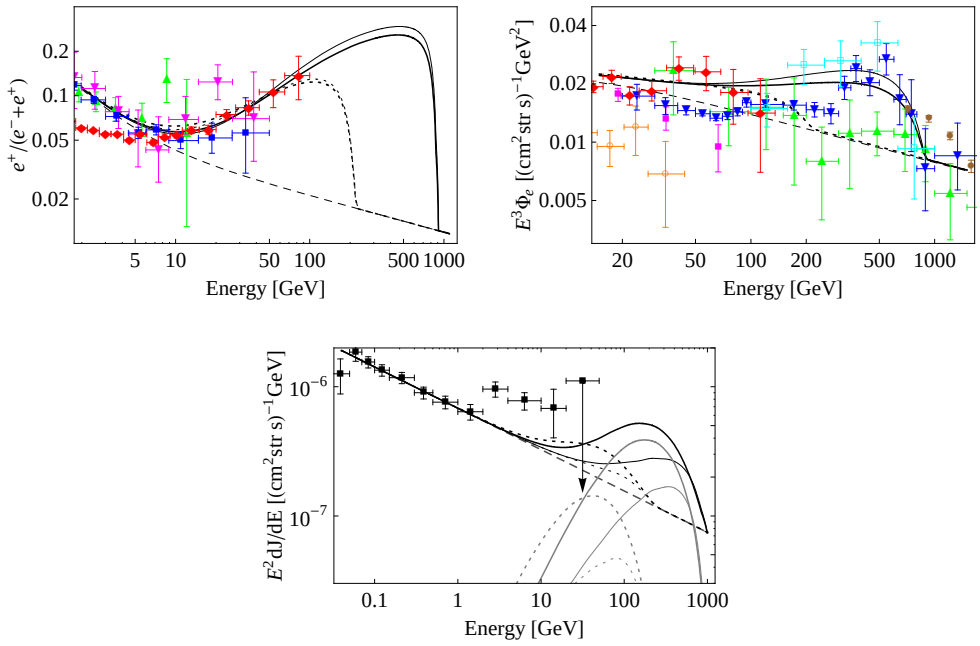

Figure 10.2: Positron fraction, total electron + positron flux and extragalactic gamma-ray flux for an idealized, three-body decaying Bino-like neutralino. We neglect effects from h^0 and Z^0 bosons and assume pure flavor-democratic three-body decays including charged lepton pairs. The masses of the neutralino and the hidden gaugino are 500 GeV and 150 GeV (thick solid lines) or 1850 GeV and 300 GeV (thick dotted lines), respectively. The thin lines show the predictions when the decay into the tau channel is neglected. The mass of the right-handed sleptons is assumed to be a factor 1.1 larger than the neutralino mass.

neutralino can be small, of the order of a few hundred GeV, and the hidden gaugino automatically possesses the "Bino-like" interactions which are desirable for the leptophilic decay. We will again assume that the lightest neutralino makes up most of the dark matter, whereas the hidden gaugino contributes only a subdominant part $\rho_X \ll \rho_{\chi_1^0}$ to the overall matter density of the Universe. Note that in this case the lifetime of the hidden gaugino can be as small as $\tau_X \sim 10^{18}$ s, around the current age of the Universe, provided that its relic abundance is small enough. Secondly, we will consider the multi-peak structure of a cascade-decaying hidden gaugino in light of the ATIC data.

mSUGRA point. The considerations in this paragraph are again based on the mSUGRA scenario described above. Depending on the mass of the hidden gaugino, its decay can produce fermions, neutralinos, charginos, Higgs and gauge bosons as described by Table 10.1. The corresponding branching ratios are summarized in Table 10.3, where we do not show the subsequent decays of the neutralinos $\chi^0_{2,3,4}$ and charginos $\chi^\pm_{1,2}$ for simplicity.[5]

[5]These subsequent decays are taken into account in our calculations. We singled out the dominant decay modes in our reference mSUGRA model and used them in the PYTHIA code: $X \to h^0\chi^0_4$, $X \to Z^0\chi^0_3$, $X \to$

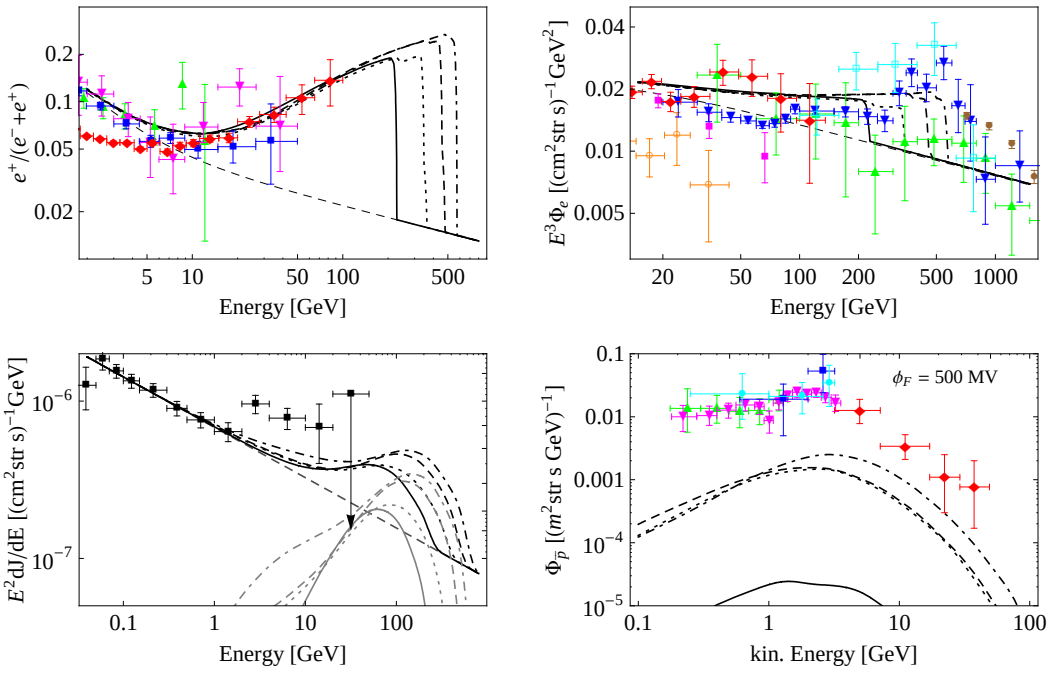

Figure 10.3: Positron fraction, extragalactic gamma-ray flux, antiproton flux and total electron + positron flux from the decay of a hidden gaugino as predicted by our mSUGRA scenario. The branching ratios are shown in Table 10.3. The mass of the hidden gaugino varies between 600 GeV (solid), 800 GeV (dotted), 1000 GeV (dashed), and 1200 GeV (dash-dotted).

As is apparent from Table 10.3, the decay into charged lepton/slepton pairs is dominant in the whole mass range $M_X \simeq 600 - 1000\,\text{GeV}$ that we consider. The decay into quarks is suppressed by the large squark masses, $m_{\tilde{q}} \gtrsim 1.1\,\text{TeV}$, whereas the decay into h^0, Z^0 and $W^\pm$ bosons is suppressed by the small mixing between Higgsinos and the hidden gaugino. However, this mixing can become enhanced when the masses of the Higgsinos become comparable to the mass of the hidden gaugino, which happens around $M_X \sim 870\,\text{GeV}$. Our results for the cosmic-ray fluxes are shown in Fig. 10.3 for hidden gaugino masses between 600 GeV and 1200 GeV, where we adjusted the lifetime of the hidden gaugino to fit the PAMELA data. For all masses of the hidden gaugino that we consider, the predictions for the positron fraction are in qualitatively good agreement with the PAMELA data. At the same time, the contribution to the antiproton flux lies well below the measurements and hence is safe in all cases. Furthermore, we obtain contributions to the extragalactic gamma-ray flux which are mainly due to $\tau^\pm$ decays. They are compatible with the EGRET measurements, but could show up in future observations as an excess above the background. The total electron + positron flux is also compatible with the different measurements and we predict a sharp step at high energies.

$W^\pm\chi_2^\mp$, $\chi_3^0 \to \chi_1^0 Z^0$, $\chi_4^0 \to \chi_1^0 h^0$ and $\chi_2^\pm \to \chi_1^\pm Z^0$ (28%), $\chi_1^\pm h^0$ (27%), $\chi_2^0 W\pm$ (36%). The decay of χ_2^0 and $\chi_1^\pm$ only produces leptons and is neglected.

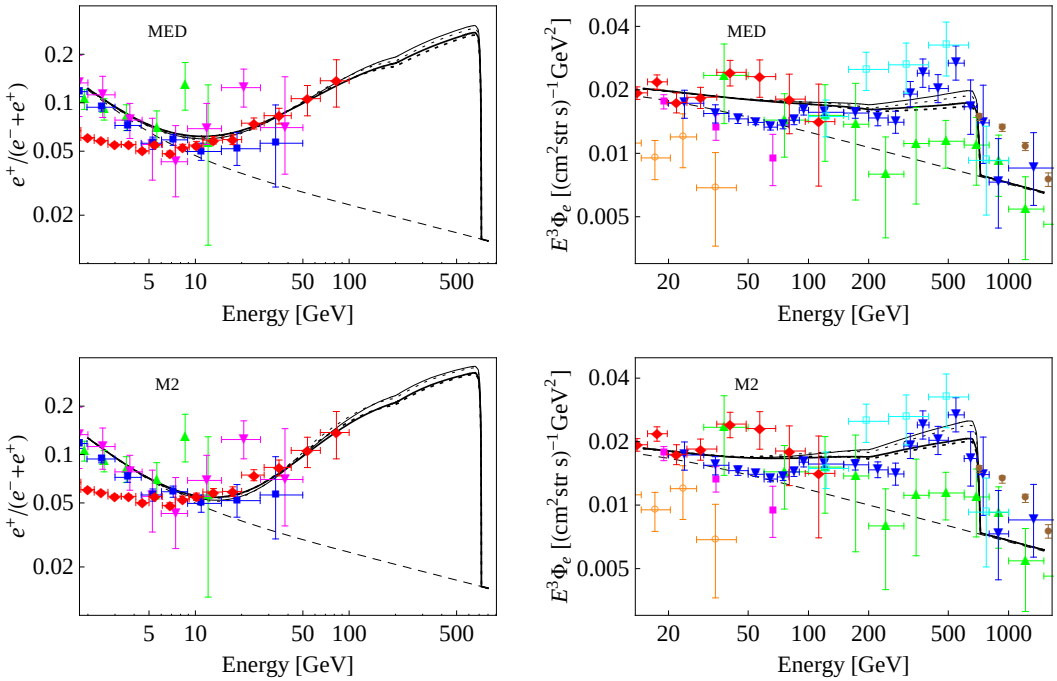

Figure 10.4: Positron fraction and total electron + positron flux for an idealized cascade-decaying hidden gaugino. As in Fig. 10.5, only leptonic decay modes are taken into account. We assume democratic decay into the three right-handed sleptons (thick lines), or into only the selectron and smuon (thin lines). The mass of the lightest neutralino varies between 150 GeV (solid) and 1 TeV (dotted). We show the plots for the propagation models MED (upper plots) and M2 (lower plots) of [142] (see Table 2.1).

Multi-peak structures from cascade decays. As already evident in Fig. 10.3, the energy distribution of particles produced in cascade decays in general features several peaks. Their exact position carries information about the masses of the different intermediate particles. It is intriguing to speculate that the apparent double-peak structure of the ATIC data originates from cascade-decaying particles [111].[6]

In the case of the decaying hidden gaugino, the energy spectrum of positrons in general possesses two pronounced peaks. These peaks stem from decays with intermediate selectrons. To simplify the discussion we will neglect decay modes that produce h^0, Z^0 and $W^\pm$ bosons or left-handed sleptons, and we will assume democratic decay into all three flavors. If we furthermore assume approximate mass degeneracy for the three right-handed sleptons, we are left with only three free parameters: the mass of the hidden gaugino M_X, the mass of the lightest neutralino $M_{\chi_1^0}$, and the mass scale of the right-handed sleptons $M_{\tilde{l}_R}$.

In Fig. 10.5 we show the corresponding energy spectrum of positrons for two different

[6]Note, however, that the electron data from Fermi LAT [216, 231] does not confirm the double-peak structure seen by ATIC. For a discussion about the implications of the Fermi LAT data see below. Other explanations for the double-peak structures can be found in [207].

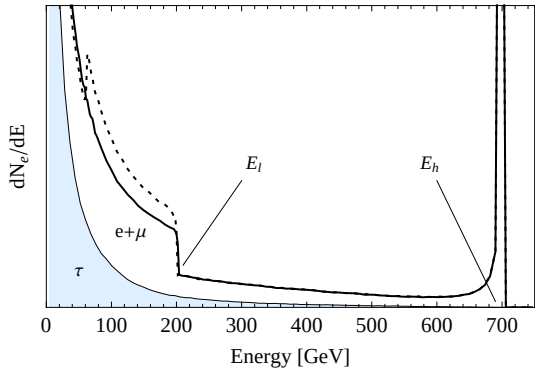

Figure 10.5: Energy spectrum of positrons from an idealized cascade-decaying hidden gaugino. Only two-body decay into right-handed slepton/lepton pairs is taken into account. The slepton subsequently decays into the lightest neutralino. The spectrum exhibits two pronounced peaks which we denote by E_h and E_l. We show plots for a lightest neutralino with mass 150 GeV (solid) and 1 TeV (dashed). The position of the peaks is fixed to $E_h = 700\,\text{GeV}$ and $E_l = 200\,\text{GeV}$, as suggested by the ATIC data. The masses of the right-handed sleptons then follow from Eq. (10.4). We also indicate the part of the positrons that comes solely from the tau/stau decay channel (blue area).

sets of particle masses. The two pronounced peaks are denoted by E_h and E_l. Fixing the neutralino mass and the position of the peaks determines the slepton and hidden-gaugino masses according to

$$M_{\tilde{l}_R}^2 = M_{\chi_1^0}^2 + 2E_l^2 \left(\sqrt{\left(\frac{E_h}{E_l} - 1\right)^2 + \left(\frac{M_{\chi_1^0}}{E_l}\right)^2} - \frac{E_h}{E_l} + 1 \right) , \tag{10.4}$$

$$M_X = E_h + \sqrt{E_h^2 + M_{\tilde{l}_R}^2} \, . \tag{10.5}$$

As a simple attempt to fit the ATIC data with an idealized cascade-decaying hidden gaugino, we take the values $E_h = 700\,\text{GeV}$ and $E_l = 200\,\text{GeV}$. After this, a neutralino mass of $M_{\chi_1^0} = 150\,\text{GeV}$ (1000 GeV) implies a slepton mass of $M_{\tilde{l}_R} = 177\,\text{GeV}$ (1117 GeV) and a hidden-gaugino mass of $M_X = 1422\,\text{GeV}$ (2018 GeV).

The resulting cosmic-ray fluxes for the two neutralino masses are shown in Fig. 10.4 (upper plots, thick lines), where we used the MED propagation model. Interestingly, the predicted fluxes are practically the same for the two cases, although the bump structure is slightly enhanced in the case of the heavier neutralino. The lower plots are based on the M2 propagation model as an example of a model with a thin diffusion zone, $L = 1\,\text{kpc}$ (as opposed to $L = 4\,\text{kpc}$ in the case of the MED model). Since in these scenarios electrons and positrons are more likely to escape the diffusion zone before having lost much of their energy, the observable spectrum becomes steeper. This effect can improve the agreement with the sharp features of the ATIC data. However, note that propagation models with thin diffusion zones have problems with the correct prediction of the flux of unstable isotopes like, for example, ^{10}Be or ^{14}C [134].[7]

[7]Furthermore, the change of the propagation model in principle also changes the predictions for the back-

Up to now we have assumed a vanishing stau mixing angle and democratic decay into all three flavors. However, if the stau mixing angle is large, the decay mode into tau/stau pairs would be suppressed, as discussed above. In Fig. 10.5 we indicated the part of the positrons that comes from the stau/tau channel in the case of democratic decay (blue region). A suppression of this channel can lead to a relative enhancement of the two-peak structure of the cascade decay. This effect is shown by the thin lines in Fig. 10.4, where we only took into account the decay modes into muon/smuon and electron/selectron pairs. As expected, the peaks at high energy become more pronounced, and the spectrum becomes harder at low energies, although the effect is not dramatic.

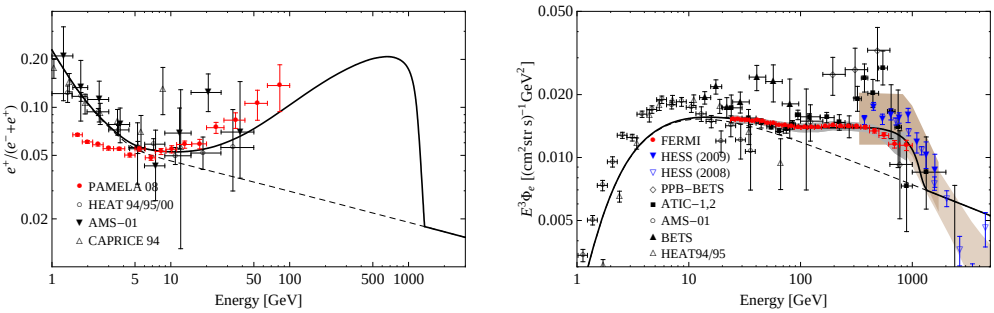

Figure 10.6: Positron fraction and total electron + positron flux for an idealized, three-body decaying Bino-like neutralino with mass 2500 GeV, decaying into a light hidden gaugino. We include the recent data by Fermi LAT [216] and H.E.S.S. [217] on the total electron flux.

The more recently released measurement of the cosmic-ray electron + positron spectrum from Fermi LAT [216] does not confirm the distinct feature seen by the ATIC experiment. Instead, Fermi LAT observes a smooth, hard spectrum which follows a power law $\sim E^{-3.0}$ for energies up to about 1 TeV. As indicated by H.E.S.S. observations [217], this power law steepens at energies above 1 TeV. There is currently some disagreement between the ATIC and Fermi LAT collaborations about the existence of the spectral feature, the reason for which is presently not well understood. We now examine the case that the true electron–positron spectrum is smooth.

In Fig. 10.6 we show the results for a three-body decaying Bino-like neutralino,[8] as discussed in Section 10.3.1. The mass of the neutralino is 2500 GeV, whereas the hidden gaugino has a small mass $\sim \mathcal{O}(100\,\mathrm{GeV})$. In the plots we assume that the decay is only mediated by right-handed sleptons with a mass close to the neutralino mass. All other supersymmetric particles must be heavy enough to make their effects on the branching ratios negligible. However, although this scenario is phenomenologically appealing, it requires some non-standard cosmology in order to avoid the thermal overproduction of the heavy Bino-like neutralino. A second way to explain the data measured by Fermi would be a cascade-decaying hidden gaugino, see Section 10.3.2. The sharp step in the electron + positron spectrum, as shown

ground of secondary positrons, which were calculated for the above M1, M2 and MED model in [139]. However, in Fig. 10.4 we used the background from [168] since the backgrounds in [139] are meant to be extreme cases.

[8] For further details about the plot, see Chapter 4.

in Fig. 10.6 disappears if the first generation sleptons are heavy enough to suppress the production of electrons or positrons in two-body decays. This, however, requires non-universal slepton masses. Note that in both of the above cases, the production and decay of taus will lead to a visible bump in the extragalactic gamma-ray flux, which should be measurable by Fermi LAT.

10.4 Conclusions

In this chapter we have shown that a simple extension of the MSSM by an additional hidden Abelian gauge group $U(1)_X$, which kinetically mixes with the hypercharge $U(1)_Y$, can account for the observed PAMELA excess if the kinetic mixing parameter is in the range of $\chi \sim 10^{-20...24}$. We also briefly discussed possible origins of such a tiny mixing in scenarios with warped extra dimensions. Depending on the masses, either the visible sector neutralino or the hidden gaugino becomes unstable and subject to decay. We have demonstrated that this decay is dominated by leptophilic modes in certain parameter regions of the MSSM where the sleptons are light (see Table 10.2 and Table 10.3). We found that a decaying hidden gaugino with a mass around $600 - 1200\,\mathrm{GeV}$ can naturally explain the observed excess in the positron fraction without overproducing antiprotons (see Fig. 10.3). Our considerations suggest a preference for supersymmetric models with relatively light sleptons as, for example, realized in mSUGRA models which lie in the coannihilation region. In any case, we predict a contribution to the extragalactic gamma-ray flux, which mainly stems from tau decays, and which should be observable in observations by the Fermi Gamma-Ray Space Telescope. We also demonstrated that it is difficult to accommodate the sharp double-peak structure in the ATIC data within our dark matter model and with standard propagation models.

Conclusions and Outlook

Despite a wealth of very interesting experimental results over the past years, the nature of the dark matter remains as mysterious as ever. While from cosmological observations we have gained some invaluable information about the overall abundance and impact of dark matter on the large-scale evolution of the cosmos, we do not know much more about the microscopic nature of the dark matter particles than at the time the existence of dark matter was first discovered almost 80 years ago. In this thesis we examined the indirect astrophysical signatures of a class of models where the dark matter is unstable, but decays with cosmological lifetimes. This kind of scenario has not been studied as thoroughly in the literature as the paradigmatic WIMP scenario, although it presents a viable alternative scenario for indirect dark matter detection apart from the usual picture of WIMP self-annihilation. In the absence of an exactly conserved stabilizing symmetry, decaying dark matter particles such as the gravitino, which we discussed in Chapter 9, must be extremely weakly coupled to the Standard Model in order to ensure sufficient stability on cosmological timescales. Since this typically implies inaccessibility to direct dark matter detection and immediate collider tests of its properties, indirect detection provides an essential handle to constrain the properties of super-weakly interacting dark matter candidates. Note, however, that we also discussed an exception to this picture in Chapter 10, where the dark matter is composed of two distinct components. In this case the dominant component can be weakly interacting and accessible to direct detection and collider searches, while it decays into a very weakly coupled subdominant dark matter component or vice versa.

Over the last years, the observation of an anomalous abundance of positrons and electrons in the cosmic radiation by PAMELA and Fermi LAT has attracted a great deal of attention since the annihilation or decay of weak-scale dark matter is expected to contribute to these fluxes in the observed energy range. In Chapter 4 we analyzed these anomalies and interpreted them as a signature of decaying dark matter in the halo. This interpretation requires a dark matter mass around a few TeV and a lifetime of the order of $10^{26}\,\mathrm{s}$, where the dark matter particles have to decay with a large branching fraction directly into charged leptons, which are then observed at Earth after their propagation through the halo. The viability of this interpretation as well as alternative astrophysical interpretations will be tested by future cosmic-ray and gamma-ray measurements. The space-based cosmic-ray instrument AMS-02 (Alpha Magnetic Spectrometer) was finally launched on May 16, 2011 after several years of delays, and was shortly thereafter installed on the International Space Station. AMS-02 is expected to significantly improve upon existing measurements of cosmic-ray leptons and nuclei up to iron. Its measurements will provide invaluable information on cosmic-ray fluxes at higher energies than currently explored and thus improve our understanding of the production and propagation of cosmic rays. As the cosmic radiation and the Galactic gamma-ray

emission are closely related, it should also help us better understand the Galactic gamma-ray emission. All these developments will hopefully lead to an improved background rejection, making it easier to identify any potential dark matter signals. Of special interest to dark matter studies will be an independent and improved determination of the positron fraction toward even higher energies and the measurement of a potential asymmetry in the arrival directions of electrons and positrons, which might allow the determination of a nearby source like a pulsar. Furthermore, one of the goals of AMS-02 is to search for cosmic antideuterons, which is a promising channel for indirect dark matter searches, especially for a low to intermediate dark matter mass. As we discussed in Chapter 5, a discovery of antideuterons by the upcoming generation of cosmic-ray telescopes, including the GAPS balloon instrument, would constitute a likely dark matter signature.

Meanwhile, the Fermi Gamma-ray Space Telescope is continuing to take data. In Chapter 6 we analyzed the peculiar angular dependence of the gamma-ray emission from dark matter decay in the halo. We computed the anisotropies in gamma-ray flux from the decay of dark matter in the Galactic halo and found that these anisotropies can be sizable, in particular for the case of the decay modes we found to reproduce the cosmic-ray anomalies observed by PAMELA and Fermi. The Fermi LAT collaboration has since released an analysis of the extragalactic gamma-ray emission, which in principle provides constraints on the gamma-ray emission from dark matter decay. However, this analysis was done in a way that allows for an independent normalization of the various contributions to the Galactic foreground gamma-ray emission in each energy bin, making it difficult to identify a deviation from the expected power-law behavior of the extragalactic background. This analysis also presents plots of the gamma-ray fluxes averaged over four different hemispheres, but no study of a possible presence of anisotropies in the data was performed so far. A dedicated analysis of possible anisotropies in the gamma-ray flux by the Fermi LAT collaboration, taking into account the full spectrum of systematic uncertainties, would hopefully shed some light on the presence or absence of such anisotropies.

In Chapter 7 we studied a subdominant effect of the decay of leptophilic dark matter, namely the radiative two-body decays into photons induced by quantum fluctuations. Despite being loop suppressed, we demonstrated that this decay may be of relevance due to its unusually clear, background-free signature. Indeed, there are some scenarios where constraints from the radiative decay can dominate over constraints from charged lepton production at leading order. At energies below 200 GeV, such lines can be searched for by Fermi LAT, while higher energies are only accessible to Cherenkov telescopes. The proposed Cherenkov Telescope Array (CTA) is expected to shed some light on this matter. However, it is still in the preparatory phase and is years away from commencing operations. When it becomes operational, the CTA should allow us to probe the gamma-ray emission from sources at energies and sensitivities unattainable with the current generation of Cherenkov telescopes. This will hopefully enable searches for gamma-ray lines in hitherto unexplored regions of the parameter space, which constitute a smoking-gun signature of dark matter as we have outlined. In principle, the techniques we used could also be used in a different energy range to constrain dark matter interpretations of the 511 keV line observed in the Galactic center by INTEGRAL/SPI.

An important complementary method of testing the decay of dark matter comes from neutrino observations. We analyzed such constraints in a model-independent manner in

Chapter 8. While current constraints from Super-Kamiokande are too weak to constrain dark matter stability at the level relevant for the leptonic cosmic-ray anomalies, this can be expected to change with the upcoming generation of neutrino telescopes that have recently begun operations or will do so in the near future. We demonstrated that the sensitivity of IceCube and other km^3 scale detectors in principle should be sufficient to constrain leptonic and hadronic dark matter decay at a level competitive with current constraints from other indirect detection channels within a few years of data taking and thus put decisive constraints on the dark matter interpretations of the cosmic-ray anomalies observed by PAMELA and Fermi LAT. With the completion of the full IceCube detector together with its DeepCore subdetector near the end of 2010, we can expect interesting results from the new generation of neutrino telescopes within the next few years.

While a dark matter interpretation of the leptonic cosmic-ray anomalies is becoming increasingly constrained from antiproton constraints, gamma-ray and radio tests of Galactic emission as well as gamma-ray emission from galaxy clusters, the scenario of dark matter decay as the origin of these anomalies has thus far resisted efforts of ruling it out. However, claims of the detection of a non-gravitational dark matter signature have to be taken with caution due to the presence of astrophysical backgrounds that are difficult to quantify, as we explained in Chapter 4. Hence, without supplemental evidence it is difficult to make a convincing case that these signatures are due to dark matter decay or annihilation. Nevertheless, no matter whether the correct explanation of the cosmic-ray anomalies eventually turns out to be astrophysical or more fundamental in nature, they have presented a genuine and very interesting puzzle for which multiple viable solutions exist, and which has helped improve our understanding of indirect dark matter detection.

The challenge of dark matter identification remains uniquely interesting, not least because of its interdisciplinary nature. It is highly unlikely that any single observation of a signal in one channel would allow the unique identification of the correct theory of dark matter. Therefore, a satisfactory solution of the dark matter puzzle will most probably necessitate a multidisciplinary approach involving direct and indirect detection as well as collider searches for new physics, which together should yield a consistent picture. Interestingly, in addition to the observed anomalies in the cosmic radiation, there currently exist tentative hints from several direct detection experiments which hint at the possible existence of a rather light WIMP with a mass around 10 GeV. As with the cosmic-ray anomalies, these observations are incompatible with the standard dark matter paradigm where the dark matter is a thermal relic population of lightest neutralinos in the MSSM. Both in the case of indirect and direct detection, such findings have motivated many studies of non-standard and non-minimal models of dark matter over the last years, involving, for instance, extended versions of the MSSM, new "dark forces," where the dark matter is charged under a new dark-sector gauge symmetry (possibly related to Sommerfeld enhancement of annihilation rates), or constructions such as isospin-violating dark matter or inelastic dark matter, where the dark matter possesses a near-degenerate excited state. Independent of whether one finds such attempts to construct more baroque models of dark matter convincing, they highlight how little we still know about its true nature. The physics of the dark sector may turn out to be more complex and thus more interesting than initially assumed. In any case, one lesson we can learn from this is that we should keep an open mind regarding the particle physics of the dark matter, as Nature may have some surprises in store for us.

Appendix A

Statistical Errors of the Large-Scale Anisotropy

We briefly discuss here the statistical errors of the large-scale anisotropy as defined in Eq. (6.1), which are due to shot noise. Statistical errors of small-scale anisotropies are discussed, *e.g.*, in [373]. The measured anisotropy A and the total number N of measured photons are related to the number of photons N_1 measured in the direction of the Galactic center and the number N_2 in the direction of the anticenter by $A = (N_1 - N_2)/(N_1 + N_2)$ and $N = N_1 + N_2$. The N_i follow a Poisson distribution with mean $\langle N_i \rangle$ and standard deviation $\sigma_i = \sqrt{\langle N_i \rangle}$. Considering the propagation of the error, it is straightforward to derive that the statistical error of the anisotropy is given by

$$\sigma_A \simeq \sqrt{\frac{1 - \langle A \rangle^2}{\langle N \rangle}}\,, \tag{A.1}$$

which is expected to hold for small enough $\langle A \rangle \simeq A$ and large enough $\langle N \rangle \simeq N$. On the other hand, one can derive the exact probability distribution function of the anisotropy A by starting with the above Poisson distributions for the N_i, performing an appropriate redefinition of the parameters and integrating out the total number of measured photons. The result is a function of the mean values $\langle A \rangle$ and $\langle N \rangle$ and can be written in the compact form

$$\mathrm{pdf}(A) = \frac{\langle N \rangle}{2\,\langle N_1 \rangle!\,\langle N_2 \rangle!} \left(\frac{1+A}{2}\right)^{\langle N_1 \rangle} \left(\frac{1-A}{2}\right)^{\langle N_2 \rangle}\,. \tag{A.2}$$

From this equation one can check, for example, that a normal distribution with mean $\langle A \rangle$ and standard deviation as in Eq. (A.1) gives errors that are accurate at the 5% level as long as $\langle A \rangle < 0.6$ and $\sigma_A < 0.2$. For small enough anisotropies A, however, the standard deviation is just given by $\sigma_A = \sqrt{N^{-1}}$ with good accuracy, and we use this approximation throughout the analysis.

Appendix B

Decay Widths for the Leptophilic Toy Model

In this appendix we present the detailed general expressions for the decay widths for fermionic and scalar dark matter for the leptophilic toy model discussed in Chapter 7.

B.1 Decay Widths for Fermionic Dark Matter

B.1.1 The Decay $\psi_{\mathrm{DM}} \to \ell^+\ell^- N$

The differential decay rate for this process is given by

$$d\Gamma(\psi_{\mathrm{DM}} \to \ell^+\ell^- N) = \frac{1}{(2\pi)^3}\frac{1}{64 m_{\psi_{\mathrm{DM}}}^3}|\mathcal{M}_t + \mathcal{M}_u|^2\, dt\, ds\,. \tag{B.1}$$

Note that there is a relative minus sign between the t- and u-channel amplitudes due to the exchange of two anticommuting fermions that is not present by a naive application of the Feynman rules for the two diagrams. Neglecting the lepton mass, one obtains for the squared amplitude

$$\begin{aligned}
|\mathcal{M}_t + \mathcal{M}_u|^2 = {} & \left(|\lambda^L_{\ell\psi}|^2 + |\lambda^R_{\ell\psi}|^2\right)\left(|\lambda^L_{\ell N}|^2 + |\lambda^R_{\ell N}|^2\right) \\
& \times \left[\frac{(t-m_N^2)(m^2_{\psi_{\mathrm{DM}}}-t)}{(t-m_\Sigma^2)^2} + \frac{(u-m_N^2)(m^2_{\psi_{\mathrm{DM}}}-u)}{(u-m_\Sigma^2)^2}\right] \\
& + 2\eta\Bigg\{\mathrm{Re}\left[\left(\lambda^{L*}_{\ell\psi}\lambda^L_{\ell N}\right)^2 + \left(\lambda^{R*}_{\ell\psi}\lambda^R_{\ell N}\right)^2\right]\frac{m_{\psi_{\mathrm{DM}}} m_N s}{(t-m_\Sigma^2)(u-m_\Sigma^2)} \\
& - \mathrm{Re}\left[\lambda^{L*}_{\ell\psi}\lambda^L_{\ell N}\lambda^{R*}_{\ell\psi}\lambda^R_{\ell N}\right]\times \\
& \times \frac{(t-m_N^2)(m^2_{\psi_{\mathrm{DM}}}-t) + (u-m_N^2)(m^2_{\psi_{\mathrm{DM}}}-u) - s(t+u)}{(t-m_\Sigma^2)(u-m_\Sigma^2)}\,,
\end{aligned} \tag{B.2}$$

where

$$s = (q_1-p_1)^2, \quad t = (q_1-p_2)^2, \quad u = (q_1-p_3)^2 = m_\psi^2 + m_N^2 + 2m_\ell^2 - s - t\,. \tag{B.3}$$

Again, $\eta = \eta_{\psi_{\rm DM}}\eta_N = \pm 1$ depending on the *CP* eigenvalues of $\psi_{\rm DM}$ and N. The integration limits for the Mandelstam variables are given by

$$0 \leq s \leq (m_{\psi_{\rm DM}} - m_N)^2 \tag{B.4}$$

and

$$t_{1,2} = \frac{1}{2}\left(m^2_{\psi_{\rm DM}} + m^2_N - s \mp \sqrt{\lambda(m^2_{\psi_{\rm DM}}, m^2_N, s)}\right), \tag{B.5}$$

where

$$\lambda(a,b,c) = a^2 + b^2 + c^2 - 2ab - 2ac - 2bc\,. \tag{B.6}$$

We can perform the kinematical integrations in the limit $m_\Sigma \gg t, u$, in which case the Mandelstam variables in the denominator can be neglected. We then get

$$\begin{aligned}\Gamma(\psi_{\rm DM} \to \ell^+\ell^- N) = \frac{1}{64(2\pi)^3}\frac{m^5_{\psi_{\rm DM}}}{6m^4_\Sigma}\Bigg\{\Big[&\left(|\lambda^L_{\ell\psi}|^2 + |\lambda^R_{\ell\psi}|^2\right)\left(|\lambda^L_{\ell N}|^2 + |\lambda^R_{\ell N}|^2\right)\\ &- \eta\,{\rm Re}\left(\lambda^{L*}_{\ell\psi}\lambda^L_{\ell N}\lambda^{R*}_{\ell\psi}\lambda^R_{\ell N}\right)\Big]F_1(x)\\ &+ 2\eta\,{\rm Re}\left[\left(\lambda^{L*}_{\ell\psi}\lambda^L_{\ell N}\right)^2 + \left(\lambda^{R*}_{\ell\psi}\lambda^R_{\ell N}\right)^2\right]F_2(x)\Bigg\},\end{aligned} \tag{B.7}$$

where $x \equiv m^2_N/m^2_{\psi_{\rm DM}}$ and $F_1(x)$, $F_2(x)$ are defined in Eqs. (7.6), (7.7).

In the case of mediation by a vector, the matrix element for vanishing lepton mass reads

$$\begin{aligned}|\mathcal{M}_t + \mathcal{M}_u|^2 = {}& 4\left(\left|\lambda^L_{\ell\psi}\lambda^L_{\ell N}\right|^2 + \left|\lambda^R_{\ell\psi}\lambda^R_{\ell N}\right|^2\right)\\ &\times\left[\frac{(u-m^2_N)(m^2_{\psi_{\rm DM}}-u)}{(t-m^2_V)^2} + \frac{(t-m^2_N)(m^2_{\psi_{\rm DM}}-t)}{(u-m^2_V)^2}\right]\\ &+ 4\left(\left|\lambda^L_{\ell\psi}\lambda^R_{\ell N}\right|^2 + \left|\lambda^R_{\ell\psi}\lambda^L_{\ell N}\right|^2\right)s(t+u)\left[\frac{1}{(t-m^2_V)^2} + \frac{1}{(u-m^2_V)^2}\right]\\ &+ 8\eta\Bigg\{{\rm Re}\left[\left(\lambda^L_{\ell\psi}\lambda^{L*}_{\ell N}\right)^2 + \left(\lambda^R_{\ell\psi}\lambda^{R*}_{\ell N}\right)^2\right]\frac{m_{\psi_{\rm DM}}m_N s}{(t-m^2_V)(u-m^2_V)}\\ &+ 2{\rm Re}\left[\lambda^L_{\ell\psi}\lambda^{L*}_{\ell N}\lambda^R_{\ell\psi}\lambda^{R*}_{\ell N}\right]\frac{s(t+u)}{(t-m^2_V)(u-m^2_V)}\Bigg\}.\end{aligned} \tag{B.8}$$

In the limit $m_{\psi_{\rm DM}} \ll m_V$ we get for the decay rate

$$\begin{aligned}\Gamma(\psi_{\rm DM} \to \ell^+\ell^- N) = \frac{1}{64(2\pi)^3}\frac{4m^5_{\psi_{\rm DM}}}{6m^4_V}\Bigg\{\Big[&\left(|\lambda^L_{\ell\psi}|^2 + |\lambda^R_{\ell\psi}|^2\right)\left(|\lambda^L_{\ell N}|^2 + |\lambda^R_{\ell N}|^2\right)\\ &+ 2\eta\,{\rm Re}\left(\lambda^L_{\ell\psi}\lambda^{L*}_{\ell N}\lambda^R_{\ell\psi}\lambda^{R*}_{\ell N}\right)\Big]F_1(x)\\ &+ 2\eta\,{\rm Re}\left[\left(\lambda^L_{\ell\psi}\lambda^{L*}_{\ell N}\right)^2 + \left(\lambda^R_{\ell\psi}\lambda^{R*}_{\ell N}\right)^2\right]F_2(x)\Bigg\}.\end{aligned} \tag{B.9}$$

B.1.2 The Decay $\psi_{\rm DM} \to \gamma N$

There are four scalar-mediated diagrams at the one-loop level contributing to the decay $\psi_{\rm DM} \to \gamma N$, which are shown in Fig. 7.2. Due to gauge invariance, in the case of *CP*-conserving interactions, the matrix element corresponding to the sum of the four diagrams can be written in the form

$$\begin{aligned}\mathcal{M} &= \frac{ig_{N\gamma\psi}}{m_{\psi_{\rm DM}}}\bar{u}(k_1)(P_R - \eta_N\eta_\psi P_L)\sigma^{\mu\nu}k_{2\mu}\epsilon^*_\nu u(p) \\ &= -\frac{g_{N\gamma\psi}}{m_{\psi_{\rm DM}}}\bar{u}(k_1)(P_R - \eta_N\eta_\psi P_L)\not{k}_2\not{\epsilon}^* u(p)\,, \end{aligned} \tag{B.10}$$

where $\sigma^{\mu\nu} = i[\gamma^\mu, \gamma^\nu]/2$ and $\eta_{\psi_{\rm DM}}$, η_N are the *CP* eigenvalues of $\psi_{\rm DM}$ and N, respectively. This is manifestly gauge invariant in the sense that it satisfies the Ward identity: the matrix element vanishes when replacing $\epsilon^*_\mu \to k_{2\mu}$ since the photon is on-shell.

The effective coupling $g^\Sigma_{N\gamma\psi_{\rm DM}}$ for an intermediate scalar can be given in terms of loop integrals as follows,

$$\begin{aligned} g^\Sigma_{N\gamma\psi_{\rm DM}} = &-\frac{e\,\eta_N m_{\psi_{\rm DM}}}{16\pi^2}\sum_{f,\Sigma} Q_f C_f \Big\{ m_f(\eta_{\psi_{\rm DM}}\lambda^L_{\ell N}\lambda^R_{\ell\psi} - \eta_N\lambda^R_{\ell N}\lambda^L_{\ell\psi})I \\ &+ (\lambda^L_{\ell N}\lambda^L_{\ell\psi} - \eta_{\psi_{\rm DM}}\eta_N\lambda^R_{\ell N}\lambda^R_{\ell\psi})[\eta_{\psi_{\rm DM}} m_{\psi_{\rm DM}}(I^2 - K) - \eta_N m_N K]\Big\}\,, \end{aligned} \tag{B.11}$$

where the sum runs over all fermions f and all mediators Σ that contribute in the loop. The loop integrals are written in terms of Feynman parameters as

$$I = \frac{1}{\Delta}\int_0^1 \frac{dx}{1-x}\log X\,, \tag{B.12}$$

$$I^2 = \frac{1}{\Delta}\int_0^1 dx \log X\,, \tag{B.13}$$

$$K = -\frac{1}{\Delta}\int_0^1 dx \left(1 + \frac{B}{\Delta\, x(1-x)}\log X\right)\,, \tag{B.14}$$

where

$$\Delta \equiv m^2_{\psi_{\rm DM}} - m^2_N\,, \tag{B.15}$$

$$B \equiv m^2_\ell x + m^2_\Sigma(1-x) - m^2_{\psi_{\rm DM}}x(1-x)\,, \tag{B.16}$$

$$X \equiv \frac{m^2_\ell x + m^2_\Sigma(1-x) - m^2_{\psi_{\rm DM}}x(1-x)}{m^2_\ell x + m^2_\Sigma(1-x) - m^2_N x(1-x)}\,. \tag{B.17}$$

In the limit $m_{\psi_{\rm DM}}, m_N \ll m_\Sigma$, the loop integrals take on the simplified form [300]

$$I = \frac{1}{m^2_\Sigma} f(m^2_\ell/m^2_\Sigma), \tag{B.18}$$

$$I^2 = -\frac{1}{2m^2_\Sigma} f_2(m^2_\ell/m^2_\Sigma), \tag{B.19}$$

$$K = \frac{1}{2}I^2, \tag{B.20}$$

where the functions f, f_2 are defined as

$$f(x) = \frac{1}{1-x}\left[1 + \frac{1}{1-x}\ln(x)\right], \tag{B.21}$$

$$f_2(x) = \frac{1}{(1-x)^2}\left[1 + x + \frac{2x}{1-x}\ln(x)\right]. \tag{B.22}$$

The expression for the effective coupling then assumes the form

$$\begin{aligned} g^{\Sigma}_{N\gamma\psi} \simeq & -\frac{e\,\eta_N m_{\psi_{\rm DM}}}{16\pi^2}\sum_{\ell,\Sigma} Q_\ell C_\ell \Big\{ m_\ell \left(\eta_{\psi_{\rm DM}}\lambda^L_{\ell N}\lambda^R_{\ell\psi} - \eta_N \lambda^R_{\ell N}\lambda^L_{\ell\psi}\right)\frac{f(m_\ell^2/m_\Sigma^2)}{m_\Sigma^2} \\ & - \left(\lambda^L_{\ell N}\lambda^L_{\ell\psi} - \eta_{\psi_{\rm DM}}\eta_N\lambda^R_{\ell N}\lambda^R_{\ell\psi}\right)\frac{\eta_{\psi_{\rm DM}} m_{\psi_{\rm DM}} - \eta_N m_N}{4m_\Sigma^2} f_2(m_\ell^2/m_\Sigma^2)\Big\} \\ \simeq & \frac{e\,\eta}{64\pi^2} m^2_{\psi_{\rm DM}}\left(1 - \frac{\eta\, m_N}{m_{\psi_{\rm DM}}}\right)\sum_{\ell,\Sigma}\frac{Q_\ell C_\ell}{m_\Sigma^2}\left\{\left(\lambda^L_{\ell N}\lambda^L_{\ell\psi} - \eta\,\lambda^R_{\ell N}\lambda^R_{\ell\psi}\right)\right\}, \end{aligned} \tag{B.23}$$

where in the last line we have taken $m_\ell \to 0$.

In the case of an intermediate vector, the same integrals I, I^2, K (with the replacement $m_\Sigma \to m_V$ in the constants B, X) appear, together with the additional integral

$$J = \frac{1}{\Delta}\int_0^1 \frac{dx}{x}\log X\,, \tag{B.24}$$

which simplifies in the limit $m_{\psi_{\rm DM}}, m_N \ll m_\Sigma$ to

$$J = \frac{1}{m_V^2}\frac{\ln(x)}{1-x} - I = -\frac{1}{m_V^2} f^V(m_\ell^2/m_V^2)\,, \tag{B.25}$$

where in this case the kinematical functions are defined as

$$f^V(x) = \frac{1}{1-x}\left[1 + \frac{x}{1-x}\ln(x)\right], \tag{B.26}$$

$$f_2^V(x) = \frac{1}{(1-x)^2}\left[1 - \frac{5x}{3} + \frac{2x(1-2x)}{3(1-x)}\ln(x)\right]. \tag{B.27}$$

Furthermore, one finds

$$I^2 - J - K = K - J = \frac{3}{4m_V^2} f^V(x)\,. \tag{B.28}$$

The effective coupling in terms of loop integrals is given by

$$\begin{aligned} g^V_{N\gamma\psi} = & \frac{e\,\eta_N m_{\psi_{\rm DM}}}{8\pi^2}\sum_\ell \Big\{(\eta\lambda^L_{\ell N}\lambda^L_{\ell\psi} - \lambda^R_{\ell N}\lambda^R_{\ell\psi})\big[\eta_{\psi_{\rm DM}} m_{\psi_{\rm DM}}(I^2 - J - K) \\ & + \eta_N m_N (J - K)\big] + 2m_\ell(\eta_{\psi_{\rm DM}}\lambda^L_{\ell N}\lambda^R_{\ell\psi} - \eta_N\lambda^R_{\ell N}\lambda^L_{\ell\psi})J\Big\}, \end{aligned} \tag{B.29}$$

For $m_{\psi_{\rm DM}} \ll m_V$ this expression then simplifies to

$$\begin{aligned} g^V_{N\gamma\psi} \simeq & -\frac{e\,\eta_N m_{\psi_{\rm DM}}}{8\pi^2}\sum_\ell \Big\{2m_\ell\left(\eta_N\lambda^L_{\ell N}\lambda^R_{\ell\psi} - \eta_{\psi_{\rm DM}}\lambda^R_{\ell N}\lambda^L_{\ell\psi}\right)\frac{f^V(m_\ell/m_V^2)}{m_V^2} \\ & - 3\left(\eta_N\eta_{\psi_{\rm DM}}\lambda^L_{\ell N}\lambda^L_{\ell\psi} - \lambda^R_{\ell N}\lambda^R_{\ell\psi}\right)\frac{\eta_{\psi_{\rm DM}} m_{\psi_{\rm DM}} - \eta_N m_N}{4m_V^4} f_2^V(m_\ell^2/m_V^2)\Big\} \\ \simeq & \frac{3e\,\eta}{32\pi^2}\frac{m^2_{\psi_{\rm DM}}}{m_V^2}\left(1 - \frac{\eta\, m_N}{m_{\psi_{\rm DM}}}\right)\sum_\ell\left(\lambda^L_{\ell N}\lambda^L_{\ell\psi} - \eta\,\lambda^R_{\ell N}\lambda^R_{\ell\psi}\right), \end{aligned} \tag{B.30}$$

where in the last line we have taken $m_\ell \to 0$.

The decay rate in both cases is finally given by

$$\Gamma(\psi_{\rm DM} \to \gamma N) = \frac{\left(g^{\Sigma/V}_{N\gamma\psi}\right)^2}{8\pi} m_{\psi_{\rm DM}} \left(1 - \frac{m_N^2}{m_{\psi_{\rm DM}}^2}\right)^3 . \tag{B.31}$$

For the scalar in the case of one mediator coupled to leptons we get in the limit $m_\ell \ll m_N$ and $m_{\psi_{\rm DM}} \ll m_\Sigma$,

$$\Gamma(\psi_{\rm DM} \to \gamma N) = \frac{e^2}{8\pi\,(64\pi^2)^2} \frac{m_{\psi_{\rm DM}}^5}{m_\Sigma^4} \left(1 - \frac{m_N^2}{m_{\psi_{\rm DM}}^2}\right)^3 \left(1 - \frac{\eta\, m_N}{m_{\psi_{\rm DM}}}\right)^2 \times \left[\sum_\ell \left(\lambda^L_{\ell N}\lambda^L_{\ell\psi} - \eta\,\lambda^R_{\ell N}\lambda^R_{\ell\psi}\right)\right]^2 , \tag{B.32}$$

whereas for the vector we have, in the limit $m_\ell \ll m_N$ and $m_{\psi_{\rm DM}} \ll m_V$,

$$\Gamma(\psi_{\rm DM} \to \gamma N) = \frac{1}{8\pi} \frac{9e^2}{(8\pi^2)^2} \frac{m_{\psi_{\rm DM}}^5}{16 m_V^4} \left(1 - \frac{m_N^2}{m_{\psi_{\rm DM}}^2}\right)^3 \left(1 - \frac{\eta\, m_N}{m_{\psi_{\rm DM}}}\right)^2 \times \left[\sum_\ell \left(\lambda^L_{\ell N}\lambda^L_{\ell\psi} - \eta\,\lambda^R_{\ell N}\lambda^R_{\ell\psi}\right)\right]^2 . \tag{B.33}$$

B.2 Decay Widths for Scalar Dark Matter

In this section we present the expressions for the decay width of the radiative decay of scalar dark matter into two photons, $\phi_{\rm DM} \to \gamma\gamma$.

For $\lambda^L_{\ell\phi} = \lambda^R_{\ell\phi} \equiv \lambda_{\ell\phi}$ the decay rate reads [302, 303]

$$\Gamma(\phi_{\rm DM} \to \gamma\gamma) = \frac{m_{\phi_{\rm DM}}^3}{4\pi} \left(\frac{e^2}{16\pi^2}\right)^2 \left|\sum_\ell \frac{\lambda_{\ell\phi}}{m_\ell} A_f(\tau_\ell)\right|^2 , \tag{B.34}$$

where $\tau_\ell \equiv m^2_{\phi_{\rm DM}}/(4m_\ell^2)$ and

$$A_f(\tau) = 2\left[\tau + (\tau - 1) f(\tau)\right]/\tau^2 , \tag{B.35}$$

$$f(\tau) = \begin{cases} \arcsin^2\sqrt{\tau}\,, & \tau \le 1 \\ -\frac{1}{4}\left[\ln\frac{1+\sqrt{1-1/\tau}}{1-\sqrt{1-1/\tau}} - i\pi\right]^2, & \tau > 1 \end{cases} . \tag{B.36}$$

In the case of interest here, $\tau_\ell \gg 1$. Then we can approximate

$$A_f(\tau) \simeq \frac{1}{\tau}\left\{2 - \frac{1}{2}(\ln(4\tau) - i\pi)^2\right\} . \tag{B.37}$$

In this limit, and taking only one lepton species into account, the decay rate is given by

$$\Gamma(\phi_{\rm DM} \to \gamma\gamma) \simeq \frac{|\lambda_{\ell\phi}|^2}{16\pi} m_{\phi_{\rm DM}} \left(\frac{e^2}{16\pi^2}\right)^2 \frac{4m_\ell^2}{m^2_{\phi_{\rm DM}}} \times \left\{\left[2 + \frac{\pi^2}{2} - \frac{1}{2}\ln^2(4\tau_\ell)\right]^2 + \pi^2 \ln^2(4\tau_\ell)\right\} . \tag{B.38}$$

Bibliography

[1] M. Garny, A. Ibarra, D. Tran, and C. Weniger, *Gamma-Ray Lines from Radiative Dark Matter Decay*, JCAP **1101** (2011), 032, arXiv:1011.3786 [hep-ph].

[2] L. Covi, M. Grefe, A. Ibarra, and D. Tran, *Neutrino Signals from Dark Matter Decay*, JCAP **1004** (2010), 017, arXiv:0912.3521 [hep-ph].

[3] A. Ibarra, D. Tran, and C. Weniger, *Detecting Gamma-Ray Anisotropies from Decaying Dark Matter: Prospects for Fermi LAT*, Phys.Rev. **D81** (2010), 023529, arXiv:0909.3514 [hep-ph].

[4] A. Ibarra, D. Tran, and C. Weniger, *Decaying Dark Matter in Light of the PAMELA and Fermi LAT Data*, JCAP **1001** (2010), 009, arXiv:0906.1571 [hep-ph].

[5] W. Buchmuller, A. Ibarra, T. Shindou, F. Takayama, and D. Tran, *Probing Gravitino Dark Matter with PAMELA and Fermi*, JCAP **0909** (2009), 021, arXiv:0906.1187 [hep-ph].

[6] A. Ibarra and D. Tran, *Antideuterons from Dark Matter Decay*, JCAP **0906** (2009), 004, arXiv:0904.1410 [hep-ph].

[7] A. Ibarra, A. Ringwald, D. Tran, and C. Weniger, *Cosmic Rays from Leptophilic Dark Matter Decay via Kinetic Mixing*, JCAP **0908** (2009), 017, arXiv:0903.3625 [hep-ph].

[8] A. Ibarra and D. Tran, *Decaying Dark Matter and the PAMELA Anomaly*, JCAP **0902** (2009), 021, arXiv:0811.1555 [hep-ph].

[9] L. Covi, M. Grefe, A. Ibarra, and D. Tran, *Unstable Gravitino Dark Matter and Neutrino Flux*, JCAP **0901** (2009), 029, arXiv:0809.5030 [hep-ph].

[10] A. Ibarra and D. Tran, *Antimatter Signatures of Gravitino Dark Matter Decay*, JCAP **0807** (2008), 002, arXiv:0804.4596 [astro-ph].

[11] A. Ibarra and D. Tran, *Gamma Ray Spectrum from Gravitino Dark Matter Decay*, Phys.Rev.Lett. **100** (2008), 061301, arXiv:0709.4593 [astro-ph].

[12] G. Jungman, M. Kamionkowski, and K. Griest, *Supersymmetric dark matter*, Phys.Rept. **267** (1996), 195–373, arXiv:hep-ph/9506380 [hep-ph].

[13] L. Bergstrom, *Nonbaryonic dark matter: Observational evidence and detection methods*, Rept.Prog.Phys. **63** (2000), 793, arXiv:hep-ph/0002126 [hep-ph].

[14] G. Bertone, D. Hooper, and J. Silk, *Particle dark matter: Evidence, candidates and constraints*, Phys.Rept. **405** (2005), 279–390, `arXiv:hep-ph/0404175` [hep-ph].

[15] J. L. Feng, *Dark Matter Candidates from Particle Physics and Methods of Detection*, Ann.Rev.Astron.Astrophys. **48** (2010), 495, `arXiv:1003.0904` [astro-ph.CO].

[16] K. Garrett and G. Duda, *Dark Matter: A Primer*, Adv.Astron. **2011** (2011), 968283, `arXiv:1006.2483` [hep-ph].

[17] J. H. Oort, *The force exerted by the stellar system in the direction perpendicular to the galactic plane and some related problems*, Bull.Astron.Inst.Neth. **6** (1932), 249–287.

[18] F. Zwicky, *Spectral displacement of extra galactic nebulae*, Helv.Phys.Acta **6** (1933), 110–127.

[19] V. C. Rubin and J. Ford, W.K., *Rotation of the Andromeda Nebula from a Spectroscopic Survey of Emission Regions*, Astrophys.J. **159** (1970), 379–403.

[20] V. Rubin, N. Thonnard, and J. Ford, W.K., *Rotational properties of 21 SC galaxies with a large range of luminosities and radii, from NGC 4605 (R = 4 kpc) to UGC 2885 (R = 122 kpc)*, Astrophys.J. **238** (1980), 471.

[21] A. Bosma, *The distribution and kinematics of neutral hydrogen in spiral galaxies of various morphological types*, Ph.D. Thesis, Groningen Univ. (1978).

[22] Y. Sofue and V. Rubin, *Rotation curves of spiral galaxies*, Ann.Rev.Astron.Astrophys. **39** (2001), 137–174, `arXiv:astro-ph/0010594` [astro-ph].

[23] SDSS Collaboration, X. Xue et al., *The Milky Way's Circular Velocity Curve to 60 kpc and an Estimate of the Dark Matter Halo Mass from Kinematics of 2400 SDSS Blue Horizontal Branch Stars*, Astrophys.J. **684** (2008), 1143–1158, `arXiv:0801.1232` [astro-ph].

[24] M. Mateo, *Dwarf galaxies of the Local Group*, Ann.Rev.Astron.Astrophys. **36** (1998), 435–506, `arXiv:astro-ph/9810070` [astro-ph].

[25] J. A. Tyson, G. P. Kochanski, and I. P. Dell'Antonio, *Detailed mass map of CL0024+1654 from strong lensing*, Astrophys.J. **498** (1998), L107, `arXiv:astro-ph/9801193` [astro-ph].

[26] A. Refregier, *Weak gravitational lensing by large scale structure*, Ann.Rev.Astron.Astrophys. **41** (2003), 645–668, `arXiv:astro-ph/0307212` [astro-ph].

[27] M. Bartelmann and P. Schneider, *Weak gravitational lensing*, Phys.Rept. **340** (2001), 291–472, `arXiv:astro-ph/9912508` [astro-ph].

[28] A. D. Lewis, D. A. Buote, and J. T. Stocke, *Chandra observations of Abell 2029: The dark matter profile at* $< 0.01\, r_{vir}$ *in an unusually relaxed cluster*, Astrophys.J. **586** (2003), 135–142, `arXiv:astro-ph/0209205` [astro-ph].

[29] Y. B. Zeldovich and R. A. Sunyaev, *The Interaction of Matter and Radiation in a Hot-Model Universe*, Astrophys.Space Sci. **4** (1969), 301.

[30] M. S. Turner, *Cosmological parameters*, (1998), 113–128, arXiv:astro-ph/9904051 [astro-ph].

[31] B. Paczynski, *Gravitational microlensing by the galactic halo*, Astrophys.J. **304** (1986), 1–5.

[32] MACHO Collaboration, C. Alcock et al., *The MACHO project: Microlensing results from 5.7 years of LMC observations*, Astrophys.J. **542** (2000), 281–307, arXiv:astro-ph/0001272 [astro-ph].

[33] EROS-2 Collaboration, P. Tisserand et al., *Limits on the Macho Content of the Galactic Halo from the EROS-2 Survey of the Magellanic Clouds*, Astron.Astrophys. **469** (2007), 387–404, arXiv:astro-ph/0607207 [astro-ph].

[34] R. Alpher, H. Bethe, and G. Gamow, *The origin of chemical elements*, Phys.Rev. **73** (1948), 803–804.

[35] B. Fields and S. Sarkar, *Big-Bang nucleosynthesis (Particle Data Group mini-review)*, J.Phys.G **G33** (2006), 1, arXiv:astro-ph/0601514 [astro-ph].

[36] S. Allen, A. Fabian, R. Schmidt, and H. Ebeling, *Cosmological constraints from the local x-ray luminosity function of the most x-ray luminous galaxy clusters*, Mon.Not.Roy.Astron.Soc. **342** (2003), 287, arXiv:astro-ph/0208394 [astro-ph].

[37] SDSS Collaboration, K. N. Abazajian et al., *The Seventh Data Release of the Sloan Digital Sky Survey*, Astrophys.J.Suppl. **182** (2009), 543–558, arXiv:0812.0649 [astro-ph].

[38] P. Peebles, *Large scale background temperature and mass fluctuations due to scale invariant primeval perturbations*, Astrophys.J. **263** (1982), L1–L5.

[39] Virgo Consortium, A. Jenkins et al., *Evolution of structure in cold dark matter universes*, Astrophys.J. **499** (1998), 20, arXiv:astro-ph/9709010 [astro-ph].

[40] J. Bond, G. Efstathiou, and J. Silk, *Massive Neutrinos and the Large Scale Structure of the Universe*, Phys.Rev.Lett. **45** (1980), 1980–1984.

[41] M. Iye, K. Ota, N. Kashikawa, H. Furusawa, T. Hashimoto, et al., *A galaxy at a redshift $z = 6.96$*, Nature **443** (2006), 186–188, arXiv:astro-ph/0609393 [astro-ph].

[42] G. Fogli, E. Lisi, A. Marrone, A. Melchiorri, A. Palazzo, et al., *Observables sensitive to absolute neutrino masses: A Reappraisal after WMAP-3y and first MINOS results*, Phys.Rev. **D75** (2007), 053001, arXiv:hep-ph/0608060 [hep-ph].

[43] U. Seljak, A. Slosar, and P. McDonald, *Cosmological parameters from combining the Lyman-alpha forest with CMB, galaxy clustering and SN constraints*, JCAP **0610** (2006), 014, arXiv:astro-ph/0604335 [astro-ph].

[44] V. Springel, S. D. White, A. Jenkins, C. S. Frenk, N. Yoshida, et al., *Simulating the joint evolution of quasars, galaxies and their large-scale distribution*, Nature **435** (2005), 629–636, arXiv:astro-ph/0504097 [astro-ph].

[45] J. Diemand, B. Moore, and J. Stadel, *Earth-mass dark-matter haloes as the first structures in the early Universe*, Nature **433** (2005), 389–391, arXiv:astro-ph/0501589 [astro-ph].

[46] SDSS Collaboration, B. A. Reid et al., *Baryon Acoustic Oscillations in the Sloan Digital Sky Survey Data Release 7 Galaxy Sample*, Mon.Not.Roy.Astron.Soc. **401** (2010), 2148–2168, arXiv:0907.1660 [astro-ph.CO].

[47] Supernova Search Team, A. G. Riess et al., *Observational evidence from supernovae for an accelerating universe and a cosmological constant*, Astron.J. **116** (1998), 1009–1038, arXiv:astro-ph/9805201 [astro-ph].

[48] Supernova Cosmology Project, S. Perlmutter et al., *Measurements of Omega and Lambda from 42 high redshift supernovae*, Astrophys.J. **517** (1999), 565–586, arXiv:astro-ph/9812133 [astro-ph].

[49] Supernova Search Team, P. M. Garnavich et al., *Supernova limits on the cosmic equation of state*, Astrophys.J. **509** (1998), 74–79, arXiv:astro-ph/9806396 [astro-ph].

[50] Supernova Cosmology Project, M. Kowalski et al., *Improved Cosmological Constraints from New, Old and Combined Supernova Datasets*, Astrophys.J. **686** (2008), 749–778, arXiv:0804.4142 [astro-ph].

[51] G. F. Smoot, C. Bennett, A. Kogut, E. Wright, J. Aymon, et al., *Structure in the COBE differential microwave radiometer first year maps*, Astrophys.J. **396** (1992), L1–L5.

[52] WMAP Collaboration, E. Komatsu et al., *Seven-Year Wilkinson Microwave Anisotropy Probe (WMAP) Observations: Cosmological Interpretation*, Astrophys.J.Suppl. **192** (2011), 18, arXiv:1001.4538 [astro-ph.CO].

[53] D. Larson, J. Dunkley, G. Hinshaw, E. Komatsu, M. Nolta, et al., *Seven-Year Wilkinson Microwave Anisotropy Probe (WMAP) Observations: Power Spectra and WMAP-Derived Parameters*, Astrophys.J.Suppl. **192** (2011), 16, arXiv:1001.4635 [astro-ph.CO].

[54] D. Clowe, M. Bradac, A. H. Gonzalez, M. Markevitch, S. W. Randall, et al., *A direct empirical proof of the existence of dark matter*, Astrophys.J. **648** (2006), L109–L113, arXiv:astro-ph/0608407 [astro-ph].

[55] M. Bradac, S. W. Allen, T. Treu, H. Ebeling, R. Massey, et al., *Revealing the properties of dark matter in the merging cluster MACSJ0025.4-1222*, Astrophys.J. **687** (2008), 959–967, arXiv:0806.2320 [astro-ph].

[56] M. Milgrom, *A Modification of the Newtonian dynamics as a possible alternative to the hidden mass hypothesis*, Astrophys.J. **270** (1983), 365–370.

[57] R. Tully and J. Fisher, *A New method of determining distances to galaxies*, Astron.Astrophys. **54** (1977), 661–673.

[58] R. H. Sanders and S. S. McGaugh, *Modified Newtonian dynamics as an alternative to dark matter*, Ann.Rev.Astron.Astrophys. **40** (2002), 263–317, arXiv:astro-ph/0204521 [astro-ph].

[59] J. D. Bekenstein, *Relativistic gravitation theory for the MOND paradigm*, Phys.Rev. **D70** (2004), 083509, arXiv:astro-ph/0403694 [astro-ph].

[60] C. Skordis, D. Mota, P. Ferreira, and C. Boehm, *Large Scale Structure in Bekenstein's theory of relativistic Modified Newtonian Dynamics*, Phys.Rev.Lett. **96** (2006), 011301, arXiv:astro-ph/0505519 [astro-ph].

[61] Particle Data Group, K. Nakamura et al., *Review of particle physics*, J.Phys.G **G37** (2010), 075021.

[62] B. Moore, S. Ghigna, F. Governato, G. Lake, T. R. Quinn, et al., *Dark matter substructure within galactic halos*, Astrophys.J. **524** (1999), L19–L22.

[63] A. A. Klypin, A. V. Kravtsov, O. Valenzuela, and F. Prada, *Where are the missing Galactic satellites?*, Astrophys.J. **522** (1999), 82–92, arXiv:astro-ph/9901240 [astro-ph].

[64] R. A. Flores and J. R. Primack, *Observational and theoretical constraints on singular dark matter halos*, Astrophys.J. **427** (1994), L1–4, arXiv:astro-ph/9402004 [astro-ph].

[65] S. S. McGaugh and W. de Blok, *Testing the dark matter hypothesis with low surface brightness galaxies and other evidence*, Astrophys.J. **499** (1998), 41, arXiv:astro-ph/9801123 [astro-ph].

[66] M. Taoso, G. Bertone, and A. Masiero, *Dark Matter Candidates: A Ten-Point Test*, JCAP **0803** (2008), 022, arXiv:0711.4996 [astro-ph].

[67] K. Jedamzik and M. Pospelov, *Big Bang Nucleosynthesis and Particle Dark Matter*, New J.Phys. **11** (2009), 105028, arXiv:0906.2087 [hep-ph].

[68] E. A. Baltz, M. Battaglia, M. E. Peskin, and T. Wizansky, *Determination of dark matter properties at high-energy colliders*, Phys.Rev. **D74** (2006), 103521, arXiv:hep-ph/0602187 [hep-ph].

[69] M. W. Goodman and E. Witten, *Detectability of Certain Dark Matter Candidates*, Phys.Rev. **D31** (1985), 3059.

[70] J. Gunn, B. Lee, I. Lerche, D. Schramm, and G. Steigman, *Some Astrophysical Consequences of the Existence of a Heavy Stable Neutral Lepton*, Astrophys.J. **223** (1978), 1015–1031.

[71] F. Stecker, *The Cosmic Gamma-Ray Background from the Annihilation of Primordial Stable Neutral Heavy Leptons*, Astrophys.J. **223** (1978), 1032–1036.

[72] J. Silk and M. Srednicki, *Cosmic Ray anti-Protons as a Probe of a Photino Dominated Universe*, Phys.Rev.Lett. **53** (1984), 624.

[73] J. Silk, K. A. Olive, and M. Srednicki, *The Photino, the Sun and High-Energy Neutrinos*, Phys.Rev.Lett. **55** (1985), 257–259.

[74] S. P. Martin, *A Supersymmetry primer*, (1997), arXiv:hep-ph/9709356 [hep-ph].

[75] T. Falk, K. A. Olive, and M. Srednicki, *Heavy sneutrinos as dark matter*, Phys.Lett. **B339** (1994), 248–251, arXiv:hep-ph/9409270 [hep-ph].

[76] W. Buchmuller, R. Peccei, and T. Yanagida, *Leptogenesis as the origin of matter*, Ann.Rev.Nucl.Part.Sci. **55** (2005), 311–355, arXiv:hep-ph/0502169 [hep-ph].

[77] W. Buchmuller, *Baryogenesis: 40 Years Later*, (2007), arXiv:0710.5857 [hep-ph].

[78] R. Kitano, H. Murayama, and M. Ratz, *Unified origin of baryons and dark matter*, Phys.Lett. **B669** (2008), 145–149, arXiv:0807.4313 [hep-ph].

[79] D. E. Kaplan, M. A. Luty, and K. M. Zurek, *Asymmetric Dark Matter*, Phys.Rev. **D79** (2009), 115016, arXiv:0901.4117 [hep-ph].

[80] J. L. Feng, A. Rajaraman, and F. Takayama, *Superweakly interacting massive particles*, Phys.Rev.Lett. **91** (2003), 011302, arXiv:hep-ph/0302215 [hep-ph].

[81] J. R. Ellis, K. A. Olive, Y. Santoso, and V. C. Spanos, *Gravitino dark matter in the CMSSM*, Phys.Lett. **B588** (2004), 7–16, arXiv:hep-ph/0312262 [hep-ph].

[82] F. D. Steffen, *Gravitino dark matter and cosmological constraints*, JCAP **0609** (2006), 001, arXiv:hep-ph/0605306 [hep-ph].

[83] M. Bolz, A. Brandenburg, and W. Buchmuller, *Thermal production of gravitinos*, Nucl.Phys. **B606** (2001), 518–544, arXiv:hep-ph/0012052 [hep-ph].

[84] J. L. Feng, A. Rajaraman, and F. Takayama, *SuperWIMP dark matter signals from the early universe*, Phys.Rev. **D68** (2003), 063504, arXiv:hep-ph/0306024 [hep-ph].

[85] W. Buchmuller, K. Hamaguchi, M. Ratz, and T. Yanagida, *Supergravity at colliders*, Phys.Lett. **B588** (2004), 90–98, arXiv:hep-ph/0402179 [hep-ph].

[86] R. Peccei and H. R. Quinn, *CP Conservation in the Presence of Pseudoparticles*, Phys.Rev.Lett. **38** (1977), 1440–1443.

[87] F. Wilczek, *Problem of Strong P and T Invariance in the Presence of Instantons*, Phys.Rev.Lett. **40** (1978), 279–282.

[88] S. Weinberg, *A New Light Boson?*, Phys.Rev.Lett. **40** (1978), 223–226.

[89] J. Preskill, M. B. Wise, and F. Wilczek, *Cosmology of the Invisible Axion*, Phys.Lett. **B120** (1983), 127–132.

[90] L. Abbott and P. Sikivie, *A Cosmological Bound on the Invisible Axion*, Phys.Lett. **B120** (1983), 133–136.

[91] L. Covi, J. E. Kim, and L. Roszkowski, *Axinos as cold dark matter*, Phys.Rev.Lett. **82** (1999), 4180–4183, arXiv:hep-ph/9905212 [hep-ph].

[92] L. Covi, H.-B. Kim, J. E. Kim, and L. Roszkowski, *Axinos as dark matter*, JHEP **0105** (2001), 033, arXiv:hep-ph/0101009 [hep-ph].

[93] G. Servant and T. M. Tait, *Is the lightest Kaluza-Klein particle a viable dark matter candidate?*, Nucl.Phys. **B650** (2003), 391–419, arXiv:hep-ph/0206071 [hep-ph].

[94] W. Buchmuller, L. Covi, K. Hamaguchi, A. Ibarra, and T. Yanagida, *Gravitino Dark Matter in R-Parity Breaking Vacua*, JHEP **0703** (2007), 037, arXiv:hep-ph/0702184 [hep-ph].

[95] X. Ji, R. N. Mohapatra, S. Nussinov, and Y. Zhang, *A Model With Dynamical R-parity Breaking and Unstable Gravitino Dark Matter*, Phys.Rev. **D78** (2008), 075032, arXiv:0808.1904 [hep-ph].

[96] P. Fileviez Perez and S. Spinner, *Spontaneous R-Parity Breaking in SUSY Models*, Phys.Rev. **D80** (2009), 015004, arXiv:0904.2213 [hep-ph].

[97] S. Shirai, F. Takahashi, and T. Yanagida, *R-violating Decay of Wino Dark Matter and electron/positron Excesses in the PAMELA/Fermi Experiments*, Phys.Lett. **B680** (2009), 485–488, arXiv:0905.0388 [hep-ph].

[98] C.-H. Chen, C.-Q. Geng, and D. V. Zhuridov, *Resolving Fermi, PAMELA and ATIC anomalies in split supersymmetry without R-parity*, Eur.Phys.J. **C67** (2010), 479–487, arXiv:0905.0652 [hep-ph].

[99] C.-R. Chen, F. Takahashi, and T. Yanagida, *Gamma rays and positrons from a decaying hidden gauge boson*, Phys.Lett. **B671** (2009), 71–76, arXiv:0809.0792 [hep-ph].

[100] A. Ibarra, A. Ringwald, and C. Weniger, *Hidden gauginos of an unbroken U(1): Cosmological constraints and phenomenological prospects*, JCAP **0901** (2009), 003, arXiv:0809.3196 [hep-ph].

[101] Y. Gong and X. Chen, *Cosmological Constraints on Invisible Decay of Dark Matter*, Phys.Rev. **D77** (2008), 103511, arXiv:0802.2296 [astro-ph].

[102] S. De Lope Amigo, W. M.-Y. Cheung, Z. Huang, and S.-P. Ng, *Cosmological Constraints on Decaying Dark Matter*, JCAP **0906** (2009), 005, arXiv:0812.4016 [hep-ph].

[103] G. Bertone, W. Buchmuller, L. Covi, and A. Ibarra, *Gamma-Rays from Decaying Dark Matter*, JCAP **0711** (2007), 003, arXiv:0709.2299 [astro-ph].

[104] E. Nardi, F. Sannino, and A. Strumia, *Decaying Dark Matter can explain the $e^{\pm}$ excesses*, JCAP **0901** (2009), 043, arXiv:0811.4153 [hep-ph].

[105] J. Hisano, M. Kawasaki, K. Kohri, and K. Nakayama, *Neutrino Signals from Annihilating/Decaying Dark Matter in the Light of Recent Measurements of Cosmic Ray Electron/Positron Fluxes*, Phys.Rev. **D79** (2009), 043516, arXiv:0812.0219 [hep-ph].

[106] J. Liu, P.-F. Yin, and S.-H. Zhu, *Prospects for Detecting Neutrino Signals from Annihilating/Decaying Dark Matter to Account for the PAMELA and ATIC results*, Phys.Rev. **D79** (2009), 063522, arXiv:0812.0964 [astro-ph].

[107] M. R. Buckley, K. Freese, D. Hooper, D. Spolyar, and H. Murayama, *High-Energy Neutrino Signatures of Dark Matter Decaying into Leptons*, Phys.Rev. **D81** (2010), 016006, arXiv:0907.2385 [astro-ph.HE].

[108] A. Boyarsky, O. Ruchayskiy, and M. Shaposhnikov, *The Role of sterile neutrinos in cosmology and astrophysics*, Ann.Rev.Nucl.Part.Sci. **59** (2009), 191–214, arXiv:0901.0011 [hep-ph].

[109] F. Takayama and M. Yamaguchi, *Gravitino dark matter without R-parity*, Phys.Lett. **B485** (2000), 388–392, arXiv:hep-ph/0005214 [hep-ph].

[110] D. Eichler, *TeV Particles as Weakly Unstable Dark Matter*, Phys.Rev.Lett. **63** (1989), 2440.

[111] A. Arvanitaki, S. Dimopoulos, S. Dubovsky, P. W. Graham, R. Harnik, et al., *Astrophysical Probes of Unification*, Phys.Rev. **D79** (2009), 105022, arXiv:0812.2075 [hep-ph].

[112] J. F. Navarro, E. Hayashi, C. Power, A. Jenkins, C. S. Frenk, et al., *The Inner structure of Lambda-CDM halos 3: Universality and asymptotic slopes*, Mon.Not.Roy.Astron.Soc. **349** (2004), 1039, arXiv:astro-ph/0311231 [astro-ph].

[113] V. Springel, J. Wang, M. Vogelsberger, A. Ludlow, A. Jenkins, et al., *The Aquarius Project: the subhalos of galactic halos*, Mon.Not.Roy.Astron.Soc. **391** (2008), 1685–1711, arXiv:0809.0898 [astro-ph].

[114] O. Y. Gnedin, A. V. Kravtsov, A. A. Klypin, and D. Nagai, *Response of dark matter halos to condensation of baryons: Cosmological simulations and improved adiabatic contraction model*, Astrophys.J. **616** (2004), 16–26, arXiv:astro-ph/0406247 [astro-ph].

[115] F. Prada, A. Klypin, J. Flix Molina, M. Martinez, and E. Simonneau, *Dark Matter Annihilation in the Milky Way Galaxy: Effects of Baryonic Compression*, Phys.Rev.Lett. **93** (2004), 241301, arXiv:astro-ph/0401512 [astro-ph].

[116] J. N. Bahcall and R. Soneira, *The Universe at faint magnitudes. 2. Models for the predicted star counts*, Astrophys.J.Suppl. **44** (1980), 73–110.

[117] J. F. Navarro, C. S. Frenk, and S. D. White, *The Structure of cold dark matter halos*, Astrophys.J. **462** (1996), 563–575, arXiv:astro-ph/9508025 [astro-ph].

[118] J. F. Navarro, C. S. Frenk, and S. D. White, *A Universal density profile from hierarchical clustering*, Astrophys.J. **490** (1997), 493–508, arXiv:astro-ph/9611107 [astro-ph].

[119] B. Moore, T. R. Quinn, F. Governato, J. Stadel, and G. Lake, *Cold collapse and the core catastrophe*, Mon.Not.Roy.Astron.Soc. **310** (1999), 1147–1152, arXiv:astro-ph/9903164 [astro-ph].

[120] A. Burkert, *The Structure of dark matter halos in dwarf galaxies*, IAU Symp. **171** (1996), 175, arXiv:astro-ph/9504041 [astro-ph].

[121] F. J. Kerr and D. Lynden-Bell, *Review of galactic constants*, Mon.Not.Roy.Astron.Soc. **221** (1986), 1023.

[122] R. Catena and P. Ullio, *A novel determination of the local dark matter density*, JCAP **1008** (2010), 004, arXiv:0907.0018 [astro-ph.CO].

[123] A. W. Graham, D. Merritt, B. Moore, J. Diemand, and B. Terzic, *Empirical models for Dark Matter Halos. I. Nonparametric Construction of Density Profiles and Comparison with Parametric Models*, Astron.J. **132** (2006), 2685–2700, arXiv:astro-ph/0509417 [astro-ph].

[124] J. F. Navarro, A. Ludlow, V. Springel, J. Wang, M. Vogelsberger, et al., *The Diversity and Similarity of Cold Dark Matter Halos*, (2008), arXiv:0810.1522 [astro-ph].

[125] P. B. Tissera, S. D. White, S. Pedrosa, and C. Scannapieco, *Dark matter response to galaxy formation*, (2009), arXiv:0911.2316 [astro-ph.CO].

[126] Pierre Auger Collaboration, J. Abraham et al., *Observation of the suppression of the flux of cosmic rays above* $4 \times 10^{19}\, eV$, Phys.Rev.Lett. **101** (2008), 061101, arXiv:0806.4302 [astro-ph].

[127] K. Greisen, *End to the cosmic ray spectrum?*, Phys.Rev.Lett. **16** (1966), 748–750.

[128] G. Zatsepin and V. Kuzmin, *Upper limit of the spectrum of cosmic rays*, JETP Lett. **4** (1966), 78–80.

[129] O. Adriani, G. Barbarino, G. Bazilevskaya, R. Bellotti, M. Boezio, et al., *A new measurement of the antiproton-to-proton flux ratio up to 100 GeV in the cosmic radiation*, Phys.Rev.Lett. **102** (2009), 051101, arXiv:0810.4994 [astro-ph].

[130] M. Malkov and L. O'C Drury, *Nonlinear theory of diffusive acceleration of particles by shock waves*, Rept.Prog.Phys. **64** (2001), 429–481.

[131] E. Fermi, *On the Origin of the Cosmic Radiation*, Phys.Rev. **75** (1949), 1169–1174.

[132] H. Ahn, P. Allison, M. Bagliesi, J. Beatty, G. Bigongiari, et al., *Measurements of cosmic-ray secondary nuclei at high energies with the first flight of the CREAM balloon-borne experiment*, Astropart.Phys. **30** (2008), 133–141, arXiv:0808.1718 [astro-ph].

[133] V. Berezinskii, S. Bulanov, V. Dogiel, V. Ginzburg (ed.), and V. Ptuskin, *Astrophysics of cosmic rays*, North-Holland, Amsterdam (1990).

[134] A. W. Strong, I. V. Moskalenko, and V. S. Ptuskin, *Cosmic-ray propagation and interactions in the Galaxy*, Ann.Rev.Nucl.Part.Sci. **57** (2007), 285–327, arXiv:astro-ph/0701517 [astro-ph].

[135] K. Blum, *Cosmic ray propagation time scales: lessons from radioactive nuclei and positron data*, (2010), arXiv:1010.2836 [astro-ph.HE].

[136] M. Regis and P. Ullio, *Testing the Dark Matter Interpretation of the PAMELA Excess through Measurements of the Galactic Diffuse Emission*, Phys.Rev. **D80** (2009), 043525, arXiv:0904.4645 [astro-ph.GA].

[137] D. Maurin, F. Donato, R. Taillet, and P. Salati, *Cosmic rays below* $Z = 30$ *in a diffusion model: new constraints on propagation parameters*, Astrophys.J. **555** (2001), 585–596, arXiv:astro-ph/0101231 [astro-ph].

[138] http://galprop.stanford.edu.

[139] T. Delahaye, F. Donato, N. Fornengo, J. Lavalle, R. Lineros, P. Salati, and R. Taillet, *Galactic secondary positron flux at the Earth*, Astron.Astrophys. **501** (2009), 821–833, arXiv:0809.5268 [astro-ph].

[140] P. Salati, *Indirect and direct dark matter detection*, PoS Cargese (2007), 009.

[141] J. Hisano, S. Matsumoto, O. Saito, and M. Senami, *Heavy wino-like neutralino dark matter annihilation into antiparticles*, Phys.Rev. **D73** (2006), 055004, `arXiv:hep-ph/0511118` [hep-ph].

[142] T. Delahaye, R. Lineros, F. Donato, N. Fornengo, and P. Salati, *Positrons from dark matter annihilation in the galactic halo: Theoretical uncertainties*, Phys.Rev. **D77** (2008), 063527, `arXiv:0712.2312` [astro-ph].

[143] J. Lavalle, J. Pochon, P. Salati, and R. Taillet, *Clumpiness of dark matter and positron annihilation signal: computing the odds of the galactic lottery*, Astron.Astrophys. **462** (2007), 827–848, `arXiv:astro-ph/0603796` [astro-ph].

[144] D. Maurin, R. Taillet, F. Donato, P. Salati, A. Barrau, et al., *Galactic cosmic ray nuclei as a tool for astroparticle physics*, (2002), `arXiv:astro-ph/0212111` [astro-ph].

[145] F. Donato, N. Fornengo, D. Maurin, and P. Salati, *Antiprotons in cosmic rays from neutralino annihilation*, Phys.Rev. **D69** (2004), 063501, `arXiv:astro-ph/0306207` [astro-ph].

[146] L. Tan and L. Ng, *Calculation of the Equilibrium Anti-Proton Spectrum*, J.Phys.G **G9** (1983), 227–242.

[147] R. Protheroe, *Cosmic Ray Antiprotons in the Closed Galaxy Model*, Astrophys.J. **251** (1981), 387–392.

[148] L. Gleeson and W. Axford, *Cosmic Rays in the Interplanetary Medium*, Astrophys.J. **149** (1967), L115.

[149] L. Gleeson and W. Axford, *Solar Modulation of Galactic Cosmic Rays*, Astrophys.J. **154** (1968), 1011.

[150] J. Perko, *Solar Cycle Modulation of Galactic Cosmic Rays*, (1986).

[151] P. L. Nolan, D. Bertsch, J. Chiang, B. Dingus, J. Esposito, et al., *EGRET observations of gamma-rays from point sources with galactic latitude* $+10^\circ < b < +40^\circ$, Astrophys.J. **459** (1996), 100, `arXiv:astro-ph/9509023` [astro-ph].

[152] A. W. Strong, I. V. Moskalenko, and O. Reimer, *Diffuse continuum gamma-rays from the galaxy*, Astrophys.J. **537** (2000), 763–784, `arXiv:astro-ph/9811296` [astro-ph].

[153] A. Cillis and R. Hartman, *EGRET diffuse gamma-ray maps between 30 MeV and 10 GeV*, Astrophys.J. **621** (2005), 291–295.

[154] C. Fichtel, G. Simpson, and D. Thompson, *Diffuse Gamma Radiation*, Astrophys.J. **222** (1978), 833–849.

[155] EGRET Collaboration, P. Sreekumar et al., *EGRET observations of the extragalactic gamma-ray emission*, Astrophys.J. **494** (1998), 523–534, `arXiv:astro-ph/9709257` [astro-ph].

[156] Fermi LAT Collaboration, A. Abdo et al., *The Spectrum of the Isotropic Diffuse Gamma-Ray Emission Derived From First-Year Fermi Large Area Telescope Data*, Phys.Rev.Lett. **104** (2010), 101101, arXiv:1002.3603 [astro-ph.HE].

[157] C. D. Dermer, *The Extragalactic Gamma Ray Background*, AIP Conf.Proc. **921** (2007), 122–126, arXiv:0704.2888 [astro-ph].

[158] L. Dugger, T. E. Jeltema, and S. Profumo, *Constraints on Decaying Dark Matter from Fermi Observations of Nearby Galaxies and Clusters*, JCAP **1012** (2010), 015, arXiv:1009.5988 [astro-ph.HE].

[159] I. V. Moskalenko, T. A. Porter, and A. W. Strong, *Attenuation of VHE gamma rays by the milky way interstellar radiation field*, Astrophys.J. **640** (2006), L155–L158, arXiv:astro-ph/0511149 [astro-ph].

[160] F. W. Stecker, M. Malkan, and S. Scully, *Intergalactic photon spectra from the far IR to the UV Lyman limit for* $0 < z < 6$ *and the optical depth of the universe to high energy gamma-rays*, Astrophys.J. **648** (2006), 774–783, arXiv:astro-ph/0510449 [astro-ph].

[161] F. W. Stecker, M. Malkan, and S. Scully, *Corrected Table for the Parametric Coefficients for the Optical Depth of the Universe to Gamma-rays at Various Redshifts*, Astrophys.J. **658** (2007), 1392, arXiv:astro-ph/0612048 [astro-ph].

[162] G. Blumenthal and R. Gould, *Bremsstrahlung, synchrotron radiation, and compton scattering of high-energy electrons traversing dilute gases*, Rev.Mod.Phys. **42** (1970), 237–270.

[163] T. A. Porter and A. Strong, *A New estimate of the Galactic interstellar radiation field between 0.1 microns and 1000 microns*, (2005), arXiv:astro-ph/0507119 [astro-ph].

[164] I. V. Moskalenko and A. W. Strong, *Anisotropic inverse Compton scattering in the galaxy*, Astrophys.J. **528** (2000), 357–367, arXiv:astro-ph/9811284 [astro-ph].

[165] L. Zhang, G. Sigl, and J. Redondo, *Galactic Signatures of Decaying Dark Matter*, JCAP **0909** (2009), 012, arXiv:0905.4952 [astro-ph.GA].

[166] A. Boulares, *The Nature of the Cosmic-Ray Electron Spectrum, and Supernova Remnant Contributions*, Astrophys.J. **342** (1989), 807–813.

[167] D. Muller and K. K. Tang, *The Cosmic Ray Positron Enigma*, Proceedings of the 21st International Cosmic Ray Conference **3** (1990), 249–252.

[168] I. Moskalenko and A. Strong, *Production and propagation of cosmic ray positrons and electrons*, Astrophys.J. **493** (1998), 694–707, arXiv:astro-ph/9710124 [astro-ph].

[169] PAMELA Collaboration, O. Adriani et al., *An anomalous positron abundance in cosmic rays with energies* $1.5-100$ *GeV*, Nature **458** (2009), 607–609, arXiv:0810.4995 [astro-ph].

[170] HEAT Collaboration, S. Barwick et al., *Measurements of the cosmic ray positron fraction from 1 GeV to 50 GeV*, Astrophys.J. **482** (1997), L191–L194, arXiv:astro-ph/9703192 [astro-ph].

[171] CAPRICE Collaboration, M. Boezio et al., *The cosmic-ray electron and positron spectra measured at 1 AU during solar minimum activity*, Astrophys.J. **532** (2000), 653–669.

[172] AMS-01 Collaboration, M. Aguilar et al., *Cosmic-ray positron fraction measurement from 1 to 30 GeV with AMS-01*, Phys.Lett. **B646** (2007), 145–154, arXiv:astro-ph/0703154 [astro-ph].

[173] J. Chang, J. Adams, H. Ahn, G. Bashindzhagyan, M. Christl, et al., *An excess of cosmic ray electrons at energies of 300-800 GeV*, Nature **456** (2008), 362–365.

[174] PPB-BETS Collaboration, S. Torii et al., *High-energy electron observations by PPB-BETS flight in Antarctica*, (2008), arXiv:0809.0760 [astro-ph].

[175] H.E.S.S. Collaboration, F. Aharonian et al., *The energy spectrum of cosmic-ray electrons at TeV energies*, Phys.Rev.Lett. **101** (2008), 261104, arXiv:0811.3894 [astro-ph].

[176] A. Atoian, F. Aharonian, and H. Volk, *Electrons and positrons in the galactic cosmic rays*, Phys.Rev. **D52** (1995), 3265–3275.

[177] D. Hooper, P. Blasi, and P. D. Serpico, *Pulsars as the Sources of High Energy Cosmic Ray Positrons*, JCAP **0901** (2009), 025, arXiv:0810.1527 [astro-ph].

[178] C. Grimani, *Pulsar birthrate set by cosmic-ray positron observations*, Astron.Astrophys. **418** (2004), 649–653.

[179] S. Rudaz and F. Stecker, *Cosmic Ray Anti-Protons, Positrons and Gamma-Rays from Halo Dark Matter Annihilation*, Astrophys.J. **325** (1988), 16.

[180] J. R. Ellis, R. Flores, K. Freese, S. Ritz, D. Seckel, et al., *Cosmic Ray Constraints on the Annihilations of Relic Particles in the Galactic Halo*, Phys.Lett. **B214** (1988), 403.

[181] M. Kamionkowski and M. S. Turner, *A Distinctive positron feature from heavy WIMP annihilations in the galactic halo*, Phys.Rev. **D43** (1991), 1774–1780.

[182] H. Matsunaga, S. Orito, H. Matsumoto, K. Yoshimura, A. Moiseev, et al., *Measurement of low-energy cosmic ray anti-protons at solar minimum*, Phys.Rev.Lett. **81** (1998), 4052–4055, arXiv:astro-ph/9809326 [astro-ph].

[183] BESS Collaboration, S. Orito et al., *Precision measurement of cosmic ray anti-proton spectrum*, Phys.Rev.Lett. **84** (2000), 1078–1081, arXiv:astro-ph/9906426 [astro-ph].

[184] WIZARD Collaboration, M. Boezio et al., *The Cosmic ray anti-proton flux between 0.62 GeV and 3.19 GeV measured near solar minimum activity*, Astrophys.J. **487** (1997), 415–423.

[185] WiZard/CAPRICE Collaboration, M. Boezio et al., *The Cosmic ray anti-proton flux between 3 GeV and 49 GeV*, Astrophys.J. **561** (2001), 787–799, arXiv:astro-ph/0103513 [astro-ph].

[186] J. Mitchell, L. Barbier, E. Christian, J. Krizmanic, K. Krombel, et al., *Measurement of 0.25 GeV to 3.2 GeV anti-protons in the cosmic radiation*, Phys.Rev.Lett. **76** (1996), 3057–3060.

[187] L. Bergstrom, J. Edsjo, and P. Ullio, *Cosmic anti-protons as a probe for supersymmetric dark matter?*, Astrophys.J. **526** (1999), 215–235, arXiv:astro-ph/9902012 [astro-ph].

[188] F. Donato, D. Maurin, P. Salati, A. Barrau, G. Boudoul, et al., *Anti-protons from spallations of cosmic rays on interstellar matter*, Astrophys.J. **563** (2001), 172–184, arXiv:astro-ph/0103150 [astro-ph].

[189] M. Cirelli, M. Kadastik, M. Raidal, and A. Strumia, *Model-independent implications of the $e^{\pm}$, anti-proton cosmic ray spectra on properties of Dark Matter*, Nucl.Phys. **B813** (2009), 1–21, arXiv:0809.2409 [hep-ph].

[190] J. L. Feng, M. Kaplinghat, and H.-B. Yu, *Halo Shape and Relic Density Exclusions of Sommerfeld-Enhanced Dark Matter Explanations of Cosmic Ray Excesses*, Phys.Rev.Lett. **104** (2010), 151301, arXiv:0911.0422 [hep-ph].

[191] G. Bertone, M. Cirelli, A. Strumia, and M. Taoso, *Gamma-ray and radio tests of the e^+e^- excess from DM annihilations*, JCAP **0903** (2009), 009, arXiv:0811.3744 [astro-ph].

[192] J. Zhang, X.-J. Bi, J. Liu, S.-M. Liu, P.-F. Yin, et al., *Discriminating different scenarios to account for the cosmic $e^{\pm}$ excess by synchrotron and inverse Compton radiation*, Phys.Rev. **D80** (2009), 023007, arXiv:0812.0522 [astro-ph].

[193] M. Cirelli and P. Panci, *Inverse Compton constraints on the Dark Matter e^+e^- excesses*, Nucl.Phys. **B821** (2009), 399–416, arXiv:0904.3830 [astro-ph.CO].

[194] L. Bergstrom, G. Bertone, T. Bringmann, J. Edsjo, and M. Taoso, *Gamma-ray and Radio Constraints of High Positron Rate Dark Matter Models Annihilating into New Light Particles*, Phys.Rev. **D79** (2009), 081303, arXiv:0812.3895 [astro-ph].

[195] K. Ishiwata, S. Matsumoto, and T. Moroi, *Synchrotron Radiation from the Galactic Center in Decaying Dark Matter Scenario*, Phys.Rev. **D79** (2009), 043527, arXiv:0811.4492 [astro-ph].

[196] S. Profumo and T. E. Jeltema, *Extragalactic Inverse Compton Light from Dark Matter Annihilation and the Pamela Positron Excess*, JCAP **0907** (2009), 020, arXiv:0906.0001 [astro-ph.CO].

[197] S. Matsumoto, K. Ishiwata, and T. Moroi, *Cosmic Gamma-ray from Inverse Compton Process in Unstable Dark Matter Scenario*, Phys.Lett. **B679** (2009), 1–5, arXiv:0905.4593 [astro-ph.CO].

[198] K. Ishiwata, S. Matsumoto, and T. Moroi, *High Energy Cosmic Rays from the Decay of Gravitino Dark Matter*, Phys.Rev. **D78** (2008), 063505, arXiv:0805.1133 [hep-ph].

[199] K. Ishiwata, S. Matsumoto, and T. Moroi, *Cosmic-Ray Positron from Superparticle Dark Matter and the PAMELA Anomaly*, Phys.Lett. **B675** (2009), 446–449, arXiv:0811.0250 [hep-ph].

[200] C.-R. Chen and F. Takahashi, *Cosmic rays from Leptonic Dark Matter*, JCAP **0902** (2009), 004, arXiv:0810.4110 [hep-ph].

[201] C.-R. Chen, M. M. Nojiri, F. Takahashi, and T. Yanagida, *Decaying Hidden Gauge Boson and the PAMELA and ATIC/PPB-BETS Anomalies*, Prog.Theor.Phys. **122** (2009), 553–559, arXiv:0811.3357 [astro-ph].

[202] P.-F. Yin, Q. Yuan, J. Liu, J. Zhang, X.-J. Bi, et al., *PAMELA data and leptonically decaying dark matter*, Phys.Rev. **D79** (2009), 023512, arXiv:0811.0176 [hep-ph].

[203] K. Hamaguchi, S. Shirai, and T. Yanagida, *Cosmic Ray Positron and Electron Excess from Hidden-Fermion Dark Matter Decays*, Phys.Lett. **B673** (2009), 247–250, arXiv:0812.2374 [hep-ph].

[204] M. Pospelov and M. Trott, *R-parity preserving super-WIMP decays*, JHEP **0904** (2009), 044, arXiv:0812.0432 [hep-ph].

[205] A. Arvanitaki, S. Dimopoulos, S. Dubovsky, P. W. Graham, R. Harnik, et al., *Decaying Dark Matter as a Probe of Unification and TeV Spectroscopy*, Phys.Rev. **D80** (2009), 055011, arXiv:0904.2789 [hep-ph].

[206] K. J. Bae and B. Kyae, *PAMELA/ATIC Anomaly from Exotic Mediated Dark Matter Decay*, JHEP **0905** (2009), 102, arXiv:0902.3578 [hep-ph].

[207] K. Cheung, P.-Y. Tseng, and T.-C. Yuan, *Double-action dark matter, PAMELA and ATIC*, Phys.Lett. **B678** (2009), 293–300, arXiv:0902.4035 [hep-ph].

[208] S.-L. Chen, R. N. Mohapatra, S. Nussinov, and Y. Zhang, *R-Parity Breaking via Type II Seesaw, Decaying Gravitino Dark Matter and PAMELA Positron Excess*, Phys.Lett. **B677** (2009), 311–317, arXiv:0903.2562 [hep-ph].

[209] J. Hisano, K. Nakayama, and M. J. Yang, *Upward muon signals at neutrino detectors as a probe of dark matter properties*, Phys.Lett. **B678** (2009), 101–106, arXiv:0905.2075 [hep-ph].

[210] H. Fukuoka, J. Kubo, and D. Suematsu, *Anomaly Induced Dark Matter Decay and PAMELA/ATIC Experiments*, Phys.Lett. **B678** (2009), 401–406, arXiv:0905.2847 [hep-ph].

[211] S. Shirai, F. Takahashi, and T. Yanagida, *Decaying Hidden Gaugino as a Source of PAMELA/ATIC Anomalies*, Phys.Lett. **B675** (2009), 73–76, arXiv:0902.4770 [hep-ph].

[212] K.-Y. Choi, D. E. Lopez-Fogliani, C. Munoz, and R. R. de Austri, *Gamma-ray detection from gravitino dark matter decay in the $\mu\nu$SSM*, JCAP **1003** (2010), 028, arXiv:0906.3681 [hep-ph].

[213] K. Kohri, A. Mazumdar, N. Sahu, and P. Stephens, *Probing Unified Origin of Dark Matter and Baryon Asymmetry at PAMELA/Fermi*, Phys.Rev. **D80** (2009), 061302, arXiv:0907.0622 [hep-ph].

[214] C. Arina, T. Hambye, A. Ibarra, and C. Weniger, *Intense Gamma-Ray Lines from Hidden Vector Dark Matter Decay*, JCAP **1003** (2010), 024, arXiv:0912.4496 [hep-ph].

[215] C. D. Carone, J. Erlich, and R. Primulando, *Decaying Dark Matter from Dark Instantons*, Phys.Rev. **D82** (2010), 055028, arXiv:1008.0642 [hep-ph].

[216] Fermi LAT Collaboration, A. A. Abdo et al., *Measurement of the Cosmic Ray $e^+ + e^-$ spectrum from 20 GeV to 1 TeV with the Fermi Large Area Telescope*, Phys.Rev.Lett. **102** (2009), 181101, arXiv:0905.0025 [astro-ph.HE].

[217] H.E.S.S. Collaboration, F. Aharonian et al., *Probing the ATIC peak in the cosmic-ray electron spectrum with H.E.S.S*, Astron.Astrophys. **508** (2009), 561, arXiv:0905.0105 [astro-ph.HE].

[218] Fermi LAT Collaboration, D. Grasso et al., *On possible interpretations of the high energy electron-positron spectrum measured by the Fermi Large Area Telescope*, Astropart.Phys. **32** (2009), 140–151, arXiv:0905.0636 [astro-ph.HE].

[219] P. Meade, M. Papucci, A. Strumia, and T. Volansky, *Dark Matter Interpretations of the $e^\pm$ Excesses after FERMI*, Nucl.Phys. **B831** (2010), 178–203, arXiv:0905.0480 [hep-ph].

[220] J. Mardon, Y. Nomura, and J. Thaler, *Cosmic Signals from the Hidden Sector*, Phys.Rev. **D80** (2009), 035013, arXiv:0905.3749 [hep-ph].

[221] D. Muller and K. Tang, *Cosmic-ray positrons from 10 to 20 GeV - A balloon-borne measurement using the geomagnetic east-west asymmetry*, Astrophys.J. **312** (1987), L183–L194.

[222] WIZARDS Collaboration, R. Golden et al., *Measurement of the positron to electron ratio in the cosmic rays above 5 GeV*, Astrophys.J. **457** (1996), L103–L106.

[223] J. Beatty, A. Bhattacharyya, C. Bower, S. Coutu, M. DuVernois, et al., *New measurement of the cosmic-ray positron fraction from 5 to 15 GeV*, Phys.Rev.Lett. **93** (2004), 241102, arXiv:astro-ph/0412230 [astro-ph].

[224] H. Gast and S. Schael, *Charge-dependent solar modulation in light of the recent PAMELA data*, Proceedings of the 31st International Cosmic Ray Conference (2009).

[225] PAMELA Collaboration, O. Adriani et al., *The cosmic-ray electron flux measured by the PAMELA experiment between 1 and 625 GeV*, (2011), arXiv:1103.2880 [astro-ph.HE].

[226] M. DuVernois, S. Barwick, J. Beatty, A. Bhattacharyya, C. Bower, et al., *Cosmic ray electrons and positrons from 1 GeV to 100 GeV: Measurements with HEAT and their interpretation*, Astrophys.J. **559** (2001), 296–303.

[227] AMS Collaboration, J. Alcaraz et al., *Leptons in near earth orbit*, Phys.Lett. **B484** (2000), 10–22.

[228] C. Grimani, S. Stephens, F. Cafagna, G. Basini, R. Bellotti, et al., *Measurements of the absolute energy spectra of cosmic-ray positrons and electrons above 7 GeV*, Astron.Astrophys. **392** (2002), 287–294.

[229] T. Kobayashi, J. Nishimura, Y. Komori, T. Shirai, N. Tateyama, T. Taira, K. Yoshida, and T. Yuda, Proceedings of the 26th International Cosmic Ray Conference **3** (1999), 61.

[230] S. Torii, T. Tamura, N. Tateyama, K. Yoshida, J. Nishimura, et al., *The energy spectrum of cosmic ray electrons from 10 GeV to 100 GeV observed with a highly granulated imaging calorimeter*, Astrophys.J. **559** (2001), 973–984.

[231] Fermi LAT Collaboration, M. Ackermann et al., *Fermi LAT observations of cosmic-ray electrons from 7 GeV to 1 TeV*, Phys.Rev. **D82** (2010), 092004, arXiv:1008.3999 [astro-ph.HE].

[232] R. Cowsik, Y. Pal, S. Tandon, and R. Verma, *Steady State of Cosmic-Ray Nuclei — Their Spectral Shape and Path Length at Low Energies*, Phys.Rev. **158** (1967), 1238–1242.

[233] P. D. Serpico, *On the possible causes of a rise with energy of the cosmic ray positron fraction*, Phys.Rev. **D79** (2009), 021302, arXiv:0810.4846 [hep-ph].

[234] R. Blandford and D. Eichler, *Particle Acceleration at Astrophysical Shocks: A Theory of Cosmic Ray Origin*, Phys.Rept. **154** (1987), 1–75.

[235] P. Blasi, *The origin of the positron excess in cosmic rays*, Phys.Rev.Lett. **103** (2009), 051104, arXiv:0903.2794 [astro-ph.HE].

[236] S. Profumo, *Dissecting Pamela (and ATIC) with Occam's Razor: existing, well-known Pulsars naturally account for the 'anomalous' Cosmic-Ray Electron and Positron Data*, (2008), arXiv:0812.4457 [astro-ph].

[237] H. Yuksel, M. D. Kistler, and T. Stanev, *TeV Gamma Rays from Geminga and the Origin of the GeV Positron Excess*, Phys.Rev.Lett. **103** (2009), 051101, arXiv:0810.2784 [astro-ph].

[238] D. Malyshev, I. Cholis, and J. Gelfand, *Pulsars versus Dark Matter Interpretation of ATIC/PAMELA*, Phys.Rev. **D80** (2009), 063005, arXiv:0903.1310 [astro-ph.HE].

[239] A. K. Harding and R. Ramaty, *The Pulsar Contribution to Galactic Cosmic Ray Positrons*, Proceedings of the 20th International Cosmic Ray Conference **2** (1987), 92–95.

[240] F. Aharonian, A. Atoian, and H. Volk, *High energy electrons and positrons in cosmic rays as an indicator of the existence of a nearby cosmic tevatron*, Astron.Astrophys. **294** (1995), L41–L44.

[241] X. Chi, E. Young, and K. Cheng, *Pulsar-wind origin of cosmic ray positrons*, Astrophys.J. **459** (1995), L83–L86.

[242] K. Ioka, *A Gamma-Ray Burst/Pulsar for Cosmic-Ray Positrons with a Dark Matter-like Spectrum*, Prog.Theor.Phys. **123** (2010), 743–755, arXiv:0812.4851 [astro-ph].

[243] N. J. Shaviv, E. Nakar, and T. Piran, *Natural explanation for the anomalous positron to electron ratio with supernova remnants as the sole cosmic ray source*, Phys.Rev.Lett. **103** (2009), 111302, arXiv:0902.0376 [astro-ph.HE].

[244] M. Ahlers, P. Mertsch, and S. Sarkar, *On cosmic ray acceleration in supernova remnants and the FERMI/PAMELA data*, Phys.Rev. **D80** (2009), 123017, arXiv:0909.4060 [astro-ph.HE].

[245] P. Blasi and P. D. Serpico, *High-energy antiprotons from old supernova remnants*, Phys.Rev.Lett. **103** (2009), 081103, arXiv:0904.0871 [astro-ph.HE].

[246] Y. Fujita, K. Kohri, R. Yamazaki, K. Ioka, K. Kohri, et al., *Is the PAMELA anomaly caused by the supernova explosions near the Earth?*, Phys.Rev. **D80** (2009), 063003, arXiv:0903.5298 [astro-ph.HE].

[247] B. Katz, K. Blum, and E. Waxman, *What can we really learn from positron flux 'anomalies'?*, (2009), arXiv:0907.1686 [astro-ph.HE].

[248] R. Cowsik and B. Burch, *On the Positron Fraction and the Spectrum of the Electronic Component in Cosmic Rays*, (2009), arXiv:0905.2136 [astro-ph.CO].

[249] T. Sjostrand, S. Mrenna, and P. Z. Skands, *PYTHIA 6.4 Physics and Manual*, JHEP **0605** (2006), 026, arXiv:hep-ph/0603175 [hep-ph].

[250] M. Cirelli, G. Corcella, A. Hektor, G. Hutsi, M. Kadastik, et al., *PPPC 4 DM ID: A Poor Particle Physicist Cookbook for Dark Matter Indirect Detection*, JCAP **1103** (2011), 051, arXiv:1012.4515 [hep-ph].

[251] A. Strong, I. Moskalenko, and O. Reimer, *A new determination of the extragalactic diffuse gamma-ray background from EGRET data*, Astrophys.J. **613** (2004), 956–961, arXiv:astro-ph/0405441 [astro-ph].

[252] T. Bringmann and P. Salati, *The galactic antiproton spectrum at high energies: Background expectation vs. exotic contributions*, Phys.Rev. **D75** (2007), 083006, arXiv:astro-ph/0612514 [astro-ph].

[253] A. M. Lionetto, A. Morselli, and V. Zdravkovic, *Uncertainties of cosmic ray spectra and detectability of antiproton mSUGRA contributions with PAMELA*, JCAP **0509** (2005), 010, arXiv:astro-ph/0502406 [astro-ph].

[254] F. Donato, N. Fornengo, and P. Salati, *Anti-deuterons as a signature of supersymmetric dark matter*, Phys.Rev. **D62** (2000), 043003, arXiv:hep-ph/9904481 [hep-ph].

[255] F. Donato, N. Fornengo, and D. Maurin, *Antideuteron fluxes from dark matter annihilation in diffusion models*, Phys.Rev. **D78** (2008), 043506, arXiv:0803.2640 [hep-ph].

[256] H. Fuke, T. Maeno, K. Abe, S. Haino, Y. Makida, et al., *Search for cosmic-ray antideuterons*, Phys.Rev.Lett. **95** (2005), 081101, arXiv:astro-ph/0504361 [astro-ph].

[257] V. Choutko and F. Giovacchini (on behalf of the AMS Collaboration), *Cosmic Rays Antideuteron Sensitivity for AMS-02 Experiment*, Proceedings of the 30th International Cosmic Ray Conference (2007).

[258] J. Koglin, T. Aramaki, S. Boggs, W. Craig, H. Fuke, et al., *Antideuterons as an indirect dark matter signature: Design and preparation for a balloon-born GAPS experiment*, J.Phys.Conf.Ser. **120** (2008), 042011.

[259] C. Hailey, W. Craig, F. A. Harrison, J. Hong, K. Mori, et al., *Development of the gaseous antiparticle spectrometer for space - based antimatter detection*, Nucl.Instrum.Meth. **B214** (2004), 122–125, arXiv:astro-ph/0306589 [astro-ph].

[260] C. Hailey, T. Aramaki, W. W. Craig, L. Fabris, F. Gahbauer, et al., *Accelerator testing of the general antiparticle spectrometer, a novel approach to indirect dark matter detection*, JCAP **0601** (2006), 007, arXiv:astro-ph/0509587 [astro-ph].

[261] P. Artoisenet and E. Braaten, *Estimating the Production Rate of Loosely-bound Hadronic Molecules using Event Generators*, Phys.Rev. **D83** (2011), 014019, arXiv:1007.2868 [hep-ph].

[262] ALEPH Collaboration, S. Schael et al., *Deuteron and anti-deuteron production in e^+e^- collisions at the Z resonance*, Phys.Lett. **B639** (2006), 192–201, arXiv:hep-ex/0604023 [hep-ex].

[263] M. Kadastik, M. Raidal, and A. Strumia, *Enhanced anti-deuteron Dark Matter signal and the implications of PAMELA*, Phys.Lett. **B683** (2010), 248–254, arXiv:0908.1578 [hep-ph].

[264] C. B. Brauninger and M. Cirelli, *Anti-deuterons from heavy Dark Matter*, Phys.Lett. **B678** (2009), 20–31, arXiv:0904.1165 [hep-ph].

[265] Y. Cui, J. D. Mason, and L. Randall, *General Analysis of Antideuteron Searches for Dark Matter*, JHEP **1011** (2010), 017, arXiv:1006.0983 [hep-ph].

[266] C.-R. Chen, F. Takahashi, and T. Yanagida, *High-energy Cosmic-Ray Positrons from Hidden-Gauge-Boson Dark Matter*, Phys.Lett. **B673** (2009), 255–259, arXiv:0811.0477 [hep-ph].

[267] P. Ullio, L. Bergstrom, J. Edsjo, and C. G. Lacey, *Cosmological dark matter annihilations into gamma-rays – a closer look*, Phys.Rev. **D66** (2002), 123502, arXiv:astro-ph/0207125 [astro-ph].

[268] L. Pieri, J. Lavalle, G. Bertone, and E. Branchini, *Implications of High-Resolution Simulations on Indirect Dark Matter Searches*, Phys.Rev. **D83** (2011), 023518, arXiv:0908.0195 [astro-ph.HE].

[269] C. Boehm, T. Delahaye, and J. Silk, *Can the morphology of gamma-ray emission distinguish annihilating from decaying dark matter?*, Phys.Rev.Lett. **105** (2010), 221301, arXiv:1003.1225 [astro-ph.GA].

[270] S. Palomares-Ruiz and J. M. Siegal-Gaskins, *Annihilation vs. Decay: Constraining dark matter properties from a gamma-ray detection*, JCAP **1007** (2010), 023, arXiv:1003.1142 [astro-ph.CO].

[271] M. D. Kistler and J. M. Siegal-Gaskins, *Gamma-ray signatures of annihilation to charged leptons in dark matter substructure*, Phys.Rev. **D81** (2010), 103521, arXiv:0909.0519 [astro-ph.HE].

[272] E. Borriello, A. Cuoco, and G. Miele, *Secondary radiation from the Pamela/ATIC excess and relevance for Fermi*, Astrophys.J. **699** (2009), L59–L63, arXiv:0903.1852 [astro-ph.GA].

[273] D. Hooper and P. D. Serpico, *Angular Signatures of Dark Matter in the Diffuse Gamma Ray Spectrum*, JCAP **0706** (2007), 013, arXiv:astro-ph/0702328 [astro-ph].

[274] C. Calcaneo-Roldan and B. Moore, *The Surface brightness of dark matter: Unique signatures of neutralino annihilation in the galactic halo*, Phys.Rev. **D62** (2000), 123005, arXiv:astro-ph/0010056 [astro-ph].

[275] I. V. Moskalenko and T. A. Porter, *Isotropic Gamma-Ray Background: Cosmic-Ray Induced Albedo from Debris in the Solar System?*, Astrophys.J. **692** (2009), 54–57, arXiv:0901.0304 [astro-ph.HE].

[276] A. W. Strong, I. V. Moskalenko, and O. Reimer, *Diffuse galactic continuum gamma rays. A Model compatible with EGRET data and cosmic-ray measurements*, Astrophys.J. **613** (2004), 962–976, arXiv:astro-ph/0406254 [astro-ph].

[277] M. Ackermann, www-conf.slac.stanford.edu/tevpa09/.

[278] E. Baltz, B. Berenji, G. Bertone, L. Bergstrom, E. Bloom, et al., *Pre-launch estimates for GLAST sensitivity to Dark Matter annihilation signals*, JCAP **0807** (2008), 013, arXiv:0806.2911 [astro-ph].

[279] V. Barger, Y. Gao, W. Y. Keung, and D. Marfatia, *Generic dark matter signature for gamma-ray telescopes*, Phys.Rev. **D80** (2009), 063537, arXiv:0906.3009 [hep-ph].

[280] PAMELA Collaboration, O. Adriani et al., *PAMELA results on the cosmic-ray antiproton flux from 60 MeV to 180 GeV in kinetic energy*, Phys.Rev.Lett. **105** (2010), 121101, arXiv:1007.0821 [astro-ph.HE].

[281] D. Spolyar, M. R. Buckley, K. Freese, D. Hooper, and H. Murayama, *High Energy Neutrinos As A Test of Leptophilic Dark Matter*, (2009), arXiv:0905.4764 [astro-ph.CO].

[282] P. J. Fox and E. Poppitz, *Leptophilic Dark Matter*, Phys.Rev. **D79** (2009), 083528, arXiv:0811.0399 [hep-ph].

[283] B. Kyae, *PAMELA/ATIC anomaly from the meta-stable extra dark matter component and the leptophilic Yukawa interaction*, JCAP **0907** (2009), 028, arXiv:0902.0071 [hep-ph].

[284] X.-J. Bi, X.-G. He, and Q. Yuan, *Parameters in a class of leptophilic models from PAMELA, ATIC and FERMI*, Phys.Lett. **B678** (2009), 168–173, arXiv:0903.0122 [hep-ph].

[285] H. Davoudiasl, *Dark Matter with Time-Varying Leptophilic Couplings*, Phys.Rev. **D80** (2009), 043502, arXiv:0904.3103 [hep-ph].

[286] T. Cohen and K. M. Zurek, *Leptophilic Dark Matter from the Lepton Asymmetry*, Phys.Rev.Lett. **104** (2010), 101301, arXiv:0909.2035 [hep-ph].

[287] E. J. Chun, J.-C. Park, and S. Scopel, *Dirac gaugino as leptophilic dark matter*, JCAP **1002** (2010), 015, arXiv:0911.5273 [hep-ph].

[288] N. Haba, Y. Kajiyama, S. Matsumoto, H. Okada, and K. Yoshioka, *Universally Leptophilic Dark Matter From Non-Abelian Discrete Symmetry*, Phys.Lett. **B695** (2011), 476–481, arXiv:1008.4777 [hep-ph].

[289] J. Kopp, V. Niro, T. Schwetz, and J. Zupan, *DAMA/LIBRA and leptonically interacting Dark Matter*, Phys.Rev. **D80** (2009), 083502, arXiv:0907.3159 [hep-ph].

[290] L. Bergstrom, *Radiative Processes in Dark Matter Photino Annhilation*, Phys.Lett. **B225** (1989), 372.

[291] T. Bringmann, L. Bergstrom, and J. Edsjo, *New Gamma-Ray Contributions to Supersymmetric Dark Matter Annihilation*, JHEP **0801** (2008), 049, arXiv:0710.3169 [hep-ph].

[292] J. B. Dent, R. J. Scherrer, and T. J. Weiler, *Toward a Minimum Branching Fraction for Dark Matter Annihilation into Electromagnetic Final States*, Phys.Rev. **D78** (2008), 063509, arXiv:0806.0370 [astro-ph].

[293] M. Kachelriess, P. Serpico, and M. Solberg, *On the role of electroweak bremsstrahlung for indirect dark matter signatures*, Phys.Rev. **D80** (2009), 123533, arXiv:0911.0001 [hep-ph].

[294] N. F. Bell, J. B. Dent, T. D. Jacques, and T. J. Weiler, *W/Z Bremsstrahlung as the Dominant Annihilation Channel for Dark Matter*, Phys.Rev. **D83** (2011), 013001, arXiv:1009.2584 [hep-ph].

[295] P. Ciafaloni, D. Comelli, A. Riotto, F. Sala, A. Strumia, et al., *Weak Corrections are Relevant for Dark Matter Indirect Detection*, JCAP **1103** (2011), 019, arXiv:1009.0224 [hep-ph].

[296] V. Berezinsky, M. Kachelriess, and S. Ostapchenko, *Electroweak jet cascading in the decay of superheavy particles*, Phys.Rev.Lett. **89** (2002), 171802, arXiv:hep-ph/0205218 [hep-ph].

[297] T. Hahn, *Generating Feynman diagrams and amplitudes with FeynArts 3*, Comput.Phys.Commun. **140** (2001), 418–431, arXiv:hep-ph/0012260 [hep-ph].

[298] T. Hahn and M. Perez-Victoria, *Automatized one loop calculations in four-dimensions and D-dimensions*, Comput.Phys.Commun. **118** (1999), 153–165, arXiv:hep-ph/9807565 [hep-ph].

[299] A. Bartl, H. Fraas, and W. Majerotto, *Production and Decay of Neutralinos in e^+e^- Annihilation*, Nucl.Phys. **B278** (1986), 1.

[300] H. E. Haber and D. Wyler, *Radiative Neutralino Decay*, Nucl.Phys. **B323** (1989), 267.

[301] M. Garny, A. Ibarra, and D. Tran, *Work in progress.*

[302] L. Resnick, M. Sundaresan, and P. Watson, *Is there a light scalar boson?*, Phys.Rev. **D8** (1973), 172–178.

[303] M. Spira, A. Djouadi, D. Graudenz, and P. Zerwas, *Higgs boson production at the LHC*, Nucl.Phys. **B453** (1995), 17–82, arXiv:hep-ph/9504378 [hep-ph].

[304] A. Abdo, M. Ackermann, M. Ajello, W. Atwood, L. Baldini, et al., *Fermi LAT Search for Photon Lines from 30 to 200 GeV and Dark Matter Implications*, Phys.Rev.Lett. **104** (2010), 091302, arXiv:1001.4836 [astro-ph.HE].

[305] HEGRA Collaboration, F. Aharonian et al., *Search for TeV gamma-ray emission from the Andromeda galaxy*, Astron.Astrophys. **400** (2003), 153–159, arXiv:astro-ph/0302347 [astro-ph].

[306] A. Boyarsky, D. Iakubovskyi, O. Ruchayskiy, and V. Savchenko, *Constraints on decaying Dark Matter from XMM-Newton observations of M31*, Mon.Not.Roy.Astron.Soc. **387** (2008), 1361, arXiv:0709.2301 [astro-ph].

[307] MAGIC Collaboration, J. Aleksic et al., *MAGIC Gamma-Ray Telescope Observation of the Perseus Cluster of Galaxies: Implications for Cosmic Rays, Dark Matter and NGC 1275*, Astrophys.J. **710** (2010), 634–647, arXiv:0909.3267 [astro-ph.HE].

[308] M. F. Struble and H. J. Rood, *A Compilation of Redshifts and Velocity Dispersions for ACO Clusters*, Astrophys.J.Suppl. **125** (1999), 35–71.

[309] M. Meyer, D. Horns, and H.-S. Zechlin, *Cross Calibration of Imaging Air Cherenkov Telescopes with Fermi*, (2009), arXiv:0912.3754 [astro-ph.IM].

[310] CTA Consortium, *Design Concepts for the Cherenkov Telescope Array*, (2010), arXiv:1008.3703 [astro-ph.IM].

[311] I. de la Calle Perez and S. Biller, *Extending the sensitivity of air Cerenkov telescopes*, Astropart.Phys. **26** (2006), 69–90, arXiv:astro-ph/0602284 [astro-ph].

[312] S. K. Mandal, M. R. Buckley, K. Freese, D. Spolyar, and H. Murayama, *Cascade Events at IceCube+DeepCore as a Definitive Constraint on the Dark Matter Interpretation of the PAMELA and Fermi Anomalies*, Phys.Rev. **D81** (2010), 043508, arXiv:0911.5188 [hep-ph].

[313] J. T. Ruderman and T. Volansky, *Decaying into the Hidden Sector*, JHEP **1002** (2010), 024, arXiv:0908.1570 [hep-ph].

[314] D. A. Demir, L. L. Everett, M. Frank, L. Selbuz, and I. Turan, *Sneutrino Dark Matter: Symmetry Protection and Cosmic Ray Anomalies*, Phys.Rev. **D81** (2010), 035019, arXiv:0906.3540 [hep-ph].

[315] A. Strumia and F. Vissani, *Neutrino masses and mixings and...*, (2006), arXiv:hep-ph/0606054 [hep-ph].

[316] T. Schwetz, M. Tortola, and J. W. Valle, *Three-flavour neutrino oscillation update*, New J.Phys. **10** (2008), 113011, arXiv:0808.2016 [hep-ph].

[317] M. Honda, T. Kajita, K. Kasahara, S. Midorikawa, and T. Sanuki, *Calculation of atmospheric neutrino flux using the interaction model calibrated with atmospheric muon data*, Phys.Rev. **D75** (2007), 043006, arXiv:astro-ph/0611418 [astro-ph].

[318] L. Volkova and G. Zatsepin, *Fluxes of cosmic ray muons and atmospheric neutrinos at high energies*, Phys.Atom.Nucl. **64** (2001), 266–274.

[319] L. Pasquali and M. Reno, *Tau-neutrino fluxes from atmospheric charm*, Phys.Rev. **D59** (1999), 093003, arXiv:hep-ph/9811268 [hep-ph].

[320] G. Ingelman and M. Thunman, *High-energy neutrino production by cosmic ray interactions in the sun*, Phys.Rev. **D54** (1996), 4385–4392, arXiv:hep-ph/9604288 [hep-ph].

[321] H. Athar, F.-F. Lee, and G.-L. Lin, *Tau neutrino astronomy in GeV energies*, Phys.Rev. **D71** (2005), 103008, arXiv:hep-ph/0407183 [hep-ph].

[322] Frejus Collaboration., K. Daum et al., *Determination of the atmospheric neutrino spectra with the Frejus detector*, Z.Phys. **C66** (1995), 417–428.

[323] M. Gonzalez-Garcia, M. Maltoni, and J. Rojo, *Determination of the atmospheric neutrino fluxes from atmospheric neutrino data*, JHEP **0610** (2006), 075, arXiv:hep-ph/0607324 [hep-ph].

[324] IceCube Collaboration, R. Abbasi et al., *Determination of the Atmospheric Neutrino Flux and Searches for New Physics with AMANDA-II*, Phys.Rev. **D79** (2009), 102005, arXiv:0902.0675 [astro-ph.HE].

[325] IceCube Collaboration, M. Ackermann et al., *The IceCube Collaboration: Contributions to the 30th International Cosmic Ray Conference (ICRC 2007)*, (2007), arXiv:0711.0353 [astro-ph].

[326] D. Chirkin (for the IceCube Collaboration), *http://www.srl.utu.fi/auxdoc/kocharov/icrc2009/pdf/icrc1418.pdf*.

[327] V. Barger, W.-Y. Keung, G. Shaughnessy, and A. Tregre, *High energy neutrinos from neutralino annihilations in the Sun*, Phys.Rev. **D76** (2007), 095008, arXiv:0708.1325 [hep-ph].

[328] W. Lohmann, R. Kopp, and R. Voss, *Energy Loss of Muons in the Energy Range 1 GeV To 10000 GeV*, (1985).

[329] A. E. Erkoca, M. H. Reno, and I. Sarcevic, *Muon Fluxes From Dark Matter Annihilation*, Phys.Rev. **D80** (2009), 043514, arXiv:0906.4364 [hep-ph].

[330] S. Schonert, T. K. Gaisser, E. Resconi, and O. Schulz, *Vetoing atmospheric neutrinos in a high energy neutrino telescope*, Phys.Rev. **D79** (2009), 043009, arXiv:0812.4308 [astro-ph].

[331] D. Cowen (for the IceCube Collaboration), *Tau neutrinos in IceCube*, J.Phys.Conf.Ser. **60** (2007), 227–230.

[332] M. D'Agostino (for the IceCube Collaboration), *A Search For Atmospheric Neutrino-Induced Cascades with IceCube*, (2009), arXiv:0910.0215 [astro-ph.HE].

[333] Super-Kamiokande Collaboration, S. Desai et al., *Search for dark matter WIMPs using upward through-going muons in Super-Kamiokande*, Phys.Rev. **D70** (2004), 083523, arXiv:hep-ex/0404025 [hep-ex].

[334] T. Montaruli, *Review on Neutrino Telescopes*, Nucl.Phys.Proc.Suppl. **190** (2009), 101–108, arXiv:0901.2661 [astro-ph].

[335] C. Wiebusch (for the IceCube Collaboration), *Physics Capabilities of the IceCube DeepCore Detector*, (2009), arXiv:0907.2263 [astro-ph.IM].

[336] E. Resconi (on behalf of the IceCube Collaboration), *Status and prospects of the IceCube neutrino telescope*, Nucl.Instrum.Meth. **A602** (2009), 7–13, arXiv:0807.3891 [astro-ph].

[337] N.-E. Bomark, S. Lola, P. Osland, and A. Raklev, *Photon, Neutrino and Charged Particle Spectra from R-violating Gravitino Decays*, Phys.Lett. **B686** (2010), 152–161, arXiv:0911.3376 [hep-ph].

[338] D. Z. Freedman, P. van Nieuwenhuizen, and S. Ferrara, *Progress Toward a Theory of Supergravity*, Phys.Rev. **D13** (1976), 3214–3218.

[339] S. Deser and B. Zumino, *Consistent Supergravity*, Phys.Lett. **B62** (1976), 335.

[340] H. Pagels and J. R. Primack, *Supersymmetry, Cosmology and New TeV Physics*, Phys.Rev.Lett. **48** (1982), 223.

[341] M. Fukugita and T. Yanagida, *Baryogenesis Without Grand Unification*, Phys.Lett. **B174** (1986), 45.

[342] M. Bolz, W. Buchmuller, and M. Plumacher, *Baryon asymmetry and dark matter*, Phys.Lett. **B443** (1998), 209–213, arXiv:hep-ph/9809381 [hep-ph].

[343] J. Feng, *Supersymmetry and cosmology*, Annals Phys. **315** (2005), 2–51.

[344] M. Endo and T. Shindou, *R-parity Violating Right-Handed Neutrino in Gravitino Dark Matter Scenario*, JHEP **0909** (2009), 037, arXiv:0903.1813 [hep-ph].

[345] W. Buchmuller, M. Endo, and T. Shindou, *Superparticle Mass Window from Leptogenesis and Decaying Gravitino Dark Matter*, JHEP **0811** (2008), 079, arXiv:0809.4667 [hep-ph].

[346] K. Hamaguchi, F. Takahashi, and T. Yanagida, *Decaying gravitino dark matter and an upper bound on the gluino mass*, Phys.Lett. **B677** (2009), 59–61, arXiv:0901.2168 [hep-ph].

[347] S. Lola, P. Osland, and A. Raklev, *Radiative gravitino decays from R-parity violation*, Phys.Lett. **B656** (2007), 83–90, arXiv:0707.2510 [hep-ph].

[348] L. Bergstrom, *Dark Matter Candidates*, New J.Phys. **11** (2009), 105006, arXiv:0903.4849 [hep-ph].

[349] K. Ishiwata, S. Matsumoto, and T. Moroi, *High Energy Cosmic Rays from Decaying Supersymmetric Dark Matter*, JHEP **0905** (2009), 110, arXiv:0903.0242 [hep-ph].

[350] J. Wess and J. Bagger, *Supersymmetry and supergravity*, Princeton University Press, Princeton (1992).

[351] S. Weinberg, *The quantum theory of fields. Vol. 3: Supersymmetry*, Cambridge University Press, Cambridge (2000).

[352] M. Grefe, *Neutrino signals from gravitino dark matter with broken R-parity*, DESY-THESIS-2008-043 (2008).

[353] L. J. Hall, H. Murayama, and N. Weiner, *Neutrino mass anarchy*, Phys.Rev.Lett. **84** (2000), 2572–2575, arXiv:hep-ph/9911341 [hep-ph].

[354] G. Altarelli and F. Feruglio, *Models of neutrino masses and mixings*, New J.Phys. **6** (2004), 106, arXiv:hep-ph/0405048 [hep-ph].

[355] R. J. Gould and G. P. Schreder, *Pair Production in Photon-Photon Collisions*, Phys.Rev. **155** (1967), 1404–1407.

[356] R. C. Gilmore, P. Madau, J. R. Primack, R. S. Somerville, and F. Haardt, *GeV Gamma-Ray Attenuation and the High-Redshift UV Background*, (2009), arXiv:0905.1144 [astro-ph.CO].

[357] F. Stecker, S. Hunter, and D. Kniffen, *The Likely Cause of the EGRET GeV Anomaly and its Implications*, Astropart.Phys. **29** (2008), 25–29, arXiv:0705.4311 [astro-ph].

[358] http://www-glast.slac.stanford.edu/software/IS/glast_lat_performance.

[359] J. Pradler and F. D. Steffen, *Thermal gravitino production and collider tests of leptogenesis*, Phys.Rev. **D75** (2007), 023509, arXiv:hep-ph/0608344 [hep-ph].

[360] S. Davidson and A. Ibarra, *A Lower bound on the right-handed neutrino mass from leptogenesis*, Phys.Lett. **B535** (2002), 25–32, arXiv:hep-ph/0202239 [hep-ph].

[361] W. Buchmuller, P. Di Bari, and M. Plumacher, *Leptogenesis for pedestrians*, Annals Phys. **315** (2005), 305–351, arXiv:hep-ph/0401240 [hep-ph].

[362] J. L. Feng, H. Tu, and H.-B. Yu, *Thermal Relics in Hidden Sectors*, JCAP **0810** (2008), 043, arXiv:0808.2318 [hep-ph].

[363] L. Randall and R. Sundrum, *Out of this world supersymmetry breaking*, Nucl.Phys. **B557** (1999), 79–118, arXiv:hep-th/9810155 [hep-th].

[364] O. Lebedev, H. P. Nilles, S. Raby, S. Ramos-Sanchez, M. Ratz, et al., *A Mini-landscape of exact MSSM spectra in heterotic orbifolds*, Phys.Lett. **B645** (2007), 88–94, arXiv:hep-th/0611095 [hep-th].

[365] S. A. Abel, J. Jaeckel, V. V. Khoze, and A. Ringwald, *Illuminating the Hidden Sector of String Theory by Shining Light through a Magnetic Field*, Phys.Lett. **B666** (2008), 66–70, arXiv:hep-ph/0608248 [hep-ph].

[366] B. Holdom, *Two U(1)'s and Epsilon Charge Shifts*, Phys.Lett. **B166** (1986), 196.

[367] K. R. Dienes, C. F. Kolda, and J. March-Russell, *Kinetic mixing and the supersymmetric gauge hierarchy*, Nucl.Phys. **B492** (1997), 104–118, arXiv:hep-ph/9610479 [hep-ph].

[368] S. Abel and B. Schofield, *Brane anti-brane kinetic mixing, millicharged particles and SUSY breaking*, Nucl.Phys. **B685** (2004), 150–170, arXiv:hep-th/0311051 [hep-th].

[369] S. Abel, M. Goodsell, J. Jaeckel, V. Khoze, and A. Ringwald, *Kinetic Mixing of the Photon with Hidden U(1)s in String Phenomenology*, JHEP **0807** (2008), 124, arXiv:0803.1449 [hep-ph].

[370] S. Kachru, R. Kallosh, A. D. Linde, and S. P. Trivedi, *De Sitter vacua in string theory*, Phys.Rev. **D68** (2003), 046005, arXiv:hep-th/0301240 [hep-th].

[371] P. Gondolo, J. Edsjo, P. Ullio, L. Bergstrom, M. Schelke, et al., *DarkSUSY: Computing supersymmetric dark matter properties numerically*, JCAP **0407** (2004), 008, arXiv:astro-ph/0406204 [astro-ph].

[372] E. A. Baltz and J. Edsjo, *Positron propagation and fluxes from neutralino annihilation in the halo*, Phys.Rev. **D59** (1998), 023511, arXiv:astro-ph/9808243 [astro-ph].

[373] A. Cuoco, S. Hannestad, T. Haugbolle, G. Miele, P. Serpico, et al., *The Signature of Large Scale Structures on the Very High Energy Gamma-Ray Sky*, JCAP **0704** (2007), 013, arXiv:astro-ph/0612559 [astro-ph].

Acknowledgements

I would like to express my gratitude to my (second-time) thesis advisor, Alejandro Ibarra, for giving me the opportunity to move to Munich to write a timely dissertation on this interesting and very active field of research, for his scientific enthusiasm and for multiple collaborations over the past four years. I am also grateful for his support and the opportunity to travel to many conferences, workshops and schools all across the world, allowing me to gain valuable experience early on.

I am lucky to have had the opportunity of collaborating scientifically with a number of people over the last few years, and therefore I am happy to thank Wilfried Buchmüller, Laura Covi, Mathias Garny, Michael Grefe, Andreas Ringwald, Tetsuo Shindou, Fumihiro Takayama and especially Christoph Weniger for pleasant and fruitful collaborations.

I also want to express my appreciation for all the members of the high-energy physics community at TUM, in particular the present and past members of T30d and T30e, Carolin Bräuninger, Anna Brunnbauer, Matthias Danner, Maximilian Fallbacher, Maximilian Fischer, Michael Klaput, Christian Paleani, Björn Petersen, Roland Schieren, Kai Schmidt-Hoberg, Cristoforo Simonetto, Christian Staudt, Yasutaka Takanishi, Jesús Torrádo Cácho, Stefan Vogl and Martin Winkler, whom I thank for a very pleasant time and many interesting discussions, scientific and otherwise. Special thanks go out to Rolf Kappl for being a delightful and tolerant office mate. Furthermore, I am thankful to Karin Ramm for helping me deal with a lot of unedifying bureaucracy and for always being a good sport.

I am very grateful to Leigh Cressman for her loving support and understanding, which have helped me greatly, as well as for proofreading my English once again. Lastly, I want to express my gratitute towards my family for their support and encouragement, which made it possible for me to pursue a path in science. This thesis is dedicated to them.